A GMRT HI study of extremely faint dwarf galaxies

A Thesis

Submitted to the
Tata Institute of Fundamental Research, Mumbai
for the degree of Doctor of Philosophy
in (Physics)

by

Ayesha Begum

National Centre for Radio Astrophysics
Tata Institute of Fundamental Research
Pune – 411 007
October 2005

DECLARATION

This thesis is a presentation of my original research work. Wherever contributions of others are involved, every effort is made to indicate this clearly, with due reference to the literature, and acknowledgment of collaborative research and discussion.

The work was done under the guidance of Dr Jayaram N. Chengalur at the National Centre for Radio Astrophysics, Tata Institute of Fundamental Research, Pune.

Ayesha Begum

In my capacity as supervisor of Ms Ayesha Begum, I certify that the above statements are true to the best of my knowledge.

Jayaram N. Chengalur

Date:

To my Ammi

Acknowledgment

Best things in life are unexpected. When I joined TIFR Mumbai as a graduate student, I had not expected at all that I would work for my PhD in a field that I was least familiar with. More than four years have gone by, since the day I started working on what has now become my Ph.D. thesis. Many people have been on my side, in different ways, in this wonderful learning experience, both on personal and scientific level. It is more than a word of thanks that I owe to all those who have made my life an enriching experience in these years. I hope to be able to reciprocate someday by giving, perhaps to another set of people, what I have received from them.

Let me start by expressing my sincere thanks and gratitude to my supervisor, Dr Jayaram N. Chengalur, for all the guidance and encouragement he has offered me throughout the period of this research. I feel that I have been extremely lucky to encounter an advisor like him. Jayaram is not only a great scientist with deep vision, but also, and most importantly, a very kind person. He was always there when I needed him; his numerous ideas, suggestions and criticism helped me in the most important moments of making right decisions. For an impulsive and jumpy person like me, it would have been impossible to finish my PhD if he would not have been there; he always made sure that I did not get carried away and loose perspective. All thank to Jayaram, for always believing in me and reminding me that the journey to a goal, is one step at a time.

I also wish to express my gratitude for numerous scientific discussions and assistance given by Prof Rajaram Nityananda. Infact, it is unlikely that I would have chosen radio astronomy as my field of research if I haven't met Rajaram in TIFR Mumbai. Much of my basic radio interferometry background was acquired from the reading course on Radio interferometric techniques that I took with him. He always had enough patience to clarify all my stupid doubts.

I thank Prof Ananth Krishnan and Prof Gopal Krishna for motivating me to become a radio astronomer. When I visited NCRA as a graduate student from TIFR, Mumbai, Gopal introduced me to the field of radio astronomy, whereas Ananth's enthusiasm about GMRT's potentials for carrying out research in problems at the frontiers of astrophysics got me started in this field.

I would like to thank my academic committee members in NCRA, Prof Pramesh Rao, Prof Vasant Kulkarni and Dr Ramana Athreya for their advice and useful comments. Special thanks to Prof D J Sakia (Sykes) for all his help. I have benefited greatly from his many suggestions regarding my thesis and other work. I also thank Dr Deepanjan Mitra for helping me in fixing my C programs and also for all the useful scientific discussions and about life

in general.

I thank my collaborators, Prof Igor Karachentsev and Dr Somnath Bharadwaj who were always quick in replying to my emails and providing me all the information that I needed for my research work. Very special thanks to Som for his very useful comments on the powerspectrum work.

A special thanks to my MSc teacher Dr S Roy Choudhary who encouraged me to take up research as a career. I also like to thank Dr Patrick Das Gupta, Dr. Amitabh Mukerjee and Dr Daksh Lohia for all their advices and help during my MSc days at Delhi University. I thank my BSc teacher Dr Bikram Phookan who has always been a source of inspiration for me.

A special acknowledgment goes to one individual, who saw me through all the joys and frustrations of this research, Mr. Kumar Vigyanik of NCRA (Dharam). Dharamji has been a very good friend; he provided me a shoulder to cry on, whenever I needed it and I take this opportunity to thank him for his invaluable help. I also thank his lovely wife Babita for all the nice dinners that she provided and for all the fun time that we had together. Dharamji and Babita are one of the sweetest couples I have met in my life.

A special thank to Nissim who has been a wonderful mentor to me (I am sure Nissim will not like this comment !!). He helped me out with lots of my problems during my stay in NCRA. I also thank Subhashis for taking some time out to clarify my understanding of image processing, and the questions that arose in that area, during this research.

Thanks to all the staff at the GMRT, specially Mangesh, Manisha, Manish, Sanjay, Jayprakash, Jitendra, Santaji, Deepak, Sachin, Aba for their assistance in carrying out the thesis observations. Special thanks for my friend Manisha, who provided me a good company which made my stay during the GMRT observations very cheerful one. I thank Charu, Shindeji, Kiran, Chouguleji, Pravin for all the fun that I had during the NCRA-GMRT cricket matches. I also like to thank the engineering staff specially NVN, TLV, Ajit Kumar and Pravin Kumar for their help in solving the telescope related problems during my observations.

I thank all my friends, Anand, Neeraj, Sandhya, Punya, Chiranjeev, Bhaswati, Jayanto, Nirupam, Ekta, Sameer for all the good times that we had together at NCRA. Special thanks to Aaaaaamir in whom I found I very good friend; he is one of the nicest people I met during my stay at Pune. Sorry Aamir for making you go through all the troubles (specially during your training in AIPS !!). A special thanks to Akila and Rajvi for going out of their way to take care of me after my accident. Thanks to Akila for giving such a nice company to me during her stay in NCRA. Special thanks to Amitesh for all the interesting scientific

discussions. Thanks to Poonam who helped me a lot when I was planning to join NCRA for my PhD. I also thank my batchmates in TIFR, Deepak, Ashutosh, Swamiji (Kanchan), Shubandhu, Ajay, Apoorva, Vaibhav who made my stay at TIFR Mumbai a pleasant one.

I would like to thank IAU for providing me complete financial support to attend the IAU General Assembly at Sydney, Australia. Thanks to Prof Lister Staveley-Smith and Prof Rachel Webster for providing me an opportunity to visit the ATNF and University of Melbourne respectively, during my visit to Australia. I special thanks to Prof Ravi Subrahmanyan and Dr Laxshmi Saripalli for the great hospitality and care they provided, and made me feel completely at home when I visited Narrabri.

I would like to thank Hemantji, Abhijit Barve, Shettiji, Solankiji and Hari for their help in administrative matters. Special thanks to VVS for coming to my rescue, even during holidays, to fix my computer related problems. Thanks to Sunita for providing me all the scientific papers that I needed for my PhD work. Thanks also to the NCRA canteen staff for feeding me for the last four years.

The episode of acknowledgment would not be complete without the mention of Annabhatt. I must say that the presence of Annaji in NCRA was like a blessing for me. His enthusiasm for everything, be it arranging for movies, treks, cultural programs, cricket matches etc. made my stay at NCRA a very cheerful one.

Most of all, I would like to thank my parents, specially my mother, for without her guidance, discipline, and love, I would not have turned out to be the person I am today.

LIST OF PUBLICATIONS

In Refereed Journals

1. *Powerspectrum analysis of HI emission in faint dwarf galaxies*
   Ayesha Begum, Jayaram N. Chengalur & Somnath Bharadwaj, 2005 (in preparation)

2. *Gas distribution, kinematics and star formation in faint dwarf galaxies*
   Ayesha Begum, Jayaram N. Chengalur, Igor D. Karachentsev, S. S. Kaisin & M. Sharina, 2005 (MNRAS, in press; astro-ph/0511253)

3. *A search for HI in some peculiar faint dwarf galaxies*
   Ayesha Begum & Jayaram N. Chengalur, MNRAS, 2005, 362, 609

4. *Resolving the mystery of the dwarf galaxy HIZSS003*
   Ayesha Begum, Jayaram N. Chengalur, Igor D. Karachentsev & M. Sharina, MNRAS(Lett), 2005, 359, L53

5. *A dwarf galaxy with a giant HI disk*
   Ayesha Begum, Jayaram N. Chengalur & Igor D. Karachentsev, A&A(Lett), 2005, 433, L1

6. *Kinematics of two dwarf galaxies in the NGC 6946 group*
   Ayesha Begum & Jayaram N. Chengalur, A&A, 2004, 424, 509.

7. *Kinematics of the faintest gas rich galaxy in the Local Group: DDO210*
   Ayesha Begum & Jayaram N. Chengalur, A&A, 2004, 413 525.

8. *Kinematics of the dwarf irregular galaxy GR8*,
   Ayesha Begum & Jayaram N. Chengalur, A&A, 2003, 409, 879.

9. *The little galaxy that could: kinematics of Camelopardalis B*
   Ayesha Begum, Jayaram N. Chengalur & Ulrich Hopp, New Ast 2003, 8, 267.

In Conference Proceedings

1. *GMRT study of extremely faint dwarf irregular galaxies*
   Ayesha Begum & Jayaram N. Chengalur, BASI, 2004, 32, 231.

2. *Kinematics of extremely faint dwarf galaxies,*
   Ayesha Begum & Jayaram N. Chengalur, IAUS. 2004, 220, 347.

Synopsis

This thesis is based on high velocity resolution ($\sim$ 1.6 km s^{-1}) GMRT HI 21 cm-line observations of a sample of fifteen extremely faint ($M_B \gtrsim -13.0$) dwarf galaxies. The broad aims of the thesis are to use these observations to (i) determine the density profiles of the dark matter halos of extremely faint dwarf galaxies and (ii) understand the interplay between the neutral ISM and star formation in these galaxies.

The high velocity resolution and high sensitivity of the GMRT observations are crucial to achieve the aims of the thesis, since the expected magnitude of the rotation velocities of such faint galaxies is very small. From our observations, we found that all the sample galaxies have large scale velocity gradients. This is in contrast to earlier coarser velocity resolution ($\sim$ 6.5 km s^{-1}) observations, from which it appeared that faint dwarfs have chaotic velocity fields (e.g. Lo et al. 1993, AJ, 106, 507). For some of our sample galaxies, (e.g. Camelopardalis B ($M_B \sim -11.8$) and DDO 210 ($M_B \sim -11.0$), the velocity fields are consistent with rotation, though the peak rotational velocities are comparable to the velocity dispersion. The observed rotational velocities hence require a substantial correction (akin to the "asymmetric drift" correction), before they can be used to model the density distribution in these galaxies. From our modeling of the corrected rotation curves, we find that, in general, the kinematics are well fitted by the traditionally used "modified isothermal halo" model, whereas theoretically favored cuspy Navarro-Frenk-White (NFW; Navarro et al. 1997, ApJ, 490, 493) halos do not provide a good fit to the data. In hierarchical models of galaxy formation, faint dwarf galaxies have the highest dark matter densities, as they are the earliest ones to form. We searched for such trends in the dark halo properties of disk galaxies by adding to our sample published data for brighter disk galaxies. This compiled sample spans a luminosity range of $\sim$ 12 magnitudes, but we find at best a weak trend for increasing halo central density with decreasing galaxy size. We also made a preliminary examination of the Tully-Fisher (TF) relation using this compiled sample. While the TF relation is generally studied using the inclination corrected 50% profile width (usually obtained from single dish observations), it is not the best measure to use for the faintest dwarf galaxies, where, (i) as mentioned above, the rotational velocities are comparable to the velocity dispersion, and (ii) the disk inclination may be difficult to determine from the patchy optical emission. HI synthesis observations provide a way around both these problems. From our examination of the TF relation, we find, in broad agreement with earlier studies, (which used single dish HI data; see McGaugh et al. 2000; ApJL, 533, 99), that dwarf galaxies tend to lie below the TF relation defined by brighter galaxies.

Some of our sample galaxies have velocity fields that are not well fit by the patterns

expected from rotating gas disks. This may be a consequence of energy input from star formation processes or supernovae; indeed it has for long been a theoretical prediction that the energy input from a vigorous star burst should be sufficient to cause the faintest dwarf galaxies to completely lose their ISM. For one galaxy viz. GR8 ($M_B \sim -12.11$) in our sample which has a well defined large scale velocity field, we carried out detailed modelling of the kinematics. Our modelling showed that neither pure rotation, nor pure radial motion alone can fit the observed velocity field of the galaxy; however a combination of radial and circular motions can provide a reasonable fit. The most natural interpretation is that the neutral ISM, in addition to rotating about the center, is also expanding outwards, as a result of energy input from the ongoing star formation in the galaxy. Support for this interpretation comes from the fact that the pressure in the HII regions in the galaxy is known to be substantially ($\sim$ 55 times) more than the average pressure in the gas disk. It is, however, also possible that the velocity field is the result of the gas swirling inwards, in which case GR8 could be in the process of formation via the merger of subgalactic clumps.

It has been suggested that star formation in dwarf galaxies occurs only above a threshold HI column density (e.g. Skillman, 1987, NASA, 263; Taylor et al. 1994 AJ, 107, 971), although it is unclear whether this threshold is a consequence of disk dynamics (e.g. related to Toomre's (1964, ApJ, 139, 1217) instability criterion) or is a consequence of some other physical process (e.g. self shielding). In this context, our sample of galaxies is particularly interesting, since they have systematic rotation which is at best of comparable magnitude to the velocity dispersion. Since the observed column density is resolution dependent, a comparison of HI column densities at the same linear resolution is important for such studies. The GMRT observations are particularly well suited to this problem since, from a single observation, one can make maps with angular resolutions varying from, $\sim$ 40 arc-seconds to a few arc-seconds. For this study we also included two faint irregular galaxies viz. SagDIG ($M_B \sim -11.5$) and Leo A ($M_B \sim -11.3$), for which multi-configuration VLA data could be obtained from the VLA archive. The archival data was reanalyzed to make maps at the appropriate angular resolution. We find that (at a linear resolution of $\sim$ 300 pc), star formation in extremely faint dwarfs occurs only above a threshold density of $\sim 10^{21}$ cm^{-2}. This is comparable to the thresholds found in much brighter dwarfs (e.g. vanZee et al. 1997, AJ, 113, 1618). Interestingly, the average metallicity of our sample galaxies is quite low (12+log[O/H]$\sim$7.45), indicating that the star formation threshold is not much affected by metallicity. We also find that this threshold density is applicable only when one smooths over relatively large spatial scales; when looked at with sufficiently high spatial resolution ($\sim 50 - 100$ pc) many of the star forming regions in our sample galaxies do not in fact

coincide with peaks in the HI distribution. Finally, it has been suggested (Young et al. 2003, ApJ, 592, 111) that the shapes of the HI line profiles could be used as a tracer of star formation activity in dwarf galaxies. In particular, it has been suggested that asymmetric profiles and/or profiles which contain a narrow ("cold") component are found in regions of ongoing star formation. We carried out a detailed analysis of the HI line profile shapes across the disks of all the sample galaxies. However, no particular correlation is found between asymmetric profiles and star formation activity in our sample.

The HI distribution in some of our sample galaxies is very interesting in its own right. The most note worthy being the extremely extended disk of NGC 3741 ($M_B \sim -13.13$). GMRT observations of this galaxy showed that is has a gas disk that extends to ~ 8.3 times its Holmberg radius. This makes it probably the most extended gas disk known. Our observations allow us to derive the rotation curve (which is flat in the outer regions) out to $\sim$38 optical scale lengths. NGC 3741 has a dynamical mass to light ratio of $\sim$107 and is one of the "darkest" irregular galaxies known. However, the bulk of the baryonic mass in NGC 3741 is in the form of gas and the ratio of the dynamic mass to the baryonic mass (~ 8), falls within the range that is typical for galaxies. Thus the dark matter halo of NGC 3741 has acquired its fair share of baryons, but for some reason, these baryons have been unable to collapse to form stars. NGC 3741's dark halo properties were compared with those of a sample of galaxies with well measured rotation curves. The results showed that if we want to reconcile the observations with the theoretical expectation that low mass galaxies suffer fractionally greater baryon loss, then, the baryon loss from halos must occur in such a way that the remaining baryons occupy a fractionally smaller volume of the total halo.

Another surprise is the dwarf irregular galaxy HIZSS003. This galaxy was recently discovered during a blind HI survey of the zone of avoidance (Henning et al. 2000, AJ, 119, 2686). Follow up VLA as well as optical and near-IR imaging and spectroscopy (Massey et al. 2003, AJ, 126, 2362; Silva et al. 2005, astro-ph/0501545) confirm that it is a low metallicity dwarf irregular galaxy. However there were two puzzling aspects of the observations, (i) current star formation, as traced by Hα emission, is confined to a small region at the edge of the VLA HI image and (ii) the metallicity of the older red giant branch stars is higher than that of the gas in HII region. Our high spatial and velocity resolution GMRT observations resolved these puzzles by showing that HIZSS003 is actually a galaxy pair and that the HII region lies at the center of a much smaller companion galaxy (HIZSS003B) to the main galaxy (HIZSS003A). The HI emission from these two galaxies overlaps in projection, but can be separated in velocity space.

No HI was detected in three galaxies in our sample viz. POX 186 ($M_B \sim -12.7$), SC 24

($M_B \sim -8.4$) and KKR 25 ($M_B \sim -9.9$). Based, in part, on previous single dish HI observations, these galaxies had been classified as a BCD, a dwarf irregular and a transition galaxy respectively. However, in conflict with previous single dish detections, we did not detect HI in SC 24 or KKR 25. We suggest that the previous single dish measurements were probably confused with the local galactic emission. In the case of POX 186, we confirm the previous non detection of HI but with substantially improved limits on its HI mass. Our derived upper limits on the HI mass of SC 24 and KKR 25 are similar to the typical HI mass limits for dwarf spheroidal galaxies, whereas in the case of POX 186, we find that its gas content is somewhat smaller than is typical of BCD galaxies.

Evidence has been mounting in recent years that turbulence plays an important role in the physics of the ISM as well as in governing star formation. A major piece of observational evidence for the existence of turbulence in the neutral ISM is the fact that the power spectrum of the intensity fluctuations of HI 21cm emission is a scale free power law. This appears to be the case both in our own galaxy (Green, 1993, MNRAS, 262, 327) as well as in our companion dwarf galaxies (LMC ;Elmegreen et al, AJ, 2001, 548, 749, SMC; Stanimirovic et al. 1999, MNRAS, 302, 417). We discuss techniques for obtaining the power spectrum of the HI intensity fluctuations in our faint dwarf galaxies, where the expected signal is very weak. Our analysis is focussed on visibility based techniques, since the statistics are best understood in the visibility plane. We also present an application of this technique to some of the sample galaxies.

Contents

List of Tables

List of Figures

Chapter 1

Introduction

1.1 Introduction

Dwarf galaxies are the most abundant type of galaxies found in our local universe. In hierarchical structure formation scenarios, dwarf galaxy sized objects are the first structures to collapse in the early universe, hence the study of dwarf galaxies could provide important clues about galaxy formation and evolution. Based on their gas content and current rate of star formation, dwarf galaxies can be loosely classified into three different types viz. dwarf irregular (dIrr) galaxies, blue compact dwarf (BCD) galaxies and dwarf spheroidal (dSph) galaxies. dIrrs are gas rich and have some on-going star formation, BCDs are also gas rich but their optical appearance is dominated by an on-going star burst, while dSphs have little to no gas and generally no measurable on-going star formation.

The word "dwarf" connotes small size; when applied to a galaxy, it generally means a small optical luminosity. However there is no clear-cut definition of the dwarf galaxy class. Typically, a galaxy is called a dwarf if it has an absolute blue band magnitude (M_B) greater than -17.0 mag. However sometimes galaxies with $M_B \sim -18.0$ are also classified as dwarfs; for example the nearest neighbors to our own galaxy viz. LMC and SMC with M_B of -17.9 and -16.5, respectively, are both classified as dwarfs. In comparison, M_B for a typical L_* spiral galaxy like the MilkyWay or M31 is ~ -21.0 mag. This thesis describes a study of extremely faint $M_B \widetilde{>} -13.5$ dwarf galaxies, i.e. galaxies that are $\sim 7-8$ orders of magnitude fainter than our own galaxy.

HI 21cm aperture synthesis observations of spiral galaxies is a mature field with over three decades of history – probably something of the order of a thousand galaxies have already been imaged. However, the observations have tended to focus on bright ($\sim L_*$) galaxies with HI masses $\sim 10^9$ $M_\odot$. Dwarf galaxies require substantial investments of telescope time, and have hence not been studied in similar numbers. The situation however has changed a little

in the recent past, with at least three major HI imaging studies of dwarf galaxies ([2, 16, 15]. However, even these studies have generally been restricted to the brighter dwarf galaxies, the Côte [2] sample which contains the faintest galaxies is generally restricted to galaxies with $M_B \widetilde{<} -14$. In this thesis we present high quality observations of the atomic ISM, through GMRT observations of the 21-cm line of HI of even fainter dwarf galaxies, viz. those with $M_B \widetilde{>} -13.5$. The broad aims of the thesis are to use these observations to (i) determine the density profiles of the dark matter halos of extremely faint dwarf galaxies and (ii) understand the interplay between the neutral ISM and star formation in these galaxies.

1.2 Dark matter in dwarf galaxies

There are a number of reasons why extremely faint dwarf galaxies are interesting to study in detail. The first is related to the structure of the dark matter halos of these galaxies. Traditionally, dark matter halos have been modeled as "modified isothermal" halos for which the density is constant in the central regions. However, numerical simulations of galaxy formation in hierarchical structure formation models (such as the standard CDM or ΛCDM models) predict that galaxy halos should have cuspy central density distributions (e.g. [8, 12]). In particular, for the popular Navarro et al.(1996) model, (generally referred to as the "NFW" halo), the density in the central regions increases as r^{-1}. Unfortunately, it turns out that it is difficult to distinguish between isothermal and NFW halos from the observed kinematics of normal spiral galaxies. This is because the gravitational force in the central parts of these galaxies is usually dominated by the mass of the stellar disk. Disentangling the contribution from the dark matter halo hence requires knowledge of the mass to light ratio (M/L) of the stellar disk, which is often poorly constrained. Depending on the assumed disk M/L ratio, equally good fits to the observed kinematics can be obtained using either isothermal halos or NFW halos. Dwarf galaxies, on the other hand, are often dark matter dominated, even in their inner parts, (e.g. DDO 154 [1]) and consequently their kinematics can be used to constrain the structure of their dark matter halos with minimum uncertainties due to the unknown M/L ratio of the stellar disk.

Apart from the shapes of galaxy halos, numerical simulations also predict correlations between various physical parameters of the halo, most notably between the characteristic density and the virial mass (e.g. [11]). The characteristic density is found to anti-correlate with the virial mass, i.e. the lowest mass halos have the highest densities. In hierarchical scenarios the low mass halos form at the earliest times (at which time the background density is the highest) and if there is a constant relation between the background density and the characteristic density of the collapsed halo then such a relation is to be expected. The

correlation found in numerical simulations is however both weak (a large change in the virial mass of the halo leads to relatively small changes in the characteristic density) and noisy. To test whether such correlations are present in real galaxies, it is useful to have data on as wide a range of galaxy masses as possible. While there is already a wealth of kinematical data for bright spiral galaxies, the number of dwarf galaxies, in particular extremely faint (fainter than $M_B \sim -14$) dwarf galaxies, for which good kinematical data is available, is very limited.

However a major stumbling block in the dark matter distribution studies of such faint dwarf galaxies is that it is unclear whether the faintest dwarf irregular galaxies are rotationally supported or not. In a systematic study of 9 faint dwarf galaxies, Lo et al.(1993) found that only two galaxies showed ordered velocity fields, whereas the remaining galaxies all had chaotic velocity fields. Further, from independent observations of the extremely faint dwarf galaxy GR8, Carignan et al.(1990)($M_B \sim -12.0$,) showed that although the galaxy had a somewhat ordered HI velocity field, the implied kinematical major axis was perpendicular to the major axis of the optical and HI disk. Similarly, Cote et al.(2000) found an ordered velocity field for SDIG ($M_B \approx -11.5$), but again the kinematical major axis was found to be perpendicular to the major axis of the optical disk. All of this lead Cote et al.(2000) to suggest that normal rotation is seen only in dwarfs brighter than $M_B \sim -14$, and that by $M_B \sim -13$ one begins to find systems with misaligned axis, and other kinematical peculiarities. These peculiarities make it difficult, if not impossible, to model the kinematics of these galaxies using traditional mass models. This is unfortunate, since it is these very faint systems (which presumably formed at the earliest epochs and are the most dark matter dominated) which could be particularly useful in determining dark halo properties. For some of the galaxies studied as a part of this thesis, we found large scale gradients in their velocity field which could be modelled as systematic rotation, thus providing us a unique opportunity to study the dark matter distribution in extremely faint dwarf galaxies.

1.2.1 Tully-Fisher relation

It has been recently suggested that faint galaxies show systematic deviations from the Tully-Fisher (TF) relation as defined by bright galaxies. Swaters [16] and Stil [15] found that dwarf galaxies lie below the extrapolated TF relation for the brighter galaxies i.e. dwarf galaxies are underluminous for their velocity widths. Further, McGaugh et. al. [10] found that if instead of the luminosity one uses the total baryonic mass (i.e. the sum of stellar and gas mass) then one restores the linear TF relation even at the faint end. This would support earlier suggestions of the existence of a "baryonic" Tully-Fisher relation i.e. a relation between

the potential of the dark matter halo (as traced by the rotation velocity) and the total baryonic mass [21]. We note however that the "dwarf galaxies" of previous studies were generally brighter than -14 magnitude. Whether such "baryonic" correction is necessary (and sufficient) for galaxies fainter than -14.0 magnitude is still not known. Further, we note that the Mcgaugh et al. (2000) study was based on single dish measurements of the width of the line profile. While for the brighter galaxies W_{50} (the velocity width at 50% emission), once corrected for random motions and instrumental broadening, is a good measure of the rotational velocity of the galaxy [20], it is unclear whether this is an appropriate measure to use for the faintest dwarf galaxies, where the rotational velocities are comparable to the velocity dispersion. For such galaxies, it is important to accurately correct for the pressure support ("asymmetric drift" correction) for which one needs to know both the rotation curve as well as the distribution of the HI gas, both of which can only be obtained by interferometric observations such as those obtained as a part of this thesis. Further, for the faint dwarf irregulars, even the inclination may be difficult to estimate from the optical image and may only be obtainable from the HI distribution and kinematics. Unfortunately, the number of faint dwarf galaxies with sufficiently high quality HI synthesis images available is quite small. One of the goals of this thesis is to use the interferometric observations to obtain the TF relation for extremely faint dwarf galaxies.

1.3 Star formation in dwarf galaxies

Apart from the dark matter distribution, the study of dwarf galaxies is also interesting from the star formation point of view. Due to a lack of spiral density waves and rotational shear, dwarf galaxies are dynamically much simpler systems as compared to bright spiral galaxies. Dwarf galaxies should hence be ideal for studying the physical laws which regulate the interplay between gas and star formation. However, unlike spiral galaxies, the nature of processes regulating star formation in dwarf irregular galaxies is poorly understood. Various studies of star formation in spiral galaxies have found that star formation rate in these galaxies depend on gas surface density by the Schmidt power-law relation, and that star formation is suppressed completely at surface densities below a critical threshold value [7]. The existence of a threshold surface gas density for star formation is usually explained in terms of dynamical models of thin rotating disk in which local gravitational instability lead to a formation of molecular clouds, i.e Toomre's instability criterion [18]. On the other hand, the observations of dwarf galaxies indicate that the HI gas densities in these galaxies lie systematically below the Toomre's instability criterion, throughout the star forming disk (e.g. [19, 6]), indicating that physical processes that regulate star formation in spiral galaxies

do not work for dwarf irregular galaxies. The breakdown of Toomre's instability criterion for dwarf galaxies may not be surprising, given that this criterion is derived from the models of galaxies with thin disks, where random motions in the gas are negligible compared to rotation velocities; both of these conditions do not strictly hold for dwarfs.

The existence of a single threshold value for star formation in dwarf irregular galaxies has also been proposed (e.g. [13, 17]). Skillman (1987) [13] from a comparison of the HI distribution and HII regions in a sample of dwarf irregular galaxies, empirically derived a threshold of 1 $\times 10^{21}$ cm^{-2} (averaged over $\sim$ 500 pc) for star formation, supporting the idea of a threshold with a single value in dwarf irregular galaxies. The observed threshold was interpreted as a requisite column density of dust required for shielding the molecular gas from the ambient UV radiation field of the galaxy. The threshold column density, should then be a function of the metallicity of the galaxy, and should increase with the decrease in the metallicity of the galaxy. The number of galaxies studied so far to support the idea of a threshold with a single value is still too small to make any definite conclusions, hence, high spatial resolution HI synthesis observations of a large sample of dwarf galaxies is required. Further, as the observed column density is resolution dependent, a comparison of HI column densities at the same linear resolution is important to investigate the existence of star formation thresholds with a single value in dwarf galaxies. This in turn requires the HI maps to be made at a variety of angular resolutions, if the sample has galaxies spanning a large range in distance. The GMRT observations presented in this thesis are particularly well suited to this problem since, because of the hybrid configuration of the GMRT, maps at a range of angular resolutions varying from, $\sim$ 40 arc-seconds to a few arc-seconds, can be made from a single observing run. For all our galaxies we produced HI maps at an angular resolution corresponding to a linear scale of $\sim$ 300 pc at the distance to the galaxy. We thus have a unique data set which spans a wide range of star formation rates, but for which maps are available at a similar linear resolution.

As mentioned in Sect.1.2, it is widely believed that the smallest dwarf galaxies have chaotic gas velocity fields. Lack of rotation in faint dwarf irregular galaxies raises an issue about what supports the gravity in these galaxies. The faint dwarfs are typically gas rich, hence the presence of substantial amount of HI gas that is not rotationally supported is rather puzzling. The absence of any rotational support in these systems would lead to a collapse of HI clouds and eventually to star formation on time scales shorter than the age of the galaxies, unless kinetic energy is injected into the ISM by episodes of star formation [9]. The rate of injection of kinetic energy, if self regulated (i.e. the current star formation activity is suppressed due to disruption of the ISM by the previous episodes of star formation),

could prevent the collapse of gas on short time scales. However, this is in conflict with the quiescent current and past star formation rate observed in the many faint dwarf galaxies. What supports the HI gas against collapse and star formation in faint dwarf galaxies is hence not understood.

The cold phase of HI is usually assumed to be a necessary ingredient of star formation [22], hence a lack of cold neutral medium (CNM) could suppress the star formation activity in dwarf galaxies. From a high velocity and high spatial resolution HI images of a sample of nearby faint dwarf galaxies, observed with the VLA, Young & Lo (1996, 1997) and Young et al.(2003) found a broad HI component with the dispersion of $\sigma \sim 8-10$ km s^{-1}, throughout each galaxy, whereas a narrow HI component with $\sigma \sim 3-5$ km s^{-1}, located near the high HI column density regions. The broad and narrow HI components were interpreted as warm and cold phases of the HI medium, respectively, a feature similar to that seen in our own galaxy. Young et al. [23] found that CNM is present at all sites of current star formation (although the converse does not hold), supporting the idea that CMN is necessary (but not sufficient!) for star formation. It would be interesting to see if the same statement holds for our sample.

We have hence carried out a detailed analysis of the HI line profile shapes across the disks of our sample galaxies to check for correlations (if any) between complex profiles and star formation activity in faint dwarf galaxies.

1.4 Powerspectrum analysis of HI emission in dwarf galaxies

Evidence has been mounting in recent years that turbulence plays an important role in the physics of the ISM as well as in governing star formation. A major piece of observational evidence for the existence of turbulence in the neutral ISM is the fact that the power spectrum of the intensity fluctuations of HI 21cm emission is a scale free power law. This appears to be the case both in our own galaxy [5] as well as in our companion dwarf galaxies LMC [4] and SMC [14]. The powerspectrum analysis of HI intensity fluctuations is hence an important technique to probe the structure of neutral ISM in galaxies.

As the powerspectrum is the Fourier transform of the autocorrelation of the HI intensity distribution, it is conceptually straight forward to compute it from cubes of HI 21cm emission (e.g. [4, 14]). Although most of the studies of the powerspectrum of the HI emission in galaxies are based on image plane analysis techniques, there has been some work on visibility based techniques (e.g. [3, 5]). Since the complex visibility measured by an interferometer is

the Fourier transform of HI intensity distribution, the squared modulus of the visibility is a direct estimator of the powerspectrum. Both Crovisier & Dickey [3] and Green [5], using the visibility based analysis, found that the powerspectrum of HI emission in our own galaxy is a power law. So far, however, visibility based techniques to measure the powerspectrum have been applied only to our own galaxy.

In this thesis, we discuss techniques for obtaining the power spectrum of the HI intensity fluctuations in the faint dwarf galaxies of our sample, where the expected signal is very weak. Our analysis is focused on visibility based techniques, since the statistics are best understood in the visibility plane.

1.5 Outline of this thesis

This thesis is based on high velocity resolution (~ 1.6 km s^{-1}), high sensitivity, GMRT HI 21 cm-line observations of a sample of fifteen extremely faint ($M_B \gtrsim -13.5$) dwarf galaxies. The thesis is divided into nine chapters, including the present one. The second chapter describes our galaxy sample along with their GMRT HI observations and the HI data analysis. The optical observations and analysis of some of our sample galaxies are also presented in this chapter.

For some of our sample galaxies, the observed kinematics could be modelled as systematic rotation. The derived rotation curves of those galaxies along with the derivation of the dark matter distribution in the galaxies (i.e. as obtained through mass modelling) is presented in Chapter 3. Various trends expected in the dark halos in hierarchical galaxy formation models and the Tully-Fisher relation for faint dwarf galaxies are explored using our galaxy sample, in conjugation with data for brighter galaxies. These are also presented in Chapter 3. For one of our sample galaxies, viz. GR 8, (which has a velocity field that cannot be modelled as an axi-symmetric rotating disk) detailed kinematical modelling of this galaxy and the possible connection between the observed kinematics and the energy input from star formation processes is presented in Chapter 4. In Chapter 5, an investigation of a connection between the gas distribution, kinematics and star formation in faint dwarf galaxies is presented. The existence of a threshold HI column density for star formation in faint dwarf galaxies is studied by comparing multiresolution HI images of our sample galaxies with the regions of ongoing star formation (as traced by Hα emission). Possible connections between the shapes of the HI line profiles and star formation activity in faint dwarf galaxies are also explored in this chapter.

The HI distribution in some of our sample galaxies viz. NGC 3741 and HIZSS003 are very interesting in their own right and are presented in Chapter 6 and Chapter 7 respectively.

Chapter 6 describes the study of the HI distribution in NGC 3741; our GMRT observations showed that NGC 3741 has possibly the most extended HI gas disk (the HI disk extends to ~ 8.3 times its Holmberg radius) known. The implication of such an extended disk on the dark halo properties of this galaxy is explored in this chapter. Chapter 7 describes the results of the GMRT HI observations of the recently discovered dwarf irregular galaxy HIZSS003. We find that HIZSS003 is actually a galaxy pair; this helps to resolve otherwise puzzling inconsistencies between the broadband optical distribution, the ongoing star formation and metallicity in this galaxy.

The GMRT nondetection of HI in three peculiar dwarf galaxies, POX 186, SC 24 and KKR 25 along with the impact of our non detection of HI on the classification of these galaxies is discussed in Chapter 8.

Finally, Chapter 9 describes the visibility based formalism that we have developed for determining the power spectrum of the HI intensity fluctuations in faint dwarf galaxies, where the expected signal is very weak. The application of this technique to some of the sample galaxies along with the comparison of the power spectrum in our faint, largely quiescent galaxies, with those observed in much brighter galaxies is presented.

Bibliography

[1] Carignan, C., & Freeman, K. C., 1988, ApJL 332, 33

[2] Côté, S., Carignan, C. & Freeman, K. C. 2000, Ap.J, 120, 3027

[3] Crovisier, J. & Dickey, J. M., 1983, A&A, 122, 282

[4] Elmegreen, B. G., Kim, S. & Staveley-Smith, L., AJ, 2001, 548, 749

[5] Green, D. A., 1993, MNRAS, 262, 327

[6] Hunter, D. A., Elmegreen, B. G. & Baker, A. L., 1998, ApJ, 493, 595

[7] Kennicutt, R. C., 1989, ApJ, 344, 685

[8] Klypin, A. A., Kravtsov, A. V., Bullock, J. S. & Primack, J. R., 2001, ApJ 554, 903

[9] Lo, K. Y., Sargent, W. L. W. & Young, K., 1993, Ap.J., 106, 507

[10] McGaugh, S. S., Schombert, J. M., Bothun, G. D., & de Blok, W. J. G. 2000, ApJL, 533, 99

[11] Navarro, J. F., Frenk, C. S. & White S. D. M.,1997, ApJ 490, 493

[12] Navarro, J. F., Frenk, C. S. & White S. D. M., 1996, ApJ 462, 563

[13] Skillman, E. D., 1987, in Star Formation in Galaxies, edited by C. J. Lonsdale Persson, NASA, 263

[14] Stanimirovic, S., Staveley-Smith, L., Dickey, J. M., Sault, R. J., & Snowden, S. L., 1999, MNRAS, 302, 417

[15] Stil & Israel. A&A, 2002,389,42

[16] Swaters, R. 1999, Ph.D. thesis, Rijksuniversiteit Groningen.

[17] Taylor, C. L., Brinks, E., Pogge, R. W. & Skillman, E. D., 1994, AJ, 107, 971

[18] Toomre, A. 1964, ApJ, 197, 551

[19] van Zee, L., Haynes, M. P., Salzer, J. J. & Broeils, A. H., 1997, AJ, 113 1618

[20] Verheigen, M., 1997, Ph.D. thesis, Rijksuniversiteit Groningen.

[21] Walker, M, 1999, MNRAS, 308, 551

[22] Wolfire, M. G., McKee, C. F., Hollenbach, D. & Tielens, A. G. G. M., 2003, ApJ, 587, 278

[23] Young, L. M., van Zee, L., Lo, K. Y., Dohm-Palmer, R. C. & Beierle, M. E., 2003, ApJ, 592, 111

[24] Young, L. M. & Lo, K. Y., 1997, ApJ, 490, 710

[25] Young, L. M. & Lo, K. Y., 1996, ApJ, 462, 203

Chapter 2

Observations and analysis

2.1 Introduction

In this chapter we present observations of a sample of 15 extremely faint dwarf galaxies, in the HI 21 cm line emission, with the Giant Metrewave Radio Telescope (GMRT). The GMRT [20] is an interferometric array of 30 fully steerable parabolic dishes, each of 45m diameter each. It has a hybrid configuration with 14 of its 30 antennas located in a central compact array with size $\approx$ 1 km ($\approx$ 5 kλ at 21cm) and the remaining antennas distributed in a roughly "Y" shaped configuration, giving a maximum baseline length of $\approx$ 25 km ($\approx$ 120 kλ at 21 cm). The baselines obtained from antennas in the central square are similar in length to those of the "D" array of the VLA, while the baselines between the arm antennas are comparable in length to the "B" array of the VLA. A single observation with the GMRT hence yields information on both large as well as small angular scales.

For most of our sample galaxies, optical data was already available in the literature. However, some galaxies with no existing optical data, were observed using the HFOSC (Himalayan Faint Object Spectrograph Camera), at the 2.0 m Himalayan Chandra Telescope (HCT). In this chapter we will also present the optical observations and analysis of those galaxies.

2.2 Sample

As this thesis involves the study of extremely faint dwarf galaxies, our galaxy sample was mainly selected on the basis of blue band luminosity; dwarf galaxies for our sample were chosen with absolute blue magnitude, $M_B \gtrsim -13.5$. Apart from having a constraint on the absolute magnitude, certain other selection criterion were also kept in mind while choosing our galaxy sample. In-order to achieve the objectives of this thesis, HI maps with good

signal-to-noise ratio are crucial. Hence, a lower limit on the HI flux integral of 1.5 Jy km $s^{-1}$was chosen for selecting our sample. Further, derivation of accurate rotation curves for dark matter studies require many independent HI beams across each galaxy, hence a lower limit of $\sim$ 1.0 arcmin on the Holmberg diameter (D_{Ho}) was applied. However we note that, the above mentioned criterion on the HI flux and D_{Ho} were not strictly followed in few cases. Some unusual, faint dwarf galaxies viz. SC 24 and Pox 196, although not satisfying our selection criterion were still included in our sample as they are very interesting cases to study in detail in HI (see Chapter 8 for details). Similarly, the dwarf galaxy KK98 250 (detected in the same pointing as our sample galaxy KK98 251), though too bright ($M_B \sim -14.5$) to satisfy our criterion was still included in our sample, as the HI data for this galaxy is useful for the dark matter and the Tully-Fisher studies.

The dwarf galaxies in our sample are described in Table 2.1. The description of the entries in each column are as follows:

Column(1): Name of the galaxy,
Column(2): Right ascension (α) in J2000,
Column(3): Declination (δ) in J2000,
Column(4): Systemic velocity of the galaxy (V_{sys}) in km s^{-1}, determined from single dish HI observations. In the case of POX 186, V_{sys} was determined from the optical (Hα) observations,
Column(5): Absolute blue magnitude M_B, corrected for galactic foreground absorption,
Column(6): Distance to the galaxy (D) in Mpc. Except for SC 24, POX 186, KK98 250 & KK98 251, the distance to all galaxies in our sample are estimated from the tip of the red giant branch (TRGB). In case of SC 24, KK98 250 & KK98 251, the distance is determined from the group membership, while for POX 186, the Hubble relation using H_0=75 km s^{-1} Mpc^{-1}, combined with a correction for the peculiar motion of the Local Group, is used to determine the distance to the galaxy,
Column(7): Holmberg radius (R_{Ho}) of the galaxy in arcmin,
Column(8): Inclination of the galaxy determined from the optical isophotes (i_{opt}),
Column(9): Group membership of the galaxy and
Column(10): References to the parameters listed in the preceding columns.

The sample presented here is considerable larger than the published studies of faint dwarf galaxies ($M_B \gtrsim -13.5$), with comparable velocity resolution and sensitivity. At the time when this thesis project was initiated, high velocity resolution HI interferometric observations of only four extremely faint dwarf galaxies were know [25, 24]. Recently, Young et al.(2003)

Table 2.1: Sample of galaxies for HI observations

Galaxy	α(J2000)	δ(J2000)	V_{sys}	M_B	D	R_{Ho}	i_{opt}	Group	Ref
	h m s	° ′ ″	km s^{-1}	mag	Mpc	′	°		
SC 24	00 36 38.0	−32 34 28	79.0	−8.39	1.66	0.3	57	Sculptor	4,10
KK 44	04 53 06.9	+67 05 57	77.0	−11.85	3.34	0.7	62	IC432	4,12
HIZSS003	07 00 29.3	−04 12 30	290.0	−12.19	1.69	–	55	Field	4,8,9
KDG 52	08 23 56.0	+71 01 46	113.0	−11.49	3.55	0.65	24	M 81	4
UGC 4459	08 34 06.5	+66 10 45	20.0	−13.37	3.56	0.8	30	M 81	4,7
NGC 3741	11 36 06.4	+45 17 07	230.0	−13.13	3.03	0.8	58	CVn I	1,4
CGCG 269-049	12 15 46.7	+52 23 15	160.0	−12.46	3.4	0.6	77	CVn I	4
UGC 7298	12 16 28.6	+52 13 38	173	−12.27	4.21	0.55	58	CVn I	4,7
GR 8	12 58 40.4	+14 13 03	215.0	−12.11	2.2	1.1	25	Field	4,11
POX 186	13 25 48.6	−11 36 38	1170.0	−12.74	18.5	–	–	Field	3,5
KK 230	14 07 10.7	+35 03 37	62.0	−9.55	1.9	0.87	35	CVn I	4,12
KKR 25	16 13 47.6	+54 22 16	−139.0	−9.96	1.86	0.6	55	LG	4
KK98 250	20 30 15.3	+60 26 25	127.0	−14.54	5.6	0.9	66	NGC6946	4,2
KK98 251	20 30 32.6	+60 21 13	130.0	−13.72	5.6	0.8	62	NGC6946	4,2
DDO 210	20 46 53.0	−12 50 57	−139.0	−11.09	1.0	1.8	62	LG	4,6

1-Bremnes et al.(2000), 2-Huchtmeier et al.(2000), 3-Guseva et al.(2004), 4-Karachentsev et al.(2004), 5-Kunth et al.(1988), 6-Lee et al.(1999), 7-Makarova (1999), 8- Massey et al.(2003), 9-Silva et al.(2005), 10-Skillman et al.(2003), 11-Tolstoy et al.(1995), 12-This thesis

presented the HI maps of four faint dwarf galaxies with the VLA, with two of the galaxies in common between their sample and our galaxy sample. However, all these VLA studies were mainly focused on the local connection between the ISM and star formation; a detailed modelling of dark matter distribution and star formation thresholds were not explored in those studies.

2.3 The Observations

2.3.1 GMRT HI Observations

A total of ∼350 hrs of GMRT observations were carried out for this thesis work, spread over a period of 4 years (2001−2004). The setup of the GMRT observations is given in Table. 2.2.

The description of the entries in each column is as follows:

Column(1): The galaxy name,
Column(2): The date of observations,
Column(3): Total integration time on source (TOS) in hours,
Column(4): The observing bandwidth (BW) used in MHz,
Column(5): The frequency at the center of the band in MHz and
Column(6): The velocity resolution in km s^{-1}(the total observing bandwidth is divided into 128 spectral channels).

For each observing run, absolute flux and bandpass calibration was done by observing one of the standard flux calibrators 3C 48, 3C 286 and 3C 147, at the start and end of the observations. For the sample galaxies with low LSR velocities, particular care was taken to choose a bandpass calibrator which does not have any absorption feature in the relevant velocity range. Phase calibration was done once in every 30 min by observing the standard VLA calibrator sources. The phase calibrators chosen for the observations for our sample galaxies are 0410+769 (KK 44), 2008-068 (DDO 210), 2022+616 (KK98 250, KK98 251), 1252+119 (GR 8), 0831+557 (UGC 4459), 1216+487 (UGC 7298, CGCG 269-049), KK 230 (3C 286) and 0834+555 (KDG 52), 1349-145 (POX 186), 0025-260 (SC 24), 1634+627 (KKR 25), 0744-064 (HIZSS003) and 1227+365 (NGC 3741). The galaxies UGC 7298 and KK98 251 are close enough in space as well as in velocity to the galaxies CGCG 267-049 and KK98 250 respectively, hence both were included in a single GMRT pointing (the field of view of the GMRT $\sim 24'$).

2.4 Optical Observations

CCD images of KK98 250 and KK98 251 in the Bessell I and V filters were obtained on $29^{\rm th}$ and $30^{\rm th}$ May 2003, using the HFOSC (Himalayan Faint Object Spectrograph Camera), at the 2.0 m Himalayan Chandra Telescope. The camera has a field of view of $10'\times10'$, with a scale of $0.3''$/pixel. Both the galaxies were covered in the same pointing. The total exposure time on the target was 40 min in I and 50 min in the V band. The Full Width Half Maximum (FWHM) seeing of the co-added images was $\sim 1.7''$. Since the first night was not photometric, standard fields (from Landolt 1983) were observed only on the second night. These, incidentally, are one of the earliest observations made using the HCT.

Table 2.2: Parameters of the GMRT observations

Galaxy	Obs. date	TOS	BW	Central freq	Vel. resol
		hrs	MHz	MHz	km s^{-1}
SC 24	15, 27 June 2003	3	4	1420.00	6.6
KK 44	4−6 Nov. 2001	16	1	1420.04	1.65
HIZSS003	23 Aug. 2003	4	1	1419.00	1.65
KDG 52	21−23, 27 June 2002	18	1	1419.85	1.65
UGC 4459	15, 23, 24 Nov. 2002	14	1	1420.39	1.65
NGC 3741	22 July, 26 Aug. 2004	8	1	1419.40	1.65
CGCG 269-049	23−25 Nov. 2002	16	1	1419.68	1.65
UGC 7298	23−25 Nov. 2002	16	1	1419.68	1.65
GR 8	16−18 Nov. 2002	16	1	1419.48	1.65
POX 186	30Nov−2 Dec 2002	16	1	1414.88	1.65
KK 230	6 Jun, 8 May, 26 Nov. 2001	18	1	1420.15	1.65
KKR 25	25, 26 Oct. 2001	10	1	1421.05	1.65
KK98 251	22 June 2001	6	1	1419.80	1.65
KK98 250	22 June 2001	6	1	1419.80	1.65
DDO 210	13−15 July 2002	16	1	1421.07	1.65

2.5 Optical data analysis

Debiasing, flat-fielding and cosmic ray filtering of the CCD images were done in the usual manner, using standard IRAF routines. The exposures taken on the $30^{\rm th}$ were calibrated and then added after alignment. This combined frame was used to calibrate the individual exposures taken on the $29^{\rm th}$. No fringe subtraction was done for the I band images.

Surface photometry for KK98 250 was done using the ellipse fitting algorithm of Bender & Möllenhoff (1987). Ellipse fitting in the I band was restricted to the inner regions of the galaxy, since the outer low surface brightness emission is affected by fringing. The average ellipticity was found to be 0.72 ± 0.02 (corresponding to an inclination of $\sim 79^\circ$, for an intrinsic thickness ratio $q_0 = 0.2$). The position angle, measured between the north direction on the sky and the major axis of the receding half of the galaxy, was found to be $\sim 270^\circ$. The surface brightness profiles obtained from the ellipse fitting in V and I bands are well described by exponential disk with the scale length of $41.0''$ ($\sim$1.1 kpc) and $62.0''$ ($\sim$1.7 kpc) respectively. The average <V-I> color is $\sim$1.2, with little variation with radius. The total magnitude after correcting for galactic extinction (using A_V=1.01 mag and A_I=0.59 mag [16] is 13.8$\pm$0.3 mag in V and 12.6$\pm$0.4 mag in I. No correction for internal extinction was applied.

KK98 251 has several bright stars superposed on it which could not be accurately removed. Hence, for this galaxy we will use the results of the I band photometry derived by Karachentsev et al. (2000), who derived an I band exponential scale length and a total I magnitude of $22.8''$ ($\sim$0.6 kpc) and 14.42 mag respectively.

2.6 HI Data Analysis

The GMRT data were reduced in the usual way using standard tasks in classic AIPS. For each observing run, bad visibility points were edited out, after which the data were calibrated. The GMRT does not do online doppler tracking – any required doppler shifts have to be applied during the offline analysis. Except for the galaxies UGC 4459, KK230, NGC 3741 and KDG 52, the differential doppler shift over our observing interval for all the galaxies in our sample was much less than the channel width, hence, there was no need to apply any offline correction. For the galaxies with significant differential shifts, the calibrated (u,v) data set for each day was shifted in frequency space to the heliocentric velocity of each galaxy, using the task CVEL in AIPS. Data for all the runs, for each galaxy, were then combined using the AIPS task DBCON. From the combined (u,v) data sets, low resolution data cubes were generated for each galaxy, using the AIPS task IMAGR, and the individual

Table 2.3: Parameters of the HI data cubes and continuum maps

Galaxy	Line			Continuum	
	Resolution		Noise	Resolution	Noise
	(arcsec^2)	(parsec^2)	(mJy/Bm)	(arcsec^2)	(mJy/Bm)
KK 44	$40'' \times 38''$	648×615	2.5	$46'' \times 37''$	1.8
	$24'' \times 22''$	389×356	2.0	$3.6'' \times 3.2''$	0.6
	$19'' \times 17''$	308×275	1.6		
	$4'' \times 4''$	65×65	1.0		
HIZSS003	$42'' \times 39''$	344×320	2.2	$28'' \times 26''$	1.0
	$28'' \times 26''$	229×213	2.0	$3'' \times 3''$	0.3
	$23'' \times 18''$	188×148	1.8		
	$18'' \times 11''$	148×90	1.6		
	$8'' \times 6''$	66×49	1.4		
	$4'' \times 3''$	33×25	1.2		
KDG 52	$42'' \times 39''$	723×671	1.7	$26'' \times 22''$	0.9
	$26'' \times 23''$	447×396	1.5	$3'' \times 3''$	0.4
	$16'' \times 15''$	275×258	1.3		
	$6'' \times 6''$	103×103	0.9		
UGC 4459	$45'' \times 38''$	777×656	1.9	$26'' \times 22''$	1.0
	$29'' \times 27''$	500×466	1.6	$3'' \times 3''$	0.5
	$18'' \times 16''$	310×276	1.4		
	$3'' \times 3''$	52×52	1.2		
NGC 3741	$52'' \times 49''$	756×713	3.8	$28'' \times 26''$	1.2
	$42'' \times 38''$	611×553	3.2	$6'' \times 6''$	0.7
	$26'' \times 24''$	378×349	2.9		
	$19'' \times 15''$	276×218	1.5		
	$13'' \times 11''$	189×160	2.0		
CGCG 269-049	$42'' \times 39''$	692×643	2.0	$26'' \times 23''$	0.5
	$28'' \times 24''$	461×396	1.8	$3'' \times 3''$	0.3

Table 2.3: Parameters of the HI data cubes and continuum maps (*continued*)

Galaxy	Line			Continuum	
	Resolution		Noise	Resolution	Noise
	(arcsec^2)	(parsec^2)	(mJy/Bm)	(arcsec^2)	(mJy/Bm)
CGCG 269-049	$18'' \times 17''$	297×280	1.7		
	$4.0'' \times 3''$	66×50	1.2		
UGC 7298	$42'' \times 37''$	857×755	2.0	$26'' \times 23''$	0.5
	$26'' \times 24''$	530×490	1.8	$3'' \times 3''$	0.3
	$16'' \times 15''$	326×306	1.6		
	$4.0'' \times 4''$	82×82	1.1		
GR 8	$41'' \times 39''$	437×416	2.0	$46'' \times 37''$	1.8
	$30'' \times 30''$	320×320	1.7	$6.4'' \times 5.8''$	0.6
	$25'' \times 25''$	267×267	1.6		
	$4'' \times 3''$	43×32	1.0		
KK 230	$48'' \times 45''$	442×415	1.6	$27'' \times 26''$	0.4
	$34'' \times 31''$	313×286	1.4	$3'' \times 3''$	0.2
	$26'' \times 24''$	240×221	1.2		
	$4'' \times 3''$	37×28	0.8		
KK98 251	$43'' \times 38''$	1167×1032	3.5	$26'' \times 22''$	1.8
	$26'' \times 21''$	706×570	2.8	$6'' \times 5''$	1.0
	$16'' \times 14''$	434×380	2.2		
	$11.5'' \times 10''$	312×271	1.9		
KK98 250	$43'' \times 38''$	1167×1032	3.5	$26'' \times 22''$	1.8
	$26'' \times 21''$	706×570	2.8	$6'' \times 5''$	1.0
	$16'' \times 14''$	434×380	2.2		
	$11.5'' \times 10''$	312×271	1.9		
DDO 210	$61'' \times 60''$	296×291	2.8	$30'' \times 23''$	1.2
	$44'' \times 37''$	213×179	2.2	$4.0'' \times 3.0''$	0.5
	$29'' \times 23''$	141×112	1.8		

Table 2.3: Parameters of the HI data cubes and continuum maps (*continued*)

Galaxy	Line			Continuum	
	Resolution		Noise	Resolution	Noise
	(arcsec^2)	(parsec^2)	(mJy/Bm)	(arcsec^2)	(mJy/Bm)
DDO 210	$20'' \times 15''$	97×73	1.6		
	$12'' \times 11''$	58×53	1.4		
	$4'' \times 3''$	19×15	1.0		

channels were inspected using the task TVMOVIE to identify the channels with HI emission.

In the case of SC 24, KKR 25 and POX 186 no HI emission was detected. The HI observations and analysis for these galaxies will be discussed in detail in Chapter 8. For the rest of the galaxies, after identifying the frequency channels with emission, continuum maps were made using the average of the remaining line free channels. No continuum was detected from the disk of any of our sample galaxies. The 3σ flux limits along with the beam size of the continuum maps for our sample galaxies are given in Table 2.3. We also checked for the presence of any compact continuum sources in the disk of our sample galaxies by making high resolution maps – except for the galaxy HIZSS003, no continuum sources associated with the disk of any galaxy were detected down to a 3σ limit given in Table 2.3. In the case of HIZSS003, the only continuum source detected in the disk of the galaxy is NVSS J070023-041255. The HI column density (as derived from the $42'' \times 39''$ resolution image) along the line of sight to this source is $5.7\times\ 10^{20}$ atoms cm^{-2}. A search for HI absorption, in the direction of this source, gave negative results at all resolutions. The implied lower limit on the spin temperature of the gas (assuming a velocity width of 10 km s^{-1}) is 723K. The association of this continuum source with HIZSS003 is discussed in Chapter 7. For all galaxies, continuum sources in the field of view were subtracted using the task UVSUB.

As mentioned in Sect. 2.1, the GMRT has a hybrid configuration, hence data cubes were made at various (u,v) ranges using robust weighting. At each (u,v) range, a circularly symmetric gaussian taper with a FWHM equal to 80% of the (u,v) range was applied, in order to reduce the sidelobes of the synthesized beam. The FWHM of the GMRT synthesized beam obtained for various (u,v) ranges, for each galaxy, along with the RMS noise per channel corresponding to each beam are given in Table 2.3. Except for the highest resolution data cube for each galaxy, the data cubes at all the resolutions were deconvolved using the the

AIPS task IMAGR (in HIZSS003 even the $8'' \times 6''$ resolution data cube, listed in Table 2.3 could not be deconvolved). For the highest resolution data cube for each galaxy, the signal to noise ratio was too low for CLEAN to work reliably and hence these data cubes could not be deconvolved. Despite this, the low SNR of highest resolution HI image for each galaxy implies that the inability to deconvolve it does not greatly degrade its dynamic range or fidelity. The morphology of the emission in each galaxy should hence be accurately traced, apart from an uncertainty in the scaling factor (this essentially arises because the main effect of deconvolving weak emission at about the noise level corresponds to multiplying by a scale factor [5, 15]).

The line profiles in each galaxy were examined at various locations and were found (to zeroth order) to be symmetric and single peaked. Although at some locations double gaussians or Gauss-Hermite polynomials provide a better fit to the data (particularly in the higher column density regions) in some of our sample galaxies, the peak velocity of the profile in these regions matches (within the errorbars) with the intensity weighted mean velocity. Since we are interested here mainly in the systematic velocities, moment maps provide an adequate description of the data. Moment maps (integrated HI column density, velocity field and velocity dispersion maps) were therefore made from the data cubes using the AIPS task MOMNT. To obtain the moment maps, lines of sight with a low signal to noise ratio were excluded by applying a cutoff (generally at the 2σ level, σ being the RMS noise level in a line free channel), after smoothing in velocity (using boxcar smoothing three channels wide) and position (using a gaussian with FWHM ~ 2 times that of the synthesized beam). Figure. 2.1 shows the GMRT integrated HI column density distribution, overlayed on the optical DSS images, and the velocity field of our sample galaxies from the lowest resolution data cubes.

Maps of the velocity field and velocity dispersion were also made in GIPSY using single Gaussian fits to the individual profiles. The velocity fields produced by gaussian fitting are in reasonable agreement with that obtained from moment analysis. However, the moment2 map systematically underestimates the velocity dispersion. This can be understood as the effect of the thresholding algorithm used by the MOMNT task to identify the regions with signal. Velocity dispersion in all the galaxies was hence estimated by fitting single gaussian component to the line profiles. As mentioned above, a single gaussian is not necessary a good fit in some regions in some of our sample galaxies; we will discuss this issue in more detail in Chapter 5 of this thesis. The velocity dispersion estimated from fitting a single gaussian ($\sigma_{\rm obs}$), for each galaxy, is given in Table 2.4. Except for KK98 251, no measurable variation of velocity dispersion was seen (within the errorbars) across any of our sample galaxy. This

Table 2.4: Observed HI velocity dispersion

Galaxy	σ_{obs} (km s^{-1})	Galaxy	σ_{obs} (km s^{-1})
KK 44	7.3±0.8	KDG 52	9.0±1.0
UGC 4459	9.0±1.6	NGC 3741	–
CGCG 269-049	9.5±1.0	UGC 7289	8.5±1.3
GR 8	9.0±0.8	KK 230	7.5±0.5
KK98 250	–	KK98 251	8.4 ±0.7 to 9.5 ± 0.9

lack of substantial variation of σ across each galaxy is typical of such faint dwarf irregular galaxies (e.g. [19, 10]). For KK98 250 and NGC 3741, the profile widths are dominated by rotational motion, even within a single synthesized beam, hence for these galaxies we assumed a typical value of velocity dispersion of ~ 8 km s^{-1}(e.g. [10, 19]).

2.6.1 Global HI profiles

The global HI profiles for each galaxy were obtained using the AIPS task BLSUM, by summing the HI flux in each spectral channel of the data cube. The lowest resolution data cube (see Table 2.3) was used to obtain the global profile, as it is most sensitive to any diffuse emission from the galaxy. The zeroth moment map at the same resolution was used to mask the region over which the flux is estimated in each spectral channel. The flux integral ($\int S_v dv$) obtained from the global profile was used to estimate the total HI mass using the relation:

$$M_{HI}(M_\odot) = 2.35 \times 10^5 D^2 \int S_v dv \tag{2.1}$$

where D is the distance to the galaxy in Mpc and $\int S_v dv$ is the flux integral in Jy km s^{-1}.

2.6.2 HI rotation curves

The rotation curves of the galaxies were derived separately from the various resolution velocity fields using the usual tilted ring model [22]. The tilted ring analysis assumes the gas to be in the circular orbits. The line of sight velocity (V_{los}) of a ring moving with a systemic

velocity (V_{sys}), rotating with a velocity (v_{rot}) on the sky and with no radial motions is given by

$$V_{los} = V_{sys} + v_{rot}(r)\cos(\theta)\sin(i) \tag{2.2}$$

where,

$$\cos(\theta) = \frac{-(x - X_0)\sin(PA) + (y - Y_0)\cos(PA)}{r} \tag{2.3}$$

where (X_0, Y_0), PA and i are the dynamical center, position angle of the major axis and inclination angle of each ring. (x,y) are the coordinates in the plane of the galaxy and r is the galactocentric radius. The inclination angle i of the galaxy is zero for the face-on orientation. The position angle of the major axis (PA) is defined as the angle, taken in anti-clockwise direction between the north direction on the sky and the major axis of the receding half of the galaxy.

For deriving the rotation curve for each galaxy, the HI disk was divided into concentric rings and the six parameters which define the observed radial velocity at each point in the ring, viz. (X_0,Y_0), V_{sys}, PA,i and v_{rot} were fitted to each ring iteratively. The program ROTCUR included in the GIPSY package was used to derive the rotation curve. The width of each ring was chosen such that there are two rings within each synthesized beam. The convergence of the fit was monitored through a χ^2 minimization. The initial guess for the parameters (X_0, Y_0), PA and i were obtained from the ellipse fit to the HI column density distribution, whereas the initial guess to V_{sys} was obtained from the global HI profile. In the iterative scheme used for each galaxy, the value of (X_0, Y_0) and V_{sys} were determined first and then kept fixed for all the rings. In the case of solid body rotation, the isovelocity contours are parallel to each other, hence one cannot determine the dynamical center and the systemic velocity independently from the velocity field. In such cases, the HI morphological center was chosen as the dynamical center.

Keeping (X_0, Y_0) and V_{sys} fixed for all the rings, i was fitted to each ring in the galaxy. Again, in the case of solid body rotation curve, one cannot determine the kinematical inclination from the velocity field, hence in such case the kinematical inclinations was taken to be the same as the HI morphological inclination of the galaxy. Keeping i fixed to the value obtained from the fit, the PA was fitted to each ring. Finally, v_{rot} as a function of the galactocentric radius was determined by keeping all other parameters fixed.

Further, the rotation curve was also determined separately for each half of the galaxy. For deriving the rotation curve for each half, (X_0, Y_0) and V_{sys} was kept fixed to the value obtained from the whole galaxy, whereas the PA and i was fitted again, separately for each half of the galaxy.

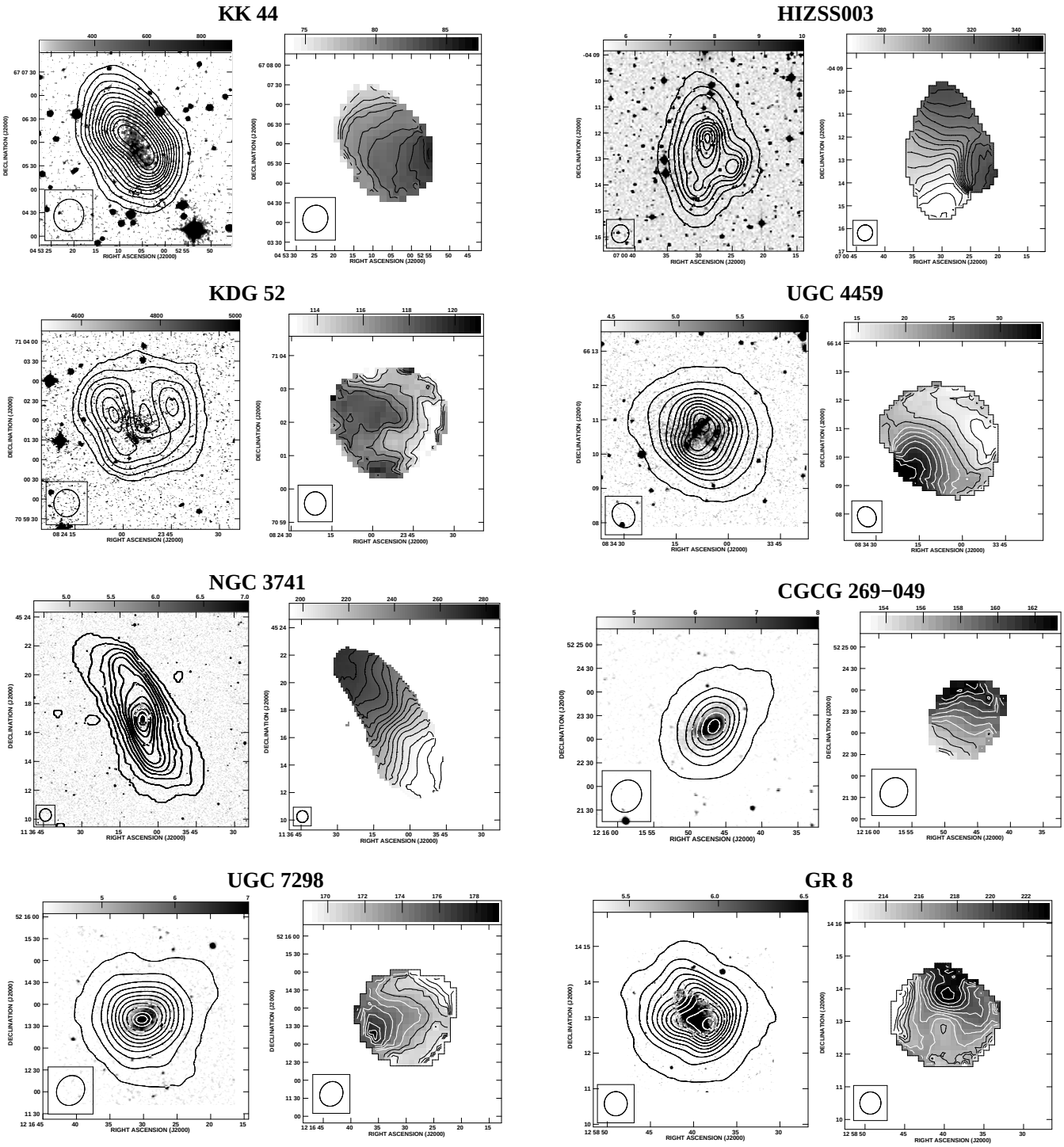

Figure 2.1: The GMRT integrated HI column density distribution (contours) overlayed on the optical DSS images (grey scales) and the velocity field (contours and grey scales) of our sample galaxies from the lowest resolution data cubes (see Table. 2.3).

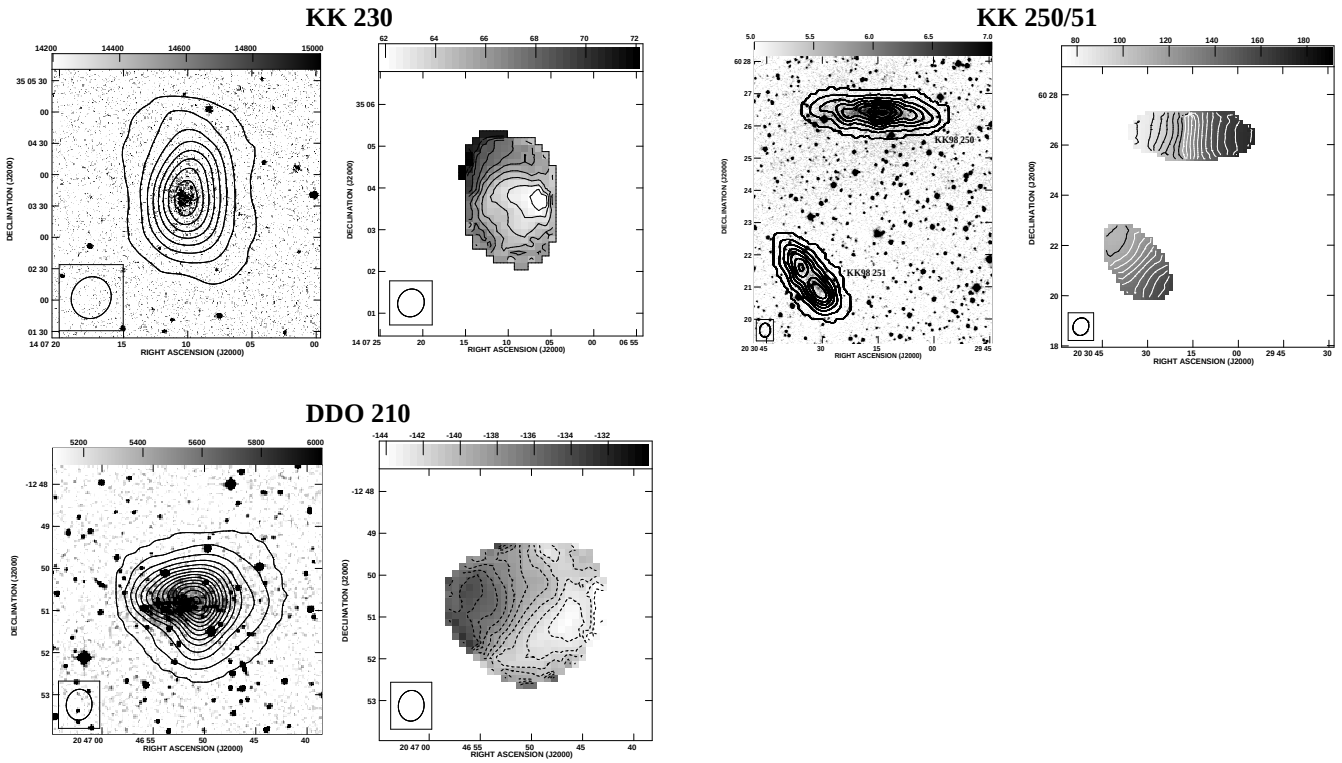

Figure 2.1: (*continued*)The GMRT integrated HI column density distribution (contours) overlayed on the optical DSS images (grey scales) and the velocity field (contours and grey scales) of our sample galaxies from the lowest resolution data cubes (see Table. 2.3).

Bibliography

[1] Bender, R., & Möllenhoff, C. 1987, A&A, 177, 71

[2] Bremnes, T., Binggeli, B. & Prugniel, P., A&AS,2000,141,211.

[3] Guseva, N.G., Papaderos, P., Izotov, Y.I., Noeske, K.G. & Fricke, K.J., A&A, 2004, 421, 519

[4] Huchtmeier, W. K., Karachentsev, I. D., Karachentseva, V. E., & Ehle, M. 2000, A&AS, 141,469

[5] Jörsäter S. & van Moorsel G. A.,1995, AJ, 110, 2037

[6] Karachentsev, I. D., Karachentseva, V.E., Huchtmeier, W.K. & Makarov, D.I., 2004, AJ, 127, 2031

[7] Karachentsev, I. D., Sharina, M. E., Dolphin, A. E. & Grebel, E. K., 2003, A&A, 408, 111

[8] Karachentsev, I. D., Sharina, M. E. & Huchtmeier, W. K. 2000, A&A, 362, 544

[9] Kunth, D., Maurogordato, S. & Vigroux, L., 1988, A&A, 204, 10

[10] Lake, G., Schommer, R. A. & van Gorkom, J. H., 1990, AJ, 99, 547

[11] Landolt A. U. 1983, AJ, 88, 439

[12] Lee, M. G., Aparicio, A., Tikonov, N., Byun, Y. & Kim, E., 1999, AJ, 118, 853.

[13] Makarova, L., 1999, A&AS, 139, 491

[14] Massey, P., Henning, P.A. & Kraan-Korteweg, R.C., 2003, AJ, 126, 2362.

[15] Rupen, M. P., 1999, ASP Conf. Ser. 180: Synthesis Imaging in Radio Astronomy II, 229

[16] Schlegel, D. J., Finkbeiner, D. P., & Davis, M. 1998, ApJ, 500, 525

[17] Silva, D.R., Massey, P., DeGioia-Eastwood, K. & Henning, P.A., 2005, ApJ, 623

[18] Skillman, E. D., Côte, S. & Miller, B. W., 2003, AJ, 125, 593

[19] Skillman, E. D., Terlevich, R., Teuben, P. J. & H. van Woerden. 1988, A&A, 198, 33.

[20] Swarup, G., Ananthakrishnan, S., Kapahi, V. K., Rao, A. P., Subrahmanya, C. R., & Kulkarni, V. K. 1991, Current Science, 60, 95

[21] Tolstoy, E., Saha, A., Horssel, J.G. & Danielson, E. 1995, AJ, 109, 579

[22] Warner, P. J., WRight, M. C. H. & Baldwin, J. E., 1973, MNRAS, 163 163

[23] Young, L. M., van Zee, L., Lo, K. Y., Dohm-Palmer, R. C. & Beierle, M. E., 2003, ApJ, 592, 111

[24] Young, L. M. & Lo, K. Y., 1997, ApJ, 490, 710

[25] Young, L. M. & Lo, K. Y., 1996, ApJ, 462, 203

Chapter 3

Dark matter distribution in faint dwarf galaxies

3.1 Introduction

Numerical simulations of hierarchical galaxy formation models, such as CDM/ΛCDM models, predict a "universal" cusped density core for the dark matter halos of galaxies (e.g. [6, 27, 39, 41]). A cusped density core corresponds to a steeply rising rotation curve. The observed kinematics of galaxies can hence be used to test such numerical models of galaxy formation. Dwarf and low surface brightness (LSB) galaxies are best suited for such a test, since they, unlike larger galaxies, are generally dominated by dark matter. In large spiral galaxies, both gas and stars make significant contributions to the total mass, particularly in the inner regions of the galaxy. Since the exact contribution of the baryonic material to the total mass of the galaxy depends on the unknown mass to light ratio of the stellar disk, it is generally difficult to unambiguously determine the density profile of the dark matter halo in the central regions of large spirals. On the other hand, in dwarf/LSB galaxies, since the stellar disk is generally dynamically unimportant, the central halo density can be much better constrained. Interestingly, the observed rotation curves of dwarf galaxies generally indicate that their dark matter halos have constant density cores (e.g. [9, 60]), unlike the cusped density cores predicted in numerical simulations.

Apart from the shapes of the dark matter profiles, numerical simulations based on hierarchical galaxy formation models also predict various correlations between the halo parameters, most notably between the characteristic density and the virial mass (e.g.[40]). In these models, the density of the dark matter halo is related to the background density at the time of the halo formation. Since dwarf galaxies form first in such models, they are expected to have the largest halo densities. The determination of the shapes and characteristic densities

of the dark matter halos of the faintest dwarf galaxies is hence a particularly interesting problem. However, a major stumbling block in such programs is that it is currently controversial whether very faint dwarf irregular galaxies show systematic rotation or not. From a systematic study of the kinematics of a sample of dwarfs, Côté et al.(2000) found that normal rotation is seen only in galaxies brighter than -14 mag, while the fainter dwarfs have disturbed kinematics. This result is consistent with the earlier findings of Lo et al.(1993), who from a study of the kinematics of a sample of nine faint dwarfs (with $M_B \sim -9.0$ to $M_B \sim -14.0$) found that most of these galaxies were characterized by chaotic velocity fields. However, as pointed out by Skillman(1996), Lo et al.'s observations had limited sensitivity to faint extended emission which is likely to have led to an underestimation of the rotation velocities. Moreover, most of these earlier studies were done with modest velocity resolutions ($\sim 6-7\,\mathrm{kms}^{-1}$), which makes it difficult to discern systematic patterns, if any, in the velocity fields of such faint systems. Do all faint dwarf irregular galaxies have disturbed kinematics? What is the dark matter distribution in very faint dwarf galaxies? In this chapter we discuss these questions in specific context of dwarf galaxies DDO 210, KK 44, KK98 250 and KK98 251.

3.1.1 Sample

3.1.1.1 DDO 210

DDO 210, the faintest known ($M_B \sim -10.6$) gas rich dwarf galaxy in our local group, was discovered by van den Berg (1959) and later detected in an HI 21 cm survey by Fisher and Tully (1975). Fisher and Tully (1979) assigned a distance of 0.7 Mpc to it, based on its proximity to NGC 6822 both on the sky and in velocity. On the other hand, Greggio et al.(1993), based on the colour-magnitude (C-M) diagram of DDO 210, estimated its distance to be 2.5 Mpc. However, recent distance estimates for DDO 210 give distances closer to the original estimate of Fisher and Tully (1979). Lee et al.(1999), based on the I magnitude of the tip of the red giant branch, estimated the distance to DD210 to be 950±50 kpc. This estimate is in excellent agreement with the value of 940±40 kpc, derived recently by Karachentsev et al.(2002) using the HST observations. At this distance, DDO 210 would be a member of the local group.

DDO 210 is classified as a dIr/dSph or "transition galaxy", with properties intermediate between dwarf irregulars and dwarf spheroidals [33]. For example, in spite of containing a significant amount of neutral gas, DDO 210 shows no signs of ongoing star formation. Hα imaging detected a single source of line emission in the galaxy; however follow up observations of this emission suggests that it does not arise in a normal HII region, but probably comes

from dense outflowing material from an evolved star [53]. Consistent with the lack of ongoing star formation, the CM diagram of DDO 210 shows that the brightest stars in the galaxy are the faintest among the brightest stars in all known dwarf irregular galaxies of our local group [29].

Prior to this work, there have been two HI interferometric studies of DDO 210, both of which used the VLA. This galaxy was a part of the sample of Lo et al.(1993) and has also been recently re-observed with a high velocity resolution in the Cs array by Young et al.(2003). The Young et al.(2003) study focused on the local connections between the ISM and star formation; however they did note that the galaxy shows a systematic large scale velocity gradient.

3.1.1.2 KK98 250 – KK98 251

Both KK98 250 and KK98 251 were identified as companions to the giant spiral galaxy NGC 6946 [25]. Prior to our observations, these galaxies have been imaged in HI with the DRAO interferometer [44]. The GMRT data presented here is however of much higher sensitivity and resolution than the previous interferometric observations. Distance estimates to KK98 250 and KK98 251 vary from 5.3 Mpc [46] to 8.2 Mpc [24]. Because of the proximity of the two galaxies to each other and to NGC 6946, on the sky as well as in the velocity, we feel that it is likely that all these galaxies belong to the same group viz. the NGC 6946 group. Hence, in this thesis we take the mean distance to the group (5.6 Mpc, estimated from the brightest stars in eight members of the group) as the distance to both the galaxies [17].

3.1.1.3 KK 44

The dwarf irregular galaxy KK 44 (Camelopardalis B or CamB) was discovered by Karachentseva & Karachentsev (1998). This galaxy is a member of IC 342 group of galaxies; based on the TRGB position from the HST data, Karachentsev et al.(2003) derived a distance of 3.34 Mpc to this galaxy.

3.2 Results

3.2.1 HI global profile

Observations and data analysis of KK 44, DDO 210, KK98 250 and KK98 251 are presented in Chapter 2. The global HI profiles for these galaxies, obtained from our coarsest resolution data cubes (see Table 2.3) are shown in Fig. 3.1. Columns (2−7) in Table 3.1 lists the HI parameters of the galaxies derived from the global HI profiles. The numbers in the

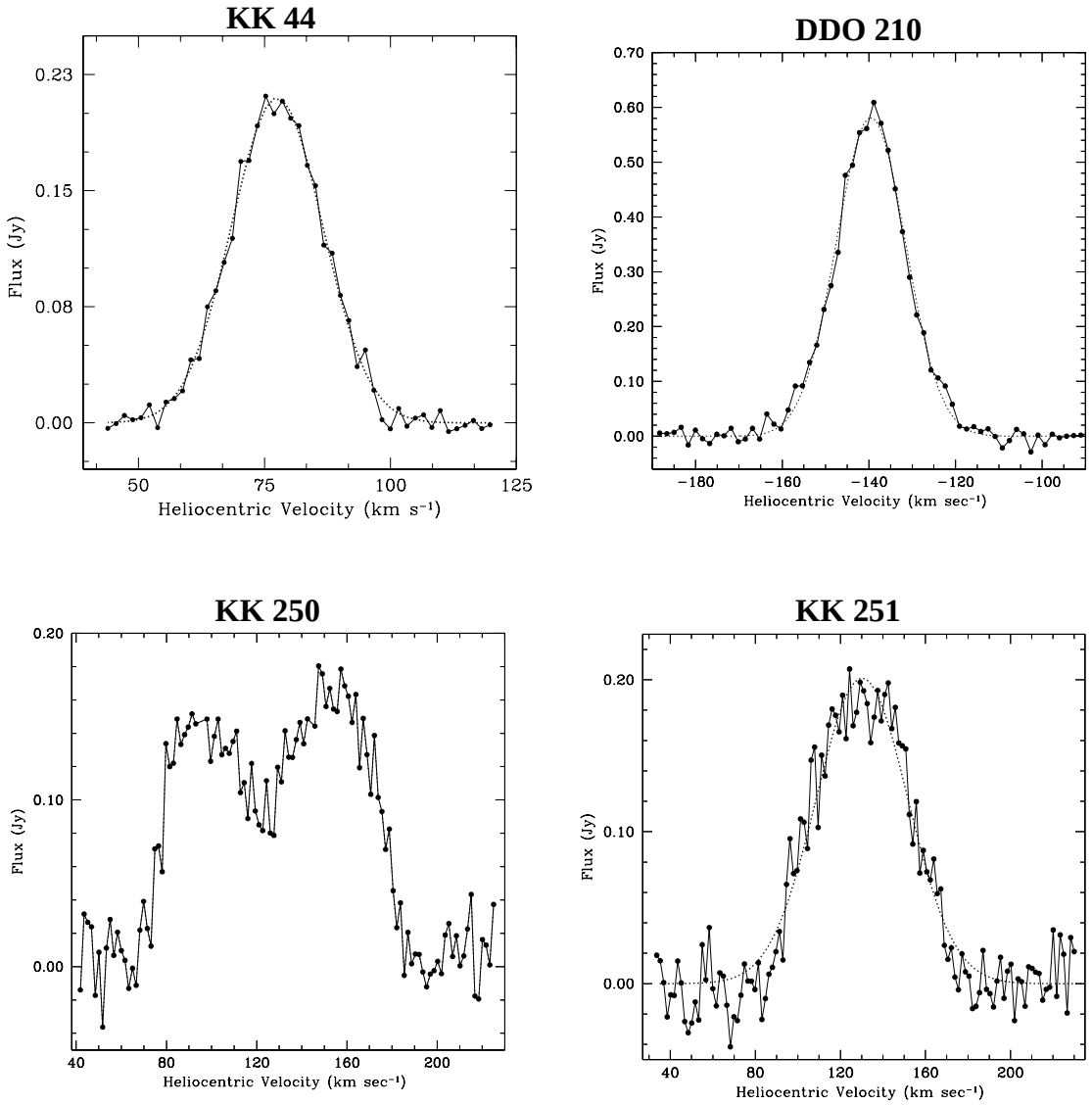

Figure 3.1: The HI global profile for our sample galaxies derived from our coarsest resolution HI distribution. The channel separation is 1.65 km s^{-1}. The dotted line shows a gaussian fit to the line profiles.

brackets represent errorbars on the derived parameters. Col (1) gives the galaxy name, (2) the integrated HI flux (FI) obtained from our GMRT observations, (3) the velocity width at 50% level of peak emission (ΔV_{50}), derived from a gaussian fit to the global profile (4) the central heliocentric velocity ($V_{\odot}$) from the gaussian fit (5) the HI mass obtained from the integrated profile (6) the HI mass to light ratio (M_{HI}/L_B), (7) the ratio of flux estimated from our GMRT observations to the single dish flux (FI/FI_{SD}). The reference for the single dish flux, for each galaxy, is given in Col (11).

Table 3.1: Results from GMRT observations

Galaxy	FI (Jy km s^{-1})	ΔV_{50} (km s^{-1})	$V_\odot$ (km s^{-1})	M_{HI} ($10^7 M_\odot$)	$\frac{M_{HI}}{L_B}$	$\frac{FI}{FI_{SD}}$	d_{HI} (′)	$\frac{d_{HI}}{d_{Ho}}$	σ_T (km s^{-1})	Ref
DDO 210	12.1(1.2)	19.1(1.0)	−139.5(2.0)	0.28(0.03)	1.00	1.05	4.8	1.3	6.0	2
KK 44	4.6(0.4)	21.4(1.0)	77.5(1.0)	1.2(0.1)	1.4	1.02	3.2	2.3	7.0	1
KK98 250	16.4(1.6)	95.5(2.3)	126.0(1.6)	12.1(1.1)	1.2	0.82	5.8	3.2	8.0*	3
KK98 251	10.6(1.0)	51.7(1.8)	130.3(1.7)	7.8(0.8)	1.6	0.73	4.2	2.6	8.0	3

* Assumed value.
Ref: 1-Huchtmeier et. al.(2000) 2-Huchtmeier & Richter (1986) 3-Huchtmeier et. al.(1997)

In the case of KK 44 and DDO 210, the HI parameters derived from the gaussian fit to the global HI profiles show good agreement (within the errorbars) with the values obtained from the single dish observations. A good agreement between the HI flux derived from the GMRT observations and the single dish fluxes for DDO 210 and KK 44 show that no flux was missed because of the missing short spacings in our interferometric observations. On the other hand, the HI fluxes for KK98 250 and KK98 251 derived from our GMRT observations is considerably lower than the single dish fluxes. The GMRT fluxes of these galaxies could be lower than those obtained from single dish measurements either because of (i) a calibration error or (ii) a large fraction of the HI being in an extended distribution that is resolved out. However, the flux of the point sources seen in the GMRT image are in good agreement with those listed in NVSS, indicating that our calibration is not at fault. Further, from our past experience in HI imaging of galaxies (with sizes similar to KK98 250 and KK98 251) with the GMRT, it seems unlikely that we have resolved out a large fraction of the total flux. Interestingly, a large discrepancy between the interferometric fluxes and the single dish fluxes was also seen in the DRAO images of these galaxies [44], although the comparison in that case is complicated by the very poor signal to noise ratio of the DRAO data. Finally, we note that for both the galaxies there is strong local HI emission at velocities very close to the systemic velocities. Hence, it is likely that the single dish integrated flux measurements were contaminated by blending of the HI emission from the galaxies with that of the galactic emission due to both the coarse velocity resolution ($\sim$10.0 km s^{-1}), as well as imperfect subtraction of the foreground emission in the position switching mode used in those observations.

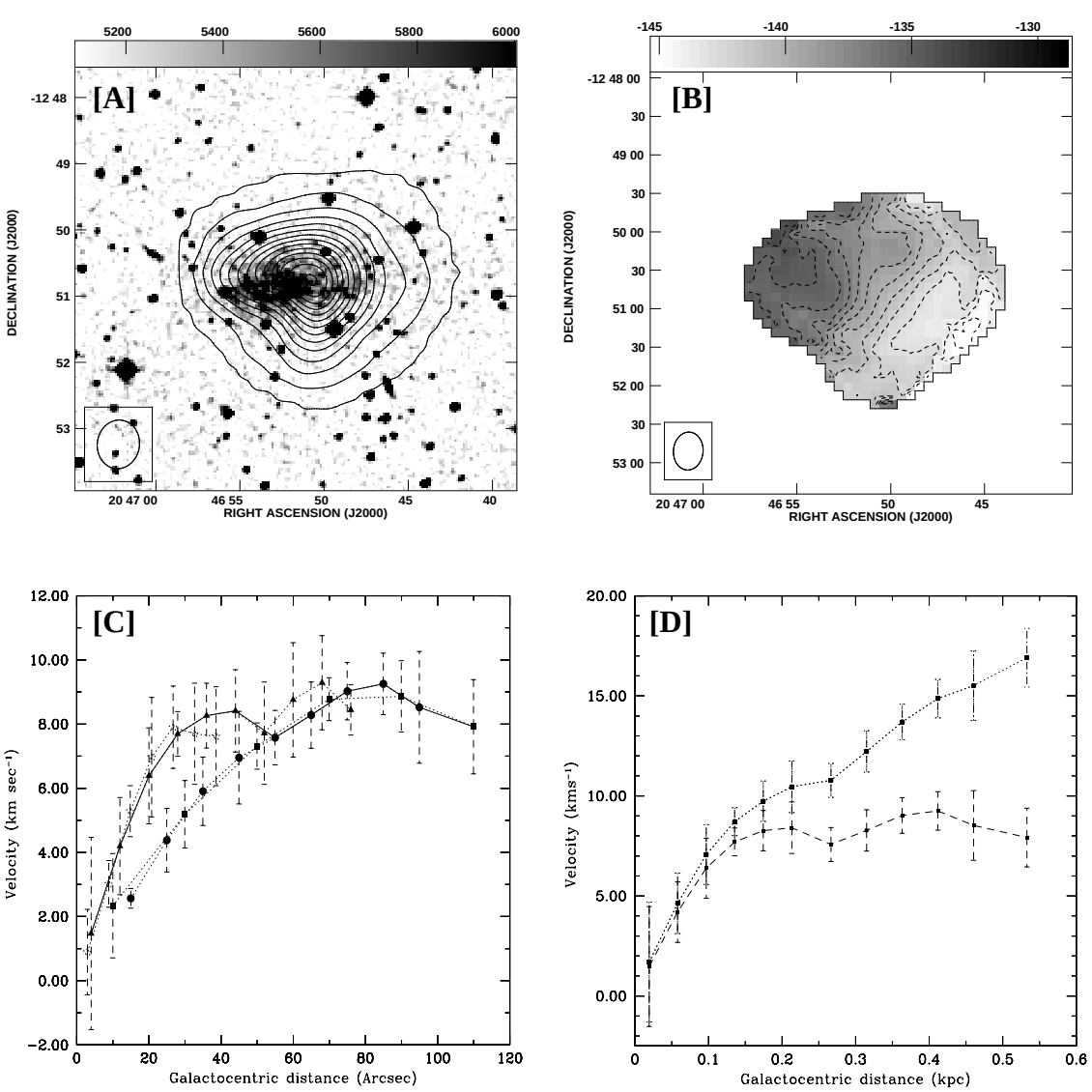

Figure 3.2: [**A**] The optical DSS image of DDO 210 (greyscales) with the GMRT $44'' \times 37''$ resolution integrated HI emission map (contours) overlayed. The contour levels are 0.06, 0.92, 1.80, 2.66, 3.54, 4.40, 5.24, 6.13, 7.00, 7.88, 8.75, 9.61, 11.03, 11.35 $\times 10^{20}$ atoms cm^{-2} [**B**]The HI velocity field of DDO 210 at $29'' \times 23''$ resolution. The contours are in steps of 1 km sec^{-1} and range from -145.0 km sec^{-1} to -133.0 km sec^{-1}. [**C**]The rotation curves derived from the intensity weighted velocity field at various resolutions. Crosses, triangles, circles and squares show the rotation velocity derived from the $12'' \times 11''$,$20'' \times 15''$, $29'' \times 23''$ and $44'' \times 37''$ resolution respectively. The adopted hybrid rotation curve is shown by a solid line. [**D**] The hybrid rotation curve (dashes) and the rotation curve after applying the asymmetric drift correction (dots).

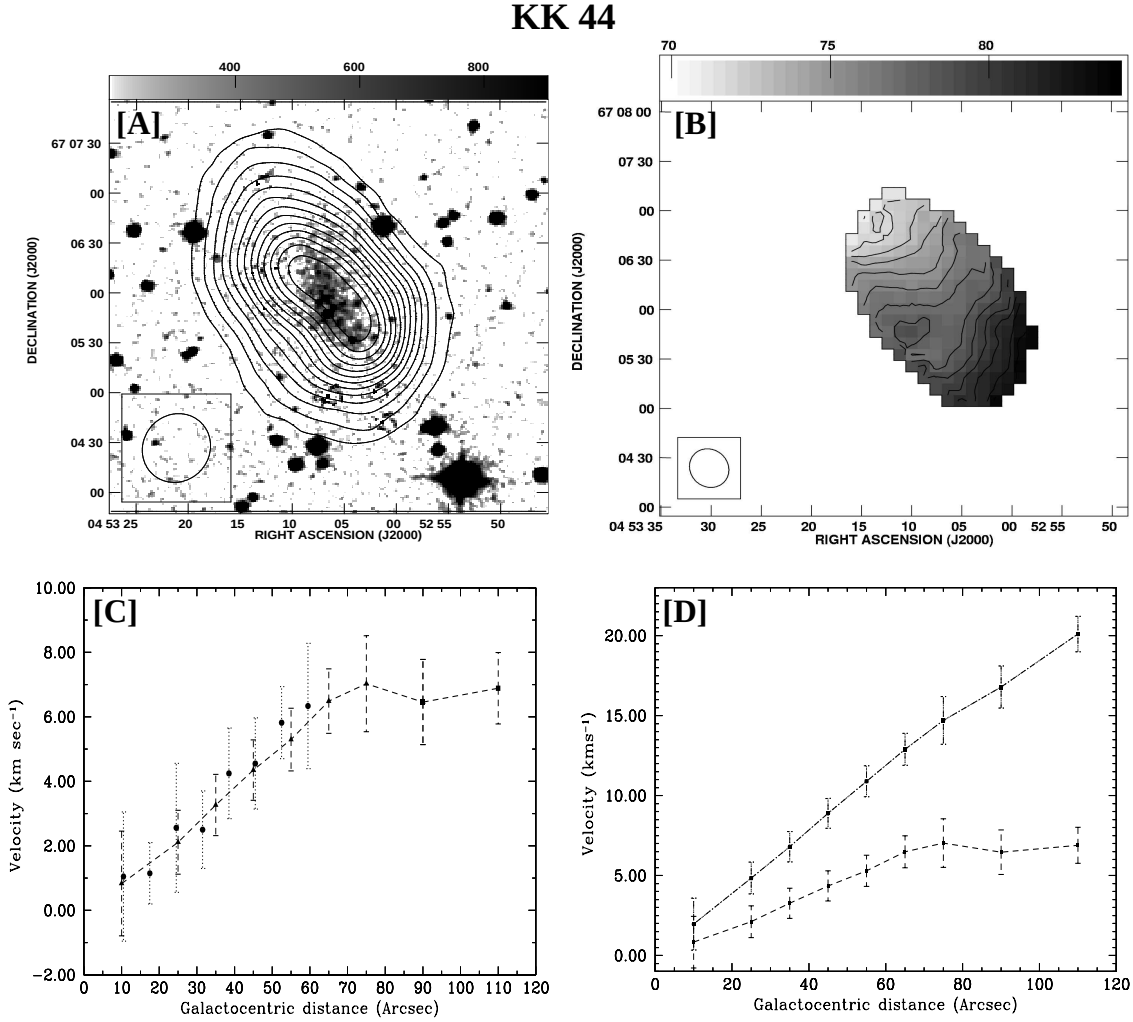

Figure 3.3: [**A**]The digitized Palomar Sky Survey image of KK 44 with the GMRT $40'' \times 38''$ resolution integrated HI emission (moment 0) map overlayed. The contour levels are $3.7, 8.8, 19.1, 24.3, 29.4, 34.6, 39.8, 44.9, 50.1, 55.2, 60.4, 65.5\&70.7 \times 10^{19}$ atoms cm^{-2}. [**B**] The HI velocity field of KK 44 at $24'' \times 22''$ arcsec resolution. The contours are in steps of 1 km sec^{-1} and range from 70.0 km sec^{-1} (the extreme North east contour) to 84.0 km sec^{-1} (the extreme South west contour). [**C**]Rotation curve derived from the intensity weighted velocity field. Filled circles, triangles and squares show the rotation curve derived from the $16'' \times 14''$, $24'' \times 22''$ and $40'' \times 38''$ resolution velocity fields respectively. The dotted line shows the adopted rotation curve. [**D**]The final adopted rotation curve (dashes) and the rotation curve after applying the asymmetric drift correction (dash dots).

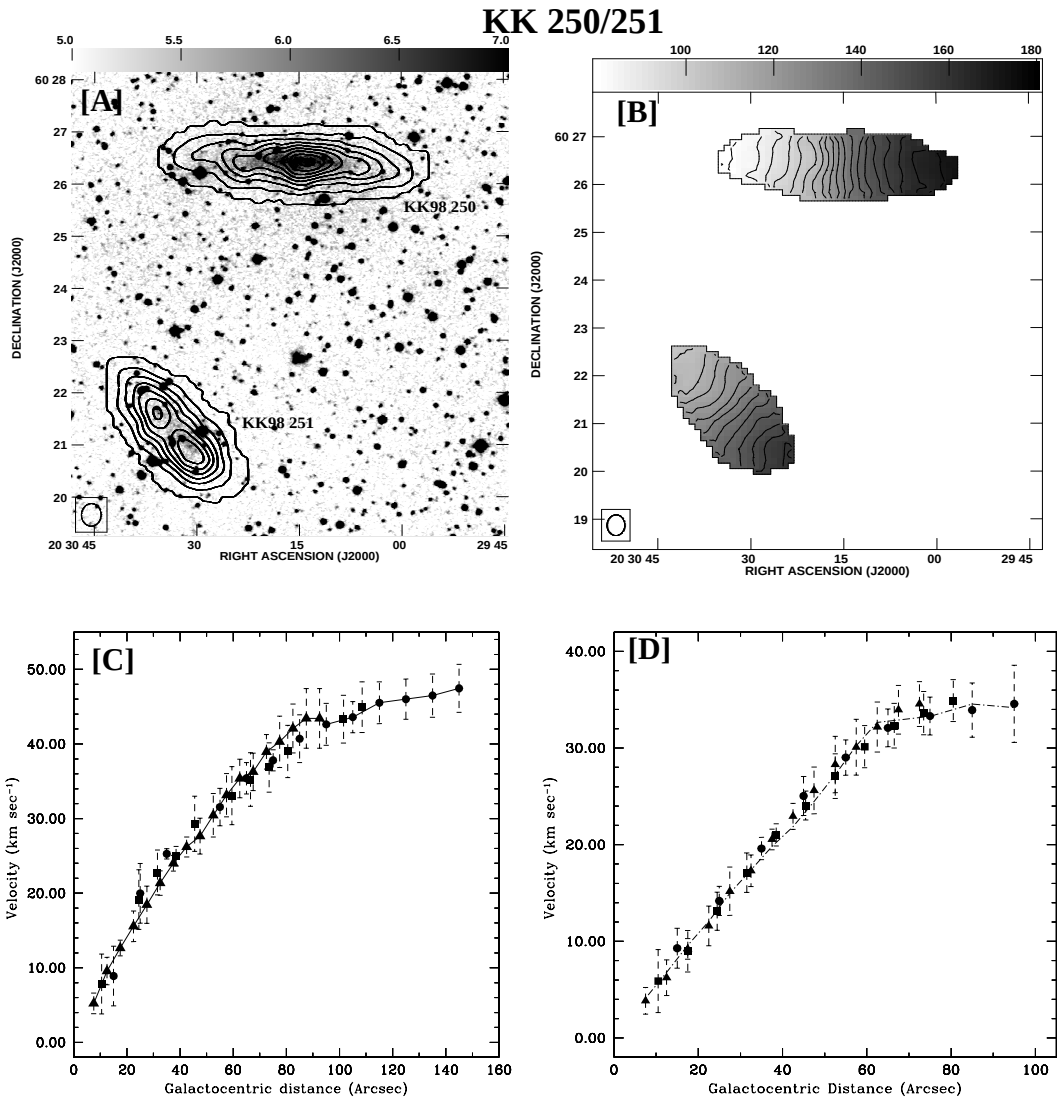

Figure 3.4: [**A**]The optical DSS image of KK98 250 (north) and KK98 251 (south-east), shown in greyscales, with the GMRT $26'' \times 21''$ resolution integrated HI emission map (contours) overlayed. The contour levels are 0.02, 2.8, 5.7, 8.7, 11.6, 14.4, 17.5, 20.1, 22.9, 25.8, 28.9, 31.7, 34.4, 37.4 and 40.2 $\times 10^{20}$ atoms cm^{-2}. [**B**]The HI velocity fields of KK98 250 and KK98 251 at $26'' \times 21''$ resolution. The contours are in steps of 5 km s^{-1}and range from 80.0 km s^{-1}to 170.0 km s^{-1}. [**C**] The rotation curves for KK98 250 derived from the intensity weighted velocity field at various resolutions. Circles, squares and triangles represent the rotation velocity derived from the $26'' \times 21''$, $16'' \times 14''$ and $11.5'' \times 10''$ resolution respectively. The adopted rotation curve is shown by solid line. [**D**]The rotation curves for KK98 251 derived from the intensity weighted velocity field at various resolutions. Circles, squares and triangles show the rotation velocity derived from the $26'' \times 21''$, $16'' \times 14''$ and $11.5'' \times 10''$ resolution respectively. The adopted rotation curve is shown by dash-dot line.

3.2.2 HI distribution

Figures 3.2[A], 3.3[A] & 3.4[A] show the GMRT integrated HI emission from the sample galaxies, overlayed on the digitized sky survey (DSS) images. The HI distribution in all the galaxies, except for KK98 251, are centrally peaked; for KK98 251, two high density peaks are seen near the center. In the case of KK98 250 and KK98 251, apart from the mild warp seen in the HI distribution in KK98 250, no clear signature of interaction is seen between the two galaxies.

The galaxy DDO 210 shows a peculiar HI morphology. As seen in fig. 3.2[A], the HI isodensity contours for DDO 210 are elongated in eastern and southern half of the galaxy i.e. the density is enhanced in these directions. These density enhancements are highlighted in Fig. 3.5[A], which shows the integrated HI emission at high resolution ($12'' \times 11''$). Note that the faint extended emission, seen in the low resolution map, is resolved out in this image. Apart from having a peculiar HI distribution, the stars in the galaxy also shows a peculiar distribution. The optical emission in the galaxy shows two components, a central bright compact component and an outer faint extended component; both elongated in the east-west direction [29]. However, the centers for the two components do not overlap; the bright component lies more eastwards than the center of extended component. From a visual inspection of the overlay (Fig. 3.2[A]), the eastern HI density enhancements seem to correlate with the optical emission in the galaxy. As can be seen the bright component of the optical emission is not centered on the HI emission, but is instead offset to the east. On the other hand, no optical emission is seen along the southern HI density enhancement. As a further check for optical emission associated with the southern HI density enhancement, we computed number counts of stars in that region using the deep optical image obtained by Tolstoy et al. (2000). No significant increase in the star counts from the background was detected.

3.2.3 HI surface density profiles

To obtain the deprojected HI radial surface density profiles for the sample galaxies, an estimate of the morphological center, position angle (PA) and inclination of the galaxies were obtained by fitting elliptical annuli to the HI column density maps. For KK98 250, KK98 251 and KK 44, except for the highest resolution HI maps (see Table 2.3), the integrated HI distribution at all resolutions were used. Due to the high density clumps in the center, ellipse fitting for KK98 251 was restricted only to the outer contours. In the case of DDO 210, as seen in the Fig. 3.5[A], the HI emission in the galaxy is distorted, hence the ellipse fitting to the higher resolution HI data (where the smooth emission is resolved out) is not

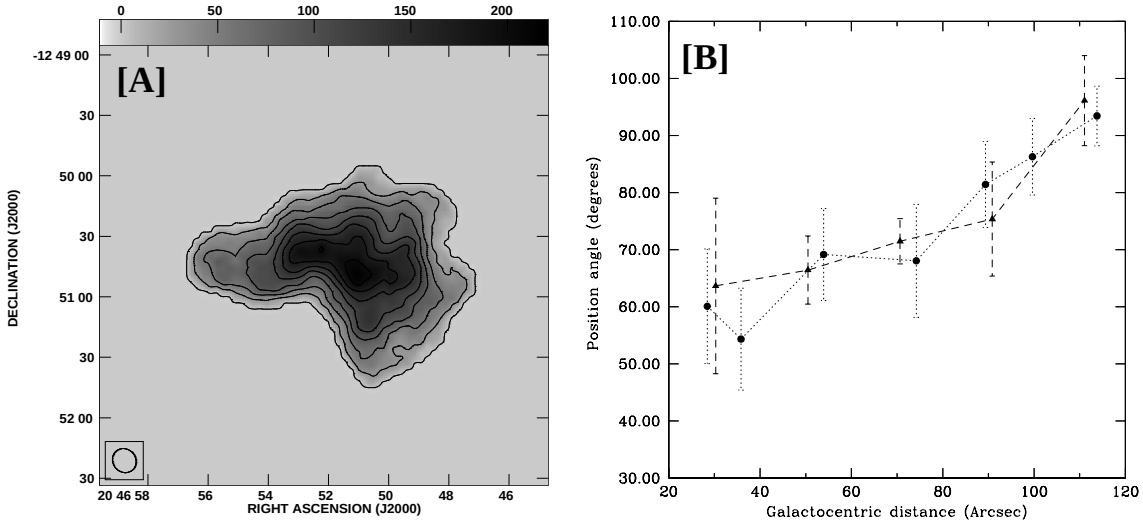

Figure 3.5: [**A**] Integrated HI emission map of DDO 210 (grey scale and contours) at $12'' \times 11''$ resolution. The contour levels are 0.001, 0.154, 0.293, 0.434, 0.576, 0.717, 0.858, 0.999, 1.141 Jy/Bm km s^{-1}. [**B**]The variation of position angle (PA) of DDO 210 with the galactocentric distance. Circles represent the morphological PA obtained from ellipse fit to the HI distribution at $44'' \times 37''$ resolution. Triangles represent the kinematical PA derived from $44'' \times 37''$ resolution velocity field.

reliable. Hence, an estimate of the HI morphological parameters of DDO 210 was obtained by fitting elliptical annuli to the faint extended emission in the two lowest resolution HI distribution (i,e. $61'' \times 60''$ and $44'' \times 37''$).

In the case of KK 44, KK98 250 and KK98 251, the estimated morphological center gave a good match to the optical center. For DDO 210, the morphological center lies close to the center of the faint extended optical component (but as noted above is offset from the center of the bright optical emission). The derived PA and inclination (assuming an intrinsic thickness (q_o) of 0.25) of KK 44, KK98 250 and KK98 251 showed no systematic variation (within the errorbars) with the galactocentric radius. The derived PA and inclination for these galaxies are given in Table. 3.1. For DDO 210, the PA shows a significant variation with the galactocentric radius, whereas the inclination is constant (within the errorbars) with the radii. The variation of the fitted morphological PA with the galactocentric radius for DDO 210 is given in Fig. 3.5[B]. For each galaxy, the values of the PA and inclination estimated from different resolution images match within the error bars. For KK 44, KK98

250 and KK98 251, the estimated parameters are also in good agreement with the values obtained from the optical images. On the other hand, the derived inclination for DDO 210 is significantly different from the optical inclination of the galaxy [12]. It is likely that the optical emission in DDO 210 does not arise from an axi-symmetric disk, but instead that the stars are concentrated in a patchy elongated region. Hence, in the absence of any other reliable estimate, the value of inclination obtained from the HI contours was assigned to the whole galaxy.

Using the derived inclination and PA, the deprojected HI radial surface density profiles for DDO 210, KK 44 and KK98 251 were obtained by fitting elliptical annuli to the integrated HI emission from the galaxies. The derived surface density $\Sigma_{\rm HI}(r)$ for the galaxies are given in Fig. 3.6. $\Sigma_{\rm HI}(r)$ for each galaxy is well represented by a gaussian:

$$\Sigma_{\rm HI}(r) = \Sigma_0 \times e^{-(r-c)^2/2r_0^2} \tag{3.1}$$

The estimated gaussian parameters for the galaxies are given in Table. 3.2.

For highly inclined galaxies, deprojection using ellipse fitting does not lead to reliable estimates for the surface density. Hence, in the case of KK98 250, Lucy's (1974) iterative decovolution scheme, as adapted and developed by Warmels (1988), was used to derive the HI surface mass density. Fig. 3.6[C] shows the best fit HI radial profile obtained from the $26'' \times 21''$ resolution HI image using Lucy's scheme. Note that the deconvolved HI surface density profile shows a steep rise of $\sim$40% in the central $\sim 25''$, i.e. within one synthesized beam. This is likely to be an artifact produced by the deconvolution; similar artifacts produced by this method have been seen earlier (e.g. [49]). We therefore fit the surface density $\Sigma_{\rm HI}(r)$ by a double gaussian (shown as dotted line in Fig. 3.6[C]) given in Eqn. 3.2, and use only the broad component for further analysis. For reference the derived double gaussian parameters are given in Table. 3.2

$$\Sigma_{\rm HI}(r) = \Sigma_1 \times e^{-(r-c_1)^2/2r_1^2} + \Sigma_2 \times e^{-(r-c_2)^2/2r_2^2} \tag{3.2}$$

3.2.4 HI kinematics

The velocity fields of the sample galaxies are shown in Fig. 3.2[B], 3.3[B] & 3.4[B]. As can be seen, the velocity fields are regular and a systematic velocity gradient is seen across each galaxy. Except for DDO 210, the isovelocity contours in all the galaxies are approximately parallel, which is a signature of rigid body rotation. Further, the kinematic major axis of all the galaxies are well aligned with the major axis of their HI distribution and optical broadband emission.

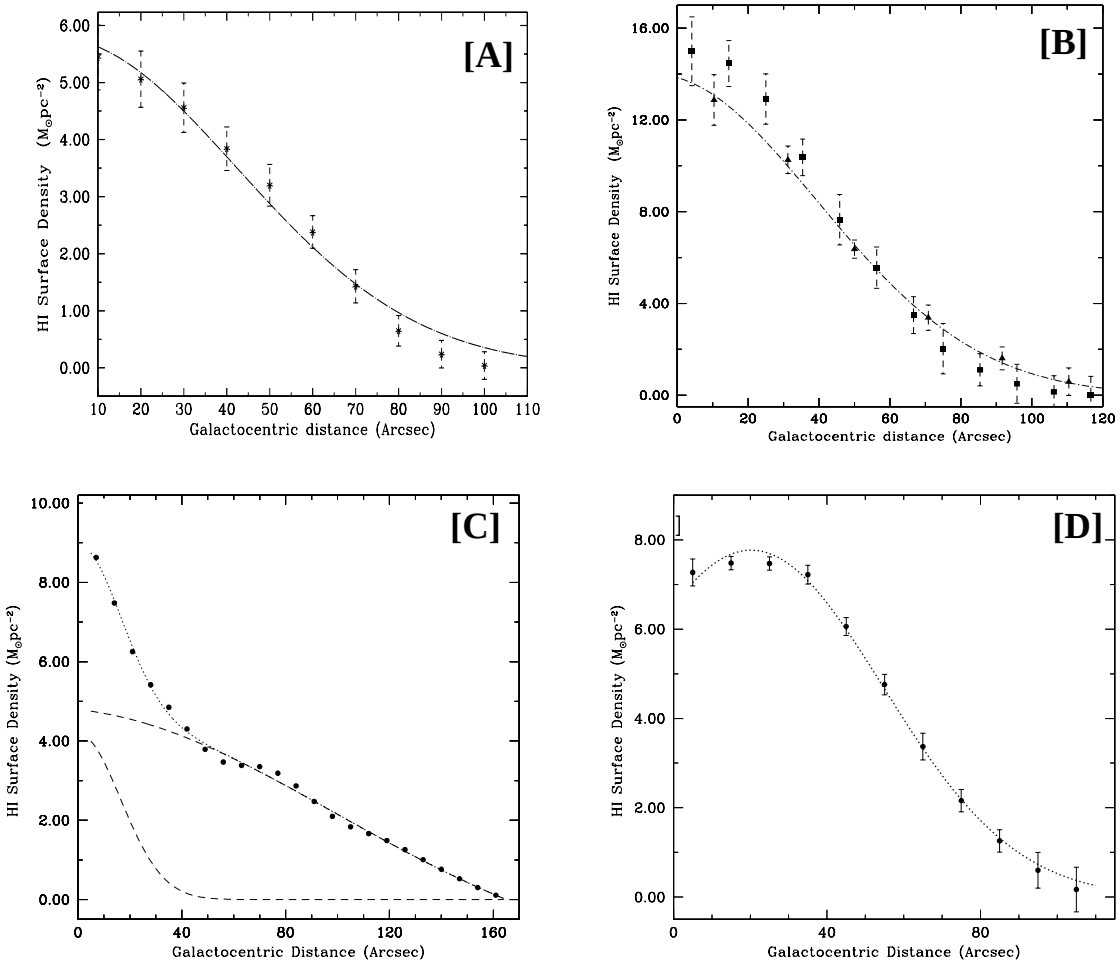

Figure 3.6: [**A**]The HI surface density profile of KK 44 derived from the HI distribution at $40'' \times 38''$ resolution. A gaussian fit is shown superimposed. [**B**] The HI surface density profile of DDO 210 derived from the HI distribution at $29'' \times 23''$ (squares) and $44'' \times 37''$ (triangles) resolution. A gaussian fit to $44'' \times 37''$ HI distribution is shown superimposed. [**C**] The HI surface density profile of KK98 250 derived from the HI distribution at $26'' \times 23''$ resolution (points). A double gaussian fit to the HI distribution is shown as dotted line. A decomposition of the double gaussian fit into a narrow and broad gaussian component is shown as dashed lines. See the text for more details. [**D**] The HI surface density profile of KK98 251 derived from the HI distribution at $26'' \times 23''$ resolution (points). The adopted gaussian fit is shown as a dotted line.

It is worth noting that the high velocity resolution (~ 1.6 km s^{-1}) and high sensitivity of our observations were critical in determining the velocity field of these faint dwarf galaxies. Synthesis observations often use much poorer resolution, which makes it difficult to discern systematic patterns, if any, in the velocity fields of faint dwarfs. For example, the systematic

Table 3.2: Results from the total HI column maps

Galaxy	PA	Incl	Σ_0	c	r_0
	(°)	(°)	($M_\odot$ pc^{-2})	(″)	(″)
DDO 210*		27.0 (7.0)	13.9 (1.0)	−4.0 (0.5)	46.0 (2.0)
KK 44	215.0 (5.0)	65.0 (5.0)	5.9 (0.2)	0.5 (0.4)	40.7 (1.6)
KK98 250a	267.0 (3.0)	80.0 (4.0)	5.0 (0.4)	1.0(0.5)	73.9 (1.7)
KK98 250b			4.2 (0.2)	0.8(0.5)	14.4 (0.8)
KK98 251	220.0 (5.0)	62.0(5.0)	7.8 (0.1)	19.2 (0.8)	34.2 (0.7)

*The variation of PA with the galactocentric radius is given in Fig. 3.5[B].

pattern seen in velocity field of DDO 210 derived from our GMRT observations is, to zeroth order, consistent with that expected from rotation. On the other hand, the velocity field of this galaxy derived by Lo et al.(1993) (based on a coarser velocity resolution of ~ 6 km s^{-1}) is chaotic. The velocity field determined from the recent high velocity resolution VLA study of DDO 210 by Young et al.(2003) matches with that obtained at the GMRT.

The velocity field of some of our galaxies shows kinematical peculiarities. For example, DDO 210 shows signatures of both warping and kinematical lopsidedness [50], i.e. the kinematical major axis is not a straight line but shows twists and the isovelocity contours in the eastern half of the galaxy are more closed than those in the western half. Both of these kinematical peculiarities become more prominent in the higher spatial resolution velocity field (see Fig. 3.9[A]). While the density enhancements in the HI in DDO 210 also become more prominent at higher spatial resolutions, there does not seem to be any particular correlation between the HI density enhancements and these kinematical peculiarities.

Another galaxy with kinematical peculiarities in KK98 251. The velocity field of this galaxy shows a mild lopsidedness; the isovelocity contours in the north-eastern half of the galaxy are more curved than the south-western half. Some small scale kinks are also seen in the isovelocity contours in the outer regions of the galaxy, indicative of a weak warping of the outer disk. These effects are more prominent in the higher spatial resolution velocity fields (not shown), which also show a mild twist in the kinematical major axis in the outer region of the galaxy, consistent with warping.

3.2.5 HI rotation curves

The rotation curves of DDO 210, KK 44, KK98 250, KK98 251 were derived separately for various resolution velocity fields using the tilted ring model described in Sect. 2.6.2.

For DDO 210, given a lack of correlation between the density enhancements in the HI distribution and the global kinematical peculiarities, it would be reasonable to assume that these density enhancements follow the same kinematics as that of the more diffuse extended emission. Under the further assumption that the kinematical peculiarities noted in the galaxy are not important (to the zeroth order; see also Sect. 3.3.1), the tilted ring model could be used to derive the rotation curve of this galaxy.

For each of our sample galaxy, the center and systemic velocity (V_{sys}), obtained from a global fit to various resolution velocity fields matched within the error bars; the V_{sys} also matched with the values obtained from the global HI profiles. Further, the derived kinematical center for each galaxy also matched with the morphological center derived from the HI distribution. In the case of DDO 210, because of distorted morphology of the galaxy at high spatial resolutions, an attempt to derive the kinematical center from a global fit to the velocity fields at these resolutions did not yield reliable results. Hence, the center for the higher resolution velocity fields was fixed to a value obtained from the lower resolution velocity fields.

Keeping V_{sys} and the kinematical center fixed to the values obtained from the global fits, the variation of the kinematical position angle (PA) and inclination with the galactocentric radii of each galaxy was derived. In the case of KK98 250, KK 44 and DDO 210, keeping inclination as a free parameter in the tilted ring fit gave unphysical results, hence, the kinematical inclinations of these galaxies were fixed to the value estimated from their HI morphology. For KK98 251, the inclination was found to be 65° (which agrees with that derived from ellipse fitting to the HI morphology), with no systematic variation with the radius.

For KK98 250, fits for the position angle gave a value of $\sim 267°$ (in good agreement with that derived from the optical image), with no systematic variation across the galaxy, whereas for KK98 251, best fit position angle was $\sim 230°$ at all radii, except in the outermost regions of the galaxy where it changes to $\sim 215°$. For KK 44, keeping PA as a free parameters did not give any meaningful results, hence PA was fixed to a value of 215°, derived from its optical and HI morphology. In the case of DDO 210, kinematical PA was found to vary significantly with radius. The variation of the derived kinematical PA with the galactocentric radius for DDO 210 for the $44'' \times 37''$ resolution velocity field is given in Fig. 3.5[B]. As can be seen, the value of kinematical PA at all galactocentric radii for DDO 210, matched with the

morphological PA estimated from the $44'' \times 37''$ resolution HI distribution. Also, all attempts to derive the kinematical position angle for DDO 210 at the higher spatial resolutions did not yield reliable estimates. Hence, in the absence of any other reliable estimate, the kinematical PA for the higher resolution velocity fields for DDO 210 was fixed to the value obtained from the lower resolution velocity fields.

Finally, the rotation curve of each galaxy was computed keeping all parameters, except the circular velocity V_c, in each elliptical annuli fixed. Fig. 3.2[C], 3.3[C] & 3.4[C]-[D] shows the rotation curves for our sample galaxies derived from the different spatial resolution velocity fields. Note that in the case of KK98 250, KK98 251 and KK 44, the rotation curves derived from the different resolution velocity fields match within the errorbars, suggesting that, the effects of beam smearing are not significant in these galaxies. On the other hand, in the case of DDO 210, the rotation curve derived from the higher resolution velocity fields (i.e. $20'' \times 15''$ and $12'' \times 11''$) is significantly steeper in the inner regions of the galaxy than those computed from the lower resolution $44'' \times 37''$ and $29'' \times 23''$ velocity fields; this could be a result of beam smearing. However, since the rotation curves from each resolution agree in the outer regions of DDO 210, this suggests that the effect of beam smearing is significant only in the inner regions of the galaxy, where the rotation velocity is increasing with the galactocentric radius. Further, the rotation curves derived from the $12'' \times 11''$ resolution velocity field in DDO 210 agrees with that obtained from the $20'' \times 15''$ resolution data, suggesting that beam smearing effects are no longer significant at such high resolutions (which corresponding to a linear scale of $\sim$ 70pc). The final adopted rotation curve for each galaxy is shown as a solid line in Fig. 3.2[C], 3.3[C] & 3.4[C]-[D].

For highly inclined galaxies, rotation velocities derived from the tilted ring fits to the velocity field could underestimate the true rotation velocities, hence in such cases the rotation curve is often estimated by fitting to the high velocity edge of the emission (e.g. [45]). While this method is well suited to large galaxies with flat rotation curves, it is not appropriate for galaxies with solid body rotation. Since the velocity field as well as the rotation curve derived from the tilted ring fit for KK98 250, indicate solid body rotation, hence, instead of using the 'edge fitting' technique, the rotation curve for KK98 250 was also derived by interactively fitting to the PV diagram, using the task INSPECTOR in GIPSY (see Fig 3.7[A]). The PA and the inclination in the interactive fitting were fixed to the values used in the tilted ring fit. The derived rotation curve matches, within the errorbars, to that derived from the tilted ring fit. As a further check of the robustness of the derived rotation curve of KK98 250, a model data cube for this galaxy was constructed using the adopted rotation curve and the observed HI column density profile, with the task GALMOD in GIPSY. The model data

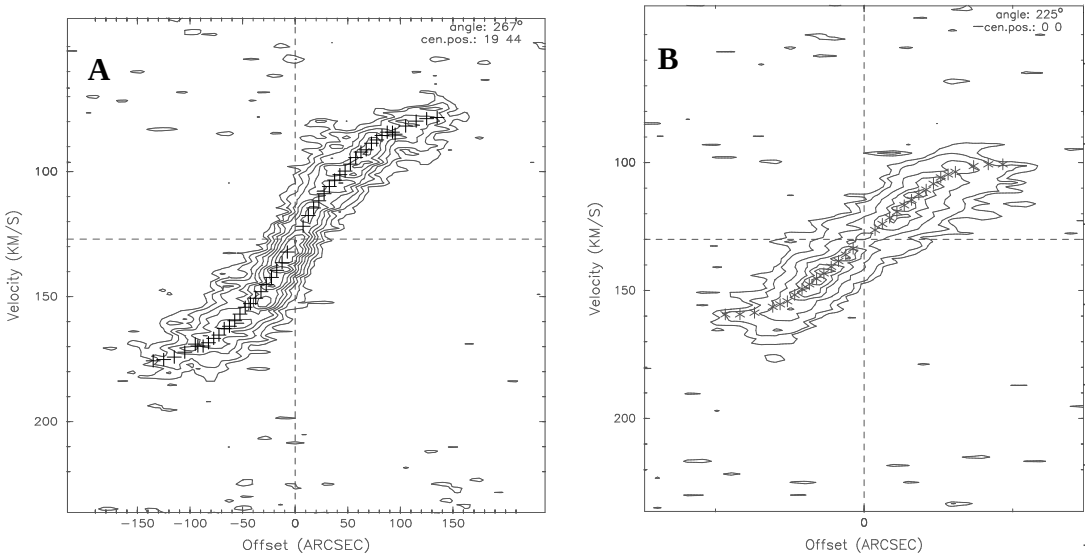

Figure 3.7: [**A**] The PV diagram of the galaxy along the kinematical major axis for KK98 250, with the adopted rotation curve overlayed. [**B**] The PV diagram of the galaxy along the kinematical major axis for KK98 251, with the adopted rotation curve overlayed.

cube was smoothed to a beam of $26'' \times 21''$ resolution and the moment maps were derived in the same manner as for the real data. Fig. 3.8[B] shows the derived model velocity field for KK98 250. A residual (data-model) velocity field is shown in Fig. 3.8[C]; as can be seen, the model velocity field provides a good match to the observed field.

Although KK98 251 is less inclined, a similar exercise of estimating the rotation velocities from the PV diagram was repeated for it. Fig 3.7[B] shows the adopted rotation curve projected onto the PV diagram – as can be seen, the rotation curve provides a reasonably good fit to the data. A model data cube for KK98 251 was also constructed using the derived rotation curve, in the same manner as for KK98 250. Again, a good match between the model (not shown) and the observed field was found. In the case of KK 44, since the peak rotation velocity is comparable to the observed velocity dispersion in HI, the method of estimating the rotation velocities from the PV diagram in this galaxy did not give any reliable results.

In the case of DDO 210, the rotation curves have been derived under the assumption that the HI density enhancements follow the same kinematics as that of the extended emission. The validity of this assumption could be tested by checking whether the derived rotation curves can reproduce the observed kinematics in the galaxy. Hence, model velocity fields were made at $44'' \times 37''$, $29'' \times 23''$ and $20'' \times 15''$ resolutions using the rotation curves and other kinematical parameters, derived from each resolution with a tilted ring model, using the task

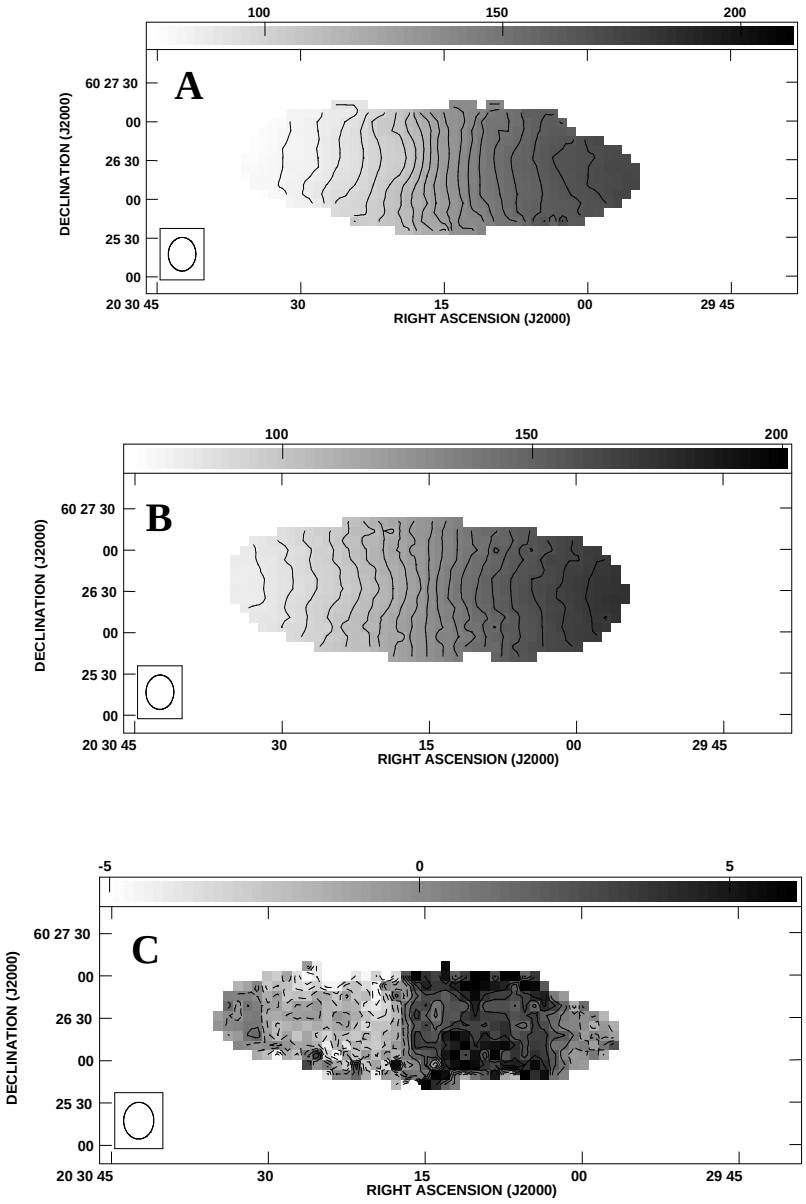

Figure 3.8: [**A**]The observed velocity field of KK98 250 at $26'' \times 21''$ resolution. [**B**]The model velocity field derived from the rotation curve at $26'' \times 21''$ resolution. The contours are in steps of 5 km s^{-1}and range from 81.0 km s^{-1}to 171.0 km s^{-1}.[**C**] The residual velocity field ([A]-[B]). The contours are in steps of 1.0 km s^{-1}and range from -4.0 km s^{-1}to 4.0 km s^{-1}.

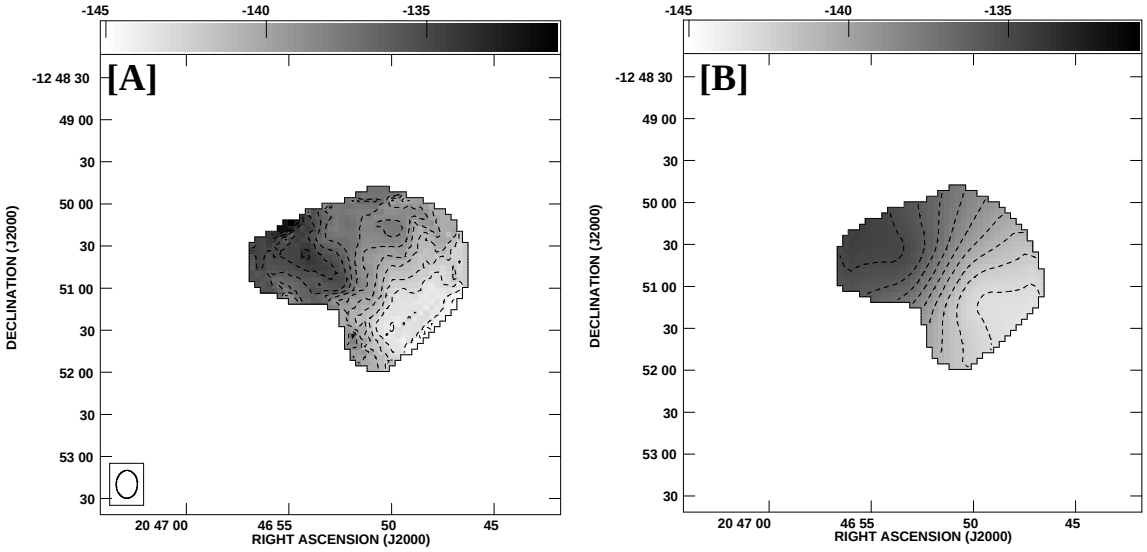

Figure 3.9: [**A**] The observed velocity field of DDO 210 at $20'' \times 15''$ resolution. [**B**]The model velocity field derived from the rotation curve at $20'' \times 15''$ resolution. The contours are in steps of 1 km sec^{-1} and range from $-$ 144.0 km sec^{-1} to -134.0 km sec^{-1}.

VELFI in GIPSY. The model velocity field at $20'' \times 15''$ resolution is shown in Fig. 3.9. As can be seen from the figure, the model provides a reasonable match to the observed velocity field. Note however that the model fails to reproduce the kinematical lopsidedness and the twist in the kinematical major axis. This is to be expected, since neither of these two features was incorporated in the model. A similar match between the observed and the model velocity fields was also found for the two lower resolution velocity fields.

The sensitivity of HI observations to the inner slope of the rotation curve has been the subject of much recent discussion (e.g. [57]). One possible way of overcoming the relatively poor resolution offered by HI observations is to instead use Hα observations. For KK98 250, an Hα based rotation curve has been derived by de Blok et al.(2001), and is shown with triangles in Fig. 3.10[A]. As can be seen, although the Hα curve is steeper than the HI curve at intermediate radii, in the innermost regions of the galaxy, (where the effects of beam smearing are expected to be most severe), the two rotation curves in fact show an excellent agreement.

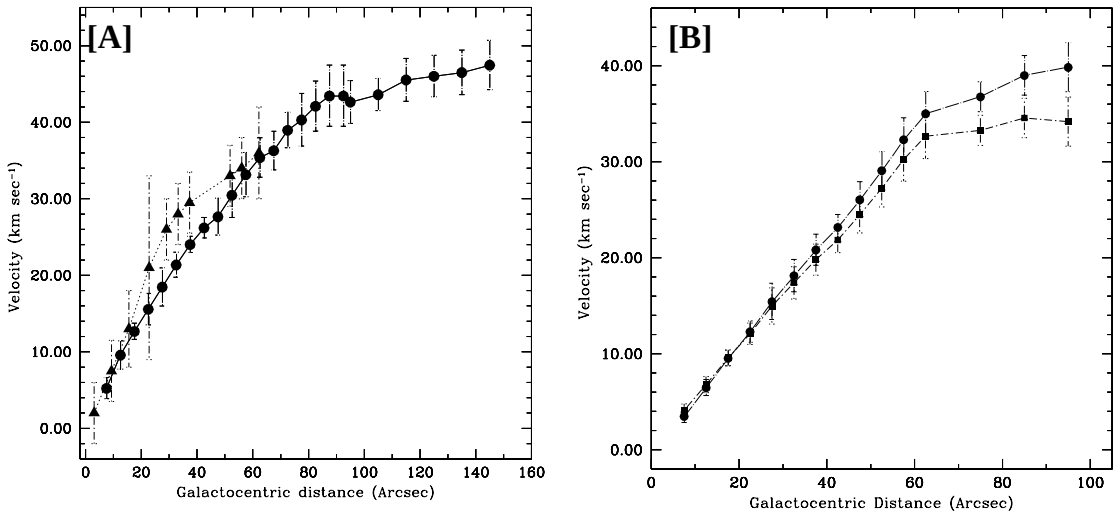

Figure 3.10: [**A**]The adopted HI rotation curve for KK98 250 (dots) along with the Hα rotation rotation curve derived by de Blok et al. (2001) (triangles). [**B**] The adopted rotation curve for KK98 251 (squares) and the rotation curve after applying "asymmetric drift" correction (circles).

3.2.5.1 Asymmetric drift correction

As seen in Fig. 3.2[C] & 3.3[C], the maximum rotation velocities (inclination corrected) of DDO 210 and KK 44 are comparable to the velocity dispersion observed in the HI gas, i.e. random motions in the gas in these galaxies provides significant dynamical support to the HI disk. Equivalently, the observed circular velocity significantly underestimates the centripetal force and hence the implied dynamical mass. The observed rotation velocities hence need to be corrected before trying to estimate the dynamical mass. This correction, generally termed an "asymmetric drift" correction is given by (e.g.Meurer et al.(1996); note that the formula below is slightly different from the one in Meurer et al. (1996), as we have used a sech^2 profile in the vertical direction instead of an exponential one)

$v_c^2 = v_o^2 - r \times \sigma^2[\frac{d}{dr}(\ln \Sigma_{HI}) + \frac{d}{dr}(\ln \sigma^2) - \frac{d}{dr}(\ln 2h_z)]$,

where v_c is the true circular velocity, v_o is the observed rotation velocity, σ is the velocity dispersion, and h_z is the scale height of the disk. Strictly speaking, asymmetric drift corrections are applicable to collisionless stellar systems for which the magnitude of the random motions is much smaller than that of the rotation velocity. However, it is often used even for gaseous disks, where the assumption being made is that the pressure support can be approximated as the gas density times the square of the random velocity. For the case of our sample galaxies, in the absence of any direct measurement of h_z we assume $d(\ln(h_z))/dr = 0$, (i.e.

that the scale height does not change with radius) and also use the fact that σ^2 is constant across the galaxy (see Sect. 2.6), to get:

$$\mathrm{v_c^2 = v_o^2 - r \times \sigma^2 [\frac{d}{dr}(\ln \Sigma_{HI})]}. \tag{3.3}$$

From Sect. 3.2.3, we find that the radial HI surface density distribution for DDO 210 and KK 44 are well represented by Gaussian profiles. Hence, using the fitted Gaussian profile to the radial surface density distribution from Eqn. 3.1, we obtain

$$\mathrm{v_c^2 = v_o^2 + r(r - c) \times \sigma^2 / r_0^2}. \tag{3.4}$$

Further, the observed $\sigma_{\rm obs}$ (see section 2.6) needs to be corrected for the finite velocity resolution of the observations, as well as the contribution of the rotation velocity gradient over the finite size of the beam. The correction is:

$$\sigma_{\rm T}^2 = \sigma_{\rm obs}^2 - \Delta v^2 - \frac{1}{2} b^2 (\nabla v_o)^2, \tag{3.5}$$

where $\sigma_{\rm T}$ is the true velocity dispersion, Δv is the channel width, b characterizes the beam width (i.e. the beam is assumed to be of form e^{-x^2/b^2}) and v_o is the observed rotation velocity. The corrected velocity dispersion using the observed velocity dispersion from Sect. 2.6, are given in Table. 3.1. Finally, using the gaussian parameters estimated from the fits to the HI surface density profiles (from Table. 3.2), the observed rotation velocities of DDO 210 and KK 44 were corrected for the "asymmetric drift" correction. The "asymmetric drift" corrected rotation curve for the galaxies DDO 210 and KK 44 are shown as the dash dot line in Fig. 3.2[D]& 3.3[D]. This correction was also applied to the rotation curves of KK98 250 and KK98 251. In the case of KK98 250, this correction is found to be small (less than 2.5 km $\mathrm{s^{-1}}$), compared to the errorbars on the rotation curve. On the other hand, the correction for KK98 251 is significant in the outer regions. The "asymmetric drift" corrected curve for KK98 251 is shown in Fig. 3.10[B].

3.2.6 Mass model

In this section we attempt to decompose the mass distribution of DDO 210, KK 44, KK98 250 and KK98 251 into contributions from the stellar disk, the gaseous disk and the dark matter (DM) halo.

The contribution of the stellar mass to the observed rotation curve for each galaxy was computed by assuming the galaxy to have exponential stellar disk, with a constant mass to light ratio (Υ) and an intrinsic thickness ratio (q_0) of 0.25. We further assumed that the

density distribution in the vertical (z) direction falls off like $\mathrm{sech}^2(z/z_0)$, with z_0 independent of galacto-centric radius. This is a reasonable approximation for disk galaxies (see e.g. [11, 58]). In the absence of any prior knowledge of Υ, it is taken to be a free parameter during the modeling.

The contribution of the gaseous disks of our sample galaxies to their observed rotation curves are calculated using HI surface mass density profiles given in Fig. 3.6. The contribution of primordial Helium is taken into account by multiplying HI densities by a factor of 1.4. There is little evidence that dwarf galaxies contain substantial amounts of molecular gas (see e.g. [20, 51]), so no correction has been made for molecular gas. We also neglect the contribution of ionized gas, if any. Not much is known about the vertical distribution of gas in disk galaxies, however there is some evidence for similar vertical distributions of the HI and stellar disk (e.g. [4]). For the intrinsic thickness ratio of the gaseous disks we hence assume $q_0 = 0.25$ and also assume that the shape of the profile in the vertical direction is given by $\mathrm{sech}^2(z/z_0)$. To check the validity of these assumptions we tried modeling the HI distributions and velocity fields with various vertical profiles and intrinsic thickness ratios using the GIPSY task GALMOD. It was found that the best (visual) match between the model and the observed maps were obtained with a $\mathrm{sech}^2(z/z_0)$ profile and an intrinsic thickness ratio of 0.25. The geometries of all the disk components being thus fixed, the circular velocities of the disk components were computed using the formulae given by Casertano (1983).

For the dark matter we considered two types of density profiles, a modified isothermal halo and an NFW halo. The modified isothermal halo has a density profile given by:

$\rho_{iso}(r) = \rho_0[1 + (r/r_c)^2]^{-1}$,

where, ρ_0 is the central density of the halo and r_c is the core radius. The corresponding circular velocity is given by

$v(R) = \sqrt{4\pi G\rho_0 r_C^2[1 - \frac{r}{r_c}\tan^{-1}(\frac{r}{r_c})]}$.

The NFW halo density is given by

$\rho_{NFW}(r) = \rho_i/[(r/r_s)(1 + r/r_s)^2]$,

where, r_s is the characteristic radius of the halo and ρ_i is the characteristic density. The circular velocity can be written as:

$v(R) = v_{200}\sqrt{\frac{\ln(1+cx)-cx/(1+cx)}{x[\ln(1+c)-c/(1+c)]}}$,

where, $c = r_{200}/r_s$, $x = r/r_{200}$; r_{200} is the distance at which the mean density of the halo is equal to 200 times the critical density and v_{200} is the circular velocity at this radius.

We will now discuss the mass modelling for each galaxy in turn.

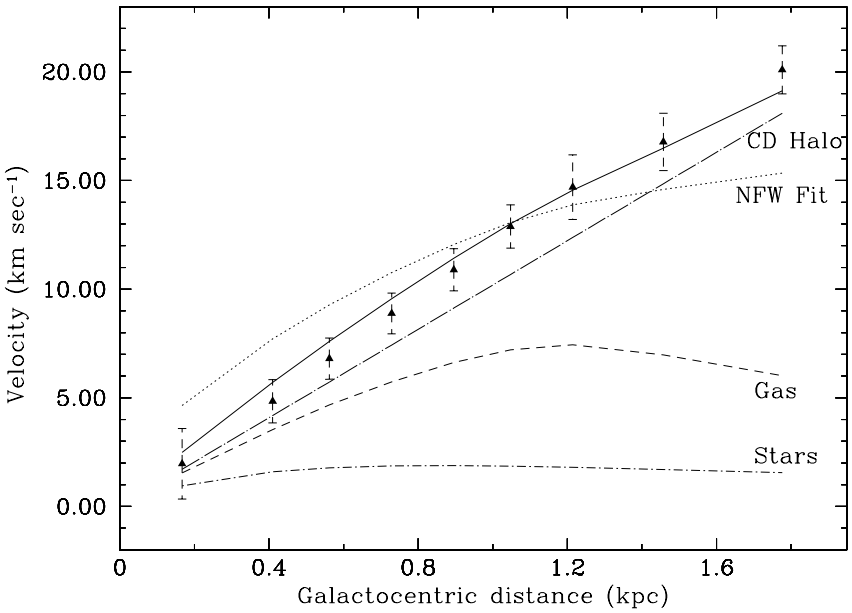

Figure 3.11: Mass models for KK 44 using the corrected rotation curve. The points are the observed data. The total mass of gaseous disk (dashed line) is $1.68 \times 10^7 M_\odot$.The stellar disk (short dash dot line) has $\Upsilon_V = 0.2$, giving a stellar mass of $1.72 \times 10^6 M_\odot$. The best fit total rotation curve for the constant density halo model is shown as a solid line, while the contribution of the halo itself is shown as a long dash dot line (the halo density is density $\rho_0 = 5.7 \times 10^{-3} M_\odot$ pc^{-3}). The best fit total rotation curve for an NFW type halo (for $c = 1.0$ and $\Upsilon_V = 0.0$) is shown as a dotted line. See the text for more details.

3.2.6.1 KK 44

For the mass modelling of KK 44, we have used the V band scale length. The results of the optical photometry of KK 44 in V band were kindly provided by U Hopp. The exponential scale lengths for this galaxy in V band is $26.2''$.

We consider first the mass models for this galaxy using a modified isothermal halo. Because the "asymmetric drift" corrected rotation curve for KK 44 is rising till the last measured point (Fig. 3.3[D]), the parameter r_c could not be constrained (inorder to constrain r_c one needs the rotation curve to transition from rising linearly to being more or less flat, as is typically seen for spiral galaxies). We were therefore left with two free parameters, viz., the mass to light ratio of the stellar disk, Υ_V, and the core density of the halo ρ_0. Keeping both these parameters free in the fit gave unphysical fits, hence the best fit ρ_0 was determined keeping Υ_V fixed to the values corresponding to the maximum disk (which substantially

overpredicts the observed rotation curve at small radii, and is hence an upper limit to Υ_V), minimum disk and for Υ_V=1.8 (from observed B-V ∼0.8, using the low metallicity Bruzual & Charlot SPS model for a modified Salpeter IMF [1]). The derived ρ_0 for each value of Υ_V is given in Table 3.3, along with the reduced χ^2 for each fit. Since there are heuristics involved in computing the error bars on the rotation velocities, it is not possible to rigorously translate the minimum χ^2 value into a confidence interval for the parameters of the fit. However, a lower χ^2 value does imply a better fit (see also the discussion in[57]). We found that the χ^2 continuously decreases as Υ_V decreases. As can be seen from the χ^2 value in Table 3.3, Υ_V=1.8 gives a very poor fit to the data as it is much larger than Υ_V corresponding to the maximum disk. Further, except for the case of Υ_V obtained from modelling the observed colours (which in any case gives a very poor fit to the data), the central halo density ρ_0 is relatively insensitive to the assumed Υ_V, and is well determined. To illustrate the general quality of fit, we show in Fig. 3.11 the mass decomposition for a modified isothermal halo using $\Upsilon_V = 0.2$. The mass of the gas disk in KK 44 is M_{gas}=$1.68 \times 10^7 M_\odot$ and the adopted ($\Upsilon_V = 0.2$) model gives the mass of stellar disk to be M_*=$1.72 \times 10^6 M_\odot$. From the last measured point of the observed rotation curve, we get a total dynamical mass of M_T=$1.67\times10^8 M_\odot$, i.e. at the last measured point more than 89% of the mass of KK 44 is dark. Like other faint dwarf galaxies, KK 44 is also dark matter dominated in the inner regions, by the time one reaches a galacto-centric radius of two (optical) disk scale lengths, the mass of the stellar and gas disks is small compared to the mass in the dark matter.

A similar procedure was tried using a dark matter halo of the NFW type, but no reasonable fit could be obtained for any value of Υ_V. Essentially, KK 44 is dark matter dominated and has a linear rotation curve while the NFW halo provides a poor fit for linear rotation curves. As an illustration, we show in Fig. 3.11 the best fit rotation curve for an NFW halo with $c = 1.0$, $\Upsilon_V = 0.0$, and v_{200} chosen to minimize the χ^2. These are already unphysical values for these parameters, and increasing either c or Υ_V only worsens the quality of the fit.

3.2.6.2 DDO 210

As discussed in Sect. 3.2.2, the optical emission in DDO 210 is not axi-symmetric but is instead patchy and elongated. For the purpose of mass modeling however, we approximated the optical emission to be axi-symmetric, but we will return to this issue in Sect 3.3.1. Assuming that the optical emission was axi-symmetric, Lee et al.(1999) estimate the B band scale length (α_B) of DDO 210 to be 35.0″ (∼ 0.17 kpc).

As seen in Fig. 3.2[D], the "asymmetric drift" corrected rotation curve for DDO 210 is

Table 3.3: Mass decomposition using a constant density halo

	KK 44			DDO 210		
HI Curve	Υ_V	ρ_0	χ^2	Υ_B	ρ_0	χ^2
		(10^{-3}M$_\odot$pc^{-3})			(10^{-3}M$_\odot$pc^{-3})	
Best fit	–	–	–	3.4±0.5	29.3±5.4	0.6
Maximum disk	0.5	5.2 ± 0.5	1.2	5.0	14.2±4.1	0.9
Observed <B-V>	1.8	3.8 ± 1.1	5.7	0.5	59.0 ± 7.0	2.1
Minimum disk	0.0	5.9 ± 0.3	0.3	0.0	65.2±7.9	2.9

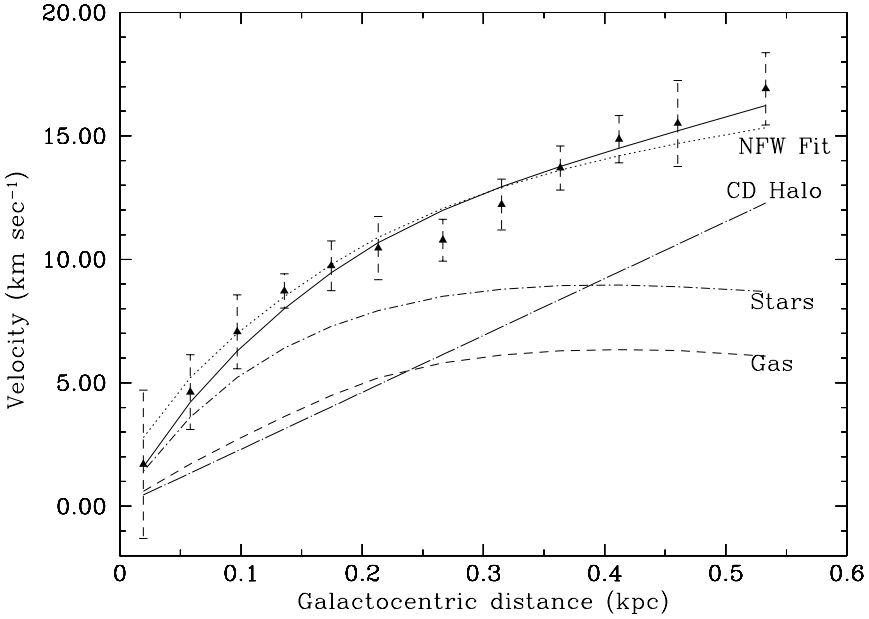

Figure 3.12: Mass models for DDO 210 using the corrected rotation curve. The points are the observed data. The total mass of gaseous disk (dashed line) is 3.6×10^6M$_\odot$.The stellar disk (short dash dot line) has $\Upsilon_B = 3.4$, giving a stellar mass of 9.2×10^6M$_\odot$. The best fit total rotation curve for the constant density halo model is shown as a solid line, while the contribution of the halo itself is shown as a long dash dot line (the halo density is density $\rho_0 = 29 \times 10^{-3}M_\odot$ pc^{-3}). The best fit total rotation curve for an NFW type halo, using $\Upsilon_B = 0.5$, c=5.0 and v_{200}=38.0 km s^{-1}is shown as a dotted line. See the text for more details.

rising till the last measured point, hence the core radius r_c could not be constrained from mass modelling of this galaxy. Hence, in this case, the modified isothermal dark halo fit

reduces to a constant density halo fit. The derived halo parameters for the best fit constant density dark halo model are given in Table 3.3. For comparison, the dark halo parameters for the modified isothermal dark halo using the $\Upsilon_{\rm B}$ corresponding to the maximum disk, minimum disk and for $\Upsilon_{\rm B}$=0.5 from the observed (B-V)$\sim$0.25 [12] (from the low metallicity Bruzual & Charlot SPS model using a modified Salpeter IMF [1]) are also given in Table 3.3. The quality of fit for each model in terms of the reduced χ^2 corresponding to each fit is also listed in Table 3.3. We find that the minimum disk model gives a very poor fit to the data; this model underestimates the "asymmetric drift" corrected rotation velocities significantly in the inner regions of the galaxy.

Fig. 3.12 shows the best fit mass model for DDO 210 for a constant density halo. The best fit model ($\Upsilon_{\rm B} = 3.4$) gives the mass of stellar disk to be $\rm M_*$=$9.2 \times 10^6 \rm M_\odot$. The mass of the gas disk in DDO 210 is $\rm M_{gas}$=$3.5 \times 10^6 \rm M_\odot$. From the last measured point of the observed rotation curve, we get a total dynamical mass of $\rm M_T$=$3.4 \times 10^7 \rm M_\odot$, i.e. at the last measured point more than 63% of the mass of DDO 210 is dark.

A similar procedure was also tried using a dark matter halo of the NFW type. Keeping $\Upsilon_{\rm B}$ as a free parameter in the fit gave unphysical results, hence, it was kept fixed to a more likely value (viz. $\Upsilon_{\rm B} = 0.5$). We found that an NFW type halo provides a good fit to the data, for a wide range of values of v_{200} and c. The range of parameters which provide acceptable fits are (v_{200} $\sim$20 km s^{-1}, $c \sim 10$) to (v_{200} $\sim$500 km s^{-1}, $c \sim 0.001$). As an illustration we show in Fig. 3.12 the best fit rotation curve for an NFW halo, using $\Upsilon_B = 0.5, c = 5, v_{200} = 38$ km s^{-1}. As can be seen, NFW type halos also provide a good fit to the data. However, it should be noted that the best fit values of the concentration parameter c, at any chosen v_{200} was found to be consistently smaller than the value predicted by numerical simulations for the ΛCDM universe [32].

Recall that all the above mass models for DDO 210 have been derived by assigning an inclination of 30 degrees to the galaxy (obtained from the outer HI contours, as discussed in Sect.3.2.2). In-order to estimate the effect of using an erroneous inclination on the derived halo parameters, mass modeling was also tried with two other values of inclination viz. 60 degrees (i.e. that estimated from the optical isophotes[12]) and 45 degrees (a value between the optical and HI inclination). The derived halo parameters for the best fit constant density halo model using these values of inclinations, along with the reduces χ^2 for each fit, are given in Table 3.4. For comparison, the best fit ρ_0 and $\Upsilon_{\rm B}$ for an inclination of 30 degree are also given. As can be seen, the central halo density is relatively insensitive to the assumed inclination. However, the best fit $\Upsilon_{\rm B}$ changes significantly with the assumed inclination.

For the NFW halo fit, keeping $\Upsilon_{\rm B}$ as a free parameter in the fit gave unphysical results,

Table 3.4: Mass decomposition for DDO 210 using a constant density halo for various values of inclination for the galaxy

Inclination (°)	Υ_B	ρ_0 ($10^{-3}M_\odot$ pc^{-3})	χ^2
60	1.4±0.2	27.0±2.0	0.3
45	1.8±0.2	31.0±2.0	0.2
30	3.4±0.5	29.1±5.0	0.4

hence, it was kept fixed to a value of 0.5, as suggested by the observed colours in the galaxy. The best fit NFW model with an inclination of 60 degrees gave a reduced $\chi^2 = 4.0$, while for 45 degrees a reduced $\chi^2 = 1.6$ was obtained from the best fit. As can be seen, the NFW halo provides a poor fit to the data for higher values of inclination (for comparison, an inclination of 30 degrees gave the best fit NFW model with a reduced $\chi^2 = 0.5$). Hence, an NFW type halo seems unlikely, if the inclination of the galaxy is higher than 30 degrees.

3.2.6.3 KK98 250

As described in Sect. 2.5, optical broadband emission from only the brightest central regions of KK98 250 could be traced in the I band, hence we have used the more accurately determined V band scale length for the mass modeling of this galaxy. Fig. 3.13[A] shows the best fit mass models for KK98 250. The derived halo parameters are given in Table 3.5. For comparison, apart from the best fit mass model, the derived halo parameters are also given for the maximum disk, minimum disk and $\Upsilon_V = 0.7$ (which was obtained from the observed color <V-I> of ~ 1.3 using the low metallicity Bruzual & Charlot SPS model using a modified Salpeter IMF [1]). The total dynamical mass of KK98 250, estimated from the last measured point of the rotation curve is $22.6 \times 10^8 M_\odot$ – at this radius more than 92% of the mass of KK98 250 is dark.

For mass models with an NFW halo, keeping Υ_V as a free parameter in the fit gave unphysical results. Even after setting $\Upsilon_V = 0$, no reasonable fit could be obtained. As an illustration, Fig. 3.13[A] shows an NFW fit to the data, keeping the concentration parameters c fixed to 1, Υ_V=0.0 and v_{200} chosen to minimize χ^2. As can be seen, even at these extreme values for the parameters, the quality of fit is poor.

We also fit mass models to a hybrid rotation curve (see Fig. 3.13[B]), consisting of Hα data [9] in the inner regions of the galaxy and the "asymmetric drift" corrected HI rotation curve in the outer regions. Again, keeping Υ_V as a free parameter in the fit gave unphysical

Table 3.5: Mass decomposition using isothermal halo

	KK98 250				KK98 251			
HI Curve	Υ_V	r_c	ρ_0	χ^2	Υ_I	r_c	ρ_0	χ^2
		kpc	$10^{-3}M_\odot pc^{-3}$			kpc	$10^{-3}M_\odot pc^{-3}$	
Best fit	0.20±0.05	1.5 ± 0.2	37.6 ± 1.2	0.1	–	–	–	
Maximum disk	3.0	4.1 ± 1.0	10.0 ± 1.1	0.5	1.0	10.5 ± 14.5	13.4 ± 1.6	1.3
From <V-I>	0.7	1.6 ± 0.1	30.4 ± 1.0	0.1	0.5	4.2 ± 1.6	15.7 ± 1.3	0.7
Minimum disk	0.0	1.4 ± 0.04	39.0 ± 1.0	0.1	0.0	2.8 ± 0.5	18.5 ± 1.0	0.4
Hybrid (HI+Hα)	0.2	0.9 ± 0.1	65.4 ± 5.6	0.1	–	–	–	
Hα Curve*	0.0	0.63 ± 0.08	117.8 ± 16.5		–	–	–	

*From de Blok et al.(2001)

results, hence it was fixed to the value of 0.2, obtained from the best fit isothermal halo model, derived using the HI rotation curve alone. In any case, fixing Υ_V to a common value allows a meaningful comparison of the halo parameters derived using both the rotation curves. The isothermal halo parameters derived from the hybrid rotation curve are also given in Table 3.5. The table also shows the isothermal halo parameters derived by de Blok et al.(2001) using only the Hα rotation curve. We note that apart from the (probably not physically meaningful) maximum disk case, the halo parameters derived from the HI rotation curve are in good agreement with one another, but that they are substantially different from the parameters derived from the Hybrid or Hα rotation curves. In this context it is worth repeating, that the discrepancy between the Hα rotation curve and the HI rotation curve is largest at intermediate radii, and not at small radii as one would have expected, if the HI rotation curve suffered from beam smearing.

Also shown in Fig. 3.13[B] is the $\Upsilon_V = 0$, NFW halo fit to the Hybrid rotation curve. As can be seen, this fit overestimates the observed rotation velocity in the inner regions of the galaxy; fixing Υ_V to more reasonable values worsens this discrepancy. The NFW halo parameters (corresponding to $\Upsilon_V = 0$) are c=6.5±1.4 and $v_{200} = 66.0 \pm 13.0$. The value of 6.5 for the concentration parameter is much lower than the range of NFW concentration parameters predicted by LCDM simulations [6]. It is worth mentioning here that even for the Hα rotation curve alone, isothermal halos provide a substantially better fit than an NFW halo [9].

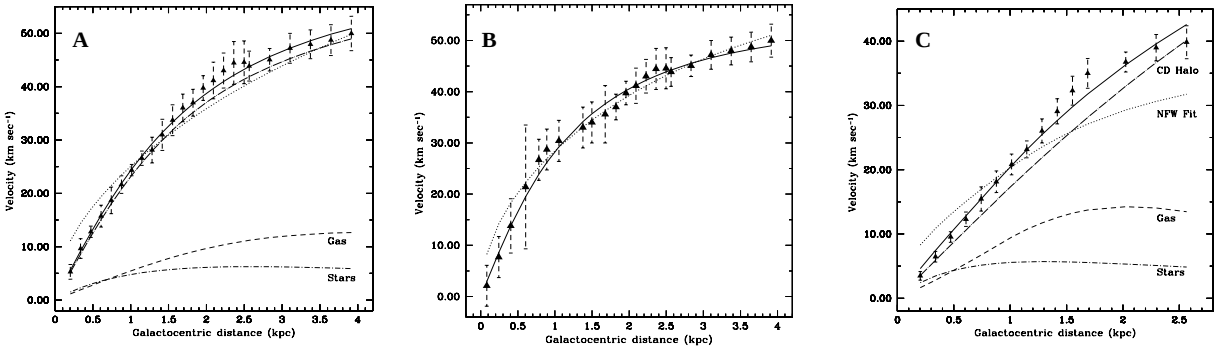

Figure 3.13: [**A**] Mass models for KK98 250 using the corrected rotation curve. The points are the observed data. The total mass of gaseous disk (dashed line) is $3.6 \times 10^6 M_\odot$.The stellar disk (short dash dot line) has $\Upsilon_V = 0.2$, giving a stellar mass of $3.4 \times 10^7 M_\odot$. The best fit total rotation curve for the constant density halo model is shown as a solid line, while the contribution of the halo itself is shown as a long dash dot line (the halo density is $\rho_0 = 37.6 \pm 1.2 \times 10^{-3}$ $M_\odot$ pc^{-3} and core radius $r_c = 1.5 \pm 0.2$). The best fit total rotation curve for an NFW type halo, using $\Upsilon_V = 0.0$, c=1.0 and v_{200}=331.0 km $s^{-1}$is shown as a dotted line. [**B**]The best fit mass model for an isothermal halo (solid line) to the hybrid rotation curve of KK98 250 consisting of the Hα rotation velocities in the center and the "asymmetric drift" corrected HI data in the outer regions of the galaxy. Also shown in the figure is the minimum disk fit mass model for an NFW type halo (dotted line). [**C**]Mass models for KK98 251 using the corrected rotation curve. The total mass of gaseous disk is $9.75 \times 10^7 M_\odot$. The stellar disk has $\Upsilon_I = 0.5$, giving a stellar mass of $1.2 \times 10^7 M_\odot$. The best fit constant density halo model is $\rho_0 = 15.7 \pm 1.3 \times 10^{-3}$ $M_\odot$ pc^{-3} and core radius $r_c = 4.2 \pm 1.6$ (solid line). Also shown is the best fit total rotation curve for an NFW type halo, using $\Upsilon_I = 0.0$, c=1.0 and v_{200}=180.0 km s^{-1}as a dotted line. See the text for more details.

3.2.6.4 KK98 251

As discussed in section 2.5, for the mass modelling of KK98 251, we have used the I band scale length derived by Karachentsev et al. (2000). For an isothermal halo model, keeping Υ_I as a free parameter in the fit gave negative values for Υ_I. Further, if one keeps Υ_I fixed, the χ^2 continuously decreases as Υ_I is decreased. Fig. 3.13[C] shows the best fit mass model for KK98 251 for a constant density halo using $\Upsilon_I = 0.5$ (which corresponds to the observed <V-I> color, from the low metallicity Bruzual & Charlot SPS model using a modified Salpeter IMF). The derived halo parameters using various values of Υ_I are given in Table 3.5. As can be seen from Table 3.5, the halo parameters are relatively insensitive to the assumed value of Υ_I. The total dynamical mass (at the last measured point of the rotation curve) is M_T=$9.5 \times 10^8 M_\odot$.

The "asymmetric drift" corrected rotation curve for KK98 251 was also fitted using an

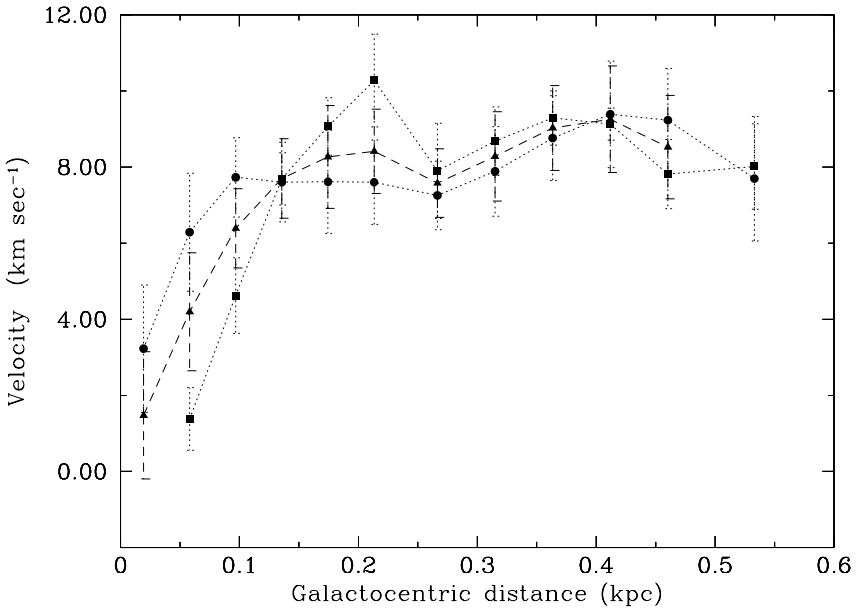

Figure 3.14: Rotation curve of DDO 210. Filled triangles show the rotation velocities derived from the whole galaxy while circles and squares represent the rotation velocities derived from the receding and the approaching side respectively.

NFW halo model. We found that even for $\Upsilon_I = 0$, with no value of c and v_{200} could a good fit using an NFW halo be obtained. The best fit NFW model is shown in Fig. 3.13[C]; as can be seen, the data deviate substantially from the model.

3.3 Discussion

3.3.1 Kinematical peculiarities in DDO 210

As discussed in Sect. 3.2.4, DDO 210 is kinematically peculiar; it has a lopsided velocity field and also shows a twisting of the kinematic major axis. These peculiarities may be related to the lopsidedness seen in the optical disk; the bulk of the optical emission (i.e. the "bright component" discussed in Sect. 3.2.3) lies in the eastern half of the HI disk. A similar pattern of kinematical lopsidedness and lopsidedness in the optical disk is also seen in other galaxies (e.g. M101 [3]). To quantify the kinematical lopsidedness in the galaxy, rotation curves were derived at various spatial resolutions separately for the approaching and receding halves of the galaxy. Fig. 3.14 shows the hybrid rotation curves for the approaching and receding sides as well as for the galaxy as a whole. The rotation curves obtained from the two lowest

resolution velocity fields ($44'' \times 37''$ and $29'' \times 23''$) matched within the errorbars with the one derived from the whole galaxy. On the other hand, for the higher resolution data, the rotation curves were found to be different (at ~ 2.0 km s^{-1}level) from the rotation curve derived from the whole galaxy. While part of this difference may be due to the kinematical lopsidedness, it is also possible that part of it arises as a result of the difference in the sampling of the velocity field between the two sides of the galaxy. Because of the distorted morphology of the HI distribution, the distribution of data points available to estimate rotation velocity are different for the approaching and receding halves. This effect gets more important at the higher spatial resolutions and could also contribute to the observed differences in the rotation curves. Further, as can be seen in Fig. 3.14, the difference between the rotation curve derived using the whole galaxy and the rotation curves derived separately for the two halves are small compared to both the error bars on the average curve as well as the magnitude of the asymmetric drift correction. Ignoring the kinematical lopsidedness for the mass modeling is hence probably reasonable.

The derived rotation curve of DDO 210 (Fig. 3.2[C]), can also be used to put limits on the dynamical ages of the density enhancements in the HI distribution. The derived rotation curve for the galaxy is flat from a galactocentric radii of 0.2 kpc to 0.5 kpc. The timescales required for one rotation in the inner regions of the galaxy is ~ 160 Myr, while the rotation period at the edge of the galaxy is ~ 400 Myr. Hence, this differential rotation will wind up these density enhancements on a time scale of a few 100 Myrs. These density enhancements are hence likely to be recently developed perturbations in the HI disk. The origin of these perturbations is unknown, and it also surprising that despite their presence and relative dynamical youth there is not much evidence for star formation in the galaxy.

3.3.2 The Tully-Fisher relation

In this section we study the Tully-Fisher relation for faint dwarf galaxies, using the galaxies from our sample, whose HI observations are presented in this chapter viz. KK 44, DDO 210, KK98 250, KK98 251. For this study, we have also included one of our sample galaxy viz. NGC 3741. The HI results for this galaxy are described in Chapter. 6.

It has been recently suggested that dwarf galaxies deviate systematically from the Tully-Fisher (TF) relation defined by bright galaxies (i.e. [34, 48, 49]), with small galaxies being underluminous compared to what would be expected had they followed the same TF relation as $\sim L_*$ galaxies. Swaters(1999) noted this effect for the R band TF relationship and suggested that the problem could be ameliorated by applying a "baryonic correction" i.e. a correction for the fact that dwarf galaxies have still to convert much of their gas into stars.

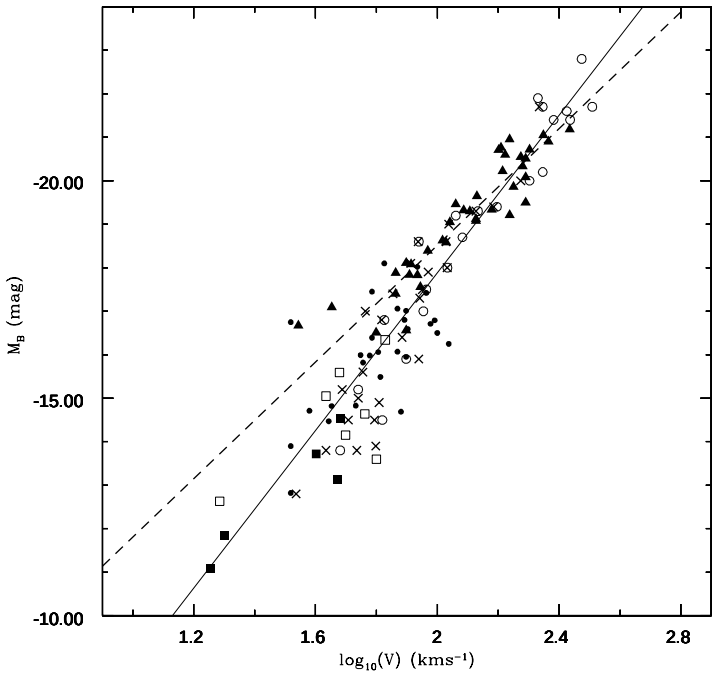

Figure 3.15: Absolute B magnitude vs the log of the maximum rotation velocity. Empty circles are galaxies from Broeils (1992), empty squares galaxies from Côté et al. (2000), filled triangles from Verheijen (1997,2001), crosses from Stil (1999) and filled circles from Swaters (1999). Galaxies from our sample are shown by a filled squares. The dashed line is the best fit to the galaxies from the Verheijen (1997,2001) sample alone, while the solid line is the best fit to the entire sample.

Pierini (1999) found that the adopted correction for internal extinction makes a substantial difference to the slope of the B band TF relationship, and that depending on the internal extinction correction applied, one could reduce (but not completely eliminate) the need for a baryonic correction. Finally, Mcgaugh et al.(2000) state that due to the problem of internal extinction, the blue band TF relation actually gives no clear evidence for the need for a baryonic correction, but that the need for such a correction is clear when one uses near infrared absolute magnitudes (i.e. bands which are little affected by internal extinction).

We note that while the TF relation is generally studied using the inclination corrected 50% profile width (usually obtained from single dish observations), it is not the best measure to use for the faintest dwarf galaxies, where, (i) the disk inclination may be difficult to determine from the patchy optical emission and (ii) the 50% HI velocity width may not be a good

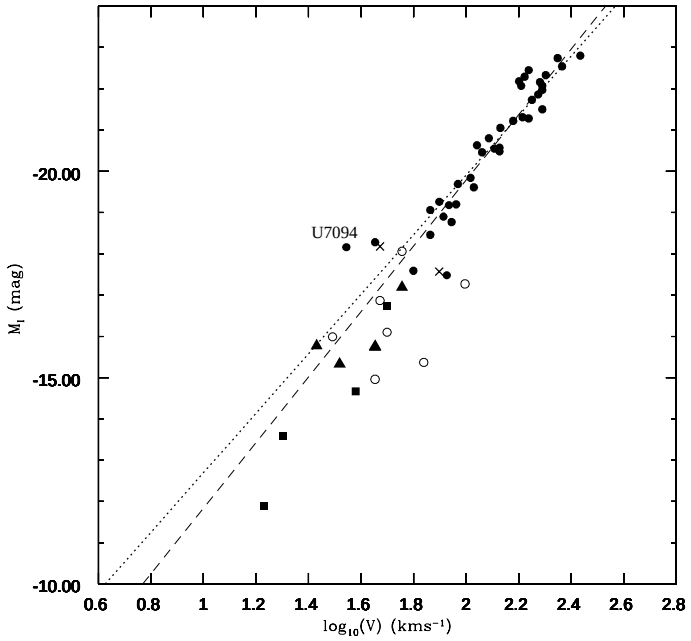

Figure 3.16: I magnitude Tully-Fisher diagram. The filled circles are from Verheijen(2001), empty circles from Swaters(1999) with I band magnitude from Patterson & Thuan (1996), filled triangles from Swaters(1999) with I band magnitude from Makarova & Karachentsev (1998) and crosses from de Blok et al.(1996) with I band from Patterson & Thuan (1996). Filled squares are from galaxies in our sample including KK98 250, KK98 251, KK 44 and DDO 210. The dotted line is the best fit to Verheijen(1997,2001) sample, while the dashed line is the best fit to the Verheijen(1997,2001) sample excluding the galaxy U7094.

indicator of the rotation velocity in faint dwarf galaxies, where random motions are comparable to the peak rotational velocities (as seen in the case of DDO 210 and KK 44 in section Sect. 3.2.5). HI synthesis observations provide a way around both these problems. For such faint galaxies, it is important to accurately correct for the pressure support ("asymmetric drift" correction), which is possible only if one has high resolution HI images. Interestingly enough, even without this correction, (or even a correction for inclination), the HI velocity widths of dwarf galaxies with well measured distances do correlate with the absolute blue luminosity, albeit with large scatter [16]. It is currently a matter of speculation as to whether the scatter would reduce significantly, once one puts in the corrections discussed above.

In Fig. 3.15 the maximum "asymmetric drift" corrected rotation velocities (V_{max}) for our sample galaxies viz. NGC 3741, KK98 250, KK98 251, DDO 210 and KK 44 (after correction for "asymmetric drift") are plotted against their absolute blue magnitudes. The same quantities for several other spiral and dwarf galaxies, spanning a range in absolute

B magnitudes from $M_B \sim -23$ to $M_B \sim -11$, with measured HI rotation curves are also shown. The samples from which these galaxies have been drawn are listed in the figure caption. In case of Verheijen sample, the rotation velocities of the galaxies are obtained from Verheijen (1997), whereas the revised absolute magnitudes of these galaxies are obtained from Verheijen (2001). The absolute magnitude of the galaxies in Côté et al.(2000) sample have been corrected using the recent, more accurate distance estimates of those galaxies [21]. As can be seen in the Fig. 3.15, a clear trend is seen between the maximum velocity and absolute magnitude (which is of course the basis of TF relationship). We also show in the figure the best fit line (the solid line) between M_B and V_{max} over this entire magnitude range and the best fit line (dashed line) using only the brighter galaxies ($M_B < -17.0$). The scatter about the best fit line is ~ 1 magnitude, a large part of this is probably due to (i) uncertainties in the distances to the galaxies, and (ii) the different prescriptions for correcting for internal extinction that have been applied to the different samples. As expected from the discussion above, one can see that galaxies with large velocity widths lie systematically above this best fit slope, while galaxies with low velocity widths lie systematically below this slope (with the break occurring at ~ 100 km sec^{-1} – this corresponds well to the break velocity seen in the near infrared Tully-Fisher diagram, [34]).

Further, we note that Fig. 3.15 does not show any particular flattening of the slope around $M_B \sim -14.0$ (as found by Côté et al.(2000)). Part of the reason for this difference is probably that Côté et al.(2000) used rotation velocities from the Lo et al.(1993) sample, while we have not. The observations of Lo et al.(1993) used a velocity resolution of ~ 6.5 km sec^{-1}, and also often lacked sensitivity to the low extended HI distribution, for both of these reasons the V_{max} of the galaxies in this sample could be underestimated (see e.g. [15, 47]).

Finally, as seen in Fig. 3.15, the scatter in B band Tully-Fisher relation could be large primarily because of uncertain and absolute magnitude dependent internal extinction corrections, hence we also plot I band Tully-Fisher relation. Unfortunately, there are only few dwarf galaxies with both I band photometry and HI synthesis imaging available. We show in Fig. 3.16, the TF relation for a sample of galaxies with both HI synthesis imaging and I band photometry. For the bright galaxies, the photometry and rotation velocities are from Verheijen(1997, 2001), while for the fainter galaxies, the I band magnitudes are from Patterson & Thuan (1996) and Makarova & Karachentsev (1998), while the rotation velocities were taken from Swaters (1999) and de Blok et al. (1996). Galaxies from our sample are also shown in the figure as filled squares. For KK 44, the I magnitude is calculated using the relation $(B-V)_T = 0.85(V-I)_T - 0.2$ (Makarova & Karachentsev 1998). As can be seen from Fig. 3.16, faint dwarf galaxies do tend to lie systematically below the TF relation defined by

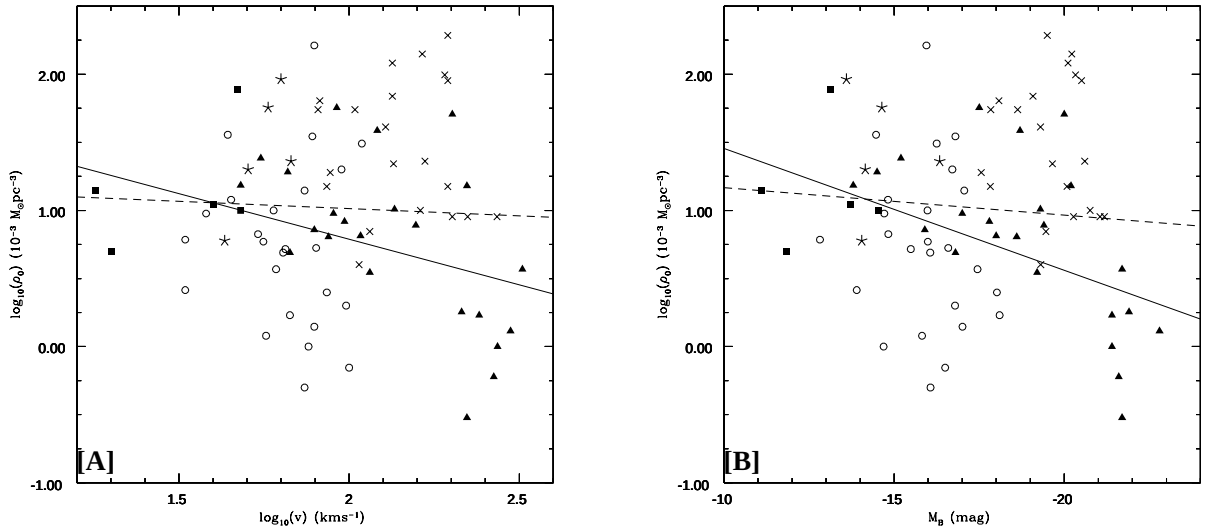

Figure 3.17: Scatter plots of the central halo density against the circular velocity (panels [A]) and the absolute blue magnitude ([B]). The data are from Verheijen (1997, 2001) (crosses), Broeils (solid triangles), Côté et al. (stars) and Swaters (empty circles).The galaxies in our sample viz. KK 44, DDO 210, KK98 250, KK98 251 and NGC 3741 are shown as solid squares. The dash line represent the best fit line to the whole data set whereas the solid line represent the best fit to the sample excluding Verheijen (1997, 2001) sample.

bright galaxies (dotted line). This trend persists even if one excludes the most discrepant bright galaxy (U7094, which has a poor quality rotation curve) in determining the bright galaxy TF relation (dashed curve). Note also that the scatter in the TF relation increases at the faint end – this may be in part due to the uncertainty in the distances to the galaxies.

3.3.3 Central halo densities

In Sec. 3.1 we had discussed that based on galaxy formation simulations, several authors have suggested that smaller galaxies should in general have a higher central halo density than bigger galaxies. We plot the halo density of galaxies (drawn from the same samples as for Fig. 3.15 excluding that of Stil (1999) for which mass decompositions are not available) as a function of their circular velocity in Fig. 3.17[A] and as a function of the absolute blue magnitude in Fig. 3.17[B]. The dashed line in the two figures represent the best fit line to the data. As can be seen, we find no clear correlation between halo density and blue magnitude or circular velocity. However when the Ursa Major sample of Verheijen(1997,2001) is excluded,

a trend of an increase in the halo density with the decrease in the absolute magnitude and the rotation velocity is seen from the best fit line to the data (shown as a solid line in Fig. 3.17[A]&[B]). If these sample differences reflect genuine effects in the galaxy halo properties, then it is perhaps related to the higher mean galaxy density of the Ursa Major sample. The solid lines shown in Fig. 3.17[A]&[B] are $\rho_0 \propto {V_{max}}^{-0.67}$ and $\rho_0 \propto {L_B}^{-0.22}$ respectively. We also note that the halo densities being plotted have been computed for "maximum disk" modified isothermal halo fits, and that the correlation we find is related to (but not identical to) the statement often made in the literature that the in centers of large galaxies the baryonic mass is more dominant than in the centers of dwarf galaxies.

3.4 Conclusions

We have presented the high velocity resolution and high sensitivity GMRT observations of KK 44, DDO 210, KK98 250 and KK98 251. From our observations we find that, inspite of being faint, all these galaxies have large scale velocity gradients, consistent with systematic rotation. This is in contrast to the earlier coarser velocity resolution (~ 6.5 km s^{-1}) observations, from which it appeared that faint dwarfs have chaotic velocity fields. In the case of KK 44 and DDO 210, we find that the velocity fields are consistent with rotation, though the peak rotational velocities are comparable to the velocity dispersion. The observed rotational velocities hence require a substantial correction (akin to the "asymmetric drift" correction), before they can be used to model the density distribution in these galaxies. From our modeling of the corrected rotation curves, we find that, in general, the kinematics of all these galaxies are well fitted by the traditionally used "modified isothermal halo" model, whereas theoretically favored cuspy NFW halos do not provide a good fit to the data.

We compile from the literature a sample of galaxies (ranging from normal spirals to faint dwarfs) with rotation curves obtained from HI synthesis observations. The complete sample covers a luminosity range of ~ 12 magnitudes. From this sample we find at best a weak trend for increasing halo central density with decreasing galaxy size. Such a trend is expected in hierarchical models of halo formation. Finally, from our examination of the TF relation using the compiled sample, we find, in broad agreement with earlier studies, (which used single dish HI data), that dwarf galaxies tend to lie below the TF relation defined by brighter galaxies.

Bibliography

[1] Bell E. F., & de Jong, R. S., 2001, ApJ 550, 212.

[2] Begeman, K. G. 1989, A&A, 223, 47

[3] Bosma, A., Goss, M. & Allen, R. J., 1981, A&A, 93, 106.

[4] Bottema, R, Shostak, G. S., & van der Kruit, P. C., 1986, A&A 167, 34.

[5] Broeils,A. 1992, Ph.D. thesis. Rijksuniversiteit Groningen.

[6] Bullock, J. S. et al., 2001, MNRAS, 321, 559

[7] Casertano S., 1983, MNRAS 203, 735-747.

[8] Côté, S., Carignan, C. & Freeman, K. C. 2000, Ap.J, 120, 3027

[9] de Blok, W. J. G., McGaugh, S. S., & Rubin, V. C. 2001, AJ, 122, 2396.

[10] de Blok, W. J. G., McGaugh, S. S., & vander Hulst, J. M. 1996, MNRAS, 283, 15.

[11] de Grijs, R & Peletier, R. F.,1997, A&A, 320, L21

[12] Fisher, J. R. & Tully, R. B., 1975, A&A, 44, 151

[13] Fisher, J. R. & Tully, R. B., 1979, AJ, 84, 62

[14] Greggio, L., Marconi, G., Tosi, M. & Focardi, P., 1993, AJ, 105, 894

[15] Hoffman, G. Lyle, Salpeter, E. E., Farhat, B., Roos, T., Williams, H., & Helou, G., 1996, ApJS, 105, 269

[16] Huchtmeier, W. K., Karachentsev, I. D., & Karachentseva, V. E. 2003, A&A, 401, 483

[17] Huchtmeier, W. K., Karachentsev, I. D., Karachentseva, V. E., & Ehle, M. 2000, A&AS, 141,469

[18] Huchtmeier, W. K., Karachentsev, I. D., & Karachentseva, V. E. 1997, A&A, 322, 375

[19] Huchtmeier, W. K. & Richter O. G., 1986, A&AS, 63, 323

[20] Israel, F. P., Tacconi, L. J., & Bass, F. 1995, A&A, 295, 599.

[21] Karachentsev, I. D., Karachentseva, V.E., Huchtmeier, W.K. & Makarov, D.I., 2004, AJ, 127, 2031

[22] Karachentsev, I. D., Sharina, M. E., Dolphin, A. E. & Grebel, E. K., 2003, A&A, 408, 111

[23] Karachentsev, I. D. et al., 2002, A&A, 389, 812.

[24] Karachentsev, I. D., Sharina, M. E., & Huchtmeier, W. K. 2000, A&A, 362, 544

[25] Karachentseva, V. E., & Karachentsev, I. D. 1998, A&AS, 127, 409

[26] Kent, S. M., 1987, AJ, 93, 816

[27] Klypin, A. A., Kravtsov, A. V., Bullock, J. S. & Primack, J. R., 2001, ApJ 554, 903

[28] Kravtsov, A. V., Klypin, A. A., Bullock, J.S. & Primack, J.R., 1998, ApJ, 502, 48

[29] Lee, M. G., Aparicio, A., Tikonov, N., Byun, Y. & Kim, E., 1999, AJ, 118, 853.

[30] Lo, K. Y., Sargent, W. L. W. & Young, K., 1993, Ap.J., 106, 507

[31] Makarova, L. N., & Karachentsev, I. D., 1998, A&AS, 133, 181

[32] Marchesini, D., D'Onghia, E., Chincarini, G., Firmani, C., Conconi, P., Molinari, E. & Zacchei, A., 2002, ApJ, 575, 801.

[33] Mateo, M., 1998, ARAA, 36,506

[34] McGaugh, S. S., Schombert, J. M., Bothun, G. D., & de Blok, W. J. G. 2000, ApJL, 533, 99

[35] Meurer, G. R., Carignan, C., Beaulieu, S. F., & Freeman, C. F., 1996, ApJ 111, 1551

[36] Moore, B., Quinn, T., Governato, F., Stadel, J. & Lake, G., 1999, MNRAS, 310, 1147

[37] Milgrom, M., 1983, ApJ, 260, 365

[38] Milgrom, M., 1988, ApJ, 333, 689

[39] Navarro, J. F., Frenk, C. S. & White S. D. M., 1996, ApJ 462, 563

[40] Navarro, J. F., Frenk, C. S. & White S. D. M.,1997, ApJ 490, 493

[41] Navarro, J. F., 1998, ASP Conf. Series, 136, 409

[42] Pierini, D., 1999, A&A 352, 49

[43] Patterson, R. J., & Thuan, T. X. 1996, ApJS, 107, 103.

[44] Pisano, D. J., & Wilcots, E. M. 2000, MNRAS, 319, 821

[45] Sancisi, R., & Allen, R. J. 1979, A&A, 74, 73

[46] Sharina, M. E., Karachentsev, I. D. & Tikhonov, N. A. 1997, AstL, 23, 373.

[47] Skillman, E. D., Neutral Hydrogen in Dwarf Galaxies, 1996, PASP Conf. Ser., 106, 208

[48] Stil J.N. 1999, Ph.D. thesis, Rijksuniversiteit Leiden.

[49] Swaters, R. 1999, Ph.D. thesis, Rijksuniversiteit Groningen.

[50] Swaters R. A., Schoenmakers R. H. M., Sancisi R., van Albada T. S., 1999, MNRAS, 304, 330

[51] Taylor, C. L., Kobulnicky, H. A. & Skillman, E. D, 1998, AJ, 116, 2746

[52] Tolstoy, E., Gallagher, J., Greggio, L., Tosi, M., De Marchi, G., Romaniello, D., Minniti, D. & Zijlstra, A. 2000, ESO Messenger, 99, 16.

[53] van Zee, L., Haynes, M. P. & Salzer, J.J., 1997, AJ, 114, 2479

[54] van Zee, Liese. 2000, AJ, 119, 2757.

[55] van den Bergh S. 1959, Pub. David Dunlap Obs., 2, 147.

[56] Verheijen, M.A.W. 2001, ApJ, 563, 694

[57] van den Bosch, F. C. & Swaters, R. A., 2001, MNRAS 325, 1017-1038.

[58] van der Kruit, P.C., Searle, L., 1981, A&A 95, 105.

[59] Warmels, R. H. 1988, A&AS, 72, 427

[60] Weldrake, D. T. F., de Blok, W. J. G., & Walter, F., 2003, MNRAS, 340, 12.

[61] Young, L. M., van Zee, L., Lo, K. Y., Dohm-Palmer, R. C. & Beierle, M. E., 2003, ApJ, 592, 111

Chapter 4

Kinematics of the dwarf irregular galaxy GR8

4.1 Introduction

Although bright irregular galaxies have rotating gas disks, it is unclear whether the faintest dwarf irregular galaxies are rotationally supported or not. Côté et al. (2000), based on a study of the kinematics of eight dwarf irregular galaxies (with magnitudes varying from $M_B \sim -16.7$ to $M_B \sim -11.3$) suggest that normal rotation is seen only in dwarfs brighter than $M_B \sim -14.0$. This is consistent with the earlier findings of Lo et al.(1993), who, based on an interferometric study of faint dwarf galaxies (with $M_B \sim -9$ to $M_B \sim -15$) found that only two of their sample of nine galaxies showed ordered velocity fields. However, this conclusion has been questioned by Skillman [27] who pointed out that the interferometric observations of Lo et al.(1993) lacked sensitivity to low extended HI distribution and could thus have been insensitive to the large scale velocity field. Further, as seen in Chapter 3 of this thesis, the dwarf irregular galaxies KK 44 ($M_B \sim -11.9$) and DDO 210 ($M_B \sim -11.0$), despite being extremely faint, have regular velocity fields, consistent with that expected from a rotating disk. So some faint galaxies at least have rotating HI disks. What about the rest? If gas in faint dwarf galaxies is not supported by rotation, what provides the energy that keeps it from collapse? For very faint dwarf irregular galaxies, the binding energy of the gas is not much larger than the energy output of a few supernovae. Star formation in such galaxies could hence have a profound effect on the kinematics of the ISM. Indeed, the faintest dwarf galaxies are expected to lose a substantial part of their gas due to the energy deposited in the ISM by supernovae from the first burst of star formation (e.g. [5]). Some observational support for such models is provided by the large expanding HI supershells seen in the ISM of some dwarf irregular galaxies with active star formation (e.g. [16]). In this chapter we

discuss the issue of the kinematics of faint dwarf galaxies, and its possible connections with energy input from stellar processes, in the specific context of the faint ($M_B \sim -12.1$) dwarf irregular galaxy GR8.

GR8 was first discovered by Reaves(1956) in the course of a survey for dwarf galaxies in the direction of the Virgo Cluster. It has also been cataloged as DDO 155 by van den Bergh(1959). The original distance estimates for GR8 were in the range 1.0 - 1.4 Mpc [6, 11, 13], which would make GR8 a probable member of the local group. However, recent estimates give somewhat larger distances. Tolstoy et al.(1995) estimated a distance of 2.2 Mpc (based on observations of the only detected Cepheid variable). This estimate is in excellent agreement with that of Dohm-Palmer(1998), which is based on the brightness of the tip of the red giant branch. From the location for the local group barycenter given by Courteau et al.(1999), one can compute that this distance places GR8 well outside the local group zero velocity surface. Consistent with this, van den Bergh(2000) does not classify GR8 as a member of the local group.

GR8 has a patchy appearance in optical images, with the emission being dominated by bright blue knots. H-α imaging (Hodge 1967) shows that these knots are sites of active star formation. However, in addition to the bright blue knots, GR8 also possesses faint extended emission ([6, 11]), indicative of earlier episodes of star formation. Indeed, CM diagrams (based on HST imaging [7]), show that although the bright star forming knots in GR8 have stars which are younger than ~ 10 Myr, the galaxy also contains stars which are older than a few Gyr. Despite this long history of star formation, the metallicity of the star forming knots in GR8 is extremely low, i.e. $\sim 3\%$ solar [26]. This makes it one of the lowest metallicity galaxies known [17]. In keeping with this low metallicity, despite the fact that the star forming regions are expected to be associated with molecular gas, CO has not been detected in the galaxy [32].

There have been two independent studies of the kinematics of HI in GR8, both using the VLA [2, 18]. However these two studies resulted in very different interpretations of the galaxy's kinematics. Carignan et al.(1990) assumed that the observed velocity field was produced by rotation and used it to derive a rotation curve. On the other hand, Lo et al.(1993) interpreted the velocity field as being due to radial motions (i.e. either expansion or contraction). Both of these studies were based on modest (~ 6 km s^{-1}) velocity resolution observations. Further, both observations used the VLA C array, and hence were not sensitive to emission from the extended low surface brightness portions of the HI disk. There has also been a recent high velocity resolution VLA (Cs array) based study of GR8 by Young et al. 2003. This study was focused on the local connections between the ISM and star formation

and not the large scale kinematics of the gas. Although Young et al.(2003) noted that velocity field in GR8 does show a large scale gradient, they chose to characterize the velocity field as giving the overall impression of resulting from random motions.

We present here deep, high velocity resolution ($\sim$ 1.6 km s^{-1}) GMRT observations of the HI emission from GR8 and use them to study the kinematics of this galaxy.

4.2 Results and Discussion

4.2.1 HI distribution

Observations and data analysis for GR8 are described in Chapter 2. Fig. 4.1 shows the global HI emission profile of GR8, obtained from the $40'' \times 38''$ resolution data cube. A Gaussian fit to the profile gives a central velocity (heliocentric) of 217 ± 2 km s^{-1}. The integrated flux is 9.0 ± 0.9 Jy km s^{-1}. These are in good agreement with the values of 214 ± 1 km s^{-1}and 8.78 Jy km s^{-1}obtained from single dish observations [14]. The good agreement between the GMRT flux and the single dish flux shows that no flux was missed because of the missing short spacings in the interferometric observation. The velocity width at the 50 % level (ΔV_{50}) is 26 ± 1 km s^{-1}, which again is in good agreement with the ΔV_{50} value of 27 km s^{-1}determined from the single dish observations. The HI mass obtained from the integrated profile (taking the distance to the galaxy to be 2.2 Mpc) is $10.3 \pm 1.0 \times 10^6 M_\odot$, and the M_{HI}/L_B ratio is found to be ~ 1.0 in solar units.

Fig. 4.2[A] shows the integrated HI emission from GR8 at $25'' \times 25''$ resolution, overlayed on the digitized sky survey (DSS) image. The HI distribution is clumpy and shows three major clumps. This is highlighted in Fig. 4.2[B], which shows the integrated HI emission at high resolution ($4.0'' \times 3.0''$). The faint extended HI gas seen in the low resolution image is resolved out in this image. One may suspect that the diffuse HI emission (particularly that seen in between the three clumps in the low resolution map) is not real but is the result of beam smearing. To check for this possibility, the individual channel maps in the $25'' \times 25''$ resolution data cube were inspected. In the channel maps, the peak of the diffuse emission in the central region of the galaxy occurs at a different heliocentric velocity than peak velocities of nearby HI clumps, contrary to what one would expect from beam smearing. As a further confirmation of this, the clean components from the $25'' \times 25''$ resolution data cube were convolved with a smaller restoring beam of $10'' \times 10''$ to generate a new data cube. The diffuse emission is visible in the channel maps in this cube, contrary to what would have been expected in case the diffuse emission was entirely due to beam smearing (in which case the clean components would have been restricted to the three clumps).

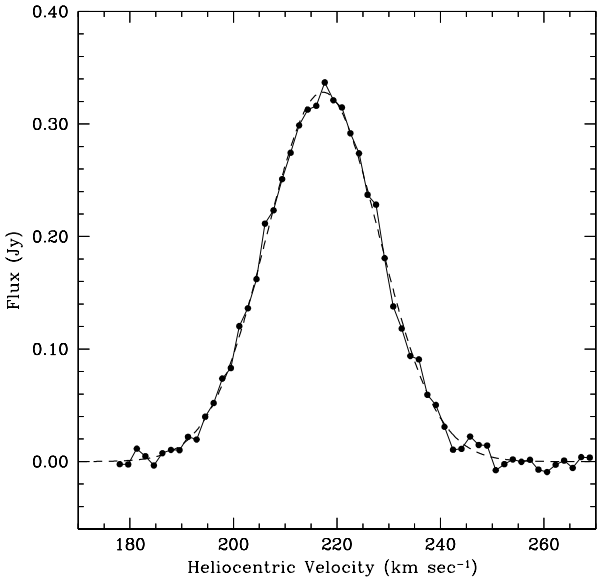

Figure 4.1: The integrated spectrum for GR8 obtained from the $40'' \times 38''$ data cube. The channel separation is 1.65 km s^{-1}. Integration of the profile gives a flux integral of 9.0 Jy km $s^{-1}$and an HI mass of $\sim 10.3 \times 10^6 M_\odot$. The dashed line shows a gaussian fit to the profile.

As can be seen in Fig. 4.2[A], each HI clump is associated with a clump of optical emission. However, for each clump, the peak optical emission is generally offset from the peak of the HI emission. The Hα image of GR 8[12] shows that the optical clumps also emit copious amounts of Hα and are hence regions of on going star formation. In addition to the bright clumps, diffuse optical emission is also seen in Fig. 4.2[A]. The optical emission has a much higher ellipticity than the HI emission and the position angles of the optical and HI major axis can also be seen to be different. Quantitatively, ellipse fitting to the outermost contours of the $40'' \times 38''$ and $25'' \times 25''$ resolution HI moment maps (which are less distorted by the presence of the HI clumps in the inner regions) gives a position angle of 77±5 degrees and an inclination (assuming the intrinsic shape of the HI disk to be circular) of 28±3 degrees. The values obtained from the two different resolution maps agree to within the error bars. On the other hand, these values are considerably different from those obtained from ellipse fitting to the optical isophotes, which yields a position angle of 38 degrees and an inclination of 58 degrees respectively [6]. We return to this issue in Sect. 4.2.3.

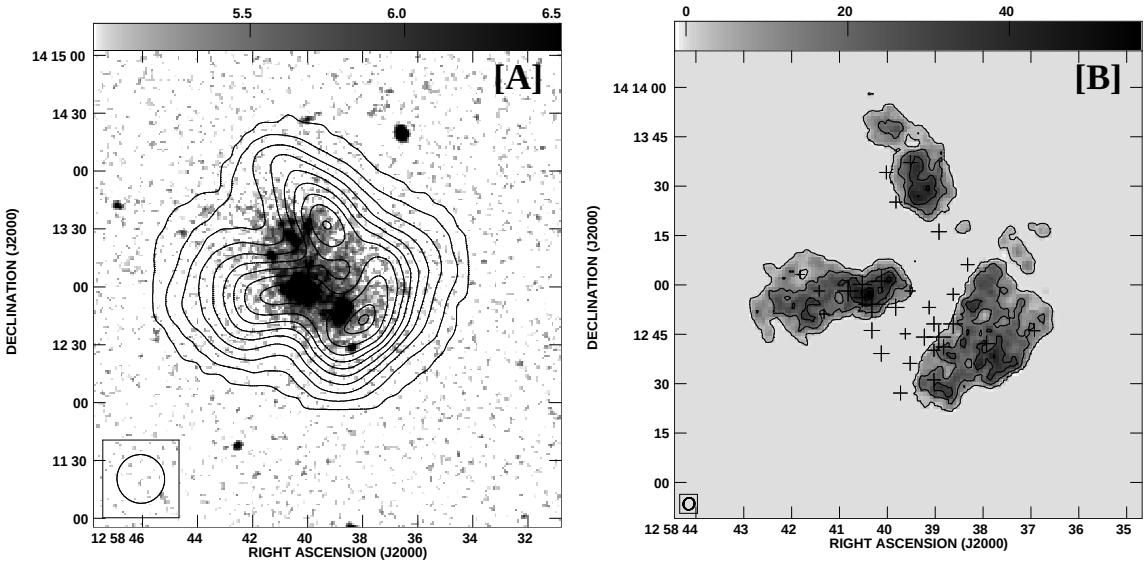

Figure 4.2: [**A**]The digitized Palomar Sky Survey image of GR8 (greyscales) with the GMRT $25'' \times 25''$ resolution integrated HI emission map (contours) overlayed. The contour levels are 0.005, 0.076, 0.146, 0.217, 0.288, 0.359, 0.429, 0.500, 0.571, 0.642 and 0.665 Jy/Bm km s^{-1}. [**B**]Integrated HI emission at $4'' \times 3''$ resolution, (grey scales and contours). The contour levels are 0.002, 0.016, 0.030, 0.044 and 0.058 Jy/Bm km s^{-1}. The locations of the HII regions identified by [12] are indicated by crosses.

4.2.2 HI Kinematics

The velocity field derived from the $25'' \times 25''$ resolution data cube is shown in Fig. 4.3. This velocity field is in reasonable agreement (albeit of better quality) with that obtained by Carignan et al.(1990). The velocity field shows closed contours and is, to zeroth order, consistent with a velocity field that would be produced by a rotating disk with an approximately north south kinematical major axis. This would make the kinematical major axis roughly perpendicular to the major axis obtained from ellipse fitting to the HI disk. The kinematical major axis is also substantially misaligned with the major axis obtained by ellipse fitting to the optical isophotes. In addition to this misalignment, the kinematical center of the velocity field is offset (to the north, as can be seen by comparing Figs. 4.3 and 4.2) from the center (as determined by ellipse fitting) of the HI disk.

Apart from the misalignments mentioned above, the velocity field of GR8 also shows clear departures from what would be expected from an axisymmetric rotating disk. The most important departure is that the isovelocity contours in the outer regions of the galaxy show large scale kinks. In addition, the velocity field shows several asymmetries. The most prominent asymmetry is between the northern and southern half of the galaxy. The closed isovelocity contours in the southern half are more elongated than those in the northern half. Further, the kinks noted above are much more prominent in the western part of the disk than in the eastern half. Since our velocity field is better sampled compared to the velocity fields derived by Lo et al.(1993) and Carignan et al.(1990), these kinematical peculiarities are more clearly seen. In particular, the offset between the morphological and kinematical center, which is apparent in our velocity field is not seen in velocity fields derived earlier. Further, because of the lower sensitivity, the kinks in the isovelocity contours seen towards the edges of the galaxy are not seen that clearly in the earlier velocity fields.

Following Carignan et al.(1990), we could try to fit GR8's velocity field to that expected from a rotating disk. In such a fit one can anticipate (based on the closed isovelocity contours) that the rotation curve would be falling and (based on the kinks in the isovelocity curves on the eastern and western edges of the disk) that either the rotation curve would need to rise again towards the edge of the disk, or the edges of the disk would need to be warped. We discuss rotation and other models for producing the observed velocity field in more detail in the next section.

4.2.3 Discussion

As described in the last two sections, the morphology and kinematics of GR8 are somewhat peculiar. If the HI gas and the stars in GR8 are both in disks, then the stellar disk would

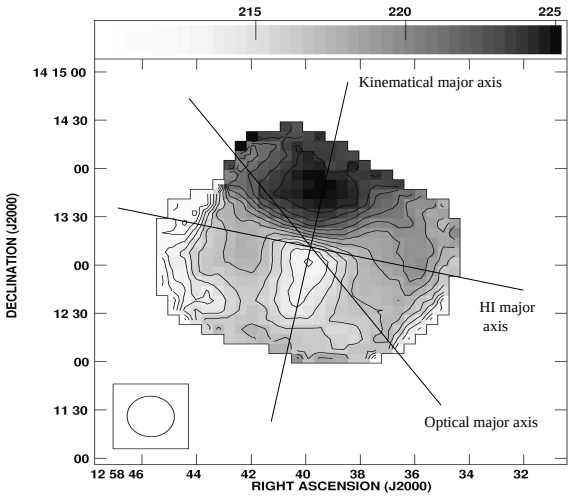

Figure 4.3: The HI velocity field of GR8 at $25'' \times 25''$ arcsec resolution. The contours are in steps of 1 km sec^{-1} and range from 210.0 km sec^{-1} to 225.0 km sec^{-1}.

have to be both more inclined and have a different position angle than the gas disk. It is more likely that the star formation in GR8 has occurred preferentially in a non axisymmetric symmetric region in the center of the galaxy. In the extreme case, the stars would have a more bar like distribution than the gas. A central stellar bar could affect the gas dynamics, however since the stellar mass is probably not dynamically dominant (from the observed B-V color of 0.38 for GR8 [6] and the low metallicity models of Bell & de Jong (2001), the the stellar mass is $\sim 5{\times}10^6$ M$_\odot$, i.e. a factor of 2 less than the HI mass) this effect may not be important.

Apart from having a peculiar morphology, the kinematics of GR8 is also unusual. The kinematical and HI major axis of this galaxy are perpendicular to each other, the kinematical center is offset from the morphological center and the observed velocity field is systematically asymmetric. GR8 is not the only dwarf galaxy which shows misalignment between kinematical and morphological axes, such misalignments have also been seen in, for e.g. Sextans A [25], NGC 625 [3] and DDO 26 [15]. However, the misalignment and off-centered kinematics does imply that GR8 cannot be modeled as a pure axisymmetric rotating disk (for which all axis and centers would be aligned). Although, Carignan et al. (1990) had noted some of these problems, they had nonetheless, modeled the kinematics of GR8 as an axisymmetric rotating disk. Their derived rotation curve had a maximum amplitude of ~ 8 km s^{-1}, and

fell sharply with increasing galacto-centric distance.

Our attempts to derive a rotation curve from our velocity field were not successful. The errors in the estimated parameters were large, as were the residuals between the model and the observed velocity field. Our failure to find a good fit (as opposed to Carignan et al.(1990), who were able to fit a rotation curve) is probably related to our better sampling of the velocity field, which, as noted above, makes the misalignments and asymmetries in the velocity field more striking. To provide a feel for the velocity field that would be produced by circular rotation, we show in Fig. 4.4[B] the model velocity field that corresponds to the rotation curve of Carignan et al.(1990). The disk has been taken to be intrinsically elliptical (with an axis ratio of 2:1), so that despite having an inclination of 60^o (the inclination angle derived from the velocity field by Carignan et al. (1990)) the projected model HI disk matches the fairly circular appearance of the observed HI disk. Essentially, the foreshortening along the kinematical minor axis is offset by the inherent ellipticity of the disk. As expected, although the model produces closed isovelocity contours along the apparent morphological HI minor axis, the asymmetries seen in the closed contours between northern and southern half of the galaxy, the kinks in the isovelocity contours towards the edges of the disk, as well as the offset between the kinematical and morphological center are not reproduced. As discussed in Sect. 4.2.2, kinks in the outer isovelocity contours can be produced by requiring the rotation curve to rise again, or by requiring the outer parts of the disk to be extremely warped. Quantitatively, to reproduce the observed kinks, the inclination angle is required to change by an amount sufficient to cause the observed velocity at the edges to increase by a factor of ~ 2, compared to the unwarped model. Such extreme warps can, in principle, lead to multiply peaked line profiles. However, because of the low signal to noise ratio towards the edges, we cannot reliably distinguish between single peaked and multiply peaked line profiles in these regions. A more serious concern in modeling the velocity field of GR8 as a rotating disk is the observed misalignment between the kinematical and HI major axes. As noted above, this requires the HI disk to be inherently elongated with an axis ratio of at least 2:1. Such a highly non circular disk would be very unusual. Further, the inner regions of the galaxy (i.e. the distance at which the rotation curve of Carignan et al.(1990) peaks) will complete one rotation in ~ 80 Myr, while the rotation period at the edge of the disk is ~ 1 Gyr. Hence, this differential rotation will wind up any elongation in the disk on a timescale that is short compared to the age of the galaxy.

Alternatively, as first proposed by Lo et al.(1993), the observed velocity field of GR8 could also be the result of radial motions in the gas i.e expansion or contraction. Since the sign of the inclination of the galaxy is unknown, it is not possible to distinguish between

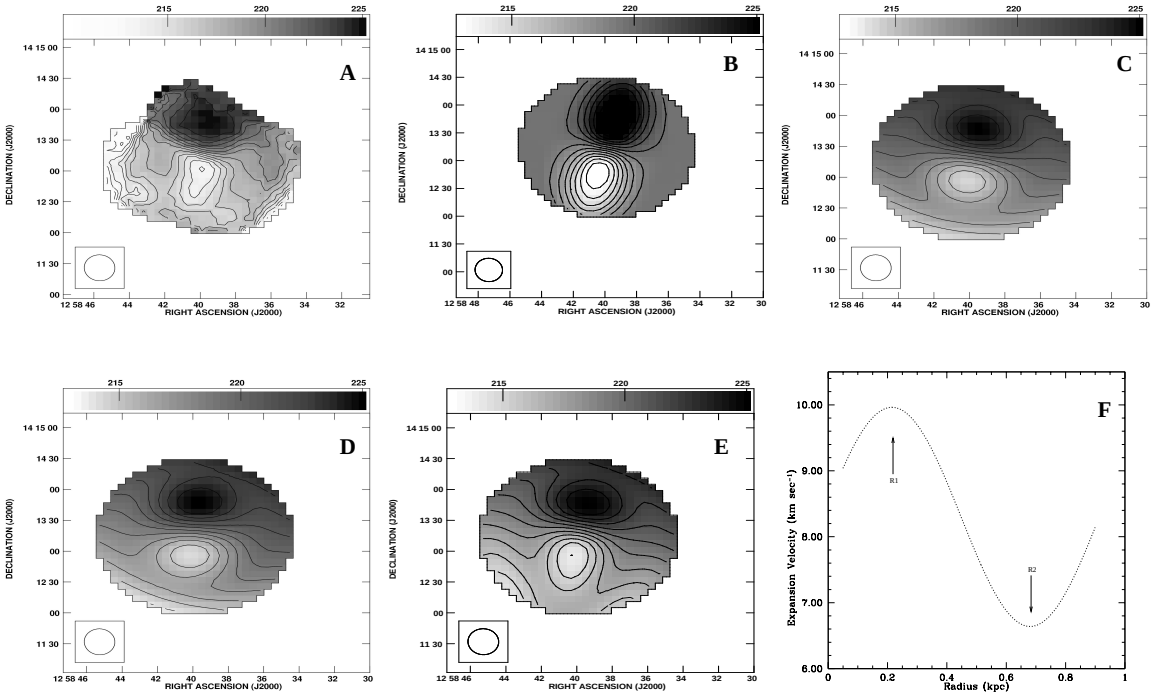

Figure 4.4: [A] The $25'' \times 25''$ resolution moment 1 map. The contour levels go from 210 to 225 km s^{-1}in steps of 1 km s^{-1}. [B] The velocity field obtained using the rotation curve of [2]. Note that we have further assumed that the HI disk is intrinsically elliptical, with an axis ratio of 2:1. See the text for more details. The contours levels in this and succeeding panels are from 213 to 225 km s^{-1}in steps of 1 km s^{-1}. [C] The model velocity field with only expansion motion in the gas. The expansion velocity used to obtain the model is given in panel [F]. See also the discussion in the text. [D] The model velocity field with both expansion and rotation motions in the gas. The expansion is the same as in panel [C]. The assumed rotation curve is linear and rises to a maximum of 6 km s^{-1}at the edge of the galaxy. [E] The model velocity field with rotational and asymmetric expansion motions. The rotational velocity is the same as used in panel [D], however the expansion curve (while similar in form to that in panels [C] and [D] has been scaled (in galacto-centric distance but not amplitude). [F] Expansion curve used to obtain the model velocity field. See the text for more details.

inward and outward radial motions. Large scale bulk radial gas flows, although difficult to understand in the context of normal spiral galaxies, could nonetheless be plausible in small galaxies like GR8. In models of dwarf galaxy formation and evolution, energy injected into the ISM from stellar winds and supernova explosions could drive significant expansive motions in the gas. In fact, in such models, dwarf galaxies below a critical halo circular velocity of $\sim$ 100 km s^{-1}are expected to lose a significant fraction of their ISM from the first burst of star formation (e.g. [5, 8]). Expulsion of the ISM because of the energy input

from supernovae is also postulated as a possible mechanism for producing dwarf elliptical galaxies from gas rich progenitors (e.g. [20]). Observationally, outflows of ionized material have been seen in star bursting dwarf galaxies (e.g. [19]). Of course, these models deal with the expulsion of hot supernovae heated gas, where as, in this instance we are dealing with cold neutral gas. For sufficiently small galaxies however, model calculations suggest that the ISM could be "blown away" i.e. that the ambient medium could be swept out by the hot expanding supernovae superbubbles [10]. This is in contrast to the situation in slightly larger galaxies where there is instead a "blow out" i.e. the supernovae heated hot gas pierces the ambient disk material and escapes into the intergalactic medium. Although a situation where the entire ISM is expanding outwards has not yet been observed, expansion of the neutral ISM on smaller scales has been observed in a number of starbursting dwarf galaxies. Such expanding HI supershells have been seen in, for example, Holmberg II [21], IC 2574 [33] and Holmberg I [16]. One should note however, that while the observational evidence for expanding shells in the ISM of these galaxies is reasonably good, the mechanism by which these shells have been created is less well established. Stewart et al.(2000) find that the giant supershell in IC 2574 is probably driven by energy input from supernovae, while Rhode et al.(1999), despite deep optical imaging, do not find the star clusters that would be expected to be present in this scenario, at the centers of the HI holes in Holmberg II

In light of the above discussion, and the ongoing star formation in GR8, it may be reasonable to assume that there are large scale radial flows in the galaxy. If we make this assumption, then the line of sight velocity $V_{\rm los}$ is related to the circular velocity $V_{\rm rot}$ and the radial velocity $V_{\rm exp}$ by the relation

$$V_{\rm los} = V_{\rm sys} + (V_{\rm rot}\cos(\phi) + V_{\rm exp}\sin(\phi))\sin(i) \tag{4.1}$$

where $V_{\rm sys}$ is the systemic velocity, i is the inclination angle, and ϕ is the azimuthal angle in the plane of the galaxy ($\phi = 0$ along the receding half of the kinematical major axis). The simplest such model is one in which there is no rotation. Fig. 4.4[C] shows such a model for GR8. In this model the inclination angle of the disk is taken to be 20^o and the position angle 350^o. These values were chosen to match the observed velocity field, and are in good agreement with the values expected from the ellipse fitting to the outer HI contours (see Sect. 4.2.1; note that in the case of radial motion, the velocity gradient is maximum along the morphological minor axis and not the morphological major axis). The expansion is taken to be centered on the kinematical center obtained from the velocity field, and not the morphological center. Since radial motions are probably driven by energy from star formation, it is not necessary for the expansion center to be coincident with the geometric

center of the HI disk. The expansion $V_{\rm exp}$ is assumed to be azimuthally symmetric, and its variation with galacto-centric distance is as shown in Fig. 4.4[F]. The rise in the expansion velocity till the radius R1 produces the parallel isovelocity contours in the central regions of the galaxy, the fall after R1 produces the closed contours. The rise in the expansion curve, from radius R2 onwards, produces the kinks seen in the eastern and western edges of the velocity field. This particular form of expansion was chosen because it provides a good match to the observed velocity field. While it is possible that detailed gas dynamic modeling might be able to reproduce this curve, we have not attempted any such modeling in this thesis.

While a pure expansion model does produce the closed contours along the morphological minor axis, it does not produce the asymmetries in the velocity field noted in Sect. 4.2.2. The next most natural model to try is hence one in which there is also some rotation. A velocity field with the same $V_{\rm exp}$ as before, but with non zero $V_{\rm rot}$ is shown in Fig. 4.4[D]. The rotation curve has been assumed to be linear; it rises to a maximum of 6 km s^{-1}at the edge of the galaxy. A linearly rising rotation curve was chosen because this form of rotation curve is typical of dwarf galaxies. Other types of rotation curves, i.e. a constant rotation curve, a Brandt and an exponential curve (which are seldom observed for dwarf galaxies) were also tried. While a constant rotation curve gives a poor fit to the data, Brandt and exponential curves do not provide a better fit to the observed velocity field than that provided by a linear curve. Since these curves introduce many more free parameters in the model without improving the fit quality they were not explored further. The rotation is assumed to be centered on the morphological center of the galaxy. The inclination and position angle are the same as for the previous model. As can be seen, this does reproduce the asymmetry in the kinks in the isovelocity contours between the eastern and western halves of the galaxy. However, it still does not reproduce the asymmetries in the closed contours. A model which does reproduce most of the features of the observed velocity field is shown in Fig. 4.4[E]. This model is similar to that used to produce Fig. 4.4[D], the difference being that the expansion curve is no longer assumed to be azimuthally symmetric. The positions of R1 and R2 in the expansion curve (see Fig. 4.4[F]) were allowed to be different at different azimuthal angles in the southern half of the galaxy. However, the maximum amplitude of the expansion curve was taken to be the same in all azimuthal directions. The effect of this was to reproduce the elongated closed contours in the southern half of the galaxy. This asymmetry between the kinematics in the northern and southern halves may be related to the corresponding asymmetry in the distribution of HII regions (see Fig. 4.2, and also the discussion below). The match can obviously be improved by also allowing an azimuth angle dependent scaling of the amplitude of the expansion curve, but in the absence of a

physically motivated prescription for the scaling factor, this would not add much to our understanding of the galaxy's kinematics. It should be noted that it has not been shown that our chosen model provides a unique (or even "best" in some rigorous statistical sense) fit to the observed kinematics of the galaxy. It is possible that one could find different forms for the expansion and rotation curves which also provide adequate fits to the observed velocity field. Strictly speaking, a more robust method would have been to determine a least squares fit to the observed velocity field, allowing for both expansion and rotation. This approach has however not been attempted in this thesis.

Fig. 4.4[E] shows that the observed velocity field of GR8 can be quite well matched by a combination of rotational and expansion motions. Assuming that this interpretation is correct, the natural question that arises is, what drives the expansion of the gas? Energy input from star formation is the obvious suspect. For an expansion velocity of ~ 10 km s^{-1}and an HI mass of $\sim 10^7 M_\odot$ the corresponding kinetic energy is $\sim 10^{52}$ erg. If we assume that the kinetic energy imparted to the ISM by one supernova explosion is $\sim 10^{51}$ erg (e.g. [23]), this implies that kinetic energy required for the expansion motion is equivalent to the energy output of ~ 10 supernovae. It is plausible that this number of supernovae have occurred in GR8 in the recent past. The lack of detection of radio continuum sources (corresponding to the supernovae remnants) would then place a limit on the magnetic field in the galaxy. On the other hand, no star clusters are located at the center of expansion. However, as can be seen from Fig. 4.2, the majority of the HII regions associated with the three HI clumps lie on the inner edges of the clumps, (i.e. towards the center of the galaxy). In a study of HII regions in dwarf galaxies Elmegreen& Hunter(2000) found that the HII regions tend to have a higher pressure than the average pressure in the disk. They suggest that the HII regions could still be in pressure equilibrium, if they preferentially lie in dense HI clumps, where the ambient pressure is higher than the average over the disk. Of the sample of galaxies studied by Elmegreen & Hunter (2000), GR8 showed the largest pressure anomaly; the pressure in the HII regions was found to be at least a factor of ~ 55 times larger than the average disk pressure. Since these HII regions tend to lie at the inner edges of the HI clumps, this over pressure could possibly drive the clumps outwards. It is interesting to note in this regard, that the star formation history of these clumps indicates that they have been forming stars continuously over at least last 500 Myr, i.e. the clumps themselves are gravitationally bound [7]. The measured expansion velocity (~ 10 km s^{-1}) is also considerably smaller than the escape velocity (which would be ~ 30 km s^{-1}, if we assume that GR8 is dark matter dominated and has a dynamic mass to light ratio ~ 10), which means that the neutral ISM is still bound. This is consistent with the models of dwarf galaxy evolution which include a

clumpy ISM– in such models the cold clumpy material does not escape from the galaxy [1].

So far we have been treating the radial motions as expansion. Since the sign of the radial motion is unconstrained, we should also note that the velocity field could instead arise from infall. In this case, gas is swirling inwards into the galaxy. The model would then be that GR8 is forming from the merger of the three clumps, and that the diffuse gas and stars are material that has be tidally stripped from the clumps and which is now settling down to form a disk. However, in this scenario, it is unclear if one would obtain the observed velocity field, which doesn't show any clear signature of tidal interaction. Another possible infall scenario is that the gas is now falling back towards the center of the potential after a previous expansion phase.

4.3 conclusions

To conclude, we have presented deep, high velocity resolution (~ 1.6 km sec^{-1}) GMRT HI 21cm synthesis images for the faint ($M_B \sim -12.1$) dwarf irregular galaxy GR8. We find that though the HI distribution in the galaxy is very clumpy, there is nonetheless substantial diffuse gas. The velocity field of the galaxy is not chaotic, but shows a systematic large scale pattern. We are unable to fit this pattern with either pure rotation or pure expansion. From an inspection of the velocity field however, the following qualitative remarks can be made. If this pattern is treated as arising because of rotation, then (i) the rotation curve would have to be sharply falling, and the disk would have to be extremely warped at the outer edges and (ii) the disk has to inherently elliptical, with an axis ratio $\tilde{>} 2$. Such a disk would get quickly wound up due to differential rotation. For these reasons we regard it unlikely that GR8's velocity field is due to pure rotation. A more likely model is one in which the kinematics of GR8 can be described as a combination of radial and circular motions. Such a model provides a reasonable fit to the observed velocity field. In this interpretation, in case the radial motions are outwards, then they could be driven by the star formation in GR8; a previous study has shown that the pressure in the HII regions in this galaxy is at least 55 times greater than the average pressure in the disk [9]. The measured expansion velocity is considerably less than the estimated escape velocity, so even in this interpretation the cold gas is still bound to the galaxy. Finally, the radial motions could also be interpreted as infall, in which case GR8 is either in the process of formation, or the ISM is falling back after a previous phase of expansion.

Bibliography

[1] Andersen, R.P. & Burkert, A. 2000, ApJ, 531, 296

[2] Carignan, C., Beaulieu, S. & Freeman, K. C. 1990, Ap.J.,99,178

[3] Côté, S., Carignan, C. & Freeman, K. C. 2000, Ap.J, 120, 3027

[4] Courteau, S. & van den Bergh, S. 1999, AJ, 118, 337

[5] Dekel, A. & Silk, J. 1986, ApJ, 303, 39

[6] De Vaucouleurs, G. & Moss, C, 1983, Ap.J., 271, 123

[7] Dohm-Palmer, R.C., Skillman, E.D., Gallagher, J. et al. 1998, Ap.J., 116,1227

[8] Efstathiou, G. 2000, MNRAS, 317, 697

[9] Elmegreen, B.G. & Hunter, D.A. 2000, ApJ, 540, 814

[10] Ferrara, A. & Tolstoy, E. 2000, MNRAS, 313, 291

[11] Hodge, P.W., 1967, Ap.J., 148,719

[12] Hodge, P., Lee, M.G. & Kennicutt, R. 1989, PASP, 101, 640

[13] Hoessel, J. G. & Danielson, D.E. 1983, ApJ., 271, 65

[14] Huchtmeier, W., Karachentsev, I., Karachentseva, V. & Ehle, M. 2000, A&A., 141, 469

[15] Hunter, D.A. & Wilcot, E.M., 2002, AJ, 123, 2449

[16] Ott J., Walter F., Brinks E. et al. 2001, AJ, 122, 3070

[17] Kunth, D. & Östlin, G. 2000, A&ARv, 10, 1

[18] Lo, K. Y., Sargent, W. L. W. & Young, K. 1993, Ap.J., 106,507

[19] Marlowe, A. T., Heckman, T. M., Wyse, R. F. G. & Schommer, R. 1995, ApJ,438,563

[20] Miralda-Escude, J. & Rees, M. J., 1997, ApJ,478, 57

[21] Puche, D., Westpfahl, D. Brinks, E. & Roy, J. R. 1992, AJ, 103, 1841.

[22] Reaves, G. 1956, AJ, 61, 69

[23] Reynolds, S. 1988, Galactic and Extragalactic Radio Astronomy, 463.

[24] Rhode, K.L., Salzer, J.J., Westpfahl, D.J. & Radice, L.A., 1999, AJ, 118, 323.

[25] Skillman, E. D., Terlevich, R., Teuben, P. J. & H. van Woerden. 1988, A&A, 198, 33.

[26] Skillman, E. D., Melnick, J.,Terlevich, R. & Moles, M. 1988, A&A, 196, 31.

[27] Skillman, E. D., Neutral Hydrogen in Dwarf Galaxies, 1996, PASP Conf. Ser., 106, 208

[28] Stewart, S. G. & Walter, F. 2000, AJ, 120, 1794

[29] Tolstoy, E., Saha, A., Horssel, J.G. & Danielson, E. 1995, AJ, 109, 579

[30] van den Bergh S. 1959, Pub. David Dunlap Obs., 2, 147

[31] van den Bergh S. 2000, PASP, 112, 529

[32] Verter, F. & Hodge, P. 1995, Ap.J., 446, 616

[33] Walter, F. & Brinks, E. 1999, AJ, 118, 273

[34] Young, L. M., van Zee L., Lo, K. Y., Dohm-Palmer, R. C. & Beirele M. E. 2003, ApJ, 592, 111

Chapter 5

Gas distribution, kinematics and star formation in dwarf galaxies

5.1 Introduction

In the currently popular hierarchical models of galaxy formation, star formation starts in small objects; these in turn later merge to form larger galaxies. In such a model, extremely small nearby galaxies are likely candidate "primeval galaxies", in the sense that they may represent the earliest units of star formation in the universe. There is some observational support for these models, even in the very local universe, viz. (i) the Milkyway itself appears to be still growing via the accretion of small companions like the Sagittarius dwarf galaxy (e.g. [37]), and (ii) nearby dwarf galaxies have stellar populations that are at least as old as the oldest stars in the Milkyway (see Grebel (2005) for a recent review).

In detail, however, the star formation history of nearby dwarf galaxies appears to be extremely varied. At the two extreme ends, dwarf spheroidals have little gas or ongoing star formation, while the relatively rare dwarf irregulars are gas rich and also generally have measurable ongoing star formation. Their past star formation histories also appear to have been different −− at a given luminosity dwarf spheroidals are more metal rich than dwarf irregulars, indicative of rapid chemical enrichment in dwarf spheroidals in the past [11]. Why is it that dwarf irregulars, despite having a substantial reservoir of gas have resisted converting it into stars? What keeps the gas in dwarf irregulars from collapse? It is widely believed that the smallest dwarf irregular galaxies have chaotic gas velocity fields (e.g. [35]); in this case the crucial question then becomes, what sustains these chaotic gas motions? In this context, it is interesting to note that the velocity field of some of the faint galaxies viz. DDO 210 and KK 44 (presented in Chapter 3 of this thesis), when observed with sufficient sensitivity and velocity resolution, has invariably turned out to have a measurable

ordered component. Does this generally hold for extreme dwarf irregulars, or do some of them genuinely have no ordered components in their velocity fields? Irrespective of the exact nature of the velocity fields, the question of why dwarf irregulars have been unable to convert their gas into stars remains. In spiral galaxies, the current star formation rate appears to depend on at most two parameters (i) the gas surface density and (ii) some measure of the dynamical time. In practice, models which depend only on the gas surface density, such as the Schmidt star formation law, or those which depend on both these parameters, such as the Toomre's instability criterion [55] appear to provide an equally good fit to the observations [27]. For irregular galaxies, Skillman (1987) has proposed that star formation occurs only above a threshold column density, and that this threshold may be related to a critical amount of dust shielding required for molecule formation. Are any of these models extrapolatable to the faintest dwarf irregulars? In this chapter we will address these issues using a sample of extremely faint dwarf galaxies.

5.2 Dwarf galaxy sample

The optical properties of a sample of galaxies used for the star formation studies in extremely faint dwarf galaxies are given in Table 5.1. Col.(1) shows the galaxy name, (2) the absolute blue magnitude, (3) the distance to the galaxy, (4) the observed (B-V) colour, (5) the Holmberg radius of the galaxy, (6) the optical inclination of the galaxy and (7) references for information in the previous columns. Results from the GMRT HI observations for five galaxies in the sample viz. KDG 52, UGC 4459, CGCG 269-049, UGC 7298 and KK 230 are presented in this chapter. The GMRT observations and data analysis of these galaxies are described in Chapter 2. GMRT HI data for KK 44, GR 8 and DDO 210 is already presented in our previous chapters of this thesis, although we include here fresh maps and measurements at angular scales that are relevant to the issues discussed in this chapter. We have also included two more faint dwarf galaxies viz. Leo A and Sag DIG in our sample. Data for these two galaxies were obtained from the VLA archive, we will present here only those maps and measurements of these galaxies that are relevant to this chapter. Notes on the individual galaxies follow:

KK 44 is a member of IC 342 group of galaxies. Using the HST data, Karachentsev et al.(2003) derived a distance of 3.34 Mpc for this galaxy. Inspite of being very faint, the HI distribution in the galaxy shows a very regular kinematics (see Chapter 3 for details).

KDG 52 (also called M81DwA) was discovered by Karachentseva(1968) and was later detected in HI by Lo & Sargent (1979). This galaxy is a member of M81 group of galaxies. Karachentsev et al.(2002) derived a TRGB distance of 3.55 Mpc to the galaxy from the HST

Table 5.1: Optical parameters of the sample galaxies

Galaxy	M_B	D (Mpc)	B-V	R_{Ho} (′)	i_{opt}(°)	references
KK 44	−11.85	3.34	0.8	0.7	65	2
KDG 52	−11.49	3.55	0.24	0.65	24	2
UGC 4459	−13.37	3.56	0.45	0.80	30	2,6
Leo A	−11.36	0.69	0.15	3.5	54	2,3,7
CGCG 269-049	−12.46	3.4	-	0.60	77	1
UGC 7298	−12.27	4.21	0.29	0.55	58	2,6
GR 8	−12.11	2.10	0.32	0.95	25	1,2
KK 230	−9.55	1.9	0.40	0.87	35	2
SagDIG	−11.49	1.1	0.3	1.8	45	2,5
DDO 210	−11.09	1.0	0.24	1.8	62	2,4

References: 1-de Vaucouleurs & Moss (1983), 2-Karachentsev et al.(2004), 3- Karachentseva & Sharina (1988) 4-Lee et al.(1999), 5- Lee & Kim (2000), 6-Makarova(1999), 7-Tolstoy et al. (1998)

data.

UGC 4459 is a member of M81 group of galaxies. Karachentsev et al.(1994) derived a distance of 3.08 Mpc to the galaxy from its brightest blue stars. We use here the more recent TRGB based distance estimate of 3.56 Mpc [22] of this galaxy. UGC 4459 is relatively metal poor, with 12+log(O/H)∼ 7.62 [29].

LeoA is a member of the local group, with a tip of the red giant branch (TRGB) distance of 0.69 Mpc [51]. VLA HI data for this galaxy has been discussed earlier by Young & Lo (1996).

CGCG 269-049 is an extremely metal poor dwarf galaxy with 12+log[O/H]∼ 7.43 [28]. It is also a member of the Canes Venatici I cloud. We assume for it the distance given in Karachentsev et al. (2004), which has been estimated from the Hubble flow.

UGC 7298 is a member of the Canes Venatici I cloud of galaxies. Tikhonov & Karachentsev (1998) derived a distance to the galaxy of 8.6 Mpc from the brightest blue and red stars. However, more recent estimate based on the I magnitude of the TRGB gives a distance of 4.2 Mpc [21]. We use the latter estimate in the rest of the chapter.

GR 8 is the only field galaxy in our sample. At a distance of 2.1 Mpc (based on the TRGB magnitude [8]), this galaxy lies well outside the local group zero velocity surface. GMRT HI data has been presented in Chapter 4 of this thesis and VLA data in Young et al.(2003).

KK 230, the faintest dwarf irregular galaxy in our sample, is yet another member of the Canes Venatici I cloud of galaxies [21]. The TRGB distance of this galaxy is 1.9 Mpc [20].

SagDIG is a member of the local group and has a (TRGB) distance of 1.04 Mpc [20]. VLA HI data for this galaxy has been presented by Young & Lo (1997).

DDO 210 is the faintest gas rich dwarf galaxy in our local group. It is classified as a transition galaxy, having properties intermediate between dwarf irregulars and dwarf spheroidals. Lee et al.(1999), estimated a TRGB distance of 950±50 kpc for this galaxy. GMRT HI data for this has been earlier discussed in Chapter 3 of this thesis, while VLA HI data can be found in Young et al. (2003).

5.3 Large Scale HI distribution and kinematics

The global HI profiles for KDG 52, UGC 4459, CGCG 269-049, UGC 7298 and KK 230, obtained from the coarsest resolution data cubes (see Table 2.3) are shown in Fig. 5.1. Columns (2−7) in Table 5.2 list the parameters derived from the global HI profiles. Col. (1) gives the galaxy name, (2) the integrated HI flux along with the errorbars, (3) the velocity width at 50% of the peak (ΔV_{50}), along with the errorbars, (4) the central heliocentric velocity ($V_{\odot}$) and its errorbars, (5) the HI mass along with its errorbars, (6) the HI mass to light ratio (M_{HI}/L_B), (7) the ratio of the GMRT flux to the single dish flux (FI/FI_{SD}). The single dish fluxes for all the galaxies are taken from the tabulation in Karachentsev et al.(2004). In the case of CGCG 269-049, single dish data is not available. The parameters measured from the GMRT HI profiles are in good agreement with those values obtained from the single dish observations, in particular the HI flux measured at the GMRT agrees with the single dish flux for all the galaxies. This indicates that no flux was missed because of the missing short spacings in our interferometric observations. Col(8) shows the HI diameter at a column density of 10^{19} atoms cm^{-2}. (9) the inclination as measured from the HI moment 0 maps. (10) the ratio of the HI diameter to the Holmberg diameter. For all the galaxies the HI emission extends to $\sim 2-3$ times the optical diameter, a typical ratio for dwarf irregular galaxies.

For comparison, we have also included in Table.5.2, the results obtained from the GMRT observations for the galaxies KK 44, GR 8 and DDO 210, presented in previous chapters and also the results from the VLA data for Leo A and Sag DIG.

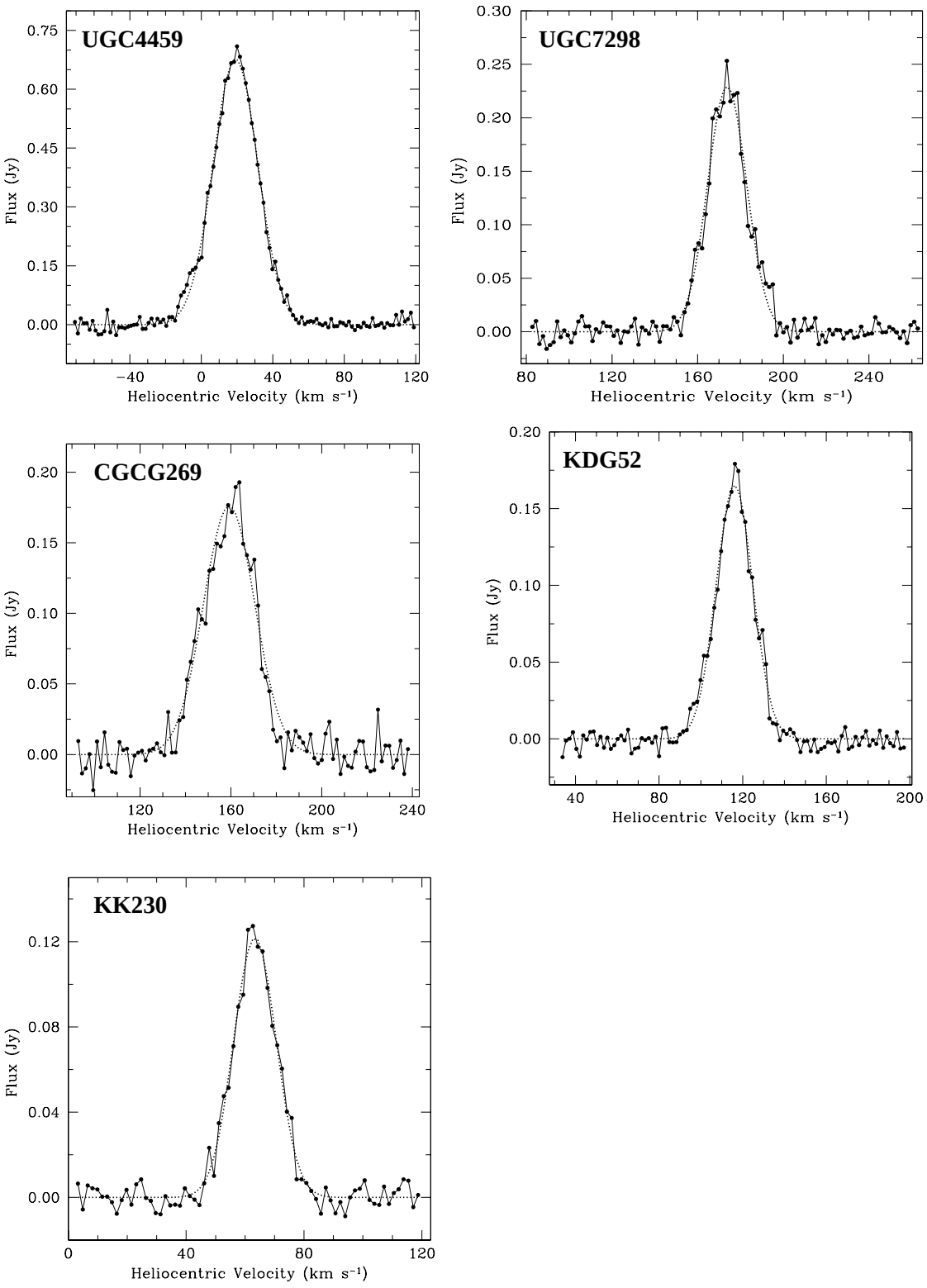

Figure 5.1: The HI global profile for our sample galaxies derived from our coarsest resolution HI distribution. The channel separation is 1.65 km s^{-1}. The dotted line shows a gaussian fit to the line profiles.

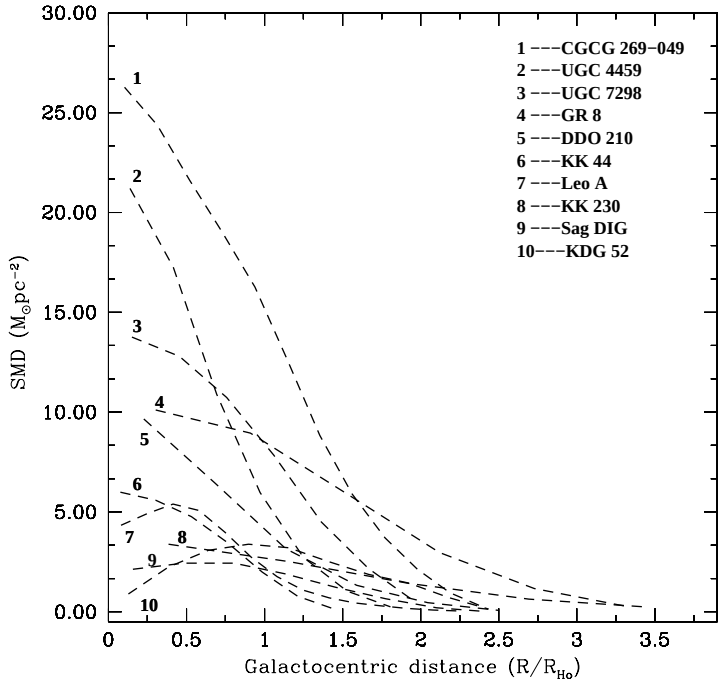

Figure 5.2: The deprojected gas surface mass density (SMD) distribution for our sample galaxies. For all galaxies (except DDO 210, Sag DIG and Leo A), the SMD was computed for a linear resolution of $\sim$ 500 pc. For DDO 210, SagDIG and Leo A the linear resolution is $\sim$ 300 pc. The actual angular resolutions are 29 $''$ $\times$ 27$''$ (UGC 4459), 26$''$ $\times$ 24$''$ (UGC 7298), 28$''$ $\times$ 24$''$ (CGCG 269-049), 48$''$ $\times$ 45$''$ (KK 230), 26$''$ $\times$ 23$''$ (KDG 52),41$''$ $\times$ 39$''$ (GR 8), 61$''$ $\times$ 56$''$ (DDO 210), 31$''$ $\times$ 29$''$ (KK 44), 67$''$ $\times$ 65$''$ (Sag DIG) and 78$''$ $\times$ 72$''$ (Leo A). The gas SMD is obtained by scaling the HI SMD profile by 1.4 to account for primordial He.

The integrated HI emission of KDG 52, UGC 4459, CGCG 269-049, UGC 7298 and KK 230, overlayed on the optical Digitized Sky Survey (DSS) images are shown in Fig.5.3[A]-5.7[A]. The HI distribution in CGCG 269-049 and KK 230 are dominated by a single clump of high column density, while the HI in UGC 4459 and UGC 7298 are concentrated in two high-column-density regions, separated by a low-column density region in the center. In the case of KDG 52, the HI is distributed in a clumpy incomplete ring.

Inclinations (i_{HI}) of our sample galaxies (except for KDG 52) were estimated from the HI moment 0 maps by fitting elliptical annuli to the two lowest resolution images. For KDG 52, only the lowest resolution HI distribution is sufficiently smooth to be used for ellipse fitting. For all other galaxies, the inclination derived from these two resolutions

Table 5.2: Results from GMRT observations

Galaxy	FI	ΔV_{50}	$V_\odot$	M_{HI}	M_{HI}/L_B	FI/FI_{SD}	d_{HI}	i_{HI}	d_{HI}/d_{Ho}
	Jy km s^{-1}	km s^{-1}	km s^{-1}	$\times 10^6 M_\odot$			$'$	$^\circ$	
KK 44	4.6(0.4)	21.4(1.0)	77.5(1.0)	12.2(1.2)	1.4	1.02	3.2	65	2.3
Leo A	42.0(4.0)	18.8(0.7)	21.7(0.7)	4.7(0.4)	1.02	0.88	16.0	62	2.3
KDG 52	3.8(0.4)	20.6(1.7)	116.0(1.9)	10.8(1.1)	1.8	0.85	3.5	23	2.7
UGC 4459	21.5(2.2)	29.6(1.8)	19.2(2.3)	64.2(6.5)	1.4	1.01	4.5	31	2.8
CGCG 269	4.7(0.5)	26.6(2.2)	159.0(3.4)	12.7(1.3)	0.9	–	2.6	43	2.3
UGC 7298	5.2(0.5)	21.4(1.7)	174.0 (2.0)	21.6(2.1)	1.7	1.06	3.5	28	3.1
GR 8	9.0(0.9)	26.0(1.2)	217.0(2.2)	10.38(1.0)	1.02	1.03	4.3	28	2.3
KK 230	2.2(0.2)	17.0(2.0)	63.3(1.8)	1.9(0.2)	1.9	0.86	3.0	51	3.3
SagDIG	23.0(1.0)	19.4(0.8)	−78.5(1.0)	5.4(0.2)	1.02	0.92	4.3	33	2.3
DDO 210	12.1(1.2)	19.1(1.0)	−139.5(2.0)	2.8(0.3)	1.00	1.05	4.8	27	1.3

images match within the errorbars. The estimated inclination for each galaxy (assuming an intrinsic thickness $q_o = 0.2$) is tabulated in Table. 5.2. Comparing this value to the optical inclination (Table. 5.1), shows that the two inclinations are in agreement for UGC 4459 and KDG 52, whereas for the rest of the sample galaxies the optical inclination is either found to be much higher (UGC 7298 and CGCG 269-049) or lower (KK 230) than the inclination derived from the HI morphology. Using the derived HI inclination, the deprojected HI radial surface mass density profile (SMD) for each galaxy was obtained by averaging the HI distribution over elliptical annuli in the plane of the galaxy. The derived SMD profiles for each galaxy are given in Fig. 5.2. For comparison we have also the SMD for KK 44, GR 8, DDO 210, Leo A and Sag DIG.

We next discuss in detail the large scale HI distribution and kinematics for the five galaxies for which fresh GMRT observations are presented in the current chapter.

5.3.1 Notes on individual galaxies

5.3.1.1 KDG 52

The neutral hydrogen in this galaxy is distributed in a clumpy broken ring surrounding the optical emission (Fig. 5.3[A]). The central HI hole has a diameter of $\sim 40''$ (~ 688 pc); similar central HI holes are seen in other faint dwarf galaxies (e.g. Sag DIG [65], DDO 88

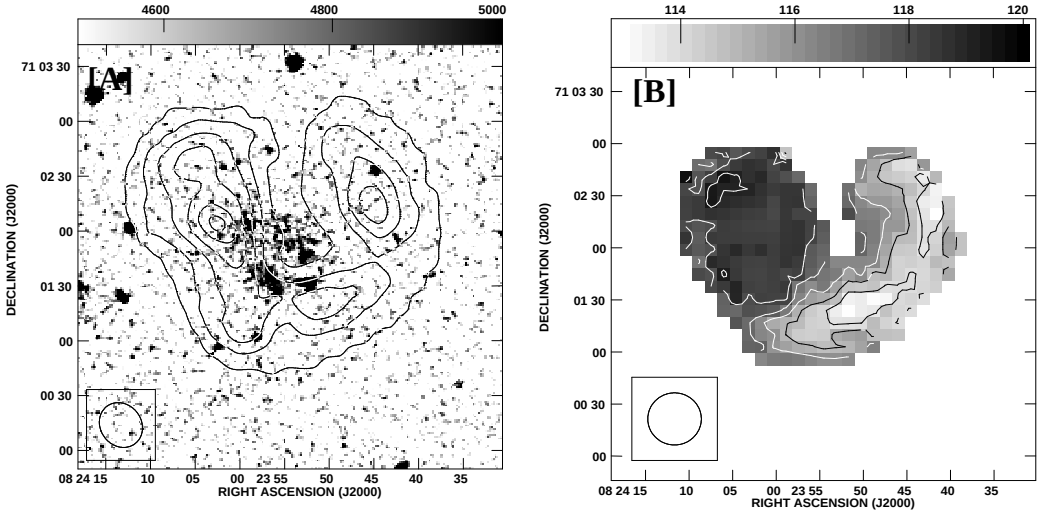

Figure 5.3: [**A**] The B band optical DSS image of KDG 52 (greyscales) with the GMRT $26'' \times 23''$ resolution integrated HI emission map (contours) overlayed. The contour levels are 0.25, 1.00, 1.75, 2.49, 3.10 & 3.67 $\times 10^{20}$ atoms cm^{-2}. [**B**] The velocity field of the galaxy at $26'' \times 23''$ resolution. The contours are in the steps of 1.0 km s^{-1}and range from 113.0 km s^{-1}to 118.0 km s^{-1}.

[45]). The HI hole is not exactly centered on the optical emission; the HI column density at the eastern side of the optical emission is $N_{HI} \sim 4 \times 10^{20}$, while the rest of the optical emission lies inside the HI hole. Prior to this work, there have been two HI interferometric studies of KDG 52. It was observed with the WSRT by Sargent et al.(1983) with a velocity resolution of ~ 8 km s^{-1}and later re-observed with a high velocity resolution in the C array of the VLA [62]. The overall morphology of the earlier images compares well with that of our image.

Our coarsest resolution HI distribution and velocity field (not shown) shows faint emission in the center and in the northern region of the galaxy, a feature that is not visible at the higher resolutions. One may suspect that this HI emission is not real but is the result of beam smearing. To check for this possibility, the individual channel maps in the $42'' \times 39''$ data cube were inspected. In the channel maps, the peak of the diffuse emission in the central as well as in the northern region in the galaxy, occurs at the same heliocentric velocity as that of nearby HI clumps, suggesting that they may arise due to beam smearing. As a further check, the clean components from the $42'' \times 39''$ resolution data cube were convolved with a smaller restoring beam of $30'' \times 30''$, to generate a new data cube. The diffuse emission which

was visible in $42'' \times 39''$ data cube is not seen in the channel maps in this cube, i.e. no clean components were found in the region of diffuse emission. Finally, the HI flux measured from a genuine $30'' \times 30''$ resolution data cube (i.e. made from the visibility data by applying the appropriate UV range and taper) is the same as that measured from the $42'' \times 39''$ resolution data cube. All these indicate that the diffuse emission in $42'' \times 39''$ cube is entirely due to beam smearing.

The velocity field obtained from $26'' \times 23''$ resolution data cube is given in Fig. 5.3[B]. The velocity field shows a large scale gradient across the galaxy with a magnitude of ~ 1.7 km s^{-1}kpc^{-1}. However the velocity field is clearly not consistent with pure rotation. One can still, crudely estimate the maximum possible circular velocity in the following way. The velocity difference from one edge of the galaxy to the other is ~ 6 km s^{-1}, this implies that the magnitude of any circular velocity component must be limited to $V_{rot}\sin(i) \leq 3$ km s^{-1}. Puche & Westpfahl (1994) have tried to model this velocity field, and find that a combination of rotation (with a magnitude of 7 km s^{-1}) and expansion (with a magnitude of 5 km s^{-1}) provides a reasonable fit. A similar combination of rotation and expansion was found to provide a good fit to the kinematics of one of our sample galaxies viz. GR 8 (see Chapter 4 of this thesis for details).

Bureau et al.(2004), have suggested that KDG 52 is probably a tidal dwarf, formed through gravitational collapse of the tidal debris from the previous interactions of Holmberg II with UGC 4483. In Sec. 5.4.1, we estimate the dynamical mass of this galaxy from the virial theorem; this mass estimate implies that the galaxy has a significant amount of dark matter. This would argue against a tidal dwarf origin for KDG 52, since tidal dwarfs are generally not expected to be dark matter dominated (e.g. [2]).

5.3.1.2 UGC 4459

The optical appearance of UGC 4459 is dominated by bright blue clumps, which emit copious amounts of Hα (Fig. 5.4[A], 5.9 & 5.12). The two high density peaks seen in the integrated HI map coincide with these star forming regions (Fig. 5.4[A]).

The velocity field of UGC 4459 (Fig. 5.4[B]) shows a large scale gradient (aligned along the line connecting the two star forming regions) across the galaxy. The magnitude of the average velocity gradient across the whole HI disk is ~ 4.5 km s^{-1}kpc^{-1}. However we note that the gradient is not uniform across the galaxy. The receding (southeastern) half of the galaxy shows a rapid change in velocity with galacto-centric distance, while the approaching (northwestern) half of the galaxy shows a much more gentle gradient. UGC 4459 is a fairly isolated dwarf galaxy with its nearest neighbor, UGC 4483 at a projected distance of $3.6°$($\sim$

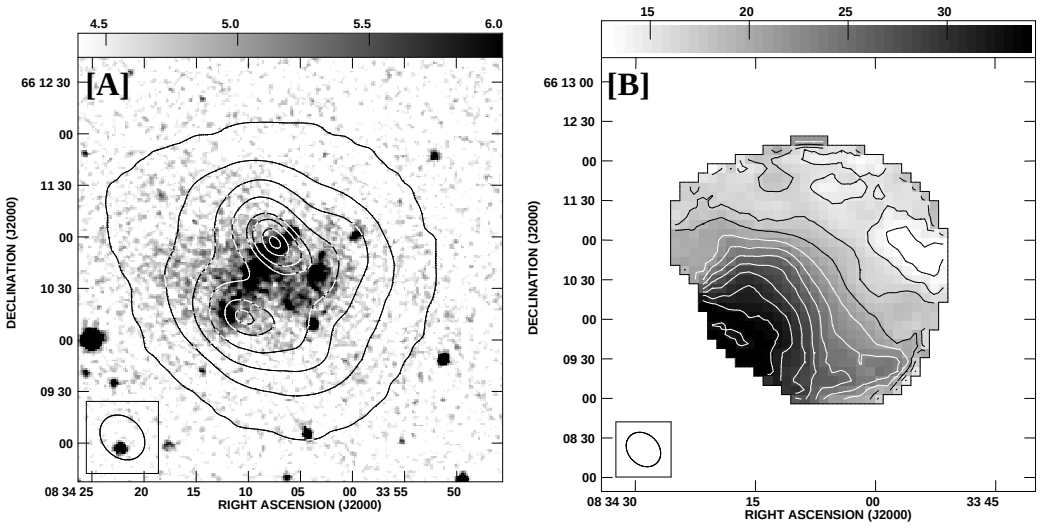

Figure 5.4: [**A**] The B band optical DSS image of UGC 4459 (greyscales) with the GMRT $29'' \times 27''$ resolution integrated HI emission map (contours) overlayed. The contour levels are 0.22, 3.33, 6.45, 9.56, 12.67, 15.79, 18.91, 22.00, 24.12, 28.25 and 31.36 $\times 10^{20}$ atoms cm^{-2}. [**B**] The HI velocity field for galaxy at $29'' \times 27''$ resolution. The contours are in the steps of 2.0 km s^{-1}and range from 13.0 km s^{-1}to 33.0 km s^{-1}.

223 kpc) and at a velocity difference of 135 km s^{-1}. Being a member of the M81 group, it is possible that interaction with intra-group gas could produce such disturbed kinematics. To check for this possibility, we estimated the ram pressure required to strip gas from this galaxy. The threshold condition for ram pressure stripping is given by [14]

$$\rho_{\rm IGM} v^2 \geq 2\Pi G \Sigma_* \Sigma_{\rm g} \tag{5.1}$$

where, $\rho_{\rm IGM}$ is the density of the intra-group medium (IGM) and v is the relative velocity of the galaxy moving through the IGM. Σ_* and $\Sigma_{\rm g}$ are stellar and gas surface density respectively. Taking v$\sim$ 190 km s^{-1}, typical for M81 group [4], and values for Σ_* and $\Sigma_{\rm g}$ from the location in the galaxy where the velocity field begins to look perturbed, we find that the IGM volume density required to strip the ISM from UGC 4459 is $n_{\rm IGM} \geq 8 \times 10^{-5}$ cm^{-3}. UGC 4459 is located at a projected separation of $\sim 8.4^\circ$ (520 kpc) to the South-West of M81 (which we can take to be the center of the M81 group). The $n_{\rm IGM}$ required for ram pressure stripping of UGC 4459 is much higher than $n_{\rm IGM}$ expected at this location ($\sim 1.4 \times 10^{-6}$ cm^{-3}; assuming that 1% of the virial mass of the group is dispersed uniformly in a hot IGM

within a sphere just enclosing UGC 4459 [4]). Hence, it seems unlikely that the peculiar kinematics of the galaxy is due to IGM ram pressure.

Given the kinematical asymmetry between the two halves of the galaxy, it is not surprising that a tilted ring fit does not give consistent results for the two halves. The difference in the peak velocities for the rotation curves derived from the two halves is ~ 15 km s^{-1}. This is a sizable compared to the peak value of 25 km s^{-1}obtained for the receding half of the galaxy. One can crudely estimate the maximum possible circular velocity in the following way. The velocity difference from one edge of the galaxy to the other is 18 km s^{-1}, this implies that the magnitude of any circular velocity component must be limited to $V_{rot}\sin(i) \leq 9$ km s^{-1}.

Pustilnik et al.(2003) found substantial small scale velocity gradients in the Hα emission along a slit placed parallel to the optical major axis (i.e. also along the direction of maximum velocity gradient in the HI velocity field), as well as a large scale gradient, with magnitude somewhat larger than what we observe in the HI.

UGC 4459 has the largest star formation rate of all the galaxies in our sample. Pustilnik et al.(2003) estimate very young ages ($\sim 3 - 8$ Myr) for the star forming knots in the galaxy. Since they find no nearby galaxy that could have triggered this recent starburst, they suggest that it could be triggered by tidal interaction with the M81 group as a whole, or by interaction with the intra group medium. As we argued above, the ram pressure of the intra group medium is likely to be small. The velocity field of UGC 4459 is however qualitatively very similar to that of DDO 26 [17] and IC 2554 [31], both of which are suspected to be late stage mergers. It seems possible therefore that UGC 4459 too represents a recent merger of two still fainter dwarfs.

5.3.1.3 CGCG 269-049

The optical emission in CGCG 269-049 shows two components, a central compact component and an outer faint extended component; both elongated in the northwest direction. The HI distribution of the galaxy also shows an elongation in the same direction. However, a misalignment of $\sim 10^\circ$ is seen between the optical and the HI major axis. The HI distribution is regular and shows a slightly off-centered peak; this signature is more prominent in the high resolution HI images.

CGCG 269-049 is undergoing a burst of star formation as indicated by strong emission lines in its spectra. It has been suggested that starbursts in dwarf galaxies could be triggered by tidal interaction with a companion [53, 60]. While CGCG 269-049 does have a nearby companion (viz. UGC 7298 discussed below) the HI distribution in neither of these galaxies is suggestive of tidal interaction.

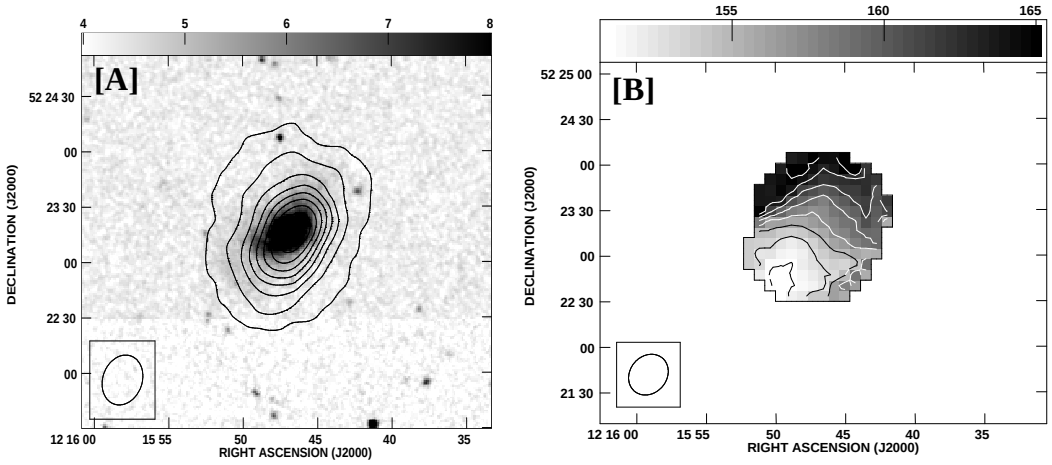

Figure 5.5: [**A**] The B band optical DSS image of CGCG 269-049 (greyscales) with the GMRT $28'' \times 24''$ resolution integrated HI emission map (contours) overlayed. The contour levels are 0.08, 1.12, 2.18, 3.23, 4.28, 5.33, 6.39, 7.44, 8.49 and 9.55 $\times 10^{20}$ atoms cm^{-2}. [**B**] The HI velocity field for galaxy at $28'' \times 24''$ resolution. The contours are in the steps of 2.0 km s^{-1}and range from 151.0 km s^{-1}to 165.0 km s^{-1}.

The velocity field of the galaxy shows a large scale gradient, roughly aligned with the morphological major axis and with a magnitude of ~ 5.2 km s^{-1}kpc^{-1} (Fig. 5.5[B]). Of all the galaxies in this subsample, CGCG 269-049 has a velocity field that most resembles that expected from a rotating disk. Substantial deviations from simple rotation can however be seen, and a tilted ring fit to the velocity field does not yield meaningful results. CGCG 269-049 has one of the highest current star formation rates among our sample galaxies; Hα imaging of this galaxy shows a bright Hα core near its center (see Fig. 5.9 & 5.12). From Fig. 5.5[B], one can see kinks in the velocity field in the regions near this star forming knot. Hence, it is likely that the energy input from the on-going star formation in the galaxy is responsible for at least some of the distortions seen in the velocity field. The maximum velocity difference from one edge of the galaxy to the other is ~ 16 km s^{-1}, hence $V_{\rm rot}\sin(i) \leq 8$ km s^{-1}.

5.3.1.4 UGC 7298

The velocity field of UGC 7298 (Fig. 5.6[B]) shows a large scale gradient roughly aligned with the line joining the two high density gas clumps. The magnitude of the gradient is $\sim$

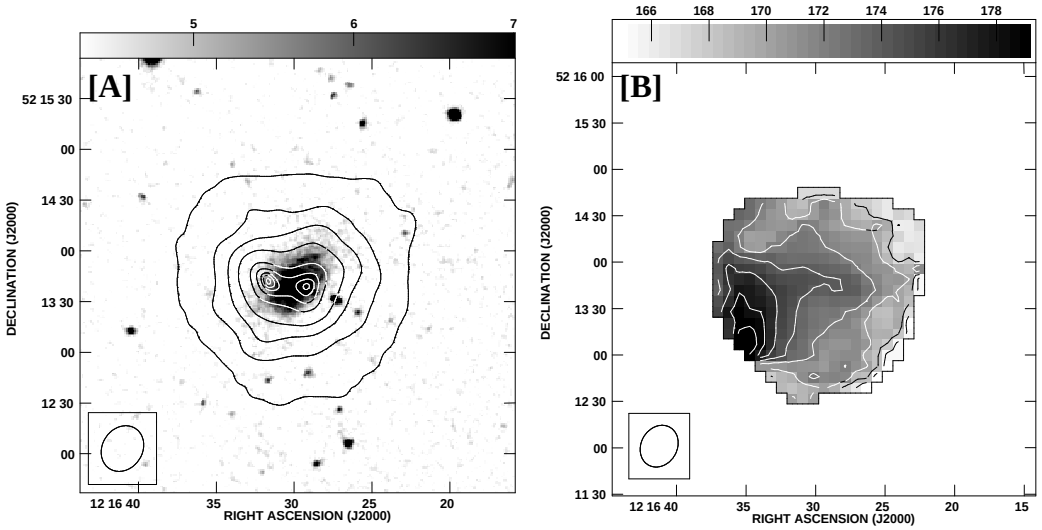

Figure 5.6: [**A**] The B band optical DSS image of UGC 7298 (greyscales) with the GMRT $26'' \times 24''$ resolution integrated HI emission map (contours) overlayed. The contour levels are 0.2, 2.7, 5.3, 7.9, 9.1, 10.5, 11.2 and 11.5 $\times 10^{20}$ atoms cm^{-2}. [**B**] The HI velocity field for galaxy at $26'' \times 24''$ resolution. The contours are in the steps of 2.0 km s^{-1}and range from 166.0 km s^{-1}to 180.0 km s^{-1}.

3.5 km s^{-1}kpc^{-1}. The velocity field is broadly similar to that in UGC 4459. The optical properties of the two galaxies are however very dissimilar. UGC 4459 is currently undergoing a starburst and its optical appearance is dominated by bright star forming knots. UGC 7298, on the other hand, has a very small current star formation rate, as inferred from very faint Hα emission from the galaxy (Fig. 5.9 & 5.12). The maximum velocity difference from one edge of the galaxy to the other is ~ 16 km s^{-1}, implying that $V_{rot}\sin(i) \leq 8$ km s^{-1}.

5.3.1.5 KK 230

KK 230 is the faintest galaxy in our sample. The velocity field (Fig. 5.7[B]) shows a gradient in the east-west direction (i.e. roughly perpendicular to the HI and optical major axis) with a magnitude of ~ 6 km s^{-1} kpc^{-1}. Even apart from this misalignment, the velocity field bears little similarity from that expected from a rotating axi-symmetric disk. The origin of the velocity gradient in KK 230 is rather puzzling. This galaxy has no measurable ongoing star formation, and no Hα emission was detected from the galaxy. It also lies at the periphery of the Canes Venatici I cloud group of galaxies; Karachentsev et al. (2004) found its tidal index

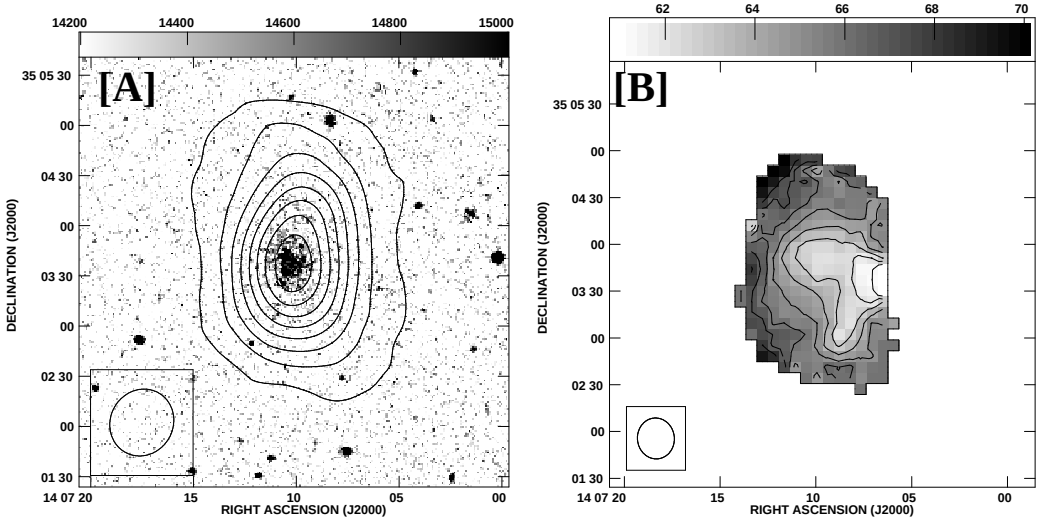

Figure 5.7: [**A**] The B band optical DSS image of KK 230 (greyscales) with the GMRT $48'' \times 45''$ resolution integrated HI emission map (contours) overlayed. The contour levels are 0.09, 0.50, 0.92, 1.33, 1.75, 2.16, 2.58, 3.00, 3.41 and 3.83 $\times 10^{20}$ atoms cm^{-2}. [**B**] The HI velocity field for galaxy at $26'' \times 24''$ resolution. The contours are in the steps of 1.0 km s^{-1}and range from 61.0 km s^{-1}to 68.0 km s^{-1}.

to be -1.0, meaning that it is a fairly isolated galaxy. This, along with the fairly regular HI distribution make it unlikely that tidal forces are responsible for the observed velocity field. The maximum velocity difference from edge of galaxy to the other is ~ 10 km s^{-1}, which gives $V_{\rm rot}\sin(i) \leq 5$ km s^{-1}.

5.4 Discussion

5.4.1 Dynamical Masses

As discussed above, large scale systematic gradients are seen across all the newly mapped galaxies. In fact, all the 10 galaxies in our sample have velocity fields with a measurable ordered component, contrary to the general belief (e.g. Lo et al.(1993)) that the velocity fields of faint dwarf galaxies are "chaotic". Some of our sample galaxies overlap with those in Lo et al. (1993), and from a comparison of the new and old determinations of the velocity fields, it appears that high sensitivity and high velocity resolution (~ 1.6 km s^{-1}as opposed to the earlier used ~ 6 km s^{-1}) are crucial to discern systematic kinematical patterns in

such faint galaxies.

The origin of these ordered fields is unclear. One would expect that in the absence of external forces, or internal energy input, gas with non zero angular momentum would settle down into a rotating disk. Tidal forces, and/or energy input from star formation could profoundly disrupt the gas velocity fields. Indeed, it has often been suggested that a strong starburst could drive out the ISM of such small galaxies (see e.g.[6, 9, 10]). For two of the galaxies in our sample, viz. GR 8 (Chapter 4 of this thesis) & KDG 52 [40], detailed modeling shows that the velocity field can be fit by a combination of circular and radial motion of the gas. In general though, there does not seem to be any particular correlation between the current star formation rate (see Table 5.4) and the distortion of the velocity fields. For example, the velocity field of CGCG 269-049 (Fig.5.5[B]) shows relatively mild deviations from that expected from rotation, as compared to that of UGC 7298 (Fig. 5.6[B]), even though both galaxies have comparable luminosities and the star formation rate in CGCG 269-049 is more than an order of magnitude more than that of UGC 7298. Tidal interactions are also not clearly implicated, as several of our galaxies are relatively isolated, and none of them show morphologies typical of tidal interaction. Interestingly, some compact high velocity clouds (notably M 31 HVC 1, M 31 HVC 16 [61]) show similar velocity gradients. Westmeier et al.(2005) argue against these velocity gradients being due to tidal forces, and suggest that they may be indicative of dark matter in these objects.

Given their peculiar kinematics, it is difficult to accurately determine the total dynamical mass of our sample galaxies. We instead compute an indicative dynamical mass using the virial theorem, assuming that the HI distribution is spherical and has an isotropic velocity dispersion. We realize that these assumptions are unlikely to be rigorously justifiable in the current situation, and therefore this mass estimate is at best indicative. Under the assumptions above, the virial mass estimate is:

$$\mathrm{M_{VT}} = \frac{5\ \mathrm{r_H} \times \sigma_\mathrm{T}^2}{\mathrm{G}} \tag{5.2}$$

where σ_T is the HI velocity dispersion corrected for the instrumental broadening as well as for the broadening due to the velocity gradient over the finite size of the beam. The observed velocity dispersion given in Sect. 2.6 is corrected using Eqn.3.5 to obtained σ_T.

Table 5.3 lists the estimated dynamical mass ($\mathrm{M_{VT}}$) for our sample galaxies. The columns in the table are: Col.(1) The galaxy name. Col.(2) The estimated σ_T. Col.(3) The stellar mass-to-light ratio Γ_B obtained from the observed B−V colour for each galaxy, using the low metallicity Bruzual & Charlot SPS model with a Salpeter IMF (Bell & de Jong 2001). In absence of any colour information for CGCG 269-049 we assume Γ_B=1 for it. Col.(4) The

Table 5.3: Dynamical mass estimate for sample galaxies

Galaxy	σ_T (km s^{-1})	Γ_B	M_* ($10^6 M_\odot$)	M_{VT} ($10^8 M_\odot$)
KDG 52	8.5	0.6	3.7	1.5
UGC 4459	8.0	1.0	45.7	1.9
CGCG 269-049	9.0	1.0	15.0	1.2
UGC 7298	8.0	0.7	8.8	1.6
KK 230	7.0	1.0	1.0	0.5

stellar mass obtained from the assumed mass to light ratio. Col.(5) The virial mass, as obtained from Eqn. 5.2.

Figure 5.8[A] is a plot of the ratio of HI mass to the dynamical mass against absolute blue magnitudes for a sample of dwarf irregular galaxies. The references from which the data are taken are listed in the figure caption. For our current sample, the dynamical masses are taken from Table 5.3, Chapter 3 (for KK 44 and DDO 210) and Young & Lo (1997) (LGS-3 and SagDIG). The ratio of M_{HI}/M_{VT} for UGC 4459 is found to be $\sim$0.34, which is larger than a value typically seen in dwarf galaxies. Such high value of M_{HI}/M_{VT} is also seen in some blue compact dwarf galaxies (e.g. [57]). Figure 5.8[B] shows M_{VT}/M_{lum} for the same sample, plotted as a function of M_B. The luminous mass M_{lum} is the sum of the stellar and gas mass. The stellar mass for all galaxies was computed in exactly the same way as for our sample galaxies; the gas mass is obtained by taking into account the contribution of primordial He i.e. $M_{gas} = 1.4 \times M_{HI}$. We note that although M_{VT}/M_{lum} does not show any correlation with M_B for the full sample, there is a trend of an increase in the M_{VT}/M_{lum} ratio with the decrease in M_B, seen in our sample galaxies. Further, a jump in M_{VT}/M_{lum} ratio is seen at the faintest luminosities ($M_B > -10.0$). While this might be indicative of increased baryon loss from these small halos (e.g. [13]), we caution that there is considerable uncertainty in the dynamical mass for the galaxies in this magnitude range, and also that the total number of galaxies is too small to substantiate such a claim.

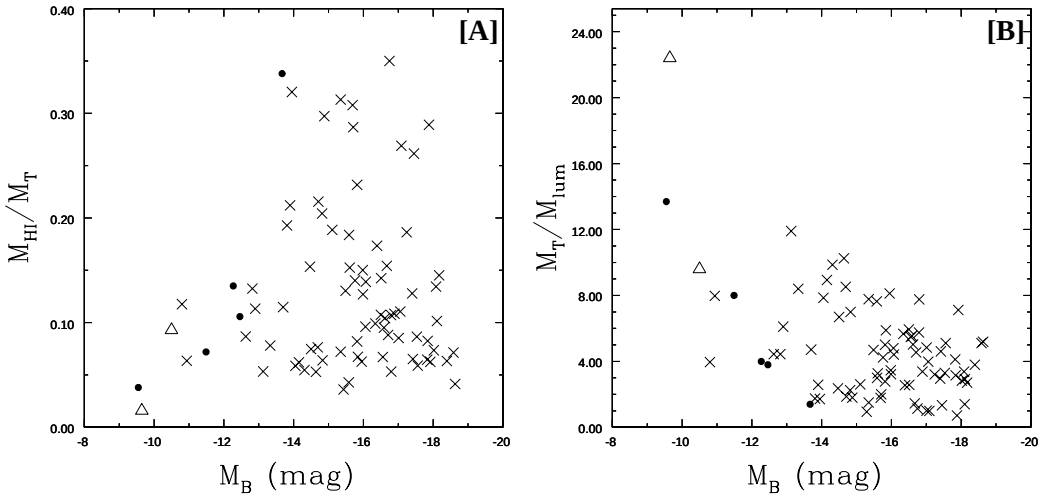

Figure 5.8: **[A]** M_{HI}/M_T as a function of M_B for a sample of dwarf irregular galaxies ($M_B \geq -19$). M_T is estimated from the last measured point of the rotation curve for Verheijen(2001), Swaters (1999) and Cote et al. (2000) (represnted as crosses), whereas for galaxies from our sample (solid dots) and for LGS-3 and SagDIG from Young & Lo (1997) (triangles), M_T is estimated from the virial theorem. **[B]** M_T/M_{lum} for the same sample. See text for more details.

5.4.2 HI column density and Star formation

Our sample galaxies have widely different star formation rates (see Table 5.4), and range from having no detectable on-going star formation (e.g. KK 230, KDG 52), to having an optical appearance that is dominated by bright star forming knots (e.g. UGC 4459, CGCG 269-049). As such, this is a well suited sample for trying to determine the connections (if any!) between the HI distribution and kinematics and star formation.For this study we have used the Hα emission from the galaxies as a tracer of on-going star formation. The Hα images of KK 44, CGCG 269-049 and UGC 7298 were provided by Prof Karachentsev. For Leo A, SagDIG and GR 8, Hα images were downloaded from NED. Details of these images can be found in Hunter & Elmegreen (2004). The Hα image of UGC 4459 was kindly provided by U. Hopp; details can be found in Schulte-Ladbeck & Hopp (1998). For DDO 210, van Zee (2000) detected a single source of Hα emission in the galaxy; however their follow up observations suggested that it does not arise in a normal HII region, but probably comes from dense outflowing material from an evolved star. In all the figures of DDO 210, presented in this chapter, we show the location of this emission by a star, but caution the reader that it may not actually represent a star forming region. For KK 230 and KDG 52, no Hα emission

was detected (private communication Prof Karachentsev).

For spiral galaxies, the star formation rate appears to be quite well correlated to the gas column density, though it is unclear if the gas column density is the only relevant parameter, as in the Schmidt law, or whether a combination of gas column density and the dynamical time are important, (as in the Toomre's instability criteria, see [27]). For dwarf irregular galaxies, it has been suggested that star formation occurs only above a critical threshold column density ($\sim 10^{21}$ cm^{-2}, when measured at a spatial resolution of $\sim$ 500 kpc) and that this may be because a critical amount of dust shielding is required before star formation can commence [47]. Since the observed column density is resolution dependent and that the distance of our sample galaxies varies from 0.70 Mpc (Leo A) to 4.2 Mpc (UGC 7298), one would require maps at angular resolutions varying by a factor of $\sim$ 6. This problem is well suited to a telescope like the GMRT, where because of the hybrid configuration, maps at a range of angular resolutions can be made from a single observing run. For all our galaxies we produced CLEANed HI maps at an angular resolution corresponding to a linear scale of $\sim$ 300 pc at the distance to the galaxy. We thus have a unique data set which spans a wide range of star formation rates, but for which maps are available at a similar linear resolution. The results of a comparison of the HI distribution with the sites of Hα emission are given in Table 5.4. Col(1) shows the galaxy name, Col(2) the absolute blue magnitude (M_B) of the galaxy, Col(3) the resolution of the HI column density map, Col(4) the corresponding linear resolution in pc, Col(5) the observed HI peak column density, Col(6) the peak gas surface density. The gas surface densities are obtained by correcting the observed HI column densities for inclination and for primordial He content (which we take to be 10% of HI by number). Note that the peak gas density need not occur at the center of the galaxy, Col(7) the column density of the HI contour that just encloses all the HII emission in the galaxy, Col(8) current star formation rate (for KK 230 and KDG 52 the limits on SFR are given), Col(9) the metallicity of the galaxy (for some of our sample galaxies no measurement of the metallicity exist) and Col(10) references for the star formation rate and the metallicity.

DDO 210 and KK 44 are the only galaxies in our sample which show systematic rotation; the rotation curves of these galaxies have been presented in Chapter 3 of this thesis. For these two galaxies, we show in Fig. 5.10 the ratio of the azimuthally averaged gas density to the threshold density predicted from Toomre's instability criterion. For both of these dwarf galaxies, this ratio is everywhere smaller than the threshold ratio for star formation in spiral galaxies ($\Sigma_g/\Sigma_{crit} \sim 0.7$; Kennicutt (1989)). A similar result was obtained by van Zee et al.(1997) albeit for brighter (and more rotation dominated, $V/\sigma > 5$) dwarfs. While this low ratio of gas density to critical density is interesting, it is unclear whether the Toomre's

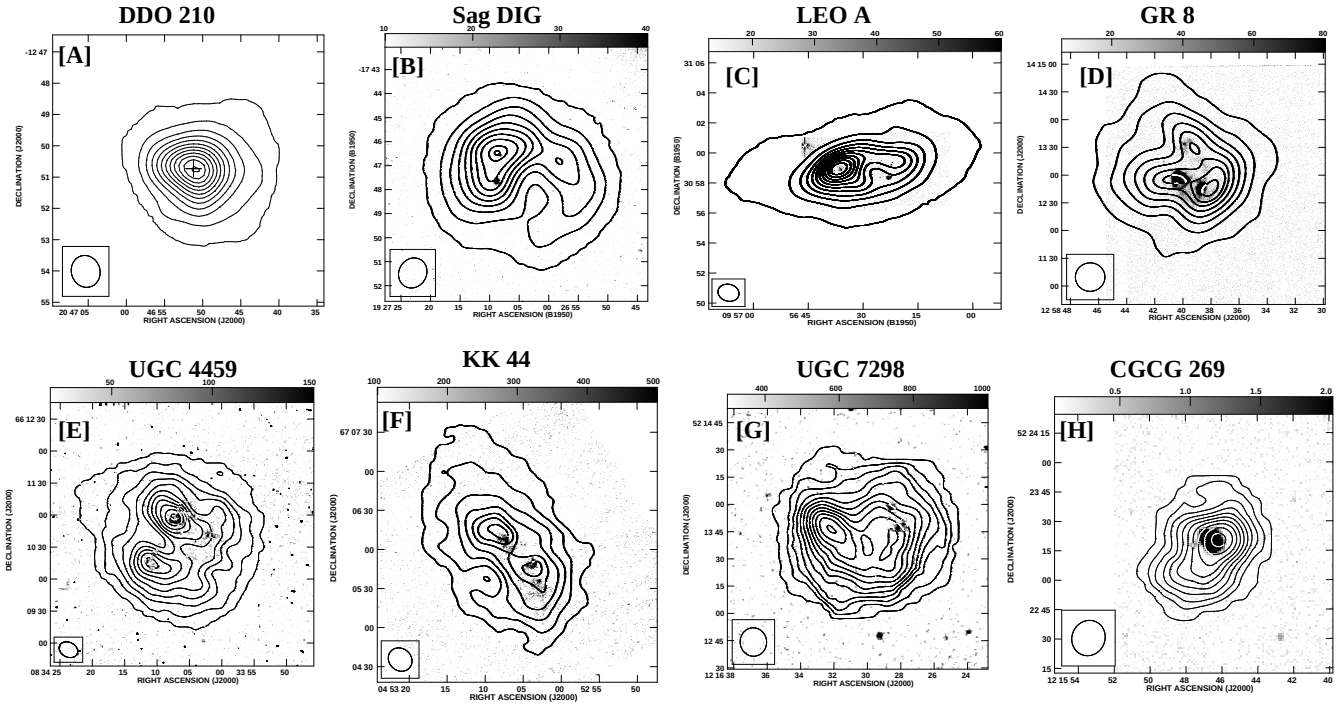

Figure 5.9: Comparison of HI integrated HI emission (contours) from the sample galaxies at a linear resolution of $\sim$ 300 pc with Hα emission (grey scales). The angular resolution of the HI images are given in Table.5.4. KK 230 and KDG 52 are not shown in the figure as no Hα was detected in these galaxies. The Hα images for UGC 7298, CGCG 269-049 and KK 44 are provided by Karachentsev. In the case of DDO 210, the only region with Hα emission [56] is show as a star; however we note that this may not be an HII region. The Hα image of UGC 4459 is kindly by U. Hopp and is previously published by Schulte-Ladbeck & Hopp (1998). Hα images of Leo A, Sag DIG and GR 8 are obtained from NED. The observations of these galaxies is described in Hunter & Elemgreen (2004). For UGC 7298, CGCG 269-049 and KK 44 the alignment of the Hα images and radio images is done by comparing the continumm+Hα images with the optical DSS images. In case of Leo A and Sag DIG in the absence of continumm images, alignment of the Hα images and radio images is done using the coordinates of the HII regions from Strobel et al.(1991), whereas for GR 8 the coordinates of the HII regions were obtained from Hodge et al. (1989)

Table 5.4: Comparison of HI and optical emission from the sample galaxies

Galaxy	M_B	Beam	Beam	N_{HI}^{Peak}	Σ_g^{peak}	Σ_{HI}^{c}(HII)	Log[SFR]	12+log($\frac{O}{H}$)	Ref
		arcsec	pc	$10^{21}cm^{-2}$	$10^{21}cm^{-2}$	$10^{21}cm^{-2}$	$M_\odot yr^{-1}$		
KK 44	−11.85	19	307	1.0	0.6	0.4	−3.44		9
Leo A	−11.36	78	262	2.1	1.4	0.8	−3.68	7.3	2,8
KDG 52	−11.49	16	275	0.6	0.8	–	> -5.1		9
UGC 4459	−13.37	18	310	3.2	3.9	1.6	−2.04	7.52	6
CGCG 269-04	−12.46	18	297	2.4	2.5	1.7	−3.08	7.43	3,9
UGC 7298	−12.27	15	306	1.5	1.9	0.8	−4.5		9
GR 8	−12.11	30	305	1.1	1.4	0.9	−2.46	7.68	4
KK 230	−9.55	33	304	0.5	0.4	–	> -5.53		9
SagDIG	−11.49	67	325	0.6	0.7	0.6	−3.56	7.42	1,7
DDO 210	−11.09	61	291	1.07	1.3	1.2	−5.42	7.4	5,8

References: 1-Hunter & Elmegreen(2004), 2-James et al.(2004), 3-Kniazev et al.(2003), 4-Legrand et al.(2001), 5-Mateo (1998), 6-Pustilnik et al.(2003), 7-Skillman et al.(1989), 8-Taylor et al.(1998), 9-Karachentsev (private communication)

instability criteria is relevant in a situation where the rotation speed is comparable to the velocity dispersion.

Fig.5.9 shows the HI column density distribution of our sample galaxies at $\sim$ 300 pc resolution, overlayed on the Hα emission from the galaxies. From the Hα overlays, one can see that if there does exist a threshold HI column density for star formation, it is only in the very loose sense that one can find an (relatively) high HI column density contour that just encloses all the star forming regions. The actual value of the column density delineating the star forming regions varies by more than a factor of 4 between the different galaxies in our sample. Further, the morphologies of the Hα emission and the high column density HI is quite dissimilar in several cases (e.g. UGC 7298, GR 8, KK 44). Thus, while high HI column density may be necessary for star formation, it clearly is not, in this sample at least, a sufficient criteria for star formation. From Table 5.4 one can also see that there is no particular correlation between the "threshold" column density and the metallicity. The metallicity of our sample galaxies is somewhat lower than that in the original sample of Skillman (1987). In that sample the galaxies, with one exception (Sextans A, with $12+\log(O/H) = 7.49$ [29]) have $12+\log(O/H)$ between $\sim$ 8 and 8.34. For the galaxies in our sample for which measurements exist, the metalicity is typically 1 dex lower, while the star

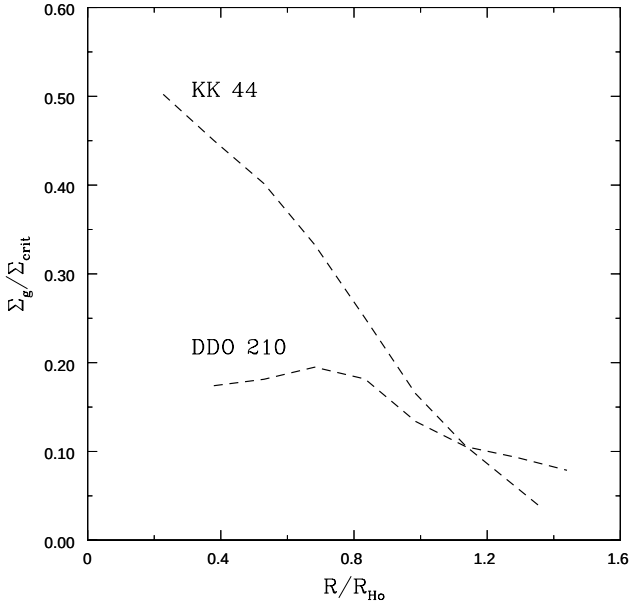

Figure 5.10: The ratio between the gas surface density and the Toomre's instability threshold density for our sample galaxies DDO 210 and KK 44, which show systematic rotation. The HI distribution used for deriving the SMD profiles are $61'' \times 56''$ (DDO 210) and $31'' \times 29''$ (KK 44).

formation "threshold" density is similar to that noted by Skillman (1987).It has also been suggested that the threshold density for star formation is related more to the presense of a cold phase; in this case, the value of this threshold does not change much with metalicity [43].

To further explore the connection between the amount of high column density gas in the galaxy and the star formation, we show in Fig. 5.11[A] and Fig. 5.11[B] the star formation rate as a function of the total HI mass as well as the star formation rate as a function of the mass of HI which has a column density greater than the "threshold" density defined in Table 5.4. The SFR rate actually correlates slightly better with the total HI mass of the galaxy (correlation coefficient ~ 0.34, excluding those galaxies where no Hα emission was detected) as compared to the mass of the gas at high HI column density (correlation coefficient ~ 0.25). Clearly, the efficiency with which gas is converted into stars in these dwarf galaxies is not a function of the amount of high column density of the gas alone. The strongest correlation between the gas distribution and indicators of current or past star formation that we find in our sample is between the peak gas density (recall that this need

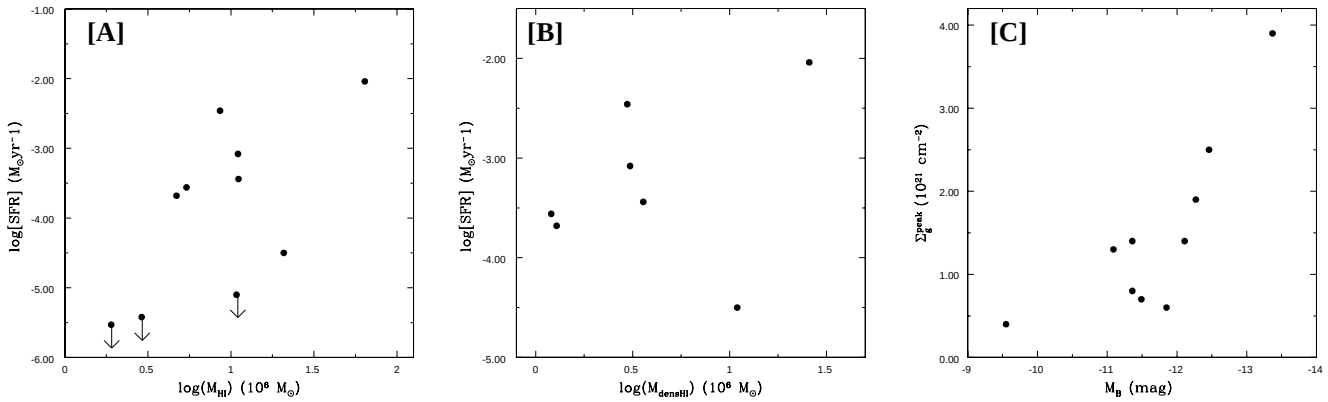

Figure 5.11: [**A**] Log of HI mass as a function of SFR for our sample galaxies. In the case of KDG 52, KK 230 and DDO 210, the limits on the SFR are shown. [**B**]HI mass of the dense gas i.e mass of HI gas which has a column density greater than the "threshold" density, defined in Table 5.4, as a function of SFR for the same sample. [**C**] The peak surface gas density as a function of absolute blue magnitude.

not occur at the center of the galaxy) and the absolute magnitude (Fig. 5.11[C]). The reason for the existence of such a correlation is unclear. The most straight forward interpretation is that bigger galaxies are more able to support high column density gas; this in turn made them, on the average, more efficient at converting their gas into stars. On the other hand, as noted above, the current star formation rate itself does not correlate particularly strongly with the local column density. One way to reconcile this would be if in such small galaxies, feedback processes rapidly destroy the correlation between the local gas column density and the local star formation rate.

If feedback from star formation is important, one might expect to see the strongest evidence for this on small scales. We hence compare the highest resolution HI images of our sample galaxies with the sites of active star formation i.e. Hα emission. Our highest resolution images have beam sizes $\sim 3'' - 4''$, which corresponds to linear scales between 19 pc and 100 pc for our sample galaxies. At this high resolution, the emission could not be CLEANed; moment maps were instead made from the dirty cubes (see Sect.2.6). As discussed earlier in Sect.2.6, this leads to a scaling uncertainity, which means that we cannot translate the observed flux distributions into corresponding HI column densities. We can however, still use our maps to search for correspondences between the morphologies of the Hα and the high column density HI. The overlays are shown in Fig. 5.12; for all the galaxies in our sample, the HI emission shows substantial fine scale structure, with shell like, filamentary as well as discrete clump like morphologies being visible. The few other dwarf

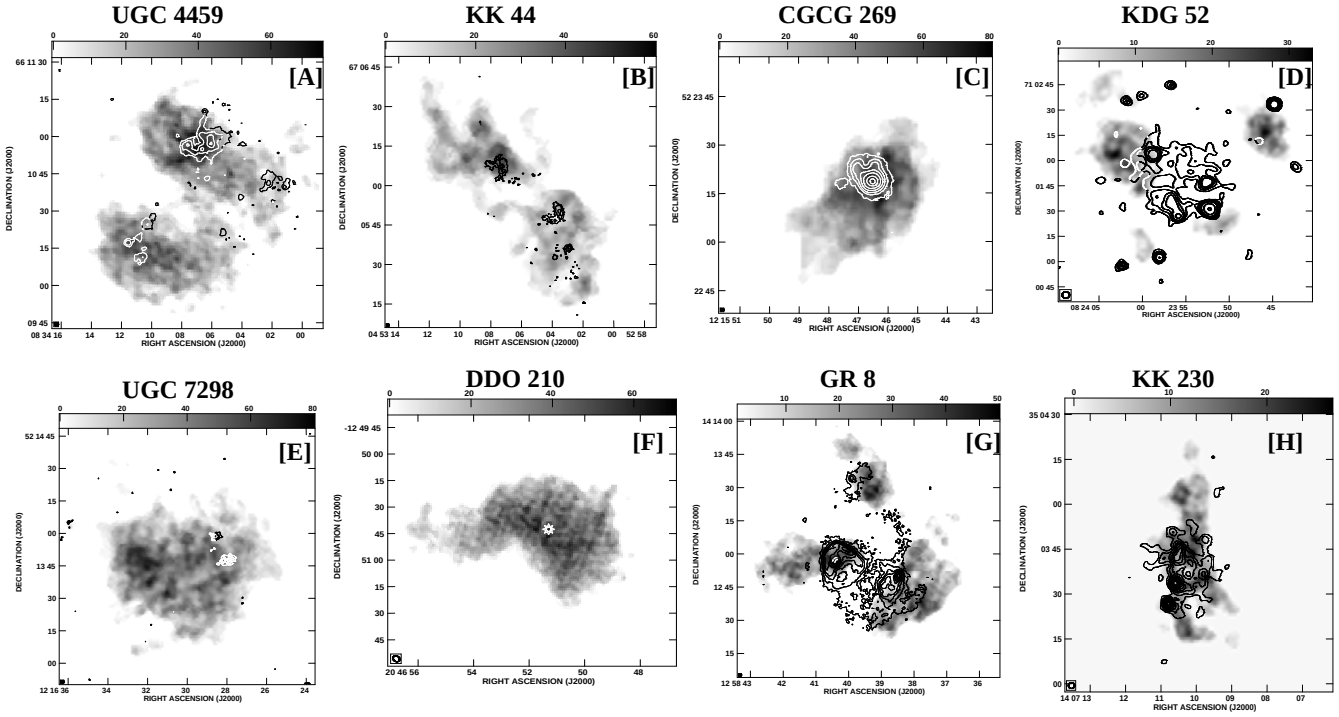

Figure 5.12: The GMRT integrated high resolution HI images of our sample galaxies (greyscales) overlayed on Hα images (contours). In case of KK 230 and KDG 52, as no Hα emission was detected, contours represent the optical broad band emission. The angular resolutions of the GMRT HI images are $3'' \times 3''$ (UGC 4459), $4'' \times 4''$ (KK 44), $4'' \times 3''$ (CCG 269-049), $6'' \times 6''$ (KDG 52), $4'' \times 4''$ (UGC 7298), $4'' \times 3''$ (DDO 210), $4'' \times 3''$ (GR 8) and $4'' \times 3''$ (KK 230). Th region of Hα emission found in DDO 210 [56] is show as a star.

galaxies that have been imaged at similar linear scales (e.g. IC10 [23] (20 pc), SMC [48] (28 pc), LMC [30] (15 pc)) also show a similar wealth of small scale structure. At these scales, the Hα emission is sometimes seen coincident with high HI column densities (e.g. the northern star forming region in UGC 4459, north-eastern region in KK 44, the Hα knot in CGC 269-049), sometimes the high HI column density gas forms a shell around the Hα emission (e.g. the south-western star forming region in KK 44, the high density HI clumps in GR 8) and sometimes there seems to be no connection at all between the high density HI gas and the Hα emission (e.g. UGC 7298). While high HI column density gas is in general present in the vicinity (as measured on linear scales < 100 pc) of current star formation, there does not seem to be a simple, universal relationship between the Hα emitting gas and the high column density neutral gas.

5.4.3 HI line profiles and star formation

Young and collaborators have found that in faint dwarfs, HI line profiles in regions of active star formation differ substantially from a simple gaussian shape (Leo A [66], Sag DIG [65], UGCA 292 [64]). Young et al.(2003) used both a two gaussian fit as well as a fit using Gauss-Hermite polynomials to parametrize the line profiles. To facilitate easy comparison, we fit the line profiles to our sample galaxies using the same two models. Apart from Leo A and Sag DIG (where we use essentially the same VLA data as used by Young et al.) our sample has two galaxies (viz. DDO 210 and GR 8) in common with the earlier sample. We include these two galaxies in the analysis that we do in this section, and compare the results obtained from the GMRT data with those obtained earlier with the VLA.

Ideally one would like to fit profiles to data cubes which correspond to the same linear resolution at the distance to the galaxy. However fitting to the line profile requires a good signal-to-noise ratio, and for the fainter galaxies, the signal to noise ratio is adequate only in the lowest resolution images. The linear resolution of the data cubes used for profile fitting is given in Table. 5.5. For all the sample galaxies, the line profiles at each location were first fitted with a single gaussian component and the residuals were inspected. HI profiles in some cases were found to deviate measurably from a simple gaussian − in such cases the profiles were often either asymmetric or symmetric but with narrower peak and broader wings than a gaussian.

The profiles were then fitted with a double gaussian and also separately with a gauss hermite polynomial. The gauss hermite polynomial used for the profile fitting is given as:

$$\phi(x) = ae^{\frac{-1}{2}y^2}[1 + \frac{h_3}{\sqrt{6}}(2\sqrt{2}y^3 - 3\sqrt{2}y) + \frac{h_4}{\sqrt{24}}(4y^4 - 12y^2 + 3)] \tag{5.3}$$

where y= $\frac{(x-b)}{c}$. Parameters a, b, c are equal to the amplitude, mean and dispersion respectively for a gaussian, (to which the Eqn.(5.3) reduces to, when parameters h_3 and h_4 are zero). Parameter h_3 is related to the skewness of the line profile i.e. in the case of an asymmetric line profile $h_3 \neq 0$. If $h_4 \neq 0$, the line profiles either have a more pointed top with broader wings ($h_4 > 0$) or have a flatter top ($h_4 < 0$) than a gaussian.

In the case of gauss hermite fits, the profiles for which both h_3 and h_4 parameters were less than 3 times the uncertainty in these parameters, were rejected as bad fits. Similarly, in the case of double gaussian fit, the profiles for which the width of the fitted narrow component was less than the velocity resolution of 1.65 km s^{-1}(within the errorbars) were rejected. Following Young & Lo (1996), we use the f-test to distinguish between profiles that are adequately fit by a single gaussian and those which are not. Locations where the

Table 5.5: Results of the profile fitting to our sample galaxies

Galaxy	Beam (arcsec)	Linear resolution (pc)	Σ^{c}_{gas} 10^{21} cm^{-2}	gauss hermite fit	Narrow comp km s^{-1}	Broad comp km s^{-1}
KK 44	40	647	–	–	–	–
KDG 52	42	723	0.2	$h_3 = 0$ $h_4 > 0$	2.0−4.5	8−14
UGC 4459 (A)	26	450	1.0	$h_3 < 0$ $h_4 = 0$	3.5−7.0	6−17
UGC 4459 (B)	26	450	2.0	$h_3 = 0$ $h_4 > 0$	6.0	10−17
UGC 4459 (C)	26	450	1.0	$h_3 = 0$ $h_4 > 0$	4.5−6.0	10−16
CGCG 269-049	42	692	0.4	$h_3 < 0$ $h_4 = 0$	2−5	7−13
UGC 7298	26	529	1.0	$h_3 = 0$ $h_4 > 0$	2.5−4	9.5−11
GR 8 (A)	30	305	0.7	$h_3 < 0$ $h_4 > 0$	2−6	7−13
GR 8 (B)	30	305	0.9	$h_3 = 0$ $h_4 > 0$	2−3	8−9.5
KK 230	48	489	–	–	–	–
DDO 210	60	291	0.4	$h_3 = 0$ $h_4 > 0$	3−6	8−14

null hypothesis (viz. that a single gaussian provides an equally good description of the line profile as compared to a double gaussian or gauss hermite polynomial) was rejected at the 90% or higher confidence level were compared with the locations of on-going star formation.

The results of the line profile fitting are given in Table 5.5. Col(1) gives the galaxy name, Col(2) gives the resolution of the HI distribution used for the profile fitting, Col(3) the liner resolution in pc, Col(4) the minimum gas surface density (the observed HI column density corrected for inclination and He content) enclosing the regions with non gaussian HI profiles, Col(5) h_3 and h_4 parameters of the best fit gauss hermite polynomial, Col(6) range of the velocity dispersion of the narrow component in the double gauss fit and Col(7) range of the velocity dispersion of the broad component in the double gauss fit. In case of UGC 4459 and GR 8, results of the line profile fitting from separate regions (as marked in the Fig. 5.13), are described separately in the Table 5.5. For KDG 52, the two separate regions showing deviation from the gaussian, near the eastern and western clump, gave similar results.

The regions in our sample galaxies where the double gaussian gave a better fit to the line profiles than a single gaussian are marked as crosses on the HI column density distribution in Fig. 5.13. The regions where the gauss hermite polynomial gave a better fit than the single gaussian are almost similar to the regions where the double gaussian gave a good fit, hence are not shown separately. We note that for most galaxies (with the exception of

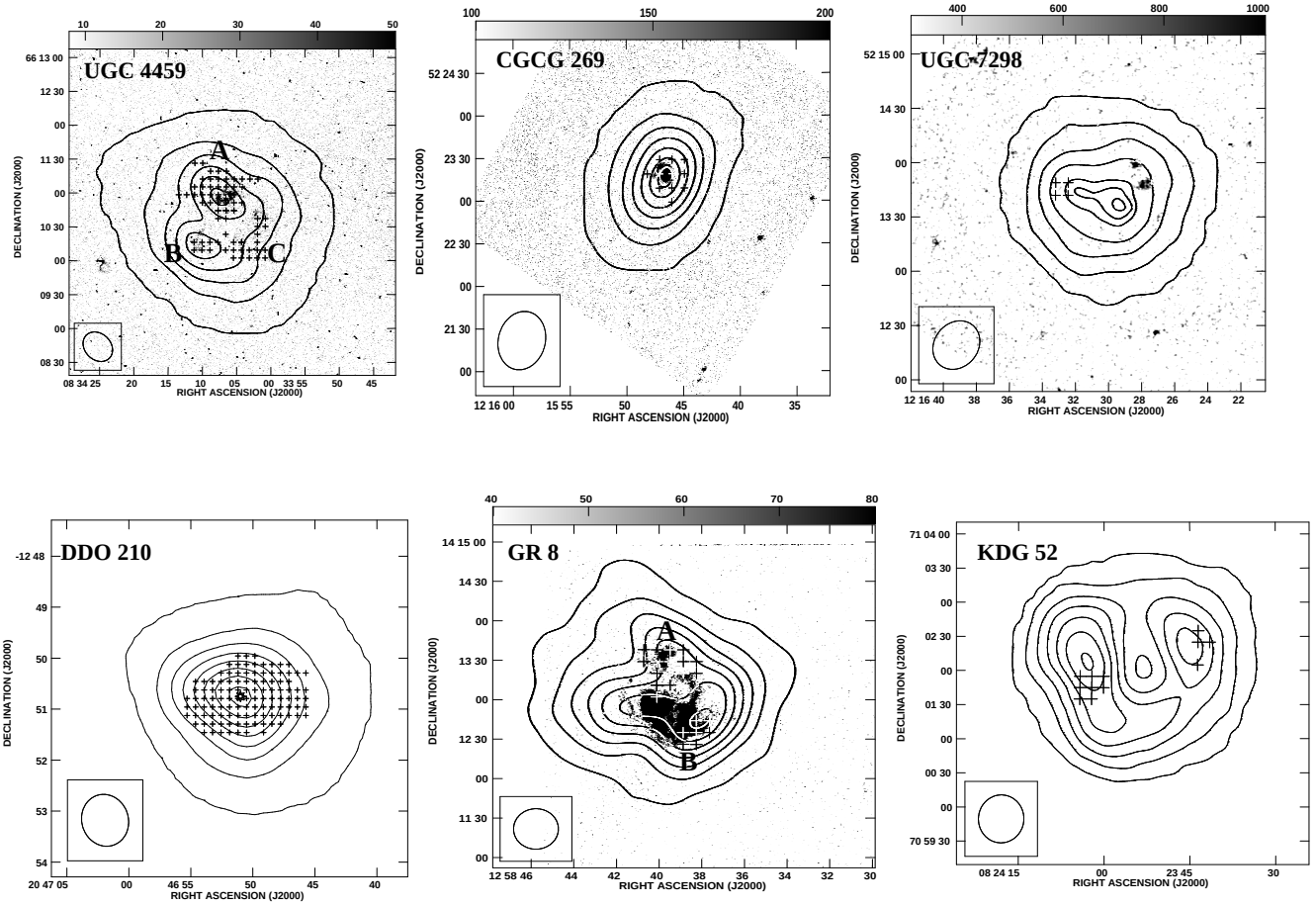

Figure 5.13: GMRT integrated HI column density distribution overlayed for our sample galaxies showing the deviation from the single gaussian line profiles. The regions where the line profile deviated from the single gaussian are marked as crosses. In the case of DDO 210, the HII region the galaxy is marked as stars, whereas for other galaxies the Hα emission is shown overlayed (greyscale). In case of KDG 52, no Hα emission was detected in the galaxy. The resolution of the HI distribution are $29'' \times 27''$ (UGC 4459), $42'' \times 39''$ (CGCG 269-049), $28'' \times 24''$ (UGC 7298), $60'' \times 58''$ (DDO 210), $30'' \times 30''$ (GR 8) and $42'' \times 39''$ (KDG 52).

DDO 210) the extent of these regions is comparable to our spatial resolution. To allow easy cross comparison with regions having on-going star formation, the the Hα emitting regions are shown as contours in Fig. 5.13. The line profiles for KK 44 and KK 230 throughout the galaxy are found to be well described by a single gaussian component, hence are not shown in the Fig. 5.13.

As seen in the Fig. 5.13, no particular correlation is seen between the location of Hα emission and the deviation of HI line profiles from single gaussians. Not all star forming regions in our sample galaxies show deviation of the line profiles e.g. UGC 7298, KK 44 and eastern clump in GR 8. Conversely, not all regions which show deviations of line profiles are associated with the star forming regions e.g. KDG 52, DDO 210 and UGC 7298. In this sample at least, the correlation found by Young et al.(2003) from their analysis of 3 dwarf irregular galaxies does not seem to hold. We also do not find any correlation between the presence of asymmetric profiles and the global star formation activity.

The dwarf galaxies DDO 210 and GR 8 are common between our sample and that of Young et al.(2003). The results derived by Young et al.(2003) for DDO 210 are similar to our results. On the other hand, for GR 8, Young et al.(2003) found few line profiles with $h_3 \neq 0$ in the southern clump, (albeit with a very small magnitude of h_3), and almost none in the eastern clump, while we found all the profiles associated with the southern and eastern clump have $h_3 = 0$, (within the 3σ uncertainty of the parameter). However, this difference is not pronounced, and one should also note that Young et al.(2003) used $14'' \times 14''$ and $18'' \times 18''$ resolution data cubes, whereas we have used a $30'' \times 30''$ resolution data cube. In general hence, there is relatively good agreement between the fits obtained with the GMRT and VLA data.

5.5 Summary

In this chapter of the thesis we compared the HI distribution, kinematics and current star formation in a sample of 10 extremely faint nearby dwarf galaxies. For 5 of these galaxies, fresh GMRT HI data were presented in this chapter. We found that the large scale gas distribution in the galaxies is generally clumpy, and the peak HI column density is often well removed from the geometric center. For all galaxies we found a large scale ordered velocity field, although the patterns are mostly not reconcilable with that expected from a rotating disk. From a simplistic virial theorem based estimate of the dynamical mass, we found very tentative evidence that the faintest dwarf irregulars have a somewhat smaller baryon fraction than brighter galaxies. We compared the regions of ongoing star formation with regions of high HI column density, with the column density being measured at a uniform

linear scale ($\sim$ 300 pc) for all galaxies in our sample. We found that while the Hα emission is confined to regions with relatively high column density, in general the morphology of the Hα emission is not correlated with that of the high column density HI gas. Thus, while high gas column density may be a necessary condition for star formation, it is not, in this sample atleast, a sufficient condition. We also examined the line profiles of the HI emission, and checked if deviations from a simple Gaussian profile is correlated with star formation activity. We did not find any such correlation in our sample – there are regions with ongoing star formation but with simple Gaussian line profiles, as well as regions with complex line profiles but no ongoing star formation. Finally, we looked at the distribution of HI gas at linear scales $\sim 20 - 100$ pc. All our sample galaxies show substantial small scale structures with shell like, filamentary as well as clumpy features being identifiable in the images. Hα emitting regions are sometimes associated with clumpy features; sometimes the Hα emission lies inside a shell like feature in the HI, and sometimes there is no particular HI column density enhancement seen ear the Hα emission. The interplay between star formation and gas density and kinematics in these galaxies hence appears to be very varied, and the general unifying patterns seen in larger irregulars and spiral galaxies seem to be absent. Star formation and feedback are complex processes, and perhaps it is the presence of simple large scale correlations in big galaxies that should surprise us more than the absence of such correlations in small galaxies.

Bibliography

[1] Bell E. F., & de Jong, R. S., 2001, ApJ 550, 212.

[2] Braine, J. Duc, P. A., Lisenfeld, U., Charmandaris, V., Vallejo, O., Leon, S. & Brinks, E., 2002, Ap&SS, 281, 407

[3] Bureau, M., Walter, F., van Gorkhom, J. & Carignan, C., 2004, IAUS, Vol 217, 452

[4] Bureau, M. & Carignan, C., 2002, AJ, 123, 1316

[5] Côté, S., Carignan, C. & Freeman, K. C. 2000, Ap.J, 120, 3027

[6] Dekel, A. and Silk, J. 1986, ApJ, 303, 39

[7] de Vaucouleurs, G. & Moss, C., 1983, ApJ, 271, 123

[8] Dohm-Palmer, R.C., Skillman, E.D., Gallagher, J. et al. 1998, Ap.J., 116,1227

[9] Efstathiou, G. 2000, MNRAS, 317, 697

[10] Ferrara, A. & Tolstoy, E., 2000, MNRAS, 313, 291

[11] Grebel E. K., 2004, Carnegie Observatories Centennial Symposia, 237.

[12] Grebel, E. K., 2005, AIP Conference Proceedings, 752, 161

[13] Gnedin, O.Y. & Zhao, H., 2002, MNRAS, 333, 299

[14] Gunn, J. E. & Gott, J. R. III, 1972, ApJ, 176, 1

[15] Hodge, P., Lee, M.G. & Kennicutt, R. 1989, PASP, 101, 640

[16] Hoffman, G.L., Salpeter, E.E., Farhat, B., Roos, T., Williams, H. & Helou, G, 1996, ApJS, 105, 269

[17] Hunter D. A. & Wilcots E. M., 2002, AJ, 123, 2449

[18] Hunter, D. A. & Elmegreen, B. G., 2004, AJ, 128, 2170

[19] James et al., 2004, A&A, 414, 23

[20] Karachentsev, I. D., Karachentseva, V.E., Huchtmeier, W.K. & Makarov, D.I., 2004, AJ, 127, 2031

[21] Karachentsev, I. D. et al., 2003, A&A, 398, 467

[22] Karachentsev, I. D. et al., 2002, A&A, 383, 125

[23] Karachentsev, I. D., Tikhonov, N. A. & Sazonova, L. N., 1994, A&AS, 106, 555

[24] Karachentseva, V. E. & Sharina M.E. 1988, Communic. of SAO, 57, 5

[25] Karachentseva, V. E., 1968, Soobshch.Byurakan Obs., 39, 62

[26] Kennicutt, R. C., 1989, ApJ, 344, 685

[27] Kennicutt R. C., 1998, ApJ, 498, 541

[28] Kniazev, A. Y., Grebel, V. K., Hao, L., Strauss, M. A., Brinkmann, J. & Fukugita, M., 2003, ApJ, 593, L73

[29] Kunth, D. & Östlin, G., 2000, A&AR, 10,1

[30] Kim, S., Staveley-Smith, L., Dopita, M. A., Sault, R. J., Freeman, K. C., Lee, Y., & Chu, Y., ApJS, 148, 473

[31] Koribalski B., Gordon S., Jones K., 2003, MNRAS, 339, 1203

[32] Lee, M. G.& Kim, S. C., 2000, AJ, 119, 777

[33] Lee, M. G., Aparicio, A., Tikonov, N., Byun, Y. & Kim, E., 1999, AJ, 118, 853.

[34] Legrand, F, Tenorio-Tangle, G., Silich, S., Kunth, D. & Cervino, M., 2001, ApJ, 560,630

[35] Lo, K. Y., Sargent, W. L. W. & Young, K. 1993, Ap.J., 106,507

[36] Lo, K. Y. & Sargent, W. L. W., 1979, ApJ, 227,756

[37] Majewski S.R., Skrutskie M.F., Weinberg M.D., Ostheimer J.C., 2003, ApJ, 599, 1082

[38] Makarova, L., 1999, A&AS, 139, 491

[39] Mateo, M., 1998, ARA&A, 36, 435

[40] Puche, D. & Westpfahl, D., 1994, Proceedings of an ESO/OHP Workshop on Dwarf galaxies, edited by Georges Meylan and Phillippe Prugniel., p.273

[41] Pustilnik, S., Zasov, A., Kniazev, A., Pramskij, A., Ugryumov, A. & Burenkov, A., 2003, A&A, 400, 841

[42] Sargent, W. L. W., Sancisi, R. & Lo, K. Y., 1983, ApJ, 265, 711

[43] Schaye J., 2004, ApJ, 609, 667

[44] Schulte-Ladbeck, R. E. & Hopp, U., 1998, AJ, 116, 2886

[45] Simpson, C. E., Hunter, D. A. & Knezek, P. M., 2005, AJ, 129, 160

[46] Skillman, E. D., Kennicutt, R. C. & Hodge, P. W., 1989, ApJ, 347, 875

[47] Skillman, E. D., 1987, in Star Formation in Galaxies, edited by C. J. Lonsdale Persson, NASA, 263

[48] Staveley-Smith, L., Sault, R. J., Hatzidimitriou, D., Kesteven, M. J. & McConnell, D.,1997, MNRAS, 289, 225

[49] Strobel, N. V., Hodge, P. & Kennicutt JR, R. C., 1991, ApJ, 383, 148.

[50] Swaters, R. 1999, Ph.D. thesis, Rijksuniversiteit Groningen.

[51] Tolstoy et al. 1998, AJ, 116, 1244

[52] Taylor, C. L., Kobulnicky, H. A. & Skillman, E. D., 1998, AJ, 116, 2746

[53] Taylor, C. L., 1997, ApJ, 480, 524

[54] Tikhonov, N.A. & Karachentsev, I.D., 1998, A&AS, 128, 325

[55] Toomre, A. 1964, ApJ, 197, 551

[56] van Zee, L. 2000, AJ, 119, 2757

[57] van Zee, L., Skillman, E. D. & Salzer, J. J., 1998, AJ, 116, 1186

[58] van Zee, L., Haynes, M. P., Salzer, J. J. & Broeils, A. H., 1997, AJ, 113 1618

[59] Verheijen, M.A.W. 2001, ApJ, 563, 694

[60] Walter, F. & Brinks, E., 2001, AJ, 121, 3026

[61] Westmeier T., Braun R. & Thilker D., 2005, A&A, 436, 101

[62] Westpfahl, D., Coleman, P. H., Alexander, J. & Tongue, T., 1999, AJ, 117, 868

[63] Wilcots, E. M. & Miller, 1998, AJ, 116, 2363

[64] Young, L., van Zee, L., Lo, K., Dohm-Palmer, R. & Beierle, M., 2003,ApJ,592,111

[65] Young, L. M. & Lo, K. Y., 1997, ApJ, 490, 710

[66] Young, L. M. & Lo, K. Y., 1996, ApJ, 462, 203

Chapter 6

NGC 3741 – A dwarf galaxy with a giant HI disk

6.1 Introduction

Numerical simulations of hierarchical galaxy formation predict that galaxies should have dark halos with virial radius $\sim 8-10$ times the size of the stellar disk and a total mass of $\sim 50-70$ times the stellar mass. Since the HI disks of galaxies typically extend to only ~ 2 times the optical radius, one cannot test these model predictions using HI rotation curves. The mass distribution on such large scales can however be probed using weak lensing or the kinematics of faint satellite galaxies. Though neither of these techniques can be applied to individual galaxies, when applied to a large sample of galaxies, they do provide at least qualitative confirmation (for L_* galaxies) of the models (e.g. [2]).

While, dark matter halos are expected to be self similar [13], there are no direct determinations of the typical virial size and mass of dwarf galaxy halos. For small galaxies, both weak lensing as well as the kinematics of still fainter companions are correspondingly difficult to measure. Further, the rotation curves for most of the faint dwarf irregulars are typically rising even at the last measured point, implying that one has been unable to probe beyond the core of the dark halo, leave alone its virial radius. There are however a few dwarf galaxies known with unusually extended HI disks (e.g. DDO154 [3], NGC 2915 [10], ES0215-G?009 [22]), where the HI extends to more than 5 times the Holmberg radius (R_{Ho}). The extended HI gas in such galaxies traces the dark matter potential upto large galacto-centric radii and hence provide a unique opportunity to measure the larger scale mass distribution around dwarf galaxies.

We discuss in this chapter GMRT HI observations of one such galaxy with an extended HI disk, viz. NGC 3741. Our GMRT observations show that this galaxy has a regular HI

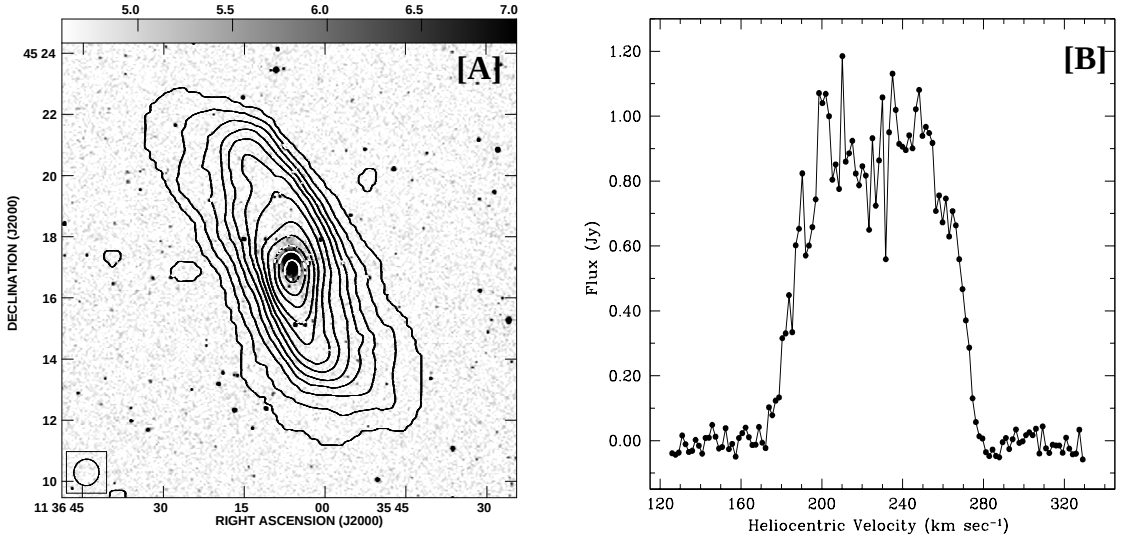

Figure 6.1: [**A**]The B band optical image of NGC 3741 (greyscales) with the GMRT $52'' \times 49''$ resolution integrated HI emission map (contours) overlayed. The contour levels are 0.1, 1.3, 2.6, 3.8, 5.0, 6.5, 7.8, 9.6, 11.3, 14.4, 17.0, 20.5 $\times 10^{20}$ atoms cm^{-2}. [**B**] The global HI profile fo NGC 3741 obtained from $52'' \times 49''$ resolution data cube. The channel separation is 1.65 km s^{-1}. Integration of the profile gives a flux integral of 74.7 ± 7.5 Jy km s^{-1}and an HI mass of $1.6 \pm 0.4 \times 10^8 M_\odot$

disk that extends out to ~ 8.3 times R_{Ho}. Like other known galaxies with unusually extended disks, NGC 3741 is also located in the vicinity of the local group.

6.2 Results

6.2.1 HI distribution and kinematics

The observations and data analysis for NGC 3741 are presented in chapter. 2. Fig. 6.1[A] shows the integrated HI emission from NGC 3741 (at $52'' \times 49''$ resolution), overlayed on the digitised sky survey image. As can be seen, the HI distribution of NGC 3741 is regular and extends to $\sim 13.8'$ in diameter, at a level of $\sim 1 \times 10^{19}$ cm^{-2} ($\sim 13.4'$ in diameter, at a level of $\sim 5 \times 10^{19}$ cm^{-2}). The Holmberg diameter of NGC 3741 measured from the B band surface brightness profile is $\sim 100''$ [1] – the HI disk is hence ~ 8.3 times the Holmberg diameter. The HI distribution has a central bar, more clearly seen in the higher resolution maps (not shown), which is approximately coincident with the optical emission. Fig. 6.1[B] shows the

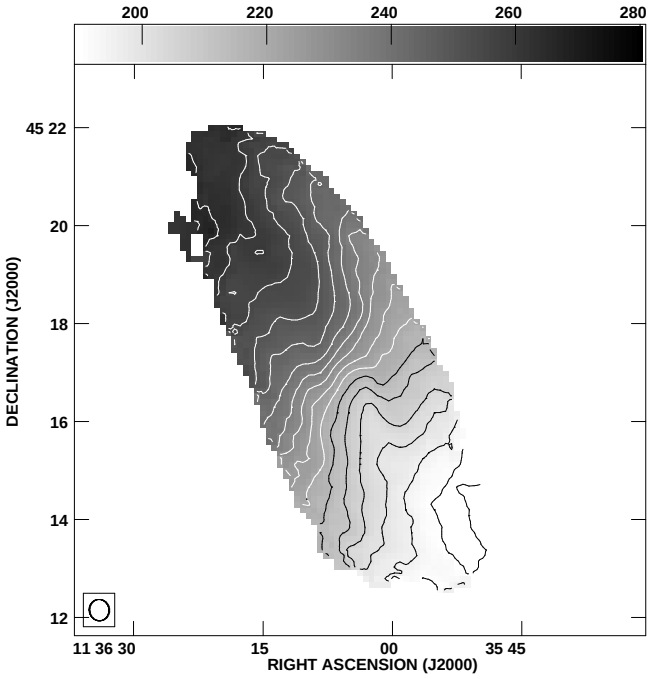

Figure 6.2: The HI velocity field of NGC 3741 at $26'' \times 24''$ resolution. The contours are in the steps of 5 km s^{-1}and range from 185.0 km s^{-1}to 265.0 km s^{-1}.

global HI profile of NGC 3741, obtained from $52'' \times 49''$ resolution data cube. The integrated flux estimated from the HI emission profile is 74.7 ± 7.5 Jy km s^{-1}(corresponding to an HI mass of $1.6 \pm 0.4 \times 10^8 M_\odot$). The HI flux measured at GMRT is more than the single dish flux (53.0 Jy km s^{-1} [15]). The single dish observations, done with the Greenbank 300ft telescope with a single pointing centered on the optical galaxy, would have underestimated the total flux of the galaxy, as the extent of the HI disk of the galaxy is bigger than the beam size of the telescope. The flux integral estimated from our GMRT observations is also likely to be a lower limit on the total HI flux of the galaxy as the GMRT is well known to resolve out flux for galaxies that are this extended (e.g. [11]). Our flux measurement hence places a lower limit on the M_{HI}/L_B ratio of $=5.8 \pm 1.4$.

The velocity field of NGC 3741 (at $26'' \times 24''$ resolution) is shown in Fig. 6.2. The velocity field is regular, with a warp being seen in the outer regions of the galaxy, as well as distortions in the central region, which correlate with the central bar. The central distortions of the isovelocity contours are more prominent in the higher resolution velocity fields.

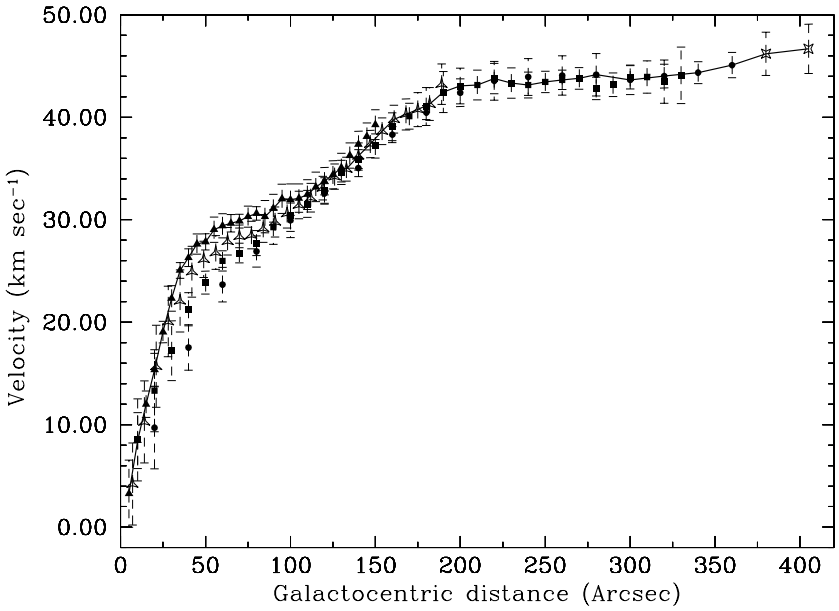

Figure 6.3: The rotation curve for NGC 3741 derived from the intensity weighted velocity field at $52'' \times 49''$, $42'' \times 38''$, $26'' \times 24''$, $19'' \times 15''$ and $13'' \times 11''$ resolution shown as stars, circles, squares, open triangles and filled triangles respectively.

Fig.6.3 shows the rotation curves for NGC 3741 derived from the various resolution velocity fields using the tilted ring model. The kinematical inclination of the galaxy was found to vary from $\sim 58^\circ$ to 70° across the galaxy, whereas the kinematical position angle varied from $\sim 33^\circ$ to 47°. The final adopted rotation curve (solid line) is measured upto ~ 38 disk scale lengths (the B band scale length is $10.75''$ [1]). The rotation curve shows a flattening beyond $\sim 200''$; NGC 3741 is one of the faintest known dwarf galaxies to show a clear flattening of the rotation curve. A steep rise in the rotation velocities within the Holmberg radius is probably related to the bar at the center of the galaxy. The rotation curve was also derived (at each spatial resolution) independently for the approaching and the receding side of the galaxy. These curves match within the errorbars. Correction for the "asymmetric drift" was also done and was found to be small compared to the errorbars at all radii.

Modified isothermal and NFW mass models were fit to derived rotation curve. Fig. 6.4[A] shows the best fit modified isothermal halo model, which has a mass to light ratio (Γ_B) for the stellar disk (which was assumed to be an exponential disk with intrinsic thickness ratio of 0.25) of 0.9 ± 0.1, a halo with core radius $r_c = 0.7 \pm 0.1$ kpc and core density $\rho_0 =$

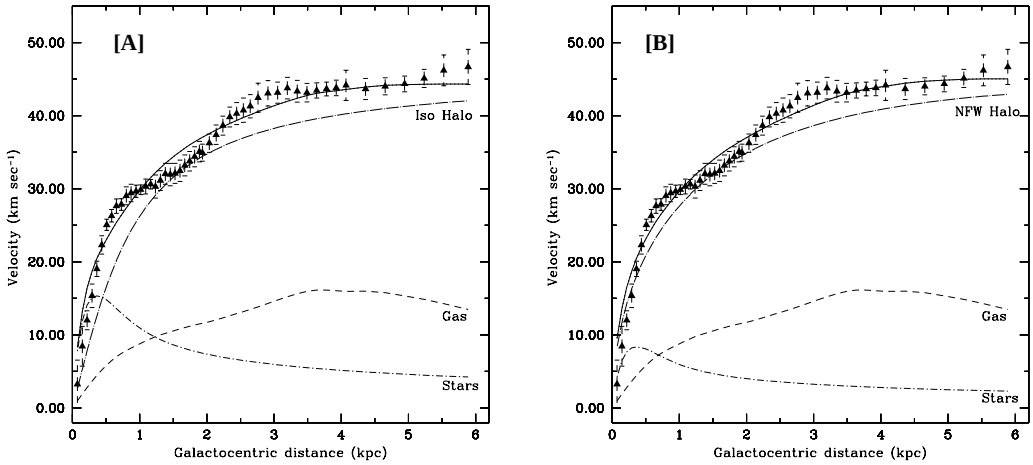

Figure 6.4: [**A**] Mass models for NGC 3741. The points are the observed data. The total mass of gaseous disk (dashed line) is $2.0 \times 10^8 M_\odot$.The stellar disk (short dash dot line) has $\Gamma_B = 0.9 \pm 0.1$, giving a stellar mass of $2.5 \times 10^7 M_\odot$. The best fit total rotation curve for the constant density halo model is shown as a solid line, while the contribution of the halo itself is shown as a long dash dot line (the halo density is density $\rho_0 = 77.9 \pm 8.9 \times 10^{-3} M_\odot$ pc^{-3} and core radius $r_c 0.7 \pm 0.1$). [**B**]The best fit mass model for an NFW type halo (solid line). The best fit halo parameters are $\Gamma_B = 0.3 \pm 0.1$, c=11.4±0.8 and v_{200}=35.0 km s^{-1}.

$77.9 \pm 8.9 \times 10^{-3} M_\odot$ pc^{-3}. The best fit NFW mass model (shown in Fig. 6.4[B]) gives Γ_B of 0.3±0.1, a concentration parameter c=11.4±0.8 and $V_{200} = 35.3 \pm 1.4$ km s^{-1}. Both type of dark halos provide a comparable fit to the derived rotation curve. The bar linked central distortion of the velocity field is a major contributor to our inability to distinguish between these two models. From the best fit NFW model, we find that the observed rotation curve for NGC 3741 is expected to fall at a radius of $\sim 2.16 \times r_{200}/c$ i.e. 10 kpc, which is well beyond the last measured point of the derived rotation curve.

6.3 Discussion

NGC 3741 probably has the most extended HI disk known. In comparison, VLA observations of DDO154, (the commonly cited example of the largest known HI disk), detected HI up to $\sim$ 5 times R_{Ho} [3]; the follow-up Arecibo observations detected HI upto $\sim$ 8.5 times R_{Ho} [7], although these last observations do not lead to a good quality rotation curve. Most other galaxies with extended HI envelopes show severe tidal distortions, e.g. IC 10 [23].

The total dynamical mass of NGC 3741 (at the last measured point of the rotation curve)

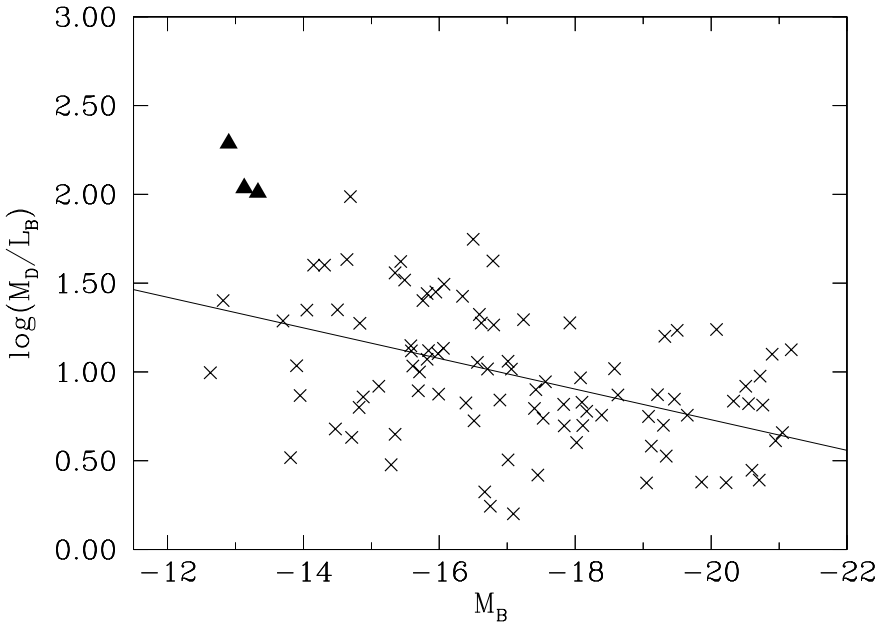

Figure 6.5: M_D/L_B as a function of M_B for a sample of galaxies with HI rotation curves from Verheijen(2001), Swaters (1999) and Cote et al. (2000). Galaxies with very extended HI disks viz. NGC 3741, DDO 154 and ESO 215-G?009 are marked as triangles. The solid line shows the best fit relation.

is $3.0\pm0.4 \times 10^9 M_\odot$, i.e. the dynamical mass to light ratio is $M_D/L_B = 107\pm16.4$; NGC 3741 is hence one of the "darkest" irregular galaxies known. A fundamental question which arises is whether NGC 3741's dark halo is the same as those of similar dwarf galaxies with less extended disks, i.e. is the extended HI just a fortuitous tracer of the gravitational potential, or does the presence of such an extended disk mean that we are dealing with a different (e.g. more massive than typical) halo? Equivalently, should we regard NGC 3741 as a 13th magnitude dwarf which somehow acquired a lot of gas, or should we regard it as a galaxy that should "rightly" have been much brighter, but for some reason it failed to convert its gas into stars? Indeed, why do some galaxies have such extended HI disks?

We start by trying to address the first set of questions, viz. regarding the nature of the dark halo of NGC 3741 as compared to those of "similar" galaxies. Fig. 6.5 shows the dynamical mass to light ratio M_D/L_B (at the last measured point of the rotation curve), as function of the absolute blue magnitude (M_B), for a sample of galaxies with measured HI rotation curves. Galaxies with the most extended HI disks viz. NGC 3741, DDO 154

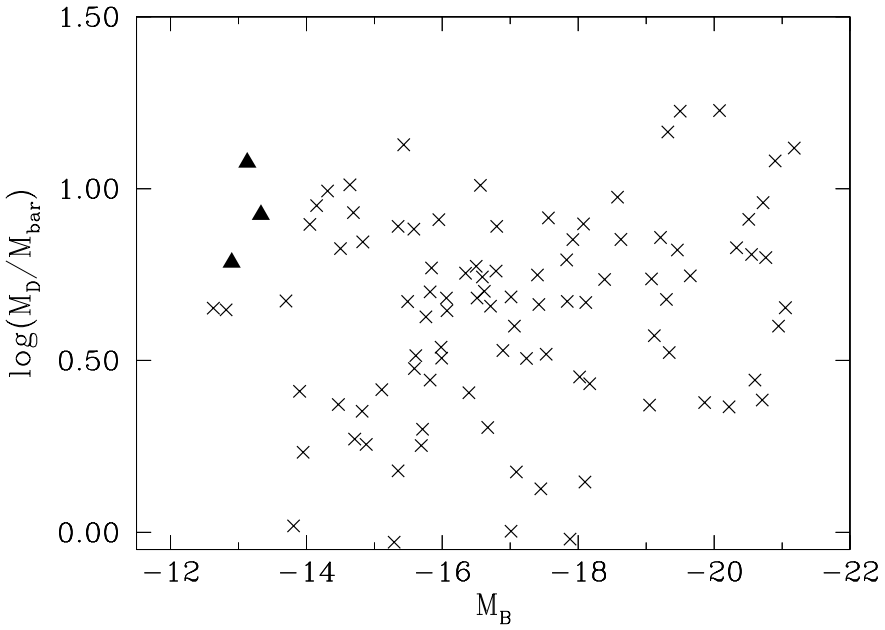

Figure 6.6: M_D/M_{bar} as a function of M_B for the same sample of galaxies as in Fig. 6.5.

and ESO 215-G?009 * are marked with triangles. As can be seen, the well known (albeit weak and noisy) trend of increasing dynamical mass to light ratio with decreasing galaxy luminosity is recovered, and in addition, dwarfs with an extended HI disks can be seen to have fairly extreme mass to light ratios. However, given that for galaxies with extended HI disks the total baryonic mass is dominated by the HI mass, instead of comparing M_D/L_B it might be more fair to compare dynamical to baryonic mass ratio (M_D/M_{bar}), where M_{bar} is the baryonic mass. We define $M_{bar}=M_{gas}+M_*$, and assume a stellar mass to light ratio, $\Gamma_B=1.0$ for all galaxies in the sample. M_{gas} is defined as $1.4\times M_{HI}$.

Fig. 6.6 shows M_D/M_{bar} as a function of M_B for the sample galaxies. As can be seen, M_D/M_{bar} does not show any correlation with M_B, i.e. (proviso the naiveness of our baryonic mass calculation). Even though dwarf irregular galaxies tend to have a higher total mass to luminosity ratio, they have dynamical to baryonic mass ratios that are similar to those of L_* galaxies. Further the dynamical mass to baryonic mass ratio for galaxies with extended HI disks, though large, lies within the range of what is observed for other galaxies in the sample. In particular, given its dynamical mass, NGC 3741 does not have an anomalously small fraction of baryons. The other interesting feature in Fig. 6.6 is the uniformly large

*ESO 215-G?009 has a very uncertain M_D/L_B. In this thesis we use the nominal value suggested by Warren et al. (2004).

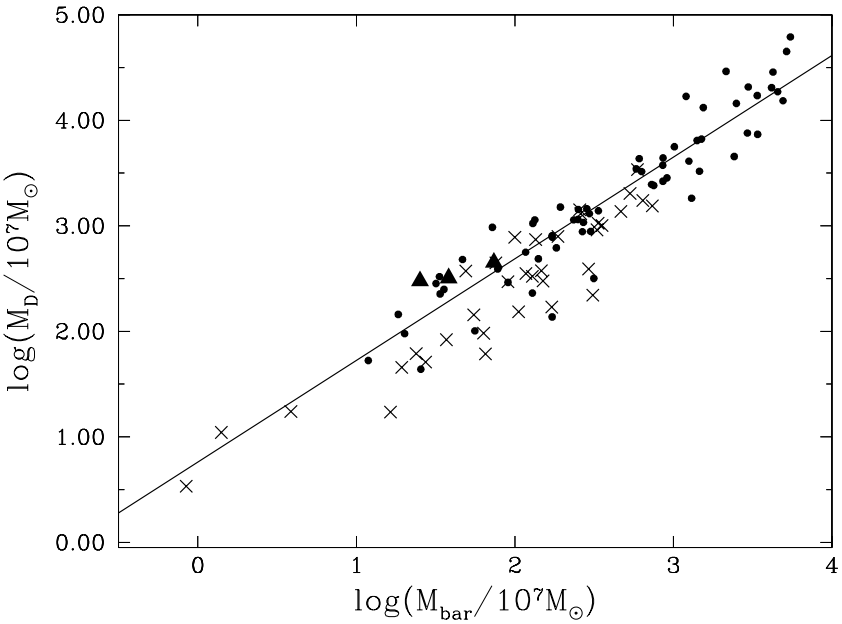

Figure 6.7: M_D as a function of M_{bar} for the same sample of galaxies as in Fig. 6.5. Galaxies with rising rotation curves are marked as crosses while galaxies with flat rotation curves shown as filled circles. The solid line is the best fit relation for galaxies with flattened rotation curves.

scatter in the dynamical to baryonic mass ratio and the lack of a statistically significant trend in M_D/M_{bar} with galaxy size. Quantitatively, the average M_{bar}/M_D is 0.30 ± 0.03 for galaxies brighter than -17 mag, and 0.28 ± 0.03 for galaxies fainter than -17 mag. This is in apparent contradiction to simulations of galaxy formation, which predict that dwarf galaxies should have both a smaller baryon fraction than large galaxies, and also a larger dispersion in the baryon fraction (e.g. [5, 19]). These differences in the baryon fractions of large and small galaxies come about because for small halos the heating of gas at reionization inhibits the capture of baryons and further a good fraction of the captured baryons are subsequently lost due to the energy input from star formation. However, it is important to distinguish between the baryonic fraction as calculated in numerical simulations (which is generally defined as the ratio of the total mass within the virial radius to the total baryonic mass) and that plotted in Fig. 6.6, which is the ratio of total dynamical mass to the total baryonic mass *within the radius to which the HI disk extends*. Since baryons cool and collect at the centers of dark matter halos, in any given halo the baryon fraction is a decreasing function of radius [6]. This means that one could reconcile the rotation curve data with the

theoretical models by requiring that the baryons in dwarf galaxies occupy a proportionately smaller fraction of their dark matter halos as compared to large galaxies. If this is what indeed happens, it is somewhat surprising that things nonetheless conspire to give a more or less constant baryon fraction within the last measured point of the rotation curve. A similarly surprising correlation between baryonic mass and velocity width (the "baryonic Tully-Fisher" relationship) has been reported by Mcgaugh et al (2000). Of course, since many dwarf galaxies have rising rotation curves (i.e. the gas and stars lie entirely within the cores of their dark matter halos), it seems intuitive to suppose that the baryons in these galaxies occupy a smaller fraction of their dark matter halos. Since all the galaxies in our sample have measured rotation curves, it is straight forward to compare the baryon fraction in galaxies with rising rotation curves with that in galaxies which have flat rotation curves.

In Fig. 6.7, M_D is plotted as a function of M_{bar}, separately for galaxies with flat rotation curves (filled circles) and rising rotation curves (crosses). As can be seen, there is a substantial range of baryonic masses at which one finds both galaxies with rising rotation curves as well as galaxies with flat rotation curves. However, at any given baryon mass, galaxies with rising rotation curves tend to have a lower dynamical mass than galaxies with flat curves. Equivalently, within the volume occupied by the baryons, galaxies with flat rotation curves have smaller baryon to dynamical mass fractions than galaxies with rising rotation curves. Quantitatively, the mean M_{bar}/M_D is 0.25 ± 0.02 for galaxies with flat rotation curves, and 0.36 ± 0.03 for galaxies with rising rotation curves.

In essence, the baryon fraction within the last measured point of the rotation curve depends on both the baryon loss as well as the maximum distance from the halo center upto which the remaining baryons extend. Which of these two ends up being dominant depends on the details of the actual baryon loss processes. If one postulates that all halos start with at most the cosmic baryon fraction (~ 0.17) and that galaxies with rising rotation curves are those that have lost baryons, then in these galaxies the smaller sampling of the halo dominates over the baryon loss. On the other hand, dwarf spheroidal galaxies which have both very large dynamical mass to light ratios [21], as well as postulated small halo occupation fractions [16], would have to be cases in which the baryon loss dominates over the decrease in halo occupation. And finally, galaxies with extremely extended gas distributions (like NGC 3741) are likely to be those for which there has been very little net baryon loss, (possibly because the gas has not been able to collapse to form stars) and the baryons sample a larger fraction of the total halo.

Which brings us back to the question that why NGC 3741 has been unable to convert its baryons into stars. It is often assumed that star formation requires a threshold column

density. All the optical emission in NGC 3741 is found to lie within a region with HI column density $> 1.6 \times 10^{21}$ cm^{-2}. This makes it very similar to typical dwarf irregular galaxies, where observationally, one sees that star formation has occurred only above a threshold column density of $\sim 10^{21}$ cm^{-2}[12, 18]. While this could be a possible explanation as to why the gas in NGC 3741 has not been converted to stars, it does not explain why the galaxy has such an unusually extended HI disk in the first place. Perhaps galaxies with extended HI disks are just those which have had a fortuitously long duration disk building history. For example the most extended galaxies known N3714, ESO215-G?009 and DDO154 have a tidal index of ~ -1.0 [8], i.e. these galaxies are neither so isolated that the probability of accreting material is small nor are they in so dense an environment so as to get perturbed (either into a burst of star formation and/or into loosing their gas disks) by larger neighbours. A location in a region of modest density enhancement is perhaps a necessary (but not sufficient!) condition for a galaxy to quiescently and inconspicuously accrete gas into a large disk.

6.4 conclusions

To conclude, in this chapter we presented GMRT HI 21cm images of a nearby dwarf irregular galaxy NGC 3741 ($M_B \sim -13.13$) which show it to have a gas disk that extends to ~ 8.3 times its Holmberg radius. This makes it probably the most extended gas disk known. Our observations allow us to derive the rotation curve (which is flat in the outer regions) out to $\sim$38 optical scale lengths. NGC 3741 has a dynamical mass to light ratio of $\sim$107 and is one of the "darkest" irregular galaxies known. However, the bulk of the baryonic mass in NGC 3741 is in the form of gas and the ratio of the dynamic mass to the baryonic mass (~ 8), falls within the range that is typical for galaxies. Thus the dark matter halo of NGC 3741 has acquired its fair share of baryons, but for some reason, these baryons have been unable to collapse to form stars. NGC 3741's dark halo properties were compared with those of a sample of galaxies with well measured rotation curves. The results showed that if we want to reconcile the observations with the theoretical expectation that low mass galaxies suffer fractionally greater baryon loss, then, the baryon loss from halos must occur in such a way that the remaining baryons occupy a fractionally smaller volume of the total halo.

Bibliography

[1] Bremnes, T., Binggeli, B. & Prugniel, P., A&AS,2000,141,211.

[2] Brainerd, T. G., 2004, AIP Conf. Proc. vol. 743, eds. R. E. Allen, D. V. Nanopoulos and C. N. Pope, 129

[3] Carignan, C. & Beaulieu, S., 1989, ApJ, 347, 760

[4] Côté S., Carignan, C. & Freeman, K.C., 2000, AJ 120, 3027.

[5] Gnedin, O.Y. & Zhao, H., 2002, MNRAS, 333, 299

[6] Hoeft, M., Yepes, G., Gottloeber, S. & Springel, V. 2005, astro-ph/0501304

[7] Hoffman, G.L., Lu, N.Y., Salpeter, E.E., Farhat, B., Lamphier, C. & Roos, T., 1993, AJ, 106, 39

[8] Karachentsev, I.D., Karachentseva, V.E., Huchtmeier, W.K. & Makarov, D.I., 2004, 127, 2031

[9] McGaugh, S.S., Schombert, J.M., Bothun, G.D., & de Blok, W.J.G. 2000, ApJL, 533, 99

[10] Meurer, G.R., Carignan, C., Beaulieu, S.F. & Freeman, K.C., 1996, AJ, 111, 1551

[11] Omar, A., PhD Thesis, JNU University, 2004

[12] Skillman, E. D., 1987, Star formation in galaxies, NASA Washington, Lonsdale Persson C.J. (ed.) p 263

[13] Navarro, J.F., Frenk, C.S. & White S.D.M., 1997,ApJ,490,493

[14] Schlegel, D.J., Finkbeiner, D.P. & Davis,M., 1998, ApJ, 500, 525

[15] Schneider, S.E., Thuan, T.X., Mangum, J.G. & Miller, J.,1992, ApJS, 81,5

[16] Stoehr, F., White, S.D.M., Giuseppe, T. & Springel. V., 2002, MNRAS, 335, L84

[17] Swaters, R.A., 1999, Ph.D. thesis, Rijksuniversiteit Groningen.

[18] Taylor, C.L., Brinks, E., Pogge, R.W. & Skillman, E.D., 1994, AJ, 107, 971

[19] Tassis, K., Bryan, G.L. & Norman, M.L., 2003, ApJ, 587, 13

[20] Verheijen, M.A.W. 2001, ApJ, 563, 694

[21] Mateo, M, ARA&A, 1998, 36, 435

[22] Warren, B.E., Jerjen, H. & Koribalski, B.S., 2004,AJ,128,1152

[23] Wilcots, E.M. & Miller, B.W., 1998, AJ, 116, 2363.

Chapter 7

Resolving the mystery of the dwarf galaxy HIZSS003

7.1 Introduction

The galaxy HIZSS003 was discovered in the course of a blind HI 21cm survey of the Zone of Avoidance (ZOA) [1, 2]. Its very low galactic latitude (b=0.09°) made identification of the optical counterpart in the Palomar Sky Survey images difficult; however, the HI properties derived from the single dish data were consistent with it being a dwarf irregular galaxy. This was later confirmed by follow-up VLA D array and optical observations [5]. The VLA map showed two peaks in the HI distribution, a resolved peak at the center of the galaxy and an unresolved secondary peak close to the edge of the HI distribution. While broadband BVRI imaging failed to detect any stars in the galaxy, narrowband Hα imaging detected an HII region spatially coincident with the unresolved secondary HI peak in the VLA map. Spectroscopy of the HII region confirmed that its radial velocity agreed with that of the HI emission. Although the identification of an HII region strengthens the conclusion that HIZSS003 is a dwarf irregular galaxy, it is puzzling that the current star formation should be concentrated at the edge of the HI disk. VLT near-IR images as well as MMT spectroscopic data of the HII region were presented by Silva et al. (2005). The near-IR images revealed a resolved stellar population and allowed the distance to the galaxy to be derived based on the K magnitude of the tip of the red giant branch (TRGB). The derived distance of 1.69 ± 0.07 Mpc agrees well with the previous estimate of 1.8 Mpc by Massey et al. (2003) (based on the assumption that HIZSS003 has zero peculiar velocity with respect to the local group centroid).

From their spectroscopic data Silva et al. (2005) estimate the metallicity ([O/H]) of the HII region in HIZSS003 to be ~ -0.9, comparable to that of other nearby metal poor

irregular galaxies. On the other hand, the metallicity ([Fe/H]) of the RGB stars (as derived from their colours) is somewhat higher, viz. -0.5 ± 0.1. That the older RGB stars in the galaxy are more metal rich than the gas associated with on going star formation in the HII region is puzzling. Silva et al. (2005) speculate that the lower metallicity of the HII region is caused by low metallicity gas that is falling into HIZSS003 for the first time.

In this chapter we present high resolution GMRT HI images of HIZSS003, which resolve the puzzles of the HII region location and metallicity by showing that HIZSS003 is in fact a galaxy pair, with the HII region being located at the center of a much smaller companion to the main galaxy.

7.2 Results and Discussion

The observations and data analysis of HIZSS003 are presented in Chapter 2. Fig. 7.1 shows the channel maps of the HI emission at a resolution of $42'' \times 39''$ from HIZSS003. HI emission is spread over 63 channels and consists of two distinct sources, one spanning 59 channels and the other spanning 26 channels. At this spatial resolution some channels show HI emission connecting the two sources, however it is not clear whether this is due to beam smearing. A HI feature connecting the two sources is also seen in $28'' \times 26''$ and $23'' \times 18''$ resolution data cubes. However, at higher resolutions no such connecting emission is seen in the channel maps. Further, as discussed in more detail below, the velocity field of the bigger source does not appear to be particularly disturbed, and neither source shows signs of two armed tidal distortions. It is hence likely that the connecting emission seen in Fig. 7.1 is due to beam smearing. In order to disentangle the HI emission, one spectral cube was made for each galaxy in which emission from the other galaxy was blanked out. In the case of channel maps which showed connecting HI, the blanking was done midway between the two sources. Fig. 7.2[A]&[B] show HI images of the two sources at $23'' \times 18''$ resolution made from these blanked cubes. In the rest of the chapter, we refer to the the bigger (eastern) galaxy as HIZSS003A and the smaller (western) one as HIZSS003B. The entire HI distribution will be referred as the "HIZSS003 system". The sources HIZSS003A and HIZSS003B correspond to the main HI peak and the secondary unresolved peak in the VLA map of Massey et al. (2003). The combination of poor spatial ($\sim 60''$) and velocity ($\sim$10 km s^{-1}) resolution of the VLA observations prevented Massey et al. (2003) from separating the two galaxies, although the near-IR VLT images do show two separate stellar concentrations, i.e. one for each galaxy. For reference we note that, as described in Chapter 2, the continumm source NVSS J070023-041255 detected along the line of sight of HIZSS003 system lies towards the source HIZSS003B, and that it is close to, but not coincident with the HII region detected

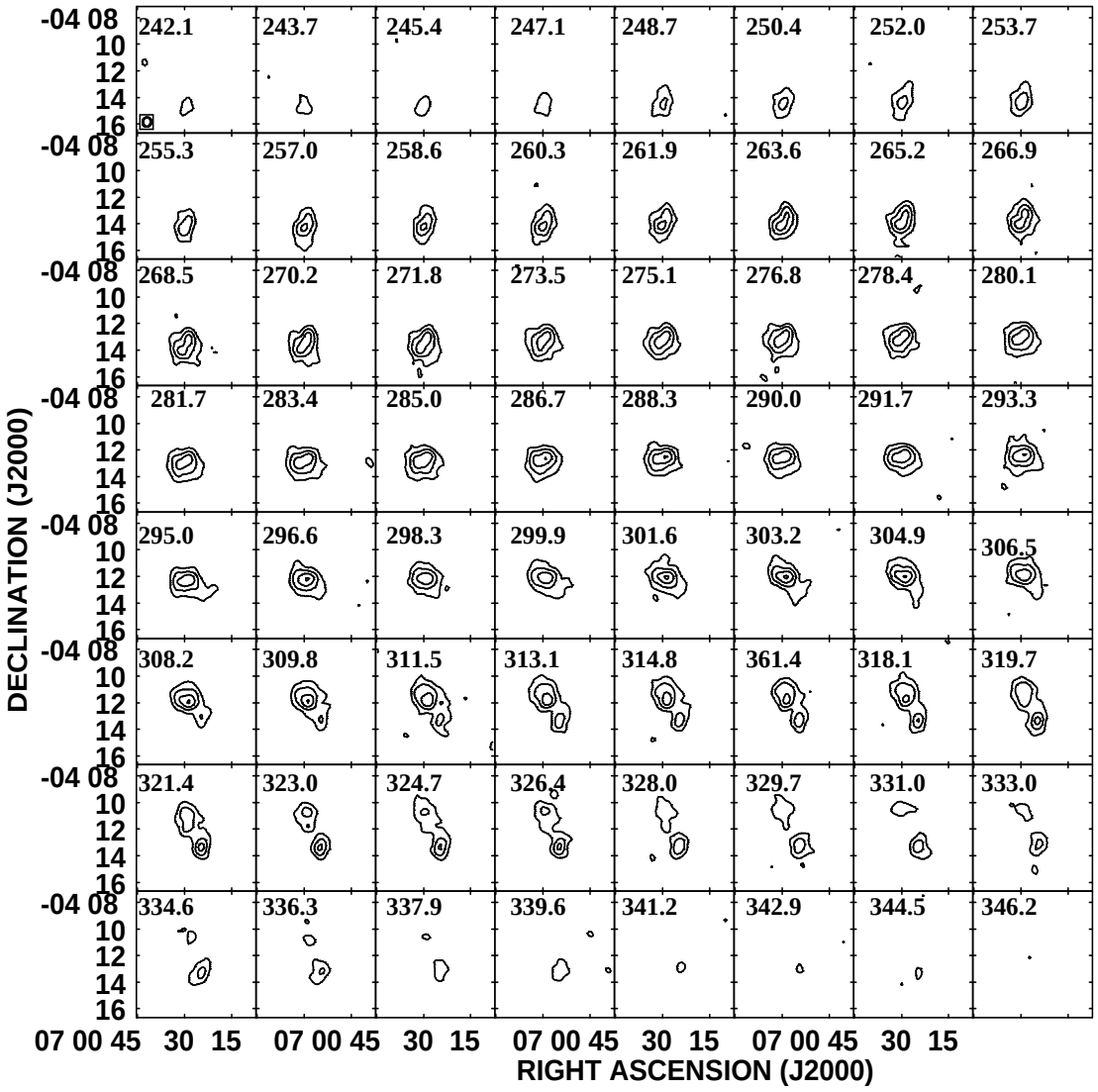

Figure 7.1: HI channel maps of HIZSS003 at $42'' \times 39''$ resolution. The contour levels are 7.5, 22.5, 45 and 75 mJy km s^{-1}. The heliocentric velocity in km s^{-1}is marked on the upper left-hand corner of every pane. The channel spacing is 1.65 km s^{-1}.

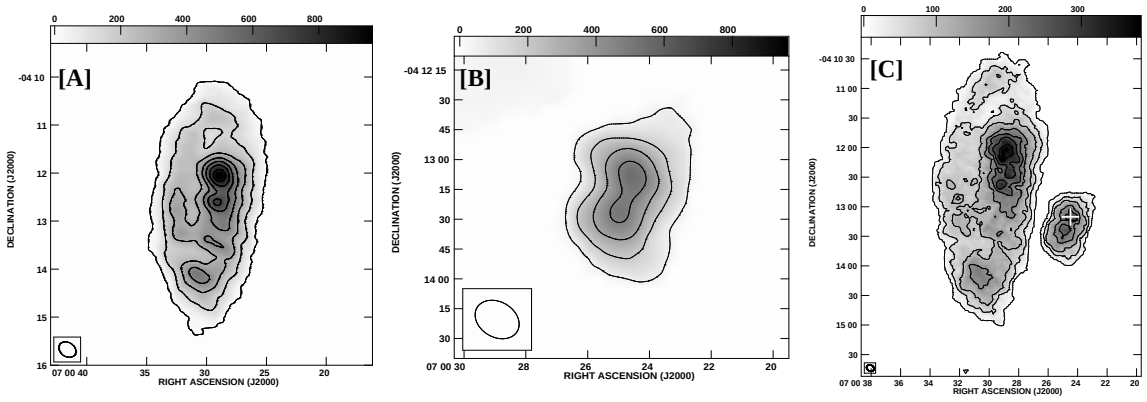

Figure 7.2: Integrated HI emission maps (grey scales and contours) of HIZSS003A (panel [**A**]) and HIZSS003B (panel [**B**]) at $23'' \times 18''$ resolution. The contour levels are 0.2, 3.9, 7.8, 11.6, 15.4, 19.1, 31.4 and 24.9 $\times 10^{20}$ atoms cm^{-2}. The angular scale for panel [**B**] has been expanded for clarity. [**C**] Integrated HI emission map of HIZSS003 system (grey scale and contours) at $8'' \times 6''$ resolution. The contour levels are 0.03, 0.05, 0.10, 0.17, 0.21, 0.27, 0.34 and 0.36 Jy/beam km s^{-1}. The location of HII region in HIZSS003B is marked by a cross.

by Massey et al. (2003). It appears likely that it is a background source, with no connection to the HI emission.

Fig. 7.2[C] shows the high resolution HI map ($8'' \times 6''$ resolution) of HIZSS003. The more diffuse emission is resolved out, and the remaining emission from the two galaxies can be disentangled without having to resort to channel by channel blanking.

As can be seen in the Fig. 7.2, the HI distribution in both the galaxies is clumpy, with three main peaks seen in the HI distribution of HIZSS003A, whereas the HI distribution of HIZSS003B is resolved into two peaks. No signature of tidal interaction is evident in the HI distribution of either galaxy. The HII region detected in the HIZSS003 system is located close to one of the peaks of the HI distribution in HIZSS003B (shown by a cross in Fig. 7.2[C]). The Hα emission is approximately aligned with the HI contours of the galaxy (i.e. from northwest to southeast), and its heliocentric velocity (335 ± 15 km s^{-1}) [5], matches within the error bars with the systemic velocity of 322.6 ± 1.4 km s^{-1}for HIZSS003B derived from the HI global profile (see below).

Fig. 7.3 shows the global HI emission profiles of the two galaxies obtained from the $42'' \times 39''$ resolution data cubes. As discussed above, emission from one galaxy was blanked before obtaining the HI profile for the other one. Gaussian fits to the HI profiles give systemic velocities of 288.0 ± 2.5 km s^{-1}and 322.6 ± 1.4 km s^{-1}for HIZSS003A and HIZSS003B respectively. The corresponding velocity widths at 50% of peak emission are 55 km s^{-1}and

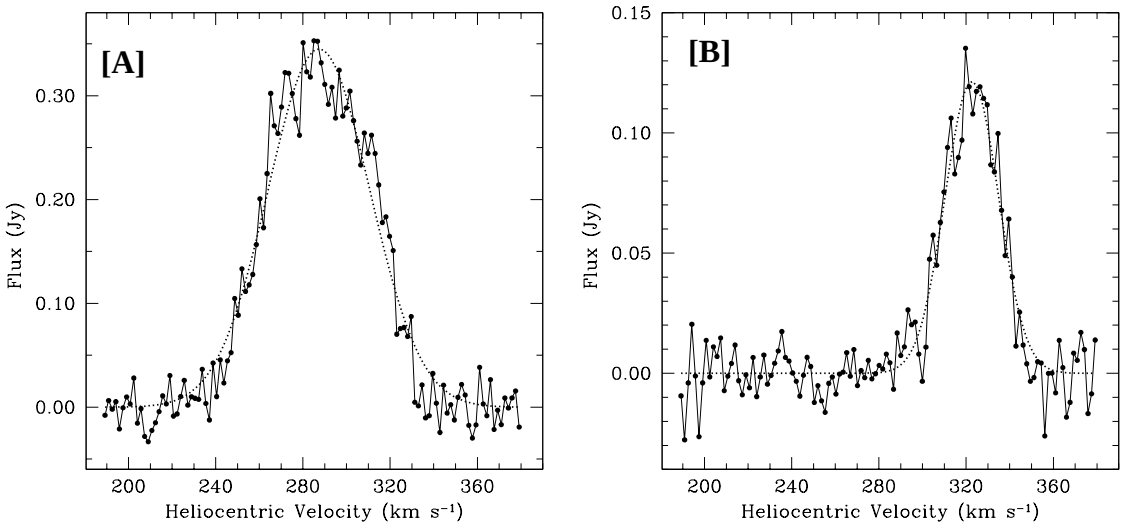

Figure 7.3: Global HI emission profiles for HIZSS003A (panel [**A**]) and HIZSS003B (panel [**B**]) obtained from the $42'' \times 39''$ data cube. The dashed lines show gaussian fits to the profiles.

28 km s^{-1}, while the integrated fluxes are 20.9 ± 2.1 Jy km s^{-1}and 3.8 ± 0.3 Jy km s^{-1}. The HI masses corresponding to these integrated flues are 1.4 $\times 10^7 M_\odot$ and 2.6 $\times 10^6 M_\odot$. The combined flux of both galaxies is 24.7 Jy km s^{-1}, which is in excellent agreement with the value of 24.9 Jy km s^{-1}obtained from the VLA observations by Massey et al. (2003). However both these values are somewhat lower than the flux integral of $\sim$32 Jy km s^{-1}, estimated from the single dish observations by Henning et al. (2000). The HI diameter of the two galaxies, measured at a level of $\sim 10^{19}$ atoms cm^{-2} (from the $42'' \times 39''$ images) are $\sim 6.5'$ (3.2 kpc) and $\sim 3'$ (1.5 kpc).

Fig. 7.4[A]&[B] show the velocity fields of the two galaxies derived from the moment analysis of $28'' \times 26''$ resolution data cube. The velocity field of HIZSS003A (Fig. 7.4[A]) is regular and a large scale velocity gradient, consistent with systematic rotation, is seen across the galaxy. The velocity field is also mildly lopsided − the isovelocity contours in the southern half of the galaxy are more curved than the northern half. Kinks are seen in the western isovelocity contours, close to the location of HIZSS003B. These kinks are more prominent in the higher resolution velocity fields (not shown).

Rotation curves for HIZSS003A were derived using $42'' \times 39''$, $28'' \times 26''$, $23'' \times 18''$ and $18'' \times 11''$ resolution velocity fields, using tilted ring fits. The center and systemic velocity for the galaxy obtained from a global fit to the various resolution velocity fields matched within the error bars; the systemic velocity of 291.0±1.0 km s^{-1}also matched with the

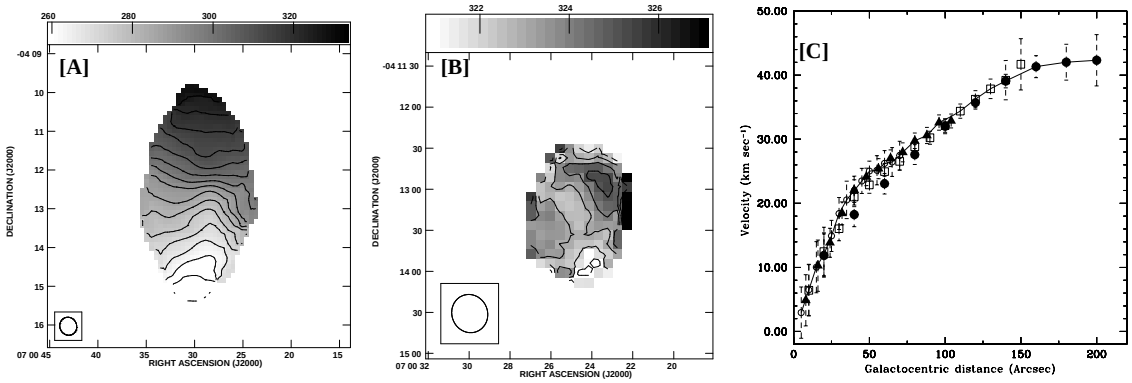

Figure 7.4: [**A**]The HI velocity field of HIZSS003A at $28'' \times 26''$ resolution. The contours are in the steps of 5 km s^{-1}and range from 251.0 km s^{-1}to 326.0 km s^{-1}. [**B**]The HI velocity field of HIZSS003B at $28'' \times 26''$ resolution. The contours are in the steps of 1 km s^{-1}and range from 321.0 km s^{-1}to 326.0 km s^{-1}. The angular scale for this figure has been expanded for clarity. [**C**]The rotation curve for HIZSS003A derived from the intensity weighted velocity field at $42'' \times 39''$, $28'' \times 26''$, $23'' \times 18''$ and $18'' \times 11''$ resolution (shown as filled circles, open squares, filled triangles and open circles respectively). The solid line shows the adopted rotation curve.

value obtained from the global HI profile of the galaxy. Keeping the center and systemic velocity fixed, we fitted for the inclination and position angle (PA) in each ring. For all resolution velocity fields, the PA was found to vary from $\sim -4^\circ$ to 4° and the inclination varied from $\sim 70^\circ$ to 55°. Keeping the PA and inclination fixed to 3° and 65° in the inner regions (upto $90''$) and 0° and 60° in the outer regions respectively, the rotation curves at various resolutions were derived. Fig. 7.4[C] shows the rotation curve of the galaxy derived at various resolutions − as can be seen, they match within the errorbars. The solid line show the final adopted rotation curve. The total dynamical mass of HIZSS003A (at the last measured point of the rotation curve) is found to be $6.5 \times 10^8 M_\odot$.

The velocity field of HIZSS003B (Fig. 7.4[B]) shows a large scale gradient in the southeast-northwest direction with a magnitude of ~ 5 km s^{-1}kpc^{-1}. This gradient is aligned along the direction of elongation of the HI contours and also with the HII region in the galaxy (Fig. 7.2[B]). However, the observed velocity pattern is clearly not rotation since the velocity gradient is not monotonic. Both ends of the galaxy are at a higher velocity than the central region. Similar kinematics are seen in other very low mass dwarf galaxies e.g. Sag DIG and LGS 3 [8]. The disturbed kinematics may be due to a combination of tidal perturbation from the companion galaxy and energy input from the ongoing star formation. The inclination of HIZSS003B derived from the ellipse fit to the HI distribution (assuming an intrinsic axial

ratio q_0=0.25) is $\sim 50^{\circ}$, which means that the upper limit to the inclination corrected rotation velocity is $5/\sin(50) \sim 6.5$ km s^{-1}. Assuming that the gas has a velocity dispersion (σ) of 8 km s^{-1}(which is a typical value seen in our sample dwarf irregular galaxies; see Chapter 2 of this thesis), implies that the systematic rotation, if any, in the galaxy is smaller than the velocity dispersion. Given the lack of any systematic rotation, it is difficult to accurately determine the total dynamical mass for the galaxy. From the virial theorem, assuming HI distribution to be spherical with an isotropic velocity dispersion and negligible rotation, the indicative mass is [3]

$$\mathrm{M_{VT}} = \frac{5\ \mathrm{r_H} \times \sigma^2}{\mathrm{G}} \tag{7.1}$$

Assuming σ of 8 km s^{-1}and taking the diameter of the galaxy $\sim$ 1.5 kpc, gives a total mass of HIZSS003B to be $\sim 5.3 \times 10^7 \mathrm{M_\odot}$. For the entire HIZSS003 system, if we assume the two galaxies to be in a bound circular orbit, then the indicative orbital mass is

$$\mathrm{M_{orb}} = \frac{32}{3\pi \mathrm{G}} \mathrm{r_p} \Delta \mathrm{V}^2 \tag{7.2}$$

where r_p is the projected separation and ΔV the radial velocity difference [4]. For a projected separation of $\sim$ 0.7 kpc and a velocity difference of $\sim$ 34.6 km s^{-1}, the indicative orbital mass is $\sim 6.7 \times 10^8$ $\mathrm{M_\odot}$, in good agreement with the total mass derived from the internal kinematics.

Silva et al. (2005) highlight a puzzle regarding the metallicity of HIZSS003. The metallicity of HIZSS003 system calculated from the younger HII region is smaller than that estimated from the color of the older red giant branch stars. Given that the bulk of the stars are associated with the bigger galaxy but that the HII region is in the smaller galaxy, the inconsistency in the derived metallicities is not surprising. The low metallicity of the gas in the HII region of the smaller galaxy HIZSS003B is also qualitatively consistent with what one would expect from the metallicity-luminosity relation. Further, going by the stars identified as belonging to the HII region (Fig. 6 of Silva et al. 2005) there is a trend for these stars to have a slightly smaller J-K color (consistent with a lower metallicity [7]) than the median color of all stars identified as belonging to HIZSS003. The HIZSS003 puzzle thus seems (at a qualitative level at least) resolved. However, as is well known, an observed colour difference cannot be uniquely ascribed to a difference in the metallicity, but could also be due to a difference in the age of the stars (the "age-metallicity" degeneracy) or from a temperature difference. A more quantitative consistency check will have to await a detailed reanalysis of the near-IR data.

Bibliography

[1] Henning, P.A., Kraan-Korteweg, R.C., Rivers, A.J., Loan, A.J., Lahav, O. & Burton, W.B., 1998, AJ, 115, 584

[2] Henning, P.A., et al. 2000, AJ, 119, 2686

[3] Hoffman, G.L., Salpeter, E.E., Farhat, B., Roos, T., Williams, H. & Helou, G, 1996, ApJS, 105, 269

[4] Karachentsev et al. 2002, A&A, 383, 125

[5] Massey, P., Henning, P.A. & Kraan-Korteweg, R.C., 2003, AJ, 126, 2362.

[6] Silva, D.R., Massey, P., DeGioia-Eastwood, K. & Henning, P.A., 2005, ApJ, 623

[7] Valenti, E., Ferraro, F.R. & Origlia, L., 2004, MNRAS, 351, 1204

[8] Young, L.M. & Lo, K.Y., 1997, ApJ, 490, 710

Chapter 8

A search for HI in some peculiar faint dwarf galaxies

8.1 Introduction

Most of the galaxies in the local universe are dwarfs. Based on their gas content and current rate of star formation, dwarf galaxies can be loosely classified into three different types viz. dwarf irregular (dIrr) galaxies, blue compact dwarf (BCD) galaxies and dwarf spheroidal (dSph) galaxies. dIrrs are gas rich and have some on-going star formation, BCDs are also gas rich but their optical appearance is dominated by an on-going star burst, while dSphs have little to no gas and generally no measurable on-going star formation. Despite these major differences, all these three types of dwarf galaxies have surface brightness profiles that are well approximated by an exponential. Motivated, in part, by the similarity of their surface brightness profiles, it has often been conjectured that these three types of galaxies are evolutionarily related. For example dIrrs could be the quiescent phase of the BCDs, and/or dIrrs may evolve into dSphs by loosing their gas either by supernova driven expansion and stellar winds or by ram pressure stripping [3, 17].

Although such evolutionary connections have often been postulated, the relationship, if any, between these different types of dwarfs is not well understood. In fact, various arguments have been advanced to show that these three galaxy types are too distinct to evolve into one other and that each of them forms a separate class of their own [6, 17]. For example, the disk scale length of BCDs is typically ~ 2 times smaller than that of dIrrs and further their surface brightness is typically ~ 2 mag brighter than that of dIrr galaxies. Hence, unless it is possible to change the radial stellar density distribution, an evolutionary link between dIrrs and BCDs can be excluded. Further, it has also been suggested that BCDs have a larger dark matter core density than is typical for dIrr galaxies [15], however an evolutionary change

in the dark matter core density is difficult to achieve. Finally, composite stellar population models suggest that the star formation rate in dIrrs has been approximately constant for atleast last 10 Gyr, making it unlikely that they undergo periodic starburst phases [22].

Apart from the difficulty in linking BCDs to dIrrs, there have also been various arguments against the possibility of gas rich dwarf irregulars evolving to gas free dwarf spheroidals. dIrrs and dSph are strongly segregated in the metallicity-luminosity plane − at a given luminosity, dIrrs are generally more metal poor than dSphs [6]. This means that if a present day dSph were to have been a dIrr in the past, it had to undergo very rapid and efficient chemical enrichment. Alternatively, for the evolution from dIrrs to dSphs to work, dIrrs have to undergo rapid fading (as they are much brighter in luminosity at a given metallicity than dSphs). However, it would take almost a Hubble time for a dIrr to fade into a dSph, assuming that the star formation in dIrr ceases now, after converting all its gas into stars. Further, mere fading would not turn a typical dIrr into dSph because, in that case, the dIrr would also fade in surface brightness. At a given luminosity, dIrrs tend to have lower surface brightness than dSphs; the fading of a dIrr would decrease it's surface brightness further, resulting in an even worse discrepancy with dSphs. Finally, dIrrs would also need to loose their angular momentum in order to evolve into dSphs; dIrr galaxies are typically rotationally supported while dSphs are not.

Apart from these three classes of dwarf galaxies, there also exists another class of dwarf galaxies called "transition" or dIrr/dSph galaxies. This class is regarded as a bridge between dIrr galaxies and dSph galaxies at the low luminosity end [14], and only a handful of such galaxies are known. Transition galaxies have stellar and optical structural properties that are like those of dSphs. Like dSph galaxies, the stellar population of transition galaxies is dominated by old stars; further these galaxies show little or no signs of on-going star formation. In the metallicity-luminosity diagram, transition galaxies occupy the same region as occupied by dSphs [6]. Finally, like dSphs, they show very little or no rotation. On the other hand, unlike dSphs, transition galaxies have a measurable HI content, and in this respect they resemble dwarf irregular galaxies. It is believed that if transition galaxies were to loose their HI, they would be indistinguishable from dwarf spheroidals.

Here we present a search for HI in three peculiar dwarf galaxies, POX 186, SC 24 and KKR 25. Based, in part, on previous, single dish HI observations, these galaxies have been classified as a BCD, a dIrr and a transition galaxy respectively. Our new GMRT observations failed to detect HI in any of these galaxies. In what follows, we discuss the known properties of these galaxies, our new GMRT observations, and finally, the impact of our non detection of HI on their classification.

8.2 Dwarf galaxy sample

8.2.1 POX 186

POX 186 is an unusually compact BCD galaxy with a linear size of only $\sim$ 300 pc*. This galaxy is thought to be one of the smallest star forming galaxies known and has been called an ultra-compact dwarf [4]. However, it should be noted that POX 186 is different from the ultra-compact dwarfs recently found in deep surveys of the Fornax cluster [5]. These galaxies have physical sizes <100 pc and are believed to be the remnant nuclei of disrupted dwarf elliptical galaxies, whereas POX 186 is believed to be a BCD [13]. Also, POX 186, unlike the ultra-compact galaxies in the Fornax cluster, lies in a void. It had originally been suggested that POX 186 was a genuinely young galaxy. However deep ground based observations of POX 186 showed that (as is typically the case for BCDs) it has faint extended red emission, and is hence unlikely to be forming stars for the first time [4]. Nonetheless, even apart from its very small size, POX 186 remains an unusual object. The luminosity of this galaxy (M_V) is ~ -14 and population synthesis models suggest that it should have a post starburst luminosity of $M_V \sim -10$. This makes it representative of the smallest known units of galaxy formation. HST observations found an unusual asymmetry in the galaxy, which Corbin & Vacca [2] interpreted as a tidal feature. They hence argued for POX 186 being the result of a recent ($< 10^8$ yr) collision between two sub-galactic sized clumps, and thus representative of a dwarf galaxy in formation. However this conclusion remains controversial as, from a study of ionized gas emission from the galaxy, Guseva et al.(2004) argued that the asymmetry in the morphology of POX 186 comes from a starburst-driven gaseous shell and not from tidal arms. As signatures of tidal interactions are often most prominent in HI, a deep HI image of POX 186 would be crucial in resolving this issue. While single dish observations did not detect any HI from the galaxy [13], the limit on the HI mass of the galaxy of $\sim 2.0 \times 10^7$ $M_\odot$ is somewhat higher than the expected HI mass for the galaxy ($\sim 6 \times 10^6$ $M_\odot$, assuming $M_{HI}/L_B \sim 2$, which is a typical value for BCDs of luminosity comparable to POX 186 − e.g. [18]).

8.2.2 SC 24

The dwarf irregular galaxy SC 24 is the lowest luminosity member of the Sculptor group and is also one of the faintest ($M_B \sim -8.39$) irregular galaxies known. This galaxy was discovered by Côte et al. (1997), as a part of a survey of dwarf galaxies of the Sculptor group. Based on the distance-velocity relationship for the Sculptor group galaxies, Skillman

*Following Guseva et al. (2004) we assume a distance of 18.5 Mpc for this galaxy.

et al.(2003) derived a distance of 1.66 Mpc to SC 24

There has been a lack of consensus regarding the total HI content of SC 24. Côte et al. (1997) from single dish observations, determined the HI flux integral to be 11.8 Jy km $s^{-1}$and the heliocentric velocity to be 79.0 km s^{-1}. However, the measured width of the HI emission at the 50% level $\Delta V_{50}\sim$ 55.0 km s^{-1}, is extremely large for such a faint galaxy. Further, the HI flux estimated from the HIPASS database at the position of SC 24, and at the same velocity as for the previous detection, is only 3.2 Jy km $s^{-1}$with $\Delta V_{50} \sim 21$ km s^{-1}[21]. Hα imaging of SC 24 detected a very faint emission, which, if it arises from an HII region would be among the faintest known extragalactic HII regions [21]. However, the coincidence of the Hα source with a continuum source suggests that it could also be an artifact of an imperfect continuum subtraction [21].

8.2.3 KKR 25

KKR 25 ($M_B \sim -9.96$) is classified as a "transition galaxy". Grebel et al.(2003) pointed out that properties of KKR 25 are consistent with those of dSph galaxies, as no Hα was detected from the galaxy and it also lies in the same region of the metallicity-luminosity plane as occupied by dwarf spheroidal galaxies. However, because of its significant HI content ($\sim 1.2 \times 10^6 M_\odot$ [9]) and the presence of a population of faint blue stars [11], this galaxy has been classified as a transition galaxy. Based on the I magnitude of the tip of the red giant branch, Karachentsev et al.(2001) estimated the distance to KKR 25 to be 1.86 Mpc.

8.3 Results

The GMRT observations and data anlysis of POX 186, SC 24 and KKR 25 are described in Sect.2.3. For all three galaxies, the data cubes were examined for line emission at a variety of spectral resolutions − in all cases no significant emission was found. Besides visual inspection, the AIPS task SERCH was also used to search for line emission in all data cubes. No statistically significant feature was detected in the cubes. To derive the final limit on the HI mass for those galaxies with previous single dish HI detections, the data were smoothed to the velocity width of the single dish spectrum. In particular, for KKR 25 a velocity width of 15 km $s^{-1}$was used [9], while velocity widths of 55 km $s^{-1}$and 21 km s^{-1}were used for SC 24 (see Sect. 8.2). For POX 186, in the absence of a previous single dish detection, a velocity width of ∼20 km s^{-1}(a typical velocity width for such faint galaxies; see Sect.2.6) was used. Finally, continuum images at $4'' \times 3''$ resolution were also made for all the galaxies by averaging central 80 channels. No continuum was detected in

Table 8.1: Results of the GMRT observations

Galaxy	HPBW	r_{HPBW}	RMS	M_{HI}	Δv	RMS_{cont}
	(arcsec^2)	(kpc)	(mJy)	($10^5 M_\odot$)	(km s^{-1})	(mJy)
KKR 25	49×44	0.44	1.3	<0.8	15	0.75
SC 24	50×42	0.40	1.2	<2.1	55	0.9
	50×40	0.40	1.6	<1.1	21	
POX 186	7×7	0.63	0.3	<24.1	20	0.6
	4×3	0.36	0.2	<16.1	20	

any galaxy. The derived 3σ limits from the continuum images are given in Table 8.1.

Table 8.1 summarizes our results for a representative selection of spatial resolutions for three galaxies. Col. (1) gives the galaxy name, (2) the spatial resolution defined by the half-power beam width (HPBW) of the synthesised beam, (3) the linear size in kpc corresponding to the HPBW of the synthesised beam, (4) the RMS noise corresponding to this spatial resolution, (5)the 5σ upper limit on the HI mass, (6) the velocity resolution (Δv) used for deriving the limit on the HI mass and (7) the derived 3σ limit from the continuum image (RMS_{cont}).

8.4 Discussion

The non detection of HI with the GMRT in KKR 25 and SC 24 (which is in conflict with the previous single dish detections of these galaxies), could be because the HI emission was resolved out by the GMRT. However, our past experience with the GMRT in successfully imaging dwarf galaxies with HI flux and optical sizes similar to SC 24 and KKR 25, makes such a possibility unlikely. Further, as discussed in more detail below, for both galaxies, a case can be made for confusion of emission from the galaxy with local HI. We discuss next the implications of the GMRT non detections for each of the galaxies in turn.

8.4.1 POX 186

Our GMRT observations for POX 186 confirms the previous single dish non detection, albeit with a much better limit on the HI mass. The upper limit on the HI mass of the galaxy

computed† from the single dish observations is $\sim 2 \times 10^7 M_\odot$ [13], whereas the 5σ upper limit on the HI mass derived from our interferometric observations is $2.4 \times 10^6 M_\odot$. Since HI in dwarf galaxies typically extends to ~ 2 times the Holmberg diameter (e.g. [10]), and the angular size of the optical emission is $\sim 3''$ [2], the upper limit we quote is derived from the $7'' \times 7''$ resolution data cube, and for a velocity width of 20 km s^{-1}. HST observations of POX 186 found a young OB stellar cluster with an estimated age of $\sim 10^6 - 10^7$ yr [2]. We searched for HI emission near the location of this cluster at the highest angular resolution of our data ($4'' \times 3''$) but did not find any statistically significant emission. Our 5σ upper limit (again for a velocity width of 20 km/s) is $1.6 \times 10^6 M_\odot$. The absence of HI in POX 186 is some-what puzzling, as these young stars must be associated with neutral HI. From a statistical study of a sample of BCDs in various environments, Pustilnik et al. (2002) found that BCDs in voids have a higher M_{HI}/L_B than those in higher density regions and that there is also a trend for increasing M_{HI}/L_B with decreasing L_B. From these correlations, the expected M_{HI}/L_B for POX 186 is ~ 2. Hence, our derived upper limit on the HI mass of POX 186, (which corresponds to $M_{HI}/L_B \lesssim 0.8$) means that the galaxy has a somewhat smaller M_{HI}/L_B than is typical for BCDs. However it should be noted that the scatter in M_{HI}/L_B for BCDs at a given luminosity is large. Further, we note that the correlations found by Pustilnik et al. (2002) were computed for galaxies brighter than $M_B \sim -16.0$ mag, and it is not clear whether the fainter BCDs follow a same trend as the brighter ones. Given the small size of the galaxy and the fact that a significant amount of ionized gas has been detected in POX 186 [7], it is possible that a sizeable fraction of HI in the galaxy has been ionized by the recent burst of star formation.

8.4.2 SC 24

As mentioned in Sect. 8.2.2, there have been two separate claims of detection of HI in SC 24, viz. Côte et al. (1997) and Skillman et al. (2003). In the case of the Côte et al. (1997) observations, we note that the signal to noise of the HI spectrum is poor and that there is a strong possibility of confusion with local HI. Indeed, the HIPASS survey detects HI from the Magellanic stream in the direction of SC 24 at the radial velocity of the galaxy [19]. It is possible that due to both the poor spatial resolution and the coarse velocity resolution used (~ 18 km s^{-1}for Skillman et al. (2003) and ~ 8 km s^{-1}for Côte et al. 1997), it was difficult to disentangle foreground emission from any genuine emission from SC 24.

If one goes by the current GMRT observations, the upper limit on the HI mass of SC 24

†The velocity width and confidence limit used to calculate the upper limit on the HI mass for POX 186 is not specified in the paper

is similar to the typical HI mass limits for dSph galaxies (see Mateo 1998 and references therein). However the optical appearance of the galaxy suggests that it is a dwarf irregular galaxy [12]. It seems more likely that SC 24 is a distant galaxy, since (i) unlike other member galaxies of the Sculptor group, HST observations failed to resolve this galaxy into stars (Karachentsev, I. D., private communication). (ii) Apart from the local HI feature at a heliocentric velocity of 79 km s^{-1}, no other emission was detected in the direction of SC 24, over the velocity range of -200 to 1800 km s^{-1}, used by Côte et al. (1997) in the original search for HI in the Sculptor group.

8.4.3 KKR 25

As mentioned in Sec. 8.2.3, KKR 25 has many structural properties in common with the dSph galaxies [6]. Its classification as a transition galaxy rests on it's relatively large HI content and the presence of faint blue stars. Given that the Leiden/Dwingeloo survey of galactic neutral hydrogen [8] detects HI in the direction of KKR 25 in the same velocity range as detected by the single dish observations for this galaxy, it is likely that the HI emission that has been associated with this galaxy actually arises from local gas. The upper limit on the HI mass from the current GMRT observations is comparable to the limits obtained for typical dwarf spheroidal galaxies (Mateo 1998 and references therein). Further, the presence of blue stars in a bona fide dwarf spheroidal galaxies is not unusual (e.g. the Fornax dwarf spheroidal galaxy [20], the Carina dwarf spheroidal [16]). Hence, it seems like that KKR 25 is a normal dwarf spheroidal galaxy and not a transition galaxy.

8.5 Conclusions

To conclude, we have presented results from a deep search of HI 21 cm emission with the GMRT in three dwarf galaxies viz. POX 186, SC 24 and KKR 25. We do not detect HI in any of these galaxies; for SC 24 and KKR 25 this is in conflict with previous detections of HI using single dish radio telescopes. The current GMRT observations suggest that the previous single dish measurements were confused with the galactic emission. Our stringent limits on the HI mass of KKR 25 suggest that it is a normal dwarf spheroidal galaxy, whereas SC 24 is more likely to be a distant dwarf irregular galaxy. In the case of POX 186, we confirm the previous non detection of HI, though with substantially better limits on its HI mass. Our observations find that the HI mass of POX 186 is somewhat smaller than is typical for BCDs, which may be because a substantial fraction of the HI in the galaxy has been ionized from the last burst of star formation.

Bibliography

[1] Côte, S., Freeman, K. C., Carignan, C. & Quinn, P. J., 1997, AJ, 114, 1313.

[2] Corbin, M. R. & Vacca, W. D., 2002, ApJ, 581, 1039

[3] Davies, J.I. & Phillipps, S., 1988, MNRAS, 233, 553

[4] Doublier, V., Kunth, D., Courbin, F. & Magain, P., 2000, 353, 887

[5] Drinkwater, M.J., Jones, J.B., Gregg, M.D. & Phillipps, S., 2000, PASA, 17, 227

[6] Grebel, E. K., Gallagher III, J. S. & Harbeck, D. 2003, AJ, 125, 1926

[7] Guseva, N.G., Papaderos, P., Izotov, Y.I., Noeske, K.G. & Fricke, K.J., A&A, 2004, 421, 519

[8] Hartman, D., 1994, Ph.D. thesis, Rijksuniversiteit Leiden.

[9] Huchtmeier, W.K., Karachentsev, I.D. & Karachentseva, V.E. , 2003, A&A, 401, 483

[10] Hunter, D., 1997, PASP, 109, 937

[11] Karachentsev, I. D. et al. 2001, A&A, 379, 407

[12] Karachentsev, I.D., Karachentseva, V.E., Huchtmeier, W.K. & Makarov, D. I., 2004, AJ, 127, 2031

[13] Kunth, D., Maurogordato, S. & Vigroux, L., 1988, A&A, 204, 10

[14] Mateo, M, ARA&A, 1998, 36, 435

[15] Meurer, G.R., Staveley-Smith, L. & Killeen, N.E.B., 1998, MNRAS, 300, 705

[16] Monelli et al. 2003, AJ, 126, 218

[17] Papaderos,H., Loose, H., Fricke, K.J. & Thuan, T.X., 1996, A&A, 314, 59

[18] Pustilnik, S.A., Martin, J. M., Huchtmeier, W. K., Brosch, N., Lipovetsky, V. A. & Richter, G. M., 2002, A&A, 389, 405

[19] Putman, M.E., Staveley-Smith, L., Freeman, K.C., Gibson, B.K. & Barnes, D.G., 2003, ApJ, 586, 170

[20] Saviane, I., Held, E.V. & Bertelli, G., 2000, A&A, 355, 56

[21] Skillman, E. D., Côte, S. & Miller, B. W., 2003, AJ, 125, 593

[22] van Zee, Liese, 2001, AJ, 121, 2003

Chapter 9

Power spectrum analysis of HI emission in dwarf galaxies

9.1 Introduction

Evidence has been mounting in recent years that turbulence plays an important role in the physics of ISM as well as in governing star formation. It is believed that turbulence is responsible for generating the hierarchy of structures present on a range of spatial scales in ISM (e.g. [4]). In such models, the ISM has a fractal structure and/or the power spectrum of the density fluctuations is a power law, indicating that there is no preferred "cloud" size.

On the observational front, power spectrum analysis of the HI intensity fluctuations is an important technique to probe the structure of the neutral ISM in galaxies. Since the power spectrum is the Fourier transform of the autocorrelation of the HI intensity distribution, it is conceptually straight forward to compute it from cubes of HI 21cm emission. Based on such an image plane analysis, the power spectrum of HI distribution was found to be a power law for the Milkyway companion dwarf galaxies LMC [3] and SMC [9]. Westpfahl et al.(1999) using a box counting method as well as a perimeter-area measure (both done on the deconvolved images) showed that the HI distribution in several galaxies in the M81 group is a fractal. Similar techniques have also been used at optical wavelengths. Willett et al.(2005) have used the Fourier transform power spectra of V and Hα images for a sample of irregular galaxies to show that the power spectra in optical and Hα passbands is a power law, indicating that there is no characteristic mass or luminosity for OB associations and star complexes.

Although most of the studies of the power spectrum of the HI emission in galaxies are based on image plane analysis techniques, there has been some work on visibility based techniques [2, 5]. Since the complex visibility measured by an interferometer is the Fourier

transform of HI intensity distribution, the squared modulus of the visibility is a direct estimator of the power spectrum. Both Crovisier & Dickey [2] and Green [5] found that the power spectrum of HI emission in our own galaxy is a power law. So far, however, visibility based techniques to measure the power spectrum have been applied only to our own galaxy.

In this chapter, we discuss techniques for obtaining the power spectrum of the HI intensity fluctuations in the faint dwarf galaxies in our sample, where the expected signal is very weak. Our analysis is focused on visibility based techniques. We prefer visibility based techniques for this analysis because (i) the statistics of the signal is better understood in the visibility plane compared to the image plane (due to the uncertainties involved in the image deconvolution) and (ii) the image plane analysis techniques requires a deconvolved HI spectral cube, however, as discussed in Sect. 2.6, the high resolution HI data for our sample galaxies could not be deconvolved.

9.2 Data

The formalism we have developed to obtain the power spectrum of HI intensity fluctuations in faint dwarf galaxies was tested using the GMRT data for DDO 210. Being both nearest as well as one of the brightest galaxies (in the HI cm line) in our sample, this dataset provides good spatial resolution as well as good signal-to-noise for power spectrum analysis. The HI emission from DDO 210 spanned the central 22 channels of the 128 channel spectral cube, viz. from channel number 58 to 80. No continuum was detected in the galaxy and continuum emission from point sources in the field of view was subtracted in the uv plane using the AIPS task UVSUB, before trying to derive the power spectrum of the galaxy.

DDO 210 has also been observed at the VLA in B,C and D configurations. We downloaded this multi-configuration data from the VLA archive and reanalyzed it. The formalism developed to obtain the power spectrum was applied independently to both the GMRT and the VLA data and the results were compared. This provides a robust check on instrumental biases.

9.3 Visibility correlations

The power spectrum of HI intensity fluctuations is the Fourier transform of the autocorrelation function of HI intensity distribution i.e. if $\rho(l, m)$ is the auto correlation function of the HI intensity fluctuations $\delta I(l, m)$, i.e.

$$\langle \delta I(l, m) \delta I(l', m') \rangle = \rho(l - l', m - m') \tag{9.1}$$

the power spectrum of HI intensity fluctuations is given as,

$$\mathrm{P_{HI}}(u,v) = \int\int \rho(l,m)\ e^{-j2\pi(ul+vm)}\ dl\ dm \tag{9.2}$$

Since the complex visibility function measured by an interferometer is a Fourier transform of the brightness distribution, the power spectrum, in principle, can be measured directly from the interferometric observations (e.g. [2, 5]). However, in practice, an interferometer does not measure exactly the Fourier transform of the sky intensity, but instead, measures the Fourier transform of the sky intensity modified by a window function. For example, if the HI emission fills the whole telescope beam, the window function is the primary beam of the telescope. On the other hand, if the extent of HI emission is smaller than the primary beam, the window function corresponds to the total extent of the emission.

In more precise terms, we assume that the HI emission intensity at some frequency ν can be written as

$$I_\nu(l,m) = W_\nu(l,m)\ [1 + \delta I_\nu(l,m)], \tag{9.3}$$

where W_ν(l,m) characterizes the large scale HI distribution in the galaxy at frequency ν, while $\delta I_\nu(l,m)$ characterizes the small scale HI fluctuations. Then (as shown in Appendix-I), at long baselines the complex visibility squared is a convolution of the power spectrum, $\mathrm{P_{HI}}(\vec{U})$ with the Fourier transform of the convolution of the window function with itself, i.e.

$$\langle V_\nu(\vec{U})\ V_\nu^*(\vec{U})\rangle = \tilde{\omega}_\nu(\vec{U})\ \otimes\ \mathrm{P_{HI}}(\vec{U}) \tag{9.4}$$

where $\vec{U}$ is the projected baseline. $\tilde{\omega}_\nu(\vec{U})$ is the Fourier transform of $\omega_\nu(\lambda,\mu)$, the convolution of the window function with itself, i.e.

$$\omega_\nu(\lambda,\mu) = \int\int W_\nu(l,m)\ W_\nu(l-\lambda, m-\mu)\ dl\ dm$$

The angular brackets in Eqn. (9.4) denotes averaging; in this case the average could be over different possible orientations of the baseline $\vec{U}$. Hence, as seen from Eqn. (9.4), the magnitude square of the complex visibility is an estimator of the power spectrum in a galaxy. Both Crovisier & Dickey(1983) and Green(1993), in their analysis, ignored the window function. This is justified as long as the averaging is done on scales larger compared to the width of the convolving function.

In practice, the measured visibility also has noise; the complex visibility in a frequency channel ν can hence be written as, $\mathrm{V}_\nu(\vec{U}) = S_\nu(\vec{U}) + N_\nu$, where $S_\nu(\vec{U})$ is the HI signal, while N_ν is the noise. Therefore,

$$\langle V_\nu(\vec{U})\ V_\nu^*(\vec{U})\rangle = \langle S_\nu(\vec{U})S_\nu^*(\vec{U})\rangle + \langle N_\nu N_\nu^*\rangle \tag{9.5}$$

As can be seen from Eqn. (9.5), squaring the complex visibility makes the noise bias positive-definite. For HI emission from our own galaxy, this noise bias is small. On the other hand, for the dwarf galaxies in our sample this the noise bias can be orders of magnitude larger than the desired power spectrum. Determination of power spectrum using this estimator thus requires extremely accurate removal of this noise bias. In principle, one could estimate $\langle N_\nu N_\nu^*\rangle$ from a line free channel and subtract it from $\langle V_\nu(\vec{U})\ V_\nu^*(\vec{U})\rangle$ from a channel with emission. However this requires that the statistics of noise should be the same in all line free and line channels, which inturn requires an extremely flat bandpass response, and/or one in which the variation of noise statistics with channels can be very well calibrated.

Inorder to avoid the problem of noise bias, instead of correlating a visibility with itself, one could instead correlate the visibilities in two adjacent channels. This estimator is

$$C_{ij}(\vec{U}) = \langle V_i(\vec{U})V_j^*(\vec{U})\rangle \tag{9.6}$$

where i,j refer to the frequency channel numbers. If noise in channel i and j is uncorrelated then $\langle N_i(\vec{U})N_j^*(\vec{U})\rangle = 0$. Further, if we assume that (i) the signal in line channels is isotropic and (ii) except for a possible shift in the centroid of emission, the signal in the two channels to be correlated is the same, then we find that the imaginary part of $C_{ij}(\vec{U})$ is zero (see Appendix-II for more details). If these assumptions are satisfied, C_{ij} (again at long baselines) can be written as

$$C_{ij}(\vec{U}) = \langle V_i(\vec{U})V_j^*(\vec{U})\rangle = P_{\rm HI}(\vec{U})W(0,0)W(\Delta l,0) \tag{9.7}$$

where $P_{\rm HI}$ is the power spectrum that we would like to measure and Δl is the shift in the centroid of emission in channel i and j. $W(l,m)$ characterizes the large scale HI distribution in the galaxy.

$\mathrm{C}_{ij}(\vec{U})$ computed for the adjacent channels 70 & 71 (which have the highest signal to noise ratio) of the GMRT DDO 210 data are shown in Fig. 9.1. C_{ij}s for every 10,000 baselines were averaged before plotting. The same analysis was also tried on line-free channels. $\mathrm{C}_{ij}(\vec{U})$ obtained by correlating the line free channels 25 & 26 is also shown in Fig. 9.1. As expected, the imaginary part of C_{ij} for both line free channels as well as channels with emission is small. Further, the real part of C_{ij} for line channels, shows a steep fall with an increasing uv-distance, upto $\sim$4 kλ, and then remains nearly flat upto the last measured point in the uv-plane. The real part of C_{ij} for line free channels also shows a constant offset from zero for the whole uv-distance. It seems likely that our assumption that noise in adjacent channels

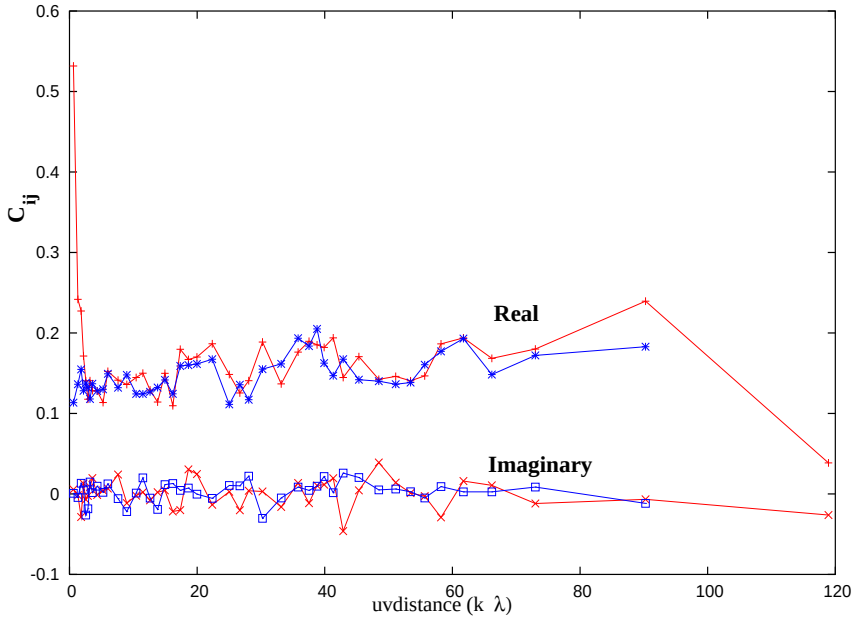

Figure 9.1: The real and imaginary part of the C_{ij} obtained by correlating the two adjacent line channels (i.e. channel 70 and 71; shown in red) and two adjacent line free channel (i.e. channel 25 and 26; shown in blue).

is uncorrelated does not hold. As a systematic check, $C_{ij}(\vec{U})$ was computed for a number of different choices of i. For each choice of i, j was allowed to vary from 1 to 128 i.e. the entire spectral cube. For this test $C_{ij}(\vec{U})$ was normalized to unity, i.e. the real part of $C_{ij}(\vec{U}) = 1$ when a channel is correlated with itself (i.e. i=j).

Fig. 9.2 & 9.3 shows the real and imaginary part of $C_{ij}(\vec{U})$, respectively, as a function of frequency (j) for various values of i. The imaginary part of C_{ij} was found to be zero over all frequency channels, on the other hand, a $\sim$ 10% correlation between adjacent channels exists in the real part of C_{ij}, regardless of whether the channels contain signal or not. The correlation seen between the adjacent channels is likely due to the $sinc^2$ shape of the spectral channels produced by the FX digital correlator used at the GMRT. C_{ij} as a function of frequency channels computed using the VLA DDO 210 data is shown in Fig. 9.5. Again, the real part of C_{ij} shows correlation between the adjacent channels regardless of whether the channels have signal or not. The correlation between the adjacent channels was found to be somewhat larger ($\sim$20 %) in the VLA data than the GMRT data. This is likely to be due to the difference in the type of correlator used at the VLA (XF correlator) and at the GMRT (FX correlator).

The offsets seen in C_{ij} due to the noise correlation in adjacent channels means that a

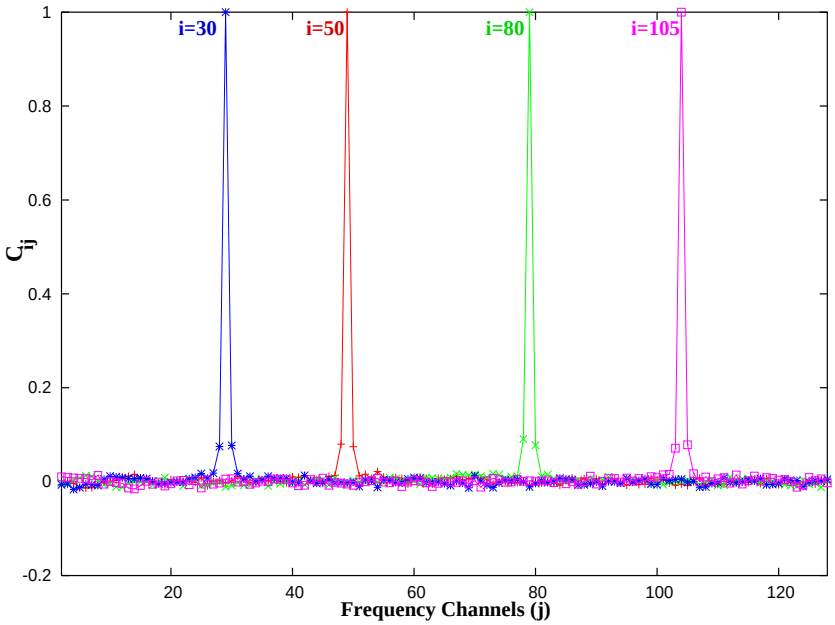

Figure 9.2: Real part of the correlation between the ith channel (for i=30,50,80,105; plotted in different colours) and the jth channel (along the x axis) for $U = 1$ and $\Delta U = 0.5$, using the GMRT data.

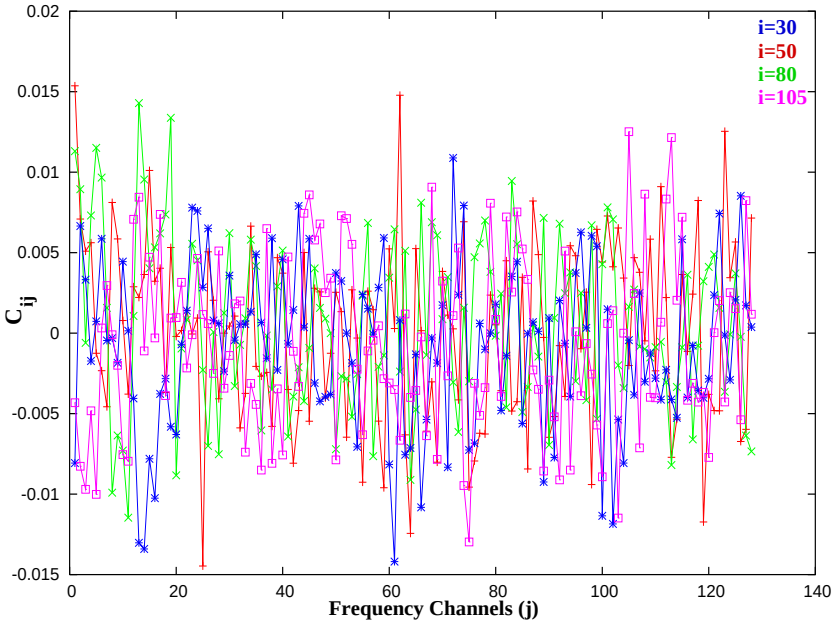

Figure 9.3: Imaginary part of the correlation between the ith channels (plotted in different colours) and the jth channels for $U = 1$ and $\Delta U = 0.5$, using the GMRT data.

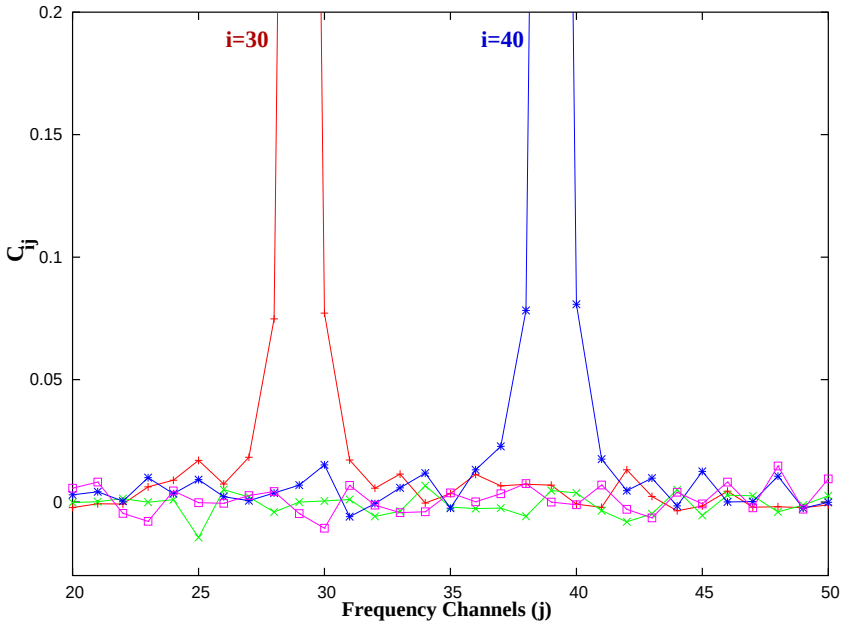

Figure 9.4: Real (red and blue) and imaginary (green and pink) parts of correlations between i=30 & 40 channels with the jth channel, respectively (same as Fig. 9.3) on a zoomed scale.

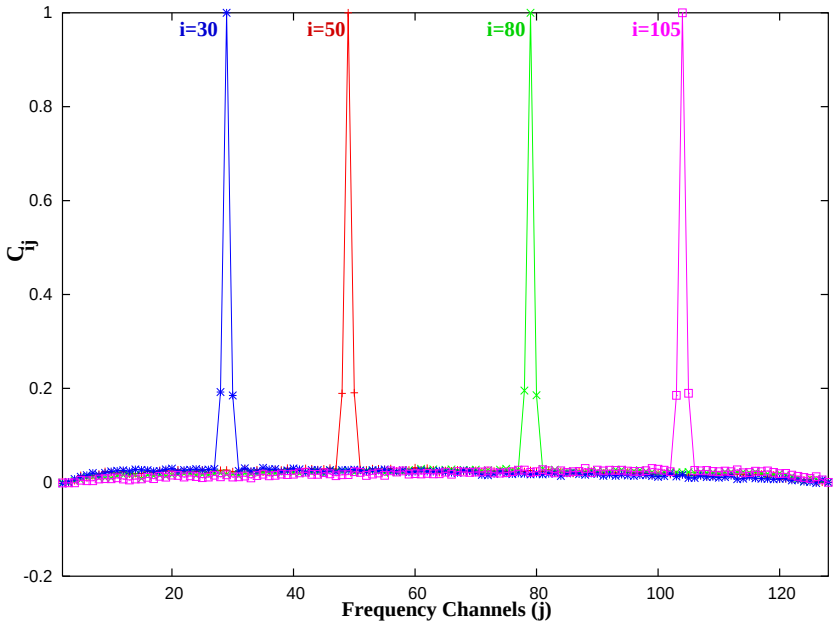

Figure 9.5: Real part of the correlation between the ith channel (same as that in Fig. 9.2) and for $U = 1$, $\Delta U = 0.5$ using the VLA data.

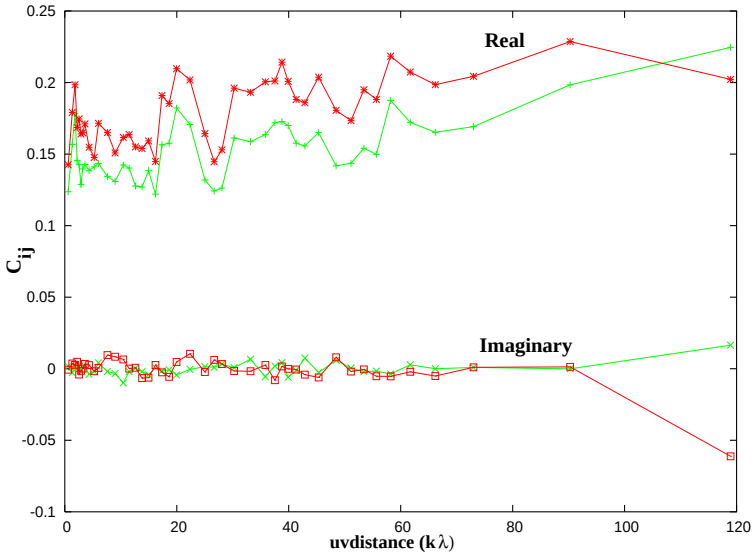

Figure 9.6: Real and imaginary part of averaged $\langle N_\nu N_\nu^* \rangle$ obtained by correlating the adjacent line free channels. Frequency channels from 20-30 (green) and 90-100 (red) are used to obtain the averaged noise bias.

measurement of the power spectrum of HI emission requires an accurate removal of a noise power spectrum from the observed C_{ij}. As discussed earlier, this requires very high accuracy of bandpass calibration. Attempts were made to remove the noise bias by estimating $\langle N_\nu N_\nu^* \rangle$ from the line free channels and subtract it from C_{ij} estimated from line channels. Different pairs of adjacent line free channels were correlated and the derived C_{ij}'s were averaged to obtain an averaged $\langle N_\nu N_\nu^* \rangle$. However, we found that the observed offset in the noise bias in the line free channel was not constant, but increased systematically with the frequency. To illustrate this, we show in Fig. 9.6 two estimates of averaged $\langle N_\nu N_\nu^* \rangle$, each obtained by averaging the correlation data of five pairs of adjacent line free channels, with one set of 5 pairs on the low frequency side of the line and other on the high frequency side. A significant offset between these two estimates can be seen.

As seen in Fig. 9.4, only two nearest neighboring channels were found to be correlated, hence instead of correlating the adjacent channels, we correlated very third channel. Fig. 9.7 shows the real and imaginary part of C_{ij}, obtained by correlating every third channel. For comparison, we also correlated the visibilities in every second channel (also shown in fig. 9.7). As can be seen, real part of C_{ij} showed offsets for correlations of every second channel, on the other hand, the offsets were reduced to zero by correlating every third channel. However as one takes a larger and larger channel separation, one expects the correlation between the

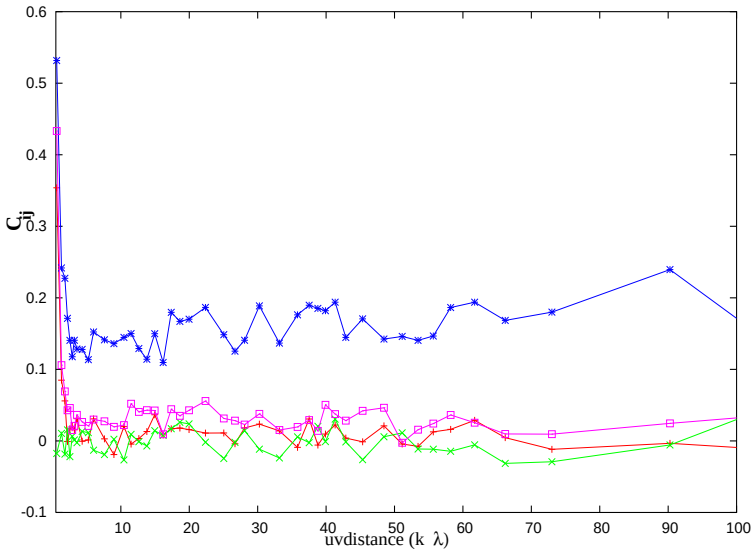

Figure 9.7: Real part of C_{ij} obtained by correlating channels 70-71 (blue), 70-72(pink) and 70-73(red).The imaginary part of C_{ij} for 70-73 (green) is also shown.

HI signal in two channels to also fall. This makes this estimator non ideal for our purpose.

9.4 Correlating the nearby baselines

As seen in Sect. 9.3, correlating the visibilities of a same baseline gives a non zero offset in the power spectrum. Instead of correlating adjacent channels, one could instead correlate adjacent baselines. An adjacent baseline could either come from (i) the same antenna pair at an adjacent time stamps or (ii) a different, but coincidentally nearly identically separated antenna pair.

If the visibilities corresponding to different baselines are correlated, the correlation C'_{ij} at longer baselines is a convolution of the power spectrum with the product of $\tilde{W}(l,m)$, corresponding to each visibility (see Appendix-III for more details) i.e.

$$C'_{ij} = \langle V_\nu(\vec{U}_i)\ V^*_\nu(\vec{U}_j)\rangle = \int P(\vec{U})\ [\tilde{W}_\nu(\vec{U}_i - \vec{U}) \times \tilde{W}^*_\nu(\vec{U}_j - \vec{U})]\ d^2\vec{U}, \tag{9.8}$$

where index i and j correspond to the two different baselines being correlated. $\tilde{W}(\vec{U})$ is the Fourier transform of $W(l,m)$, the large scale HI distribution in the galaxy. Since $\tilde{W}(\vec{U})$ is sharply peaked at $\vec{U}=0$ and falls off rapidly, the quantity in square brackets in Eqn. (9.8) is also sharply peaked at some $\vec{U}$ between $\vec{U}_i$ and $\vec{U}_j$. The peak amplitude of this quantity decreases as $|\vec{U}_i - \vec{U}_j|$ increases. If D is the width of $\tilde{W}(\vec{U})$, from Eqn. (9.8), each baseline

in the uv plane will be correlated as long as $|\vec{U}_i - \vec{U}_j| < D$. Further, if the large scale HI distribution in the galaxy is symmetric (i.e. W(l,m) is symmetric), $\tilde{W}(u,v)$ will be real, hence in that case the real part of C'_{ij} is a measure of power spectrum, while the imaginary part of C'_{ij} is zero.

In a given frequency channel, each visibility corresponding to a given baseline U_i was correlated with all the baselines U_j, such that $|U_i - U_j|$ <D, where D was taken to be 0.8kl, corresponding to the inverse of the HI extent of the galaxy. All self correlations were excluded. To increase the signal to noise ratio, C'_{ij} was averaged in bins of size 1 kλ, after sorting the data in order of increasing uv-distance. The weight associated with each estimate corresponds to the total number of baselines (U_j) correlated within a circle of radius D, centered on U_i in the uv-plane. Fig. 9.8 shows the absolute value of the real and imaginary part of C'_{ij} for a channel with emission, plotted on the logscale. As can be seen, the real part of C'_{ij} for a line channel shows detectable signal upto $\sim$ 5 kλ, after which it is dominated by noise. Further, no noise offsets are seen in the real part of C'_{ij} at longer baselines. Although the C'_{ij}'s are equally positive and negative at longer baselines i.e. averaged C'_{ij} is zero, the apparent increase in the value of C'_{ij} seen at the longer baselines in Fig. 9.8, is because of plotting the absolute value of C'_{ij}. The increase in the noise on C'_{ij}s at longer baselines is an effect of a decrease in the number of points, averaged in each bin to estimate C'_{ij}, at longer baselines because of sparse uv coverage in the outer uvplane. The imaginary part of C'_{ij} on a linear scale in shown in Fig. 9.9.

Further, we note that the imaginary part of C'_{ij} is not zero, but shows a non zero value for small baselines (see Fig. 9.9). The quantity C'_{ij} was also derived using various other values of D viz. 0.2kl and 0.5kl. We found that the imaginary part of C'_{ij} increased systematically as we increased the window within which the visibilities were averaged.

As seen in Eqn. (9.8), for C'_{ij} to be real requires $\tilde{W}(\vec{U})$ to be real, which inturn requires the window function W(l,m) to be even. Since each visibility is convolved with $\tilde{W}(\vec{U})$, the real and imaginary part of the visibilities were inspected as a function of uv-distance (for the same frequency viz. 70 channel as that used for obtaining C'_{ij}). To increase the signal to noise ratio, visibilities were averaged in bins of fixed width. Fig. 9.10, shows the real and imaginary part of averaged visibilities plotted for a uv-range of 0$-$1 kλ. The error bars represents the standard deviation of the mean of the distribution in each bin. As can be seen, the imaginary part of visibility is zero (within the errorbars) for small uv-distances ($< 0.3k\lambda$), however it becomes significant at $\sim$ 0.8kλ. On the other hand, the real part of visibility falls with the uv-distance. This should manifest itself as a non even distribution of intensity in the image plane, and indeed an image made using only visibility with

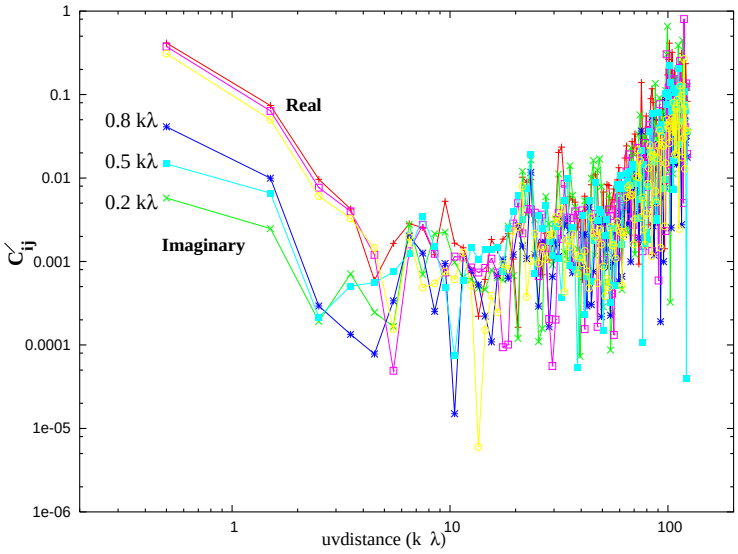

Figure 9.8: Absolute value of the real and imaginary part of binned C'_{ij} plotted as a function of uv-distance in bins of size 1 kλ using D=0.2, 0.5 and 0.8 kλ. An increase in the real and imaginary part of C'_{ij} seen at longer baselines is because of the effect of plotting the absolute value of C'_{ij} and the increase in the noise in the outer bins.

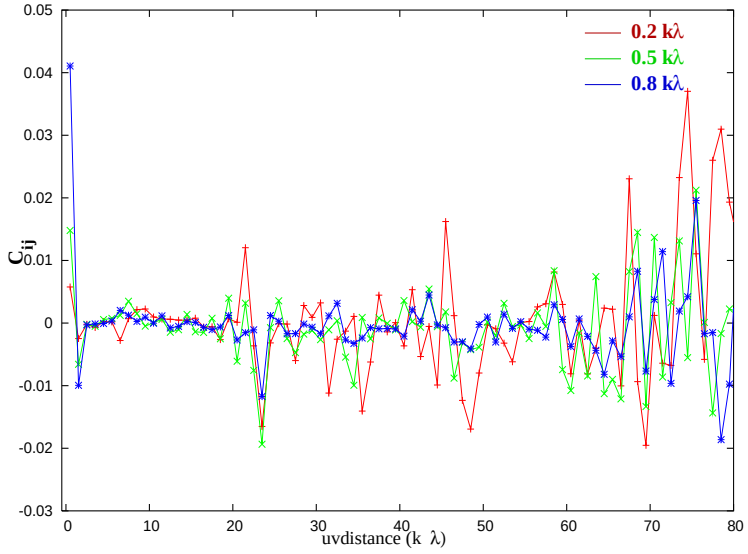

Figure 9.9: Imaginary part of binned C'_{ij} plotted on a linear scale, as a function of uv-distance in bins of size 1 kλ using D=0.2, 0.5 and 0.8 kλ.

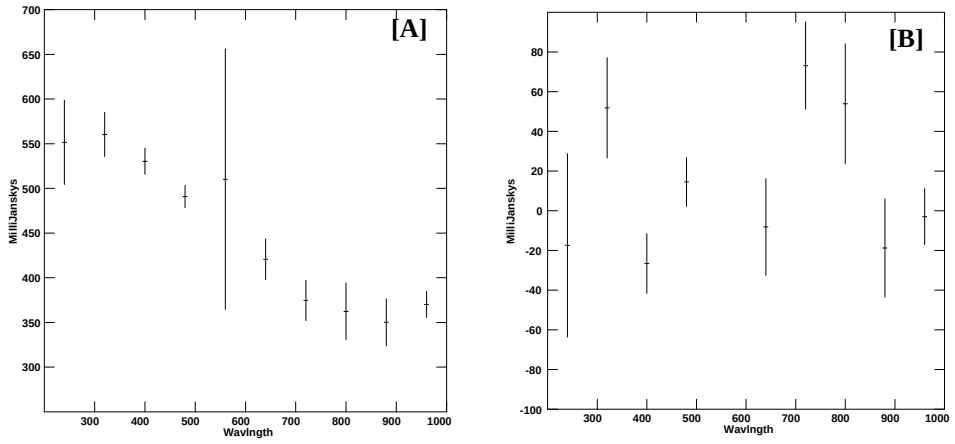

Figure 9.10: [**A**] Real part of visibilities binned in bins of width 0.08kl plotted against the uv-distance. The error bars represents the standard deviation of the mean of the distribution in each bin. [**B**] Imaginary part of the binned visibilities.

0.8 kλ of the origin is not even (Fig. 9.11). Since the window function $\tilde{W}(\vec{U})$ is real for the shortest baselines ($\leq 0.2k\lambda$), choosing D=0.2 kλ is a good compromise between keeping C_{ij} real and improving the signal to noise, hence all the baselines within 0.2 kλ were correlated. Coincidentally 0.2 kλ correspond to the GMRT dish diameter.

As seen in Fig. 9.8, the real part of the power spectrum falls sharply with the uv-distance. The derived power spectra is obtained by weighted averaging of the correlation data in bins of fixed size (i.e. 1 kλ). However, as the uv-coverage is not uniform (the uv-coverage is more dense in the inner regions, while it is sparse in the outer regions), beyond the uv-distance of $\sim$4 kλ, the number of points in each bin decreased dramatically with the increase in the uv-distance. Hence, in-order to retain same number of points in each bin, the bin size was increased with an increase in the uv-distance. The first bin was kept fixed at 1 kλ as below 1 kλ, the window function is expected to dominate the shape. The size of each bin was chosen by inspecting the weights associated with bins of 1 kλ size. We found that choosing a bin with same number of points as the innermost bins, forced us to put all the points in one bin. Hence, as a reasonable compromise between having sufficient number of bins and sufficient number of points in each bin, the bins beyond a uv-distance of 4 kλ were chosen to have nearly half the points as in the innermost bins.

Fig. 9.12 shows the real part of derived C'_{ij} for channel number 70 (plotted on a log

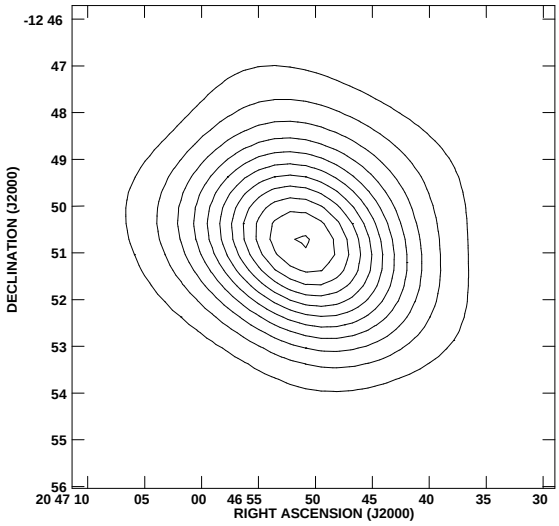

Figure 9.11: HI map for DDO 210 in channel number 70, imaged using the uv distribution upto 0.8 k λ.

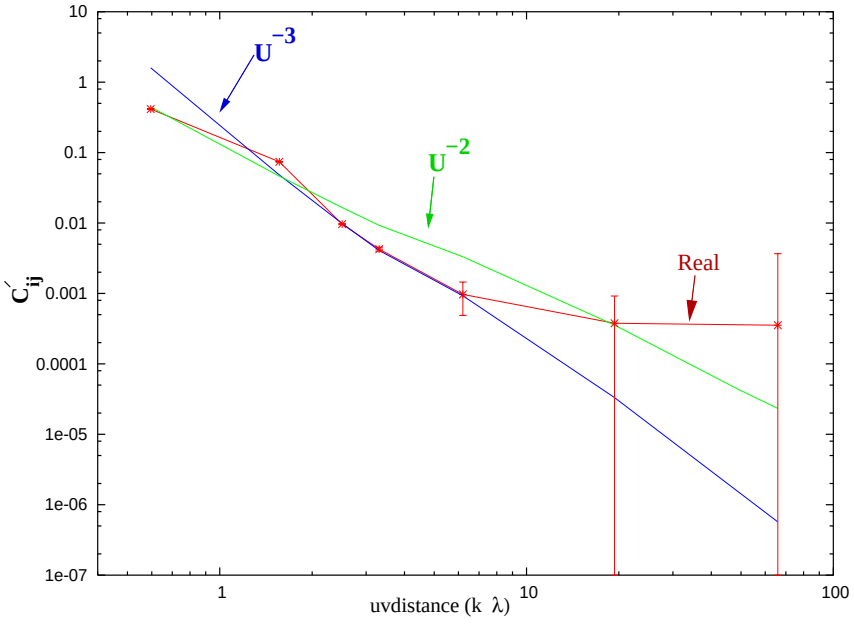

Figure 9.12: The real part of the absolute value of C'_{ij} (red) plotted against the uv-distance in the logscale for channel number 70. The model power spectra with slope α=2 (green) and $\alpha = 3$ (blue) are also shown. Only the positive values of C'_{ij} are plotted.

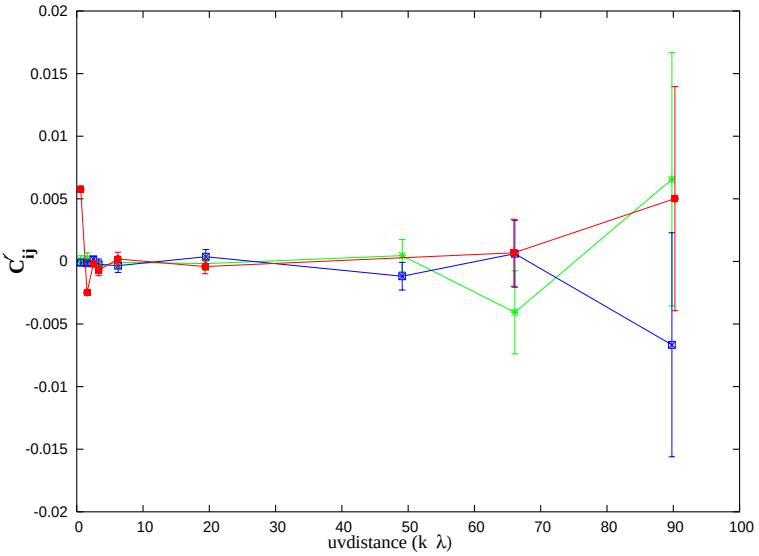

Figure 9.13: C'_{ij} plotted as a function of uv distance. Red curve shows the imaginary part of C'_{ij} for channel number 70. Green and blue curves show the real and imaginary part of C'_{ij} respectively, for a line free channel, viz. channel number 25.

scale), whereas Fig. 9.13 shows the real and imaginary part of C'_{ij} (plotted on the linear scale), estimated from a line free channel viz. channel number 25, along with the imaginary part of C'_{ij} from a line channel viz. 70. The errorbars on C'_{ij} were estimated from 10 line free channels, on either side of channels with emission. The errorbars are defined as the scatter in C'_{ij} (computed in each line free channel with the same binning as for channel with emission). We find that the real part of C'_{ij} shows a non zero signal upto 6kλ (within the errorbars). Further, real part of C'_{ij} appears to fall like a power law over a range of uv-scales from $\sim$ 1 kλ to 6 kλ. As the bins used for averaging the data are very wide (specially for large uv-distances), the signal is much stronger at the near edge of the bin than the far edge of the bin, which could inturn bias the binned data towards shallower slope. Inorder to check the effect of weighted averaging in large bins on the slope of power spectrum, a model power spectrum was generated assuming a power law functional form with an index α (i.e $U^{-\alpha}$). The model power spectrum was averaged in bins in exactly the same way as done for the observed power spectrum (i.e. using the same distribution of visibility points). Various values of the power law index α were tried. As seen in Fig. 9.12, α=3 provided a reasonable visual fit to the observed C'_{ij} (except in the innermost bin, where the effect of window function could be important). For comparison, the model power spectrum with α=2 is also shown. We note that the slope of α=3 is selected from the visual fit; we have

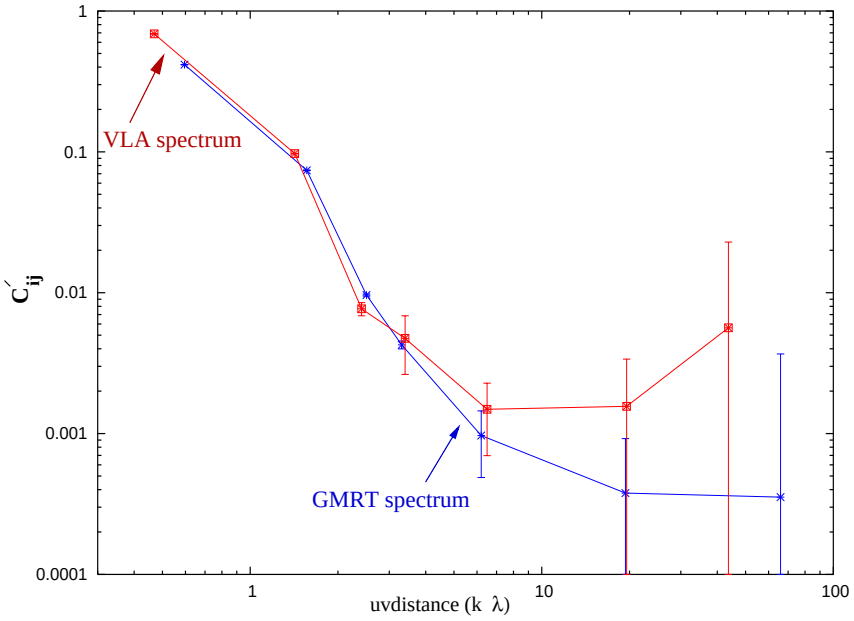

Figure 9.14: The absolute value of the real part of C'_{ij} for channel no 70 using the VLA data (shown in red) and the GMRT data (blue).

not attempted a least square fitting of the log of C'_{ij} against log of uv-distance. Fig. 9.14 shows the real part of C'_{ij} derived from the VLA data in exactly the same way as for the GMRT data. As can be seen, C_{ij} obtained from the GMRT data shows a good match to that obtained from the VLA data, providing a robust check of the reality of the signal.

9.5 Discussion

As seen in previous sections, we have developed a visibility based formalism for obtaining the power spectrum of the HI intensity fluctuations in faint dwarf galaxies, where the expected signal is very weak. We find that the statistical estimator obtained by correlating the visibilities corresponding to adjacent baselines is a measure of power spectrum of the HI intensity fluctuations. In the case of faint dwarf galaxies, where the expected signal is weak, this estimator is more ideal than the estimators obtained by correlating the visibilities with themselves (as done in the case of our galaxy) or obtained by correlating the visibilities in adjacent frequency channels.

The technique of using the visibility correlations as a statistical estimator of power spectrum of the HI intensity fluctuations has been proposed previously to determine the large scale HI distribution in the universe at earlier epochs. As the expected signal from the

individual HI clouds at high redshifts is too weak to be detected directly by existing radio telescopes, the statistical approach to detect the signal is more appropriate. Bharadwaj & Sethi(2001) have shown that the power spectrum of HI distribution due to density inhomogeneities of the HI distribution at high redshifts are related to the visibility correlation. Hence, a statistical estimator constructed directly from the visibilities measured in a radio interferometric observations can be used for probing the large scale structure in the universe at high redshifts. Similarly, the analysis of the interferometric observations of cosmic microwave background fluctuations also rely on very similar statistical estimators to determine the power spectrum of the CMBR (e.g. [6]).

9.5.1 Power spectrum of DDO 210

As seen in Sect. 9.4, the power spectrum of the HI intensity fluctuations in dwarf galaxy DDO 210 is a power law, with a slope of ~ -3, over a range of spatial scales from ~ 1000 pc to 160 pc. A slope of ~ -3 is also estimated from the HI emission in our own galaxy (on spatial scales of ~ 5 pc to 200 pc), by Crovisier & Dickey(1983) and Green(1993), respectively, and for SMC (on spatial scales between 4 kpc to 30 pc; Stanimirovic et al. 1999).

The power-law nature of the observed power spectrum, over a wide range of scales, is usually interpreted in terms of a large scale turbulence in the interstellar medium. The turbulence gives rise to density fluctuations, which lead to the observed intensity fluctuations in the HI distribution [8]. Lazarian & Pogosyan (2000) analyzed in details the real life situation, where the observed intensity fluctuations in HI emission arise from both density fluctuations as well as velocity fluctuations. Lazarian & Pogosyan (2000) found that the power index of the observed intensity fluctuations depends on the "thickness" of the velocity channel used for estimating the power spectrum. Whether a velocity channel is "thick" or "thin" depends upon the turbulent velocity dispersion. A velocity channel is "thick" when the turbulent velocity dispersion is less than the velocity channel thickness, otherwise it is "thin". The velocity resolution of an interferometric observation represents the thinnest slicing of the data available. However several channels can be combined to provide a thicker slice. In the case of thin velocity slices, the velocity fluctuation dominates, whereas in the case of very thick velocity channel, the velocity information is averaged out and the slope of intensity fluctuation is the same as the slope of the density fluctuations. Hence, the effect of density and velocity fluctuations on the observed intensity fluctuations can be disentangled from the change of the power index of the intensity fluctuation with the change in the velocity width of the channel used for estimating the power spectrum. One can understand this intuitively as follows; when one increase the velocity interval over which the intensity is

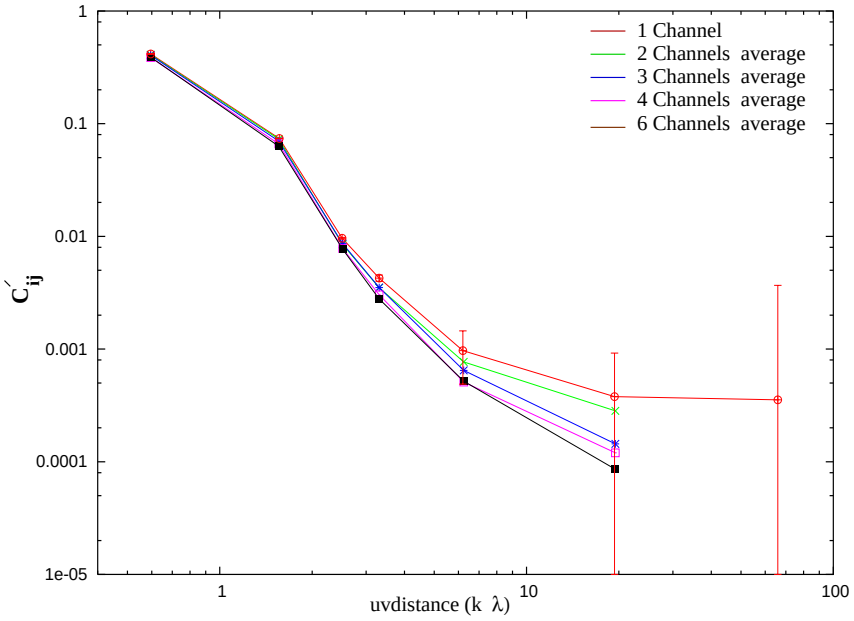

Figure 9.15: The real part of C'_{ij} plotted on the log scale for the GMRT data. Only the positive values of C'_{ij} are plotted. Plots of various colours show the number of channels averaged before estimating C'_{ij}. The errorbar of C'_{ij} is obtained from the single channel data.

being averaged, the signal to noise will increase for scales at which the turbulent line velocity width is greater than the channel width, but will decrease for scales at which the reverse is true. Hence, if the density and the velocity fluctuation power spectrum have different slopes, then this effect will leave the imprint on the channel averaged intensity fluctuation spectrum.

Inorder to check the behavior of the power spectrum with the change in the width of the velocity channel, the visibilities in various channels were averaged and C'_{ij}s were estimated using the averaged visibilities. Fig. 9.15 shows the real part of C'_{ij} derived by averaging the visibilities in 2, 3, 4 and 6 adjacent channels. As can be seen, within the errorbars no signature of steepening of C'_{ij} is seen with an increase in the width of the velocity channel. This suggests that many velocity channels can be averaged to improve the signal-to-noise on the derived power spectrum.

9.6 Future work

As seen in this chapter, we have developed a visibility based formalism for obtaining the power spectrum of the HI intensity fluctuations in faint dwarf galaxies, where the expected signal is very weak. We have shown that the statistical estimator obtained by correlating the visibilities corresponding to adjacent baselines is a practical estimator of the power spectrum of the HI intensity fluctuations in faint dwarf galaxies. The derived formalism was applied to one of the dwarf galaxies in our sample, DDO 210 for which both GMRT and VLA data were available. Using this estimator, independently on the GMRT and the VLA data, we could reliably derive a power-law power spectrum upto 6 kλ. A good match between the power spectrum derived from the two independent datasets, obtained from two different telescopes, provide a robust check on our technique and on the reality of the signal. Further, we found that the derived power spectrum for DDO 210 falls as a powerlaw with a slope ~ 3; this slope matches with the slope derived from the power spectrum of HI intensity fluctuations in brighter galaxies using other techniques. However the slope for DDO 210 has been selected from the visual fit to the binned data; ideally, a more robust method of determining the slope is a least square fit to the derived power spectrum from the unbinned data. A statistically precise statement about the distance to which we can measure the power spectrum (which from Fig. 9.12 seems to be somewhere in the 6$-$20 kλ range) would be good. As the work presented in this chapter was mainly focussed on validating the technique developed, a detailed study of the slope of the derived power spectrum was hence not explored. This will be taken up as a follow-up work. Finally, applications of the technique developed to derive the power spectrum of other faint dwarf galaxies in our sample and its scientific implications on the nature of the neutral ISM in dwarf galaxies will be taken up as a future work.

Appendix-I

Consider a galaxy projected on the plane of the sky. Let (l, m) be the direction cosines in the plane of the sky, relative to the pointing center. The HI specific intensity distribution in the galaxy at frequency ν is

$$I_\nu(l,m) = W_\nu(l,m)\ [1 + \delta I(l,m)] \tag{9.9}$$

where $W_\nu(l,m)$ is the large scale HI distribution in the galaxy at frequency ν, while $\delta I(l,m)$ is the small scale HI fluctuations. Since $I_\nu(l,m)$ is a Fourier transform of visibility function measured by an interferometer, the visibility $V_\nu(u,v)$ on a baseline with coordinates (u,v), in a frequency channel ν, is given by

$V_\nu(u,v) = \int\int I_\nu(l,m)\ e^{-j2\Pi(ul+vm)}\ dl\ dm$

Fourier transform of $W_\nu(l,m)$ i.e. $\tilde{W}(u,v)$ is peaked at (u,v)=0 and falls sharply with the increasing uv-distance. If the HI emission fills the whole telescope beam, the width of $\tilde{W}(u,v)$ is inverse of the primary beam of the telescope. On the other hand, if the HI emission from a galaxy is smaller than the primary beam, the width of $\tilde{W}(u,v)$ is the inverse of the total HI extent in that galaxy. Hence first term in Eqn. (9.9) is only dominant at small baselines, and can be neglected at longer baselines. Hence, from Eqn. (9.9), at longer baselines

$$V_\nu(u,v) = \int\int \delta I\ W_\nu(l,m)\ e^{-j2\Pi(ul+vm)}\ dl\ dm$$

Therefore,

$$\begin{aligned}\langle V_\nu(u,v)\ V_\nu^*(u,v)\rangle \ &= \ \int\int\int\int \langle \delta I(l,m)\ \delta I(l',m')\rangle\ W_\nu(l,m)\ W_\nu(l',m') \\ &\quad e^{-j2\pi[u(l-l')+v(m-m')]}\ dl\ dm\ dl'\ dm'\end{aligned}$$

We assume that

$$\langle \delta I(l,m)\delta I(l',m')\rangle = \rho(l-l', m-m')$$

Further, let, $l - l' = \lambda$ and $m - m' = \mu$. This gives us

$$\langle V_\nu(u,v)\ V_\nu^*(u,v)\rangle = \int\int \rho(\lambda,\mu)\ e^{-j2\pi(u\lambda+v\mu)}\ [\int\int W_\nu(l,m)W_\nu(l-\lambda, m-\mu)\ dl\ dm]\ d\mu\ d\lambda$$

Therefore,

$$\langle V_\nu(u,v)\ V_\nu^*(u,v)\rangle = \int\int \rho(\lambda,\mu)\ \omega_\nu(\lambda,\mu)\ e^{-j2\pi(u\lambda+v\mu)}\ d\lambda\ d\mu \tag{9.10}$$

where $\omega(\lambda,\mu)$ is the convolution of W(l,m) with itself, i.e.

$\omega_\nu(\lambda,\mu) = \int\int W_\nu(l,m)\ W_\nu(l-\lambda, m-\mu)\ dl\ dm$

The Fourier transform of the autocorrelation function $\rho(l,m)$ gives the power spectrum of the intensity fluctuations, $P_{\rm HI}$(u,v). Hence, as seen from Eqn. 9.10, complex visibility squared is a convolution of the power spectrum with the Fourier transform of $\omega_\nu(\lambda,\mu)$ i.e. $\tilde{\omega}_\nu(u,v)$.

$\langle V_\nu(u,v)\ V_\nu^*(u,v)\rangle = \tilde{\omega}_\nu(u,v)\ \otimes\ P_{\rm HI}(u,v)$

Appendix-II

Consider a galaxy projected on the plane of the sky. We will assume that the kinematical major axis of the galaxy is parallel to the direction cosine l in the sky plane.

We assume that the HI specific intensity distribution at frequency ν is

$$I_\nu(l,m) = W_\nu(l,m)[1+\delta I(l,m)] \tag{9.11}$$

Further, we assume that if $\mathrm{I}_{\nu+\Delta\nu}$ is the intensity in the adjacent frequency channel $\nu+\Delta\nu$ to be correlated, the only difference between $\mathrm{I}_{\nu+\Delta\nu}$ and I_ν is that the centroid of emission in the two channels has shifted by an amount Δl, i.e.,

$$I_{\nu+\Delta\nu}(l,m) = W_\nu(l-\Delta l,m)[1+\delta I(l,m)] \tag{9.12}$$

Hence, if V_i and V_j are the visibilities corresponding to a baseline (u,v) at frequency ν and $\nu+\Delta\nu$ respectively, we get from Eqn. (9.11)

$$V_i(u,v) = \tilde{W}(u,v) + \int du'\,dv'\tilde{W}(u',v')\Delta(u-u',v-v') \tag{9.13}$$

and

$$V_j(u,v) = e^{-iu\Delta l}\tilde{W}(u,v) + \int du'\,dv' e^{-iu'\Delta l}\tilde{W}(u',v')\Delta(u-u',v-v') \tag{9.14}$$

where i and j refer to the frequency channel numbers. $\tilde{W}(u,v)$ and $\Delta(u,v)$ are the Fourier transforms of $W(l,m)$ and $\delta I(l,m)$ respectively.

Assuming that $\tilde{W}(u,v)$ is peaked around $(u,v)=0.0$ and falls off rapidly, we can approximate

$$V_i(u,v) = \tilde{W}(u,v) + \Delta(u,v)\int du'\,dv'\tilde{W}(u',v') \tag{9.15}$$

and

$$V_j(u,v) = e^{-iu\Delta l}\tilde{W}(u,v) + \Delta(u,v)\int du'\,dv' e^{-iu'\Delta l}\tilde{W}(u',v') \tag{9.16}$$

We also have

$$W(\Delta l,0) = \int du'\,dv' e^{-iu'\Delta l}\tilde{W}(u',v') \tag{9.17}$$

which gives us

$$V_i(u,v) = \tilde{W}(u,v) + W(0,0)\Delta(u.v) \tag{9.18}$$

and

$$V_j(u,v) = e^{-iu\Delta l}\tilde{W}(u,v) + W(\Delta l, 0)\Delta(u.v) \tag{9.19}$$

An estimator of the power spectrum, C_{ij}, is given as

$$C_{ij}(U) = \langle V_i(U) V_j^*(U) \rangle \tag{9.20}$$

where $U = \sqrt{u^2 + v^2}$ and $\langle\rangle$ denotes an average over all baselines of magnitude U oriented in different directions in the $u - v$ plane. At large U the first term in the RHS of Eqn. (9.18) and (9.19) can be dropped. Assuming homogeneous, isotropic turbulence and ignoring the galaxy inclination we have at large baselines

$$C_{ij}(U) = P_{\rm HI}(U) W(0,0) W(\Delta l, 0) \tag{9.21}$$

where $P_{\rm HI}(U)$ is the turbulence HI power spectrum. At small baselines, using $u = U\,\cos\theta$ and $v = U \sin\theta$ we have

$$C_{ij}(U) = \frac{1}{2\pi} \int_0^{2\pi} e^{-iU\cos\theta\Delta l} \mid \tilde{W}(U\cos\theta, U\sin\theta) \mid^2 \, d\theta \tag{9.22}$$

Assuming $\tilde{W}(u,v) = \tilde{W}(U)$ is isotropic, we have

$$C_{ij}(U) = \frac{\mid \tilde{W}(U) \mid^2}{2\,\pi} \int_0^{2\pi} e^{-i\cos\theta\Delta l\ U} \, d\theta \tag{9.23}$$

The integral gives a Bessel function J_0 and we have

$$C_{ij}(U) = \mid \tilde{W}(U) \mid^2 \ \ J_0(U\Delta l) \tag{9.24}$$

Appendix-III

If $V_\nu(u_i, v_i)$ and $V_\nu(u_j, v_j)$ are visibilities at a frequency ν, corresponding to two baselines (u_i, v_i) and (u_j, v_j) respectively, we find at longer baselines, from Eqn. 9.11

$$V_\nu(u_i, v_i) = \int\int \delta I(l,m)\ e^{j2\pi(u_i l + v_i m)}\ W_\nu(l,m)\ dl\ dm$$

$$V_\nu(u_j, v_j) = \int\int \delta I(l,m)\ e^{j2\pi(u_j l + v_j m)}\ W_\nu(l,m)\ dl\ dm$$

Correlating the visibilities of two different baselines at a given frequency gives

$$\begin{aligned}\langle V_\nu(u_i, v_i)\ V_\nu^*(u_j, v_j)\rangle \ \ = \ \ & \int\int W_\nu(l,m) W_\nu(l',m')\ \langle \delta I(l,m)\delta I(l',m')\rangle \\ & e^{j2\pi(u_i l - u_j l' + v_i m - v_j m')}\ dl\ dl'\ dm\ dm'\end{aligned}$$

Let $P(\mu,\gamma)$ be the Fourier transform of the autocorrelation function of intensity fluctuations $\rho(l,m)$ i.e.

$$\rho(l-l',m-m') = \int\int P(\mu,\gamma)\ e^{-j2\pi(\mu(l-l')+\gamma(m-m'))}\ d\mu\ d\gamma$$

where,

$$\rho(l-l',m-m') = \langle \delta I(l,m)\delta I(l',m')\rangle$$

This gives us,

$$\begin{aligned}\langle V_\nu(u_i,v_i)\ V_\nu^*(u_j,v_j)\rangle &= \int\int P(\mu,\gamma)[\int W_\nu(l,m)e^{j2\pi(l(u_i-\mu)+m(v_i-\gamma))}\ dl\ dm \times \\ &\quad \int W_\nu(l',m')e^{-j2\pi(l'(u_j-\mu)+m'(v_j-\gamma)))}\ dl'\ dm']\ d\mu\ d\ \gamma\end{aligned}$$

Hence, we get

$$\langle V_\nu(u_i,v_i)\ V_\nu^*(u_j,v_j)\rangle = \int\int P(\mu,\gamma)\ [\tilde{W}_\nu(u_i-\mu,v_i-\gamma)\times\tilde{W}_\nu^*(u_j-\mu,v_j-\gamma)]\ d\mu\ d\gamma$$

Writing in 2-D notation

$\langle V_\nu(\vec{U}_i)\ V_\nu^*(\vec{U}_j)\rangle = \int P(\vec{U})\ [\tilde{W}_\nu(\vec{U}_i-\vec{U})\times\tilde{W}_\nu^*(\vec{U}_j-\vec{U})]\ d^2\vec{U}$

Bibliography

[1] Bharadwaj, S. & Sethi, S. K., 2001, JA&A, 22, 293

[2] Crovisier, J. & Dickey, J. M., 1983, A&A, 122, 282

[3] Elmegreen, B. G., Kim, S. & Staveley-Smith, L., AJ, 2001, 548, 749

[4] Elmegreen, B. G. & Falgarone, E., 1996, AJ, 471, 816

[5] Green, D. A., 1993, MNRAS, 262, 327

[6] Hobson, M. P., Lasenby, A. N. & Jones, M., 1995, MNRAS, 275, 863

[7] Lazarian, A. & Pogosyan, D., 2000, ApJ, 537, 720

[8] Lazarian, A., 1995, A&A, 293, 507

[9] Stanimirovic, S., Staveley-Smith, L., Dickey, J. M., Sault, R. J., & Snowden, S. L., 1999, MNRAS, 302, 417

[10] Westpfahl, D. J., Coleman, P. H., Jordan, A. & Thomas, T., 1999, AJ, 117, 868

[11] Willett, K. W., Elmegreen, B. G. & Hunter, D. A., 2005, AJ, 129, 2186